



EX LIBRIS
UNIVERSITATIS
ALBERTENSIS

The Bruce Peel
Special Collections
Library

University of Alberta

Library Release Form

Name of Author: QI YANG

Title of Thesis: EFFECTS OF HYDROGEN ON PASSIVITY AND CORROSION
RELATED BEHAVIOR OF AUSTENITIC STAINLESS STEELS

Degree: DOCTOR OF PHILOSOPHY

Year this Degree Granted: 2000

Permission is hereby granted to the University of Alberta Library to reproduce single copies of this thesis, and to lend or sell such copies for private, scholarly or scientific research purpose only.

The author reserves all other publication and other rights in association with the copyright in the thesis, and except as herein before provided neither the thesis nor any substantial portion thereof may be printed or otherwise reproduced in any material form whatever without the author's prior written permission.

University of Alberta

**EFFECTS OF HYDROGEN ON PASSIVITY AND CORROSION
RELATED BEHAVIOR OF AUSTENITIC STAINLESS STEELS**

By

QI YANG



A thesis submitted to the Faculty of Graduate Studies and Research in partial fulfillment
of the requirements for the degree of DOCTOR OF PHILOSOPHY


in

MATERIALS ENGINEERING

DEPARTMENT OF CHEMICAL AND MATERIALS ENGINEERING

EDMONTON, ALBERTA

Fall, 2000



Digitized by the Internet Archive
in 2025 with funding from
University of Alberta Library

<https://archive.org/details/0162012629612>

University of Alberta

FACULTY OF GRADUATE STUDIES AND RESEARCH

The undersigned certify that they have read, and recommend to the Faculty of Graduate Studies and Research for acceptance, a thesis entitled **EFFECTS OF HYDROGEN ON PASSIVITY AND CORROSION RELATED BEHAVIOR OF AUSTENITIC STAINLESS STEELS** submitted by QI YANG in partial fulfillment of the requirement for the degree of DOCTOR OF PHILOSOPHY in MATERIALS ENGINEERING.

To my parents, my dear wife Jun, my lovely son Jim
and daughter Julia.

ABSTRACT

In this thesis, the effects of hydrogen on the passivity and corrosion related behavior of type 304 and 310 austenitic stainless steels have been investigated.

Hydrogen was introduced into specimens by applying a constant cathodic current density. It is found that higher charging current density or longer charging time lead to higher hydrogen amounts in the specimens. Cathodical hydrogen charging can cause surface martensite transformation and cracking. There are critical hydrogen charging conditions for the phase transformation and cracking of 304 stainless steel. The critical charging time decreases with increasing charging current density. Selective martensite dissolution and a high hydrogen concentration cause a high dissolution rate in the transpassive potential range.

Passive films on the stainless steels are found to have n-type semiconductivity. Also it is found that the films are highly disordered. The donor concentration increases with charging current density or charging time, but chloride ions in solution have no obvious effect on it. The results of photoelectrochemistry measurements show that hydrogen increases the disorder of the passive films.

Hydrogen in passive films greatly affects the passivity and the breakdown processes. This research clearly shows that hydrogen promotes the breakdown process and consequent pitting corrosion. Immersion tests show that hydrogen increases the pit

density and pit growth rate. However, hydrogen promotes the breakdown of passive films only when the chloride ions are present in the solution. Hydrogen and chloride ions have a synergistic effect on the anodic current. Hydrogen also enhances the effect of chloride ions on breakdown potential. It is found that hydrogen decreases the critical chloride concentration for the film breakdown. Stress can promote the breakdown of passive films so that with an increase in stress, the critical concentration decreases. The critical concentration is always lower for charged specimens than for uncharged specimens in the testing stress range.

Effects of hydrogen and chloride ions on the breakdown process of passive films are explained by connecting electronic properties with the breakdown behavior.

ACKNOWLEDGEMENTS

The author is deeply grateful to Dr. Jingli Luo for her supervision and encouragement extended throughout the whole course of this study.

Special thanks are extended to Dr. D. G. Ivey, Dr. R. L. Eadie, Dr. M. T. McDermott, Dr. R. Winston Revie, Dr. A. E. Mather and Dr. Z. H. Xu for their stimulating and greatly helpful suggestions during the progress of this research, and their kindness in enabling the author to conduct a substantial part of the work using the facilities.

The author would also give his thanks to Ms. T. Barker, Mr. S. Merali and Mr. B. Konzuk for their assistance. The author owes a lot of debt to his colleagues: Dr. M. Z. Yang, Dr. L. J. Qiao, Dr. N. Cui, Dr. P. He, Mr. J. Bulger, Mr. J. G. Yu and Mr. G. S. Weng.

Finally, The author would like to thank his wife, Ms. Jun Lu and his lovely son Jim Yang, for their selfless support.

Abstract.....	1
Acknowledgements	1
Table of Contents	1
List of Tables	1
List of Figures.....	1
List of Symbols	1
List of Abbreviations	1
Chapter 1. Introduction.....	1
REFERENCES	2
Chapter 2. Literature Review	4
2.1. HYDROGEN IN METALS	4
2.1.1. Sources of Hydrogen in Metals	4
2.1.1.1. During Manufacturing Processes	5
2.1.1.2. During Service	5
2.1.2. The Hydrogen Evolution Reaction and Hydrogen Absorption Reaction.....	6
2.1.2.1. The Mechanism of HER	6
2.1.2.2. Controlling Factors of the HAR.....	8
2.1.2.3. The Role of Environmental Species --- Hydrogen Promoters and Inhibitors	8
2.1.2.3.1. Hydrogen Promoters.....	8
2.1.2.3.2. Hydrogen Entry-Inhibiting Species	10
2.1.3. Existing Forms and Locations of Hydrogen in Metals.....	11
2.1.3.1. Solid Solution of Hydrogen	11
2.1.3.2. Hydrogen-Defect Interactions.....	11
2.1.3.2.1. Hydrogen-Point Defect Interactions	12
2.1.3.2.2. Hydrogen –Dislocation Interactions	12

2.1.3.2.3. Hydrogen-Surface Interactions	12
2.1.3.2.4. Hydrogen-Volume Defect Interaction	13
2.1.4. Effects of Hydrogen on the Properties of Metals	16
2.1.4.1. Hydrogen Induced Cracking and Blistering	16
2.1.4.2. Hydrogen Attack	17
2.1.4.3. Effects of Hydrogen on Corrosion Behavior	18
2.1.4.3.1. Effects of Hydrogen on Pitting Corrosion	18
2.1.4.3.2. Effects of Hydrogen on Intergranular and General Corrosion	21
2.1.4.3.3. Effect of Hydrogen on Anodic Dissolution	23
2.1.4.4. Hydrogen Embrittlement	24
2.2. PASSIVITY OF METALS	26
2.2.1. Theory of Passivity and Breakdown of Passive Films	26
2.2.1.1. Definition of Passivity	26
2.2.1.2. Types of Passive Films	27
2.2.1.3. Compositions and Structures of Passive Films	28
2.2.1.3.1. Irons	28
2.2.1.3.2. Stainless Steels	29
2.2.1.3.3. Presence of Hydrogen in Films	32
2.2.1.4. Theory of Passivation	33
2.2.2. Electronic Properties of Passive Films	38
2.2.2.1. Band Structures	38
2.2.2.2. Intrinsic Semiconductors	40
2.2.2.3. Extrinsic Semiconductors	40
2.2.2.4. Effects of Defects	42
2.2.2.5. Correlation between Electronic Properties and Corrosion Behavior of Passive Films	42
2.3. ELECTROCHEMICAL METHODS TO STUDY PASSIVITY AND BREAKDOWN OF PASSIVE FILMS	44
2.3.1. Measurements of Polarization Curves	44
2.3.2. Electrochemical Impedance Spectroscopy	46

2.3.3. Electrochemical Methods to Study Electronic Properties of Passive Films	47
2.3.3.1. Mott-Schottky Method	47
2.3.3.2. Photoelectrochemical Measurement	48
2.3.3.3. Polarization Measurement (Bianchi's Method)	52
REFERENCES	53

Chapter 3. Topic Selection and Experimental Approaches	61
3.1. TOPIC SELECTION	61
3.2. APPROACH METHODS	62
REFERENCES	64

Chapter 4. Experimental	65
4.1. EXPERIMENTAL MATERIALS	65
4.2. EXPERIMENTAL EQUIPMENT	67
4.3. EXPERIMENTAL SET-UP	67
4.3.1. Surface Preparations	67
4.3.2. Hydrogen Charging	69
4.3.3. Measurements of Amount of Diffusible Hydrogen in the Specimens	70
4.3.4. Detection of Phase Transformations by X-ray Diffraction Analysis	70
4.3.5. Immersion Tests	73
4.3.6. Electrochemical Measurements	73
4.3.6.1. The Typical Three-Electrode Cell	73
4.3.6.2. Potentiodynamic Polarization and Cyclic Potentiodynamic Polarization (CPP) Measurements	75
4.3.6.3. Potentiostatic Measurements	76
4.3.6.4. AC Impedance Measurements	77
4.3.6.5. Mott-Schottky Measurements	77
4.3.6.6. Photoelectrochemical Measurements	79

REFERENCES	80
------------------	----

Chapter 5. Hydrogen-Induced Martensitic Phase Transformation, Surface Cracking and Anodic Dissolution..... 81

5.1. EFFECTS OF CHARGING PARAMETERS ON THE AMOUNT OF HYDROGEN IN TYPE 304 STAINLESS STEEL	82
5.1.1. Hydrogen Release Curves	82
5.1.2. Kinetics of Hydrogen Release	84
5.1.3. Effects of Hydrogen Charging Parameters on the Amount of Hydrogen in the Specimens.....	87
5.2. EFFECT OF CATHODIC CHARGING ON PHASE TRANSFORMATION OF TYPE 304 STAINLESS STEEL	88
5.2.1. X-Ray Diffraction (XRD) Analyses.....	88
5.2.2. Metallographic Observations Immediately after Charging	91
5.2.3. Critical Charging Conditions for Martensite Transformation.....	91
5.3. EFFECTS OF HYDROGEN ON SURFACE CRACKING OF TYPE 304 STAINLESS STEEL	97
5.3.1. In Situ Observation of Surface Cracking Process during Aging.....	97
5.3.2. Critical Charging Conditions for Surface Cracking	97
5.3.3. Surface Cracking Sites	100
5.4. RELATIONSHIP BETWEEN MARTENSITE TRANSFORMATION AND CORROSION	103
5.4.1. Effects of Hydrogen Charging on Weight Loss	103
5.4.2. Effect of Aging on Weight Loss after Hydrogen Charging	106
5.5. HYDROGEN-INDUCED SURFACE CRACKING ON 310 STAINLESS STEEL	106
5.5.1. X-ray Spectra.....	106
5.5.2. Surface Cracking	107
5.6. DISCUSSION.....	110

5.7. SUMMARY	112
REFERENCES	113

Chapter 6. Effects of Hydrogen on Electronic Properties of Passive Films 115

6.1. ELECTRONIC PROPERTIES OF PASSIVE FILMS MEASURED BY THE MOTT-SCHOTTKY METHOD	116
6.1.1. Effects of Hydrogen on the Electronic Properties of Passive Films on Type 310 Stainless Steel.....	116
6.1.2. Effects of Hydrogen on Electronic Properties of Passive Films on Type 304 Stainless Steel.....	119
6.1.2.1. Mott-Schottky Plots Measured in 0.5 M H ₂ SO ₄	119
6.1.2.2. Mott-Schottky Plots Measured in the Cl ⁻ Free Borate Buffer Solution.....	119
6.1.2.3. Mott-Schottky Plots Measured in the Cl ⁻ Containing Borate Buffer Solution---Effects of Cl ⁻ on the Donor Concentration.....	126
6.1.2.4. Effects of Hydrogen-Induced Martensite and Surface Cracking on Mott-Schottky Plots	128
6.2. PHOTOELECTROCHEMISTRY MEASUREMENTS	129
6.2.1. Variation of Light Intensity with Wavelength.....	129
6.2.2. Photocurrent Spectra	130
6.2.3. Potential Dependence of Photocurrent	136
6.2.4. Photocurrent Transients.....	142
6.3. DISCUSSION.....	142
6.4 SUMMARY	145
REFERENCES	146

Chapter 7. Effects of Hydrogen on the Passivity and Breakdown of Passive Films 148

7.1. IMMERSION TESTS	149
----------------------------	-----

7.1.1. Methods to Measure the Pit Density, Size and the Percentage of the Apparent Surface Area Occupied by Pits.....	149
7.1.2. Results of Immersion Tests for 310 Stainless Steel	151
7.1.2.1. Effects of Hydrogen on Pitting Initiation.....	151
7.1.2.2. Effects of Hydrogen on Pit Growth	157
7.1.2.3. Effects of Inclusions on the Pitting Corrosion.....	163
7.1.3. Results of Immersion Tests of 304 Stainless Steel.....	166
7.2. STATISTICAL INVESTIGATIONS OF EFFECTS OF HYDROGEN ON PITTING, PROTECTION AND CORROSION POTENTIALS.....	169
7.2.1. Results	169
7.3. CRITICAL CONCENTRATION OF CHLORIDE IONS FOR FILM BREAKDOWN	173
7.3.1. Current Responses of Uncharged Specimens.....	174
7.3.2. Effects of Hydrogen on Breakdown of Passive Films.....	176
7.3.2.1. Current Responses of Charged Specimens	176
7.3.2.2. Effects of Concentration of Chloride Ions on Breakdown of Passive Films	176
7.3.2.3. Effects of Hydrogen on Initiation Time and Critical Concentration of Chloride Ions for Film Breakdown.....	179
7.3.2.4. Effects of Stress on Breakdown of Passive Films	182
7.3.2.4.1. Effects of Stress on Critical Concentration of Chloride Ions for Breakdown of Passive Films	182
7.3.2.4.2. Surface Morphologies of Specimens after Potentiostatic Tests	185
7.4. HYDROGEN-ENHANCED EFFECTS OF CHLORIDE IONS ON PASSIVITY	188
7.4.1. Hydrogen Enhanced Effects of Cl^- on Breakdown Potential	188
7.4.1.1. Effects of Hydrogen on Breakdown Potential for Specimens in a Chloride-Free Solution.....	188
7.4.1.2. Effects of Chloride Ions on Breakdown Potential for Uncharged Specimens	189
7.4.1.3. Effects of Hydrogen on Breakdown Potential for Specimens in Chloride-	

Containing Solutions.....	191
7.4.2. Synergistic Effects of Hydrogen and Cl^- on Anodic Current Density in Passive Range.....	194
7.4.3. Effects of Hydrogen and Cl^- on Polarization Resistance and Double Layer Capacitance	198
7.5. DISCUSSION.....	200
7.5.1. Increase in $\text{H}_2\text{O}/\text{O}^{2-}$ and $\text{OH}^-/\text{O}^{2-}$ Ratios	203
7.5.2. Interactions between Hydrogen Protons and Defects in Passive Films	204
7.5.3. Changes in Electronic Structures.....	205
7.6. SUMMARY	212
REFERENCES	213
Chapter 8. Summary and Future Work.....	217
8.1. SUMMARY	217
8.2. SUGGESTIONS AND FUTURE WORK	219
Appendix: Publications and Presentations during Graduate Study.....	222
A.1. PAPERS AND PRESENTATIONS RELATED TO THIS THESIS.....	222
A.1.1. Refereed Papers: Published & Accepted	222
A.1.2. Refereed Conference Papers.....	223
A.1.3. Papers in Conference Proceedings	223
A.1.4. Conference Presentations	224
A.2. PUBLICATIONS AND PRESENTATIONS RELATED TO OTHER RESEARCH TOPICS	224
A.2.1. Refereed Paper(s)	224
A.2.2. Paper(s) in Conference Proceedings.....	225
A.2.3. Conference Presentations	225

LIST OF TABLES

Table 2-1. Hydrogen-Trap Interactions in Ferrous Alloys

Table 4-1. Chemical Composition (wt%) of USN-S30400 Stainless Steel

Table 4-2. Chemical Composition (wt%) of USN-S31000 Stainless Steel

Table 4-3. X-Ray Diffraction Peaks Used in the Quantitative Determination of Phase Components

Table 7-1. The change in the pitting initiation time with the charging current density.
The charging time is 16 hours.

Table 7-2. Test of the Hypothesis $\sigma_H^2 = \sigma_{NH}^2$ against the Alternative $\sigma_H^2 > \sigma_{NH}^2$

Table 7-3. Effects of Hydrogen and [Cl⁻] on Open Circuit Potential (U_{corr}), Passive Current Density (i_p) and Breakdown Potential (U_b) or Transpassive Potential (U_{tp})

LIST OF FIGURES

Figure 2-1. The consecutive steps of the hydrogen evolution reactions.

Figure 2-2. Portion of the Periodic Table showing the location of promoter elements.

Figure 2-3. A schematic view of energy relations in gas-metal equilibrium, including trapping.

Figure 2-4. Hydrogen-induced surface blister in an iron single crystal.

Figure 2-5. Effect of permeated hydrogen and aging of the passive film on anodic polarization curves for type 304 stainless steel. (a) just after the solution was heated to 343 K, (b) after 24 h of standing without hydrogen charging, (c) after 24 h of hydrogen charging. The solution used is 0.5 M NaCl + 0.1 M Na₂SO₄.

Figure 2-6. Effect of 70 ppm chloride ion in the electrolyte and of atomic hydrogen injected into the passivating film on nickel on the anodic current density at 400 mV (SCE).

Figure 2-7. Change of intergranular corrosion rate in Strauss solution for Type 304 and Type 304L steels sensitized at 923 K and exposed to 27 MPa hydrogen at 723 K for 16 hours.

Figure 2-8. Five types of passive films.

Figure 2-9. Polymeric Hydrated Oxide Model. (a) Dissolution of metallic ions leading to film formation; (b) Cl⁻ ions replace water molecules resulting in breakdown of the film.

Figure 2-10. The bipolar model.

Figure 2-11. The schematic of band structure.

Figure 2-12. The band structures of p-type (a) and n-type (b) semiconductors.

Figure 2-13. Types of space charge layers on n-type semiconductor: (a) depletion layer, (b) accumulation layer and (c) inversion layer.

Figure 2-14. Schematic representation of a illuminated p-type (a) and n-type (b) passive films under depletion conditions and of an insulating film under flat band conditions with a simultaneous excitation in the film ($h\nu_1$) and in the underlying metal ($h\nu_2$) (c).

Figure 2-15. Schematic representation of photoexcitation process in a passive film: (1) extended to localized states; (2) localized states to extended states and (3) photoexcitation into a localized state followed by electron tunneling into the electrolyte.

Figure 2-16. Typical current density curves for partial electron-transfer currents in the conduction band and in the valence band

Figure 4-1. A schematic of the reactions and processes involved in cathodically charging in an acid.

Figure 4-2. Setup for measurements of diffusible hydrogen in specimens.

Figure 4-3. Setup for most of electrochemical measurements.

Figure 4-4. The details of the specimen holder.

Figure 4-5. Setup for the electrochemical measurements of stressed specimens.

Figure 4-6. The electrochemical cell for the photoelectrochemical measurement (a) and the experimental setup (b).

Figure 5-1. The amount of hydrogen vs. release time curves of the specimens charged at 10 mA/cm^2 for different charging time for 304 stainless steel.

Figure 5-2. The change in the slope of the straight-line section of hydrogen release curves with charging times. The charging current density is 10 mA/cm^2 .

Figure 5-3. The change in the slope of the straight-line section of hydrogen release curves with charging current density. The charging time is 4 hours.

Figure 5-4. The time at deviation from the linear section in the hydrogen release curves changes with charging current density. The charging time is 4 hours.

Figure 5-5. The time at deviation from the linear section in the hydrogen release curves changes with charging time. The charging current density is 10 mA/cm^2 .

Figure 5-6. The amount of hydrogen escaped from the specimens charged at 10 mA/cm^2 for 24 hours at room temperature.

Figure 5-7. XRD spectra of the uncharged specimen and specimens charged at 20 mA/cm^2 for different charging periods.

Figure 5-8. Changes in martensite volume percentage with charging time for the specimens charged at 20 mA/cm^2 . The measurements were performed after being aged at room temperature for 24 hours.

Figure 5-9. The optical micrographs of the uncharged 304 stainless steel specimen (a), and the specimens charged at 20 mA/cm² for 2 minutes (b), 7 minutes (c) and 30 minutes (d). The photos were taken immediately after charging and etching.

Figure 5-10. Surface relief observed immediately after hydrogen charging. The specimen was charged at 20 mA/cm² for 15 minutes. Surface relief indicates the crystallographic direction of martensite.

Figure 5-11. The critical charging conditions for hydrogen induced martensite transformation. X: 1050°C, 1 hour annealed specimen, austenite; Δ: 1100°C, 2 hours annealed specimen, austenite; ■: 1050°C, 1 hour annealed specimen, austenite and martensite; ◆: 1100°C, 2 hours annealed specimen, austenite and martensite.

Figure 5-12. The concentrations of hydrogen corresponding to the critical charging conditions for martensite transformation.

Figure 5-13. The *in-situ* observation of surface cracking during aging after the specimen was charged at 20 mA/cm² for 12 hours. Aging time: (a) 6 minutes; (b) 15 minutes; (c) 60 minutes; (d) 240 minutes; and (e) 360 minutes.

Figure 5-14. The critical charging conditions for surface cracking. The dash line represents the critical charging conditions for martensite transformation.

Figure 5-15. The surface cracking sites. The photos were taken from the specimen charged at 20 mA/cm² for 4 hours and aged for 4 hours.

Figure 5-16. The crack density vs. charging time curve of specimens charged at 200 mA/cm². Crack densities were measured after aging for 4 hours.

Figure 5-17. The average crack length vs. charging time curve for the specimens charged at 200 mA/cm². Crack lengths were measured after aging for 4 hours.

Figure 5-18. The photomicrograph of a specimen charged at 20 mA/cm² for 16 hours, aged for 4 hours and then etched.

Figure 5-19. The weight loss vs. charging time curve. The specimens were polarized at 1.2V vs. SCE for 10 minutes in a 0.5 M H₂SO₄ + 0.1 M HCl solution. The specimens had been previously charged with hydrogen at 2 mA/cm² for different times.

Figure 5-20. The corroded surface of the specimen charged at 2 mA/cm² for 40 minutes. The specimen was corroded at 1.2 V vs. SCE for 1 minute in a 0.5 M H₂SO₄ + 0.1 M HCl solution.

Figure 5-21. Weight loss vs. aging time curve. The specimens were hydrogen charged at 2mA/cm^2 for 1 hour, aged and then corroded in a $0.5\text{M H}_2\text{SO}_4 + 0.1\text{ M HCl}$ solution at 1.2 V vs. SCE for 10 minutes.

Figure 5-22. The X-ray diffraction spectra of uncharged 310 stainless steel specimen and specimens charged at 20 mA/cm^2 after 24 hours' aging.

Figure 5-23. The surface morphologies of specimens of 310 stainless steel charged at 20 mA/cm^2 for different charging times: (a) 75 minutes, (b) 5 hours and (c) 16 hours. The specimens were observed after aging for at least 4 hours.

Figure 5-24. SEM surface morphology of a specimen of 310 stainless steel charged at 20 mA/cm^2 for 16 hours. The specimen was observed after aging for longer than 4 hours.

Figure 6-1. The capacitance, C , vs. potential, U , curves of the uncharged 310 SS specimen.

Figure 6-2. The capacitance vs. potential curve of the 310 SS specimen charged at 2 mA/cm^2 for 30 minutes.

Figure 6-3. The $1/C^2$ vs. U plots of the uncharged and charged 310 SS specimens.

Figure 6-4. Mott-Schottky plots of uncharged 304 stainless steel, pre-passivated at different potentials for 120 minutes in $0.5\text{M H}_2\text{SO}_4$ solution. The impedance was measured at 1000 Hz at 0.0125V/step .

Figure 6-5. Mott-Schottky plots of the uncharged and charged 304SS specimens, passivated at 0.5 V for 120 minutes in $0.5\text{M H}_2\text{SO}_4$ solution. The impedance was measured at 1000 Hz at 0.0125V/step .

Figure 6-6. Mott-Schottky plots of the uncharged and charged 304SS specimens, passivated at 0.7 V for 120 minutes in $0.5\text{M H}_2\text{SO}_4$ solution. The impedance was measured at 1000 Hz at 0.0125V/step .

Figure 6-7. The changes in donor concentrations of the charged and uncharged Type 304 stainless steel with passivating potential. The specimens were passivated at constant potentials for 2 hours before the measurements.

Figure 6-8. Mott-Schottky plots of the uncharged and charged specimens (charging time: 30 minutes) in Cl^- free solution. The specimens were passivated at 0.1 V for 2 hours before the measurements.

Figure 6-9. The change in donor concentration with hydrogen current density. The charging time is 30 minutes. The specimens were passivated in the chloride free borate buffer solution at a potential of 0.1 V vs. SCE for 2 hours.

Figure 6-10. Mott-Schottky plots of the uncharged and charged specimens (charging time: 30 minutes) in the Cl^- free solution. The specimens were passivated at 0.5 V for 2 hours before the measurements.

Figure 6-11. The change in the donor concentration with the charging current density. The specimens were passivated at 0.5 V for 2 hours before the measurements.

Figure 6-12. Mott-Schottky plot of type 304 stainless steel. The specimen had been hydrogen charged at 5 mA/cm^2 for 1 hour, and then passivated at 0.7 V for 2 hours.

Figure 6-13. The donor concentrations vs. charging current density plot.

Figure 6-14. Influence of the degree of Cr^{3+} substitution in $(\text{Fe}^{2+}\text{Fe}^{3+}_{2-x}\text{Cr}^{3+}_x)(\text{O}^{2-})_4$ on the donor ratio $N_{\text{D2}}/N_{\text{D1}}$.

Figure 6-15. x value vs. charging current density plot.

Figure 6-16. Mott-Schottky plots of 304 SS specimens charged at 5 mA/cm^2 for 30 minutes. The specimens were passivated at 0.1 V vs. SCE for 2 hours in borate buffer solution containing different $[\text{Cl}^-]$.

Figure 6-17. The change in donor concentration with $[\text{Cl}^-]$. The specimens were charged at 5 mA/cm^2 for 30 minutes, then passivated in the borate buffer solutions containing different $[\text{Cl}^-]$ for 2 hours.

Figure 6-18. The Mott-Schottky plots of the uncharged specimen and the specimen charged at 20 mA/cm^2 for 2 hours. The specimens were baked at 50°C for 72 hours before the measurements.

Figure 6-19. The variation of light intensity with the wavelength measured using a silicon diode.

Figure 6-20. Photocurrent action spectra of uncharged 310 stainless steel. Photocurrent was measured in the borate buffer solution at different measuring potentials.

Figure 6-21. Plots of $(I_{\text{ph}}*h\nu)^{0.5}$ vs. photon energy for the uncharged specimens passivated at 0.7V for 3.5 hours. Photocurrent was measured in the borate buffer solution at different measuring potentials.

Figure 6-22. Photocurrent action spectra of 310 stainless steel charged at 5 mA/cm² for 5 hours, passivated at 0.7V for 3.5 hours. Photocurrent was measured in the borate buffer solution at different measuring potentials.

Figure 6-23. Photocurrent action spectra of 310 SS charged at 10 mA/cm² for 5 hours and passivated at 0.7 V for 3.5 hours. Photocurrent was measured in the borate buffer solution at different measuring potentials.

Figure 6-24. Plots of $(I_{ph} \cdot h\nu)^{0.5}$ vs. photon energy for 310 stainless steel charged at 5 mA/cm² for 5 hours, passivated at 0.7V for 3.5 hours. Photocurrent was measured in the borate buffer solution at different measuring potentials.

Figure 6-25. Plots of $(I_{ph} \cdot h\nu)^{0.5}$ vs. photon energy for 310 SS charged at 10 mA/cm² for 5 hours and passivated at 0.7V for 3.5 hours. Photocurrent was measured in the borate buffer solution at different measuring potentials.

Figure 6-26. The change in the gap energy with the charging current density.

Figure 6-27. The changes in photocurrent with charging current density. Specimens were passivated at 0.7V for 3.5 hours. Photocurrent was measured in the borate buffer solution at 0.6 V.

Figure 6-28. Log I_{ph} vs. $h\nu$ plots of the uncharged specimens as derived from photocurrent spectra measured at different potentials.

Figure 6-29. Log I_{ph} vs. $h\nu$ plots as derived from photocurrent spectra measured at different potentials. The samples were charged at 5 mA/cm² for 5 hours, then passivated at 0.7 V for 3.5 hours in the borate buffer solution.

Figure 6-30. Log I_{ph} vs. $h\nu$ plots as derived from photocurrent spectra measured at different potentials. The samples were charged at 10 mA/cm² for 5 hours, then passivated at 0.7 V for 3.5 hours in the borate buffer solution.

Figure 6-31. The photocurrent vs. photon energy curves of the uncharged and charged specimens.

Figure 6-32. The change in disorder energy (kT/γ) with charging current density.

Figure 6-33. Plots of I_{ph} vs. potential for the uncharged sample. The specimen was passivated at 0.7V for 3.5 hours in the borate buffer solution, then photocurrent was measured.

Figure 6-34. Potential dependence of photocurrent of 310 SS charged at 5 mA/cm^2 for 5 hours and passivated at 0.7V for 3.5 hours in the borate buffer solution. Specimens were illuminated with monochromatic light.

Figure 6-35. Photocurrent transients of uncharged samples obtained at 0.6 V under monochromatic illumination [(a) and (b)] and white light (c).

Figure 6-36. Schematic representation for direct (1) and indirect (2) optical transitions from the valence band to the conduction band: (a) maxima and minima of the bands coincident; (b) maxima and minima of the bands non-coincident; (c) optical transitions when some of the electron levels in the conduction band are occupied (n-type semiconductor).

Figure 6-37. Schematic representations of electron band structure with localized states of an n-type passive film (a) and possible density of state distribution in the band gap (b) at $U=U_{\text{FB}}$.

Figure 7-1. A 10 by 15 square grid is marked on each video print to measure the apparent area percentage occupied by pits.

Figure 7-2. The morphologies of the 310 specimens after immersion for different periods in 6% FeCl_3 solution: a) after immersion for 5 minutes, b) after 20 minutes, c) after 60 minutes and d) after 100 minutes. The specimens were charged at 2 mA/cm^2 for 16 hours.

Figure 7-3. Pitting morphologies for the different charged 310 specimens: (a) 0.1 mA/cm^2 , after 80 minutes of immersion; (b) 0.5 mA/cm^2 , after 20 minutes of immersion; (c) 2 mA/cm^2 , after 20 minutes of immersion. The charging time is 16 hours.

Figure 7-4. Pit density vs. immersion time. The charging time is 16 hours.

Figure 7-5. The histogram plots of pit size distribution of the 310 specimens charged at 2 mA/cm^2 for 16 hours after being immersed for different immersion periods.

Figure 7-6. The percentage of pits with a size $< X$ vs. X plots for the 310 specimens charged at 2 mA/cm^2 for 16 hours after being immersed for different immersion periods.

Figure 7-7. Pit diameter distribution histogram plots for the charged specimens after 20 minutes of immersion. Solid and dashed lines are fitted curves.

Figure 7-8. The percentage of pits with a size $< X$ vs. X plots for the specimens (charged at different current densities) after being immersed for 20 minutes.

Figure 7-9. Change in average pit diameter with immersion time. The R-squared values for the best-fit lines are given in the brackets.

Figure 7-10. Change in the percentage of apparent pit area with immersion time. The R-squared values for the best-fit lines are given in the brackets.

Figure 7-11. Changes in the pit density, α_D and α_p with hydrogen charging current densities, after 120 minutes of immersion.

Figure 7-12. The effects of pickling on the density of inclusions on the 310 surface: a) unpickled specimen and b) specimen pickled in 10% HNO_3 + 2% HF for 10 minutes at 50 °C.

Figure 7-13. Pit density vs. immersion time of the unpickled and pickled 310 specimens charged at 2 mA/cm^2 for 24 hours.

Figure 7-14. Change in the average pit diameter with immersion time for the pickled and unpickled 310 specimens charged at 2 mA/cm^2 for 24 hours. The R-squared values for the best-fit lines are given in the brackets.

Figure 7-15. The surface morphology of the pickled 310 stainless steel specimen which was charged at 2 mA/cm^2 for 16 hours. The specimen was immersed in 6% FeCl_3 solution for 80 minutes.

Figure 7-16. The pit density vs. charging current density plot. The 304 stainless steel samples were hydrogen charged at different current densities for 16 hours, then immersed in 3.5 % NaCl + 1% FeCl_3 solution for 2 hours.

Figure 7-17. A schematic representation of the cyclic potentiodynamic polarization curve.

Figure 7-18. The normal distribution plots of pitting potentials for the charged and uncharged 304 samples. The charging time was 30 minutes.

Figure 7-19. The normal distribution plots of protection potential for the charged and uncharged 304 specimens. The charging time was 30 minutes.

Figure 7-20. The normal distribution plots of corrosion potential for the uncharged and charged 304 specimens. The charging time was 30 minutes.

Figure 7-21. The changes in breakdown, protection and corrosion potentials with charging current density. The charging time was 30 minutes.

Figure 7-22. The hydrogen effect on the standard deviation values of corrosion, breakdown and protection potentials.

Figure 7-23. The current responses of unstressed and uncharged 304 specimens to the application of a potential of 0.3 V vs. SCE and additions of chloride ions of different concentrations.

Figure 7-24. The details of the current transients of the uncharged and unstressed 304 specimens that appeared due to the addition of 4000 ppm chloride ions during the application of a potential of 0.3 V vs. SCE.

Figure 7-25. The current responses of the uncharged and charged 304 specimens to the application of a potential of 0.4 V vs. SCE. The charging time was 30 minutes. The samples were passivated at 400 mV in the borate buffer solution for 10 minutes, followed by addition of 200 ppm NaCl.

Figure 7-26. The current responses of the uncharged and charged 304 specimens to the application of a potential of 0.3 V vs. SCE. The charging time was 30 minutes. The specimens were passivated at 300 mV in the borate buffer solution for 10 minutes, followed by addition of 200 ppm NaCl.

Figure 7-27. The current responses of the charged 304 SS specimens to the application of a potential of 0.3 V vs. SCE. The charging time was 30 minutes. The specimens were passivated at 300 mV vs. SCE in the borate buffer solution for 10 minutes, followed by addition of 100 ppm NaCl to the solution.

Figure 7-28. The reciprocal of initiation time for film breakdown vs. charging current density. The 304 SS specimens were charged at different charging current densities for 30 minutes, and then a constant potential of 300 mV was applied for 1 hour in the borate buffer solution. 100 ppm of NaCl was added to the solution 10 minutes after the beginning of the application of the potential.

Figure 7-29. The current responses of the 304 SS specimens (charged at 0.5 mA/cm^2 for 30 minutes) to the application of a constant potential. The specimens were passivated at 300 mV in the borate buffer solution for 10 minutes, then NaCl was added.

Figure 7-30. The current response to the application of a 300 mV vs. SCE potential on the 2 mA/cm^2 charged 304 SS specimens. The test solution was borate buffer solution. After 10 minutes from the beginning of the measurements, chloride ions were added.

Figure 7-31. The critical concentration of chloride ions for film breakdown vs. charging current density curve for the unstressed 304 SS specimens.

Figure 7-32. The current response curves of the 304 SS specimens charged at 2 mA/cm^2 for 30 minutes to the application of a constant potential of 0.3 V vs. SCE. The test solution is the borate buffer solution. After 10 minutes from the beginning of the measurement, sodium chloride was added into the solution. The specimens were tensile loaded at 50 MPa during the tests.

Figure 7-33. The current response curves for the 304 SS specimens charged at 2 mA/cm^2 for 30 minutes to the application of a constant potential of 0.3 V vs. SCE. 10 minutes after the beginning of the measurement, sodium chloride was added into the borate buffer solution. The specimens were loaded at a stress of 100 MPa during the tests.

Figure 7-34. The current response curves for the 304 SS specimens charged at 2 mA/cm^2 for 30 minutes to the application of a constant potential (0.3 V vs. SCE). 10 minutes after the beginning of the measurement, sodium chloride was added into the borate buffer solution. The specimens were loaded at a stress of 150 MPa during the tests.

Figure 7-35. The effects of stress on the critical chloride concentrations for the breakdown of passive films formed on uncharged 304 SS specimens and specimens charged at 2 mA/cm^2 for 30 minutes.

Figure 7-36. The surface morphology after potentiostatic tests of 304 SS specimens charged at 2 mA/cm^2 for 30 minutes. The applied stresses are a): 50 MPa and b): 100 MPa, respectively. The concentration of chloride ions added is 50 ppm.

Figure 7-37. The surface morphologies of the 304 SS specimen after testing. The morphology around the charged/uncharged boundary a) and at the charged side b). The specimen was stressed at 100 MPa during the potentiostatic test. The concentration of chloride added is 100 ppm.

Figure 7-38. The polarization curves of the uncharged and charged 304 SS specimens. For the charged specimens the charging time was 30 minutes. The curves were measured in a borate buffer solution without chloride solution.

Figure 7-39. The polarization curves of the uncharged and charged 304 SS specimens. The curves were measured after samples were baked at 50°C for 3 days and cathodic reduced at -0.3 V vs. U_{corr} for 1000 seconds in borate buffer solution.

Figure 7-40. The polarization curves of uncharged 304 SS specimens measured in the borate buffer solutions containing different chloride concentrations.

Figure 7-41. The polarization curves of the charged 304 SS specimens in the borate buffer solutions containing different Cl^- concentrations. The specimens were charged at 5 mA/cm^2 for 30 minutes.

Figure 7-42. The polarization curves of charged 304 SS specimens containing in borate buffer solution containing 100 ppm Chloride ions. The specimens were charged at different charging current densities for 30 minutes.

Figure 7-43. The synergistic effects of hydrogen and chloride on the breakdown potential of 304 SS.

Figure 7-44. The current decay curves of the uncharged 304 SS specimens. The specimens were passivated at 0.1 V vs. SCE in the borate buffer solutions containing different $[\text{Cl}^-]$.

Figure 7-45. The current decay curves for the 304 SS specimens charged at 5 mA/cm^2 for 30 minutes. The specimens were passivated at 0.1 V vs. SCE in the borate buffer solutions containing different $[\text{Cl}^-]$.

Figure 7-46. The change in anodic current density with chloride ion concentration for the uncharged 304 SS specimens and specimens charged at 5 mA/cm^2 for 30 minutes.

Figure 7-47. The change in the anodic current density with the charging current density in the Cl^- free borate buffer solution and the solution containing 300 ppm Cl^- .

Figure 7-48. The change in the increase of current density, due to the synergistic effect of hydrogen and chloride, with concentration of chloride ions.

Figure 7-49. The change in the current increase, due to the synergistic effect of hydrogen and chloride, with charging current density.

Figure 7-50. The effects of concentration of chloride ions or hydrogen charging current density on the Nyquist plot.

Figure 7-51. The changes in the polarization resistance and double layer capacitance of the uncharged 304 SS specimens with $[\text{Cl}^-]$ in the borate buffer solution. The specimens were passivated at 0.1 V in the borate buffer solutions containing different chloride concentrations for 2 hours, then the AC impedance was measured at 0.1 V in the same solutions.

Figure 7-52. The changes in the polarization resistance and double layer capacitance with charging current density. The AC impedance was measured in the Cl^- free borate buffer solution at 0.1 V vs. SCE after 2 hour passivation in the same solution and at the same DC potential.

Figure 7-53. The changes in the polarization resistance and double layer capacitance of the charged 304 SS specimens. The specimens were charged at 5 mA/cm^2 for 30 minutes, passivated at 0.1 V in the borate buffer solutions containing different chloride concentrations for 2 hours, and then the AC impedance was measured at 0.1 V in the same solutions.

Figure 7-54. Point Defect Model.

Figure 7-55. Schematic band structures at anodic polarization ($U > U_{\text{FB}}$), distributions of the localized states at the weak surface sites of passive films and their relationships with the breakdown of the passive films.

LIST OF SYMBOLS

C: capacitance

C_{dl} : double layer capacitance

C_H : hydrogen concentration

e: electron

E: energy

E_b : binding energy

E_c : conduction band edge

E_f : Fermi energy

E_g : gap energy

E_g^{opt} : optical gap energy

E_s : heat of solution of hydrogen

E_v : valence band edge

f: frequency

h: hole

i: current density

i_H : anodic current density contributed by hydrogen

$i_{H*[Cl^-]}$: current density increase due to the synergistic effect of hydrogen and chloride ions

$i_{[Cl^-]}$: current increase contributed by chloride ions only

i_0 : anodic current density of an uncharged specimen in a chloride-ion-free solution

i_p : anodic current density

I: current

I_{ph} : photo current

k: Boltzmann's constant

M_s : martensite start temperature

M_d : the highest temperature for martensite transformation by deformation

N: carrier concentration

N_d : donor concentration

R: resistance

R_p : polarization resistance

q : the charge of electron

S : variance

t : time

T : temperature

U : potential

U_{pass} : passivating potential

U_{corr} : corrosion potential

U_{FB} : flatband potential

U_b : pitting potential or breakdown potential

U_p : protection potential

V : vacancy

$V_{\text{O}^{\cdot\cdot}}$: oxygen vacancy in passive films

V_{M}^{χ} : cation vacancy

X^- : halide ion

Z : impedance

Z' : real component of impedance

Z'' : imaginary component of impedance

$\Delta\Phi_{\text{H}}$: the potential difference across a Helmholtz layer

α : optical absorption coefficient

ϵ : relative dielectric constant

ϵ_0 : the vacuum permittivity

η : anodic overpotential

λ : wavelength

σ : stress

ω : angular frequency

$h\nu$: photon energy

θ : diffraction angle or phase angle

LIST OF ABBREVIATIONS

AC:	alternating current
AFM:	atomic force microscope
CB:	conduction band
CE:	counter electrode
DC:	direct current
EDS:	energy dispersive spectrum
f/s:	film/solution interface
HAR:	hydrogen absorption reaction
HER:	hydrogen evolution reaction
m/f:	metal/film interface
PDM:	point defect model
RE:	reference electrode
RHEED:	reflection high-energy electron diffraction
XPS:	X-ray photoelectron spectrum
XRD:	X-ray diffraction
SCE:	standard calomel electrode
SEM:	scanning electron microscope
SIMS:	secondary ion mass spectroscopy
VB:	valence band
WE:	working electrode

Chapter 1. Introduction

Passivity is the situation in which metals are prevented from corroding by thin surface films. Such films are very important because they frequently provide efficient protection for highly reactive metals.

The loss of passivity gives rise to corrosion damage of either general or localized form. Localized breakdown processes of passive films, involved in crevice corrosion, pitting and stress corrosion cracking, are of considerable theoretical and practical interest. The nature of these films plays an important role in the processes that lead to their breakdown and consequent localized corrosion. As suggested by Kruger,¹ four properties of passive films are considered to affect breakdown: (1) thickness, (2) composition, (3) structure, and (4) electronic properties.

Because in most cases passive films are formed in aqueous solutions, the presence of hydrogen in passive films is inevitable and is now well established. As proposed by Okamoto and Shibata^{2,3}, passive films consist of a hydrated oxide. In their model, the bound H₂O plays a dual function to help film formation or be replaced by aggressive ions such as chloride ions.

It is well known that metal oxidation, cathodic protection, electroplating, acid pickling and other surface treatments accompany the reduction of hydrogen ions in aqueous acid solutions. During the corrosion process, one of the most important cathodic reactions, coupled with the anodic reaction, is the reduction of protons to hydrogen atoms. When a self-passivated metal pits in acids, the large anodic current density at the pits is balanced by a distributed hydrogen-generating current on the passivating film near the pits. Part of the generated hydrogen atoms will be absorbed and permeate into the metals.^{4,5} Hydrogen in metals would affect the electrochemical properties of passive films and consequently affect the corrosion processes.

Therefore the question, “What are the effects of hydrogen upon the properties of passive films?” arises. Investigating these effects will help the understanding of the corrosion mechanism. Even though several research efforts^{6,7,8,9,10} regarding effects of hydrogen on corrosion and passivity have been carried out, the phenomenon is still not well understood. It is very worthwhile to investigate the effects of hydrogen on the passivity and corrosion related behavior of alloys.

REFERENCES

1. J. Kruger, “Nature of Passive Film on Iron: Does It Affect Breakdown?”, *Advances in Localized Corrosion*, H. Issacs and U. Bertocci, J. Kruger and S. Smialowska, Eds., NACE, Houston, Texas, (1990): p.1.

2. G. Okamoto, Corros. Sci., 13 (1973): p. 471.
3. G. Okamoto and T. Shibata, Corros. Sci., 10 (1970): p.371.
4. L. J. Qiao, W. Y. Chu and C. M. Hsiao, Scripta. Metall., 22 (1988): p. 627.
5. R. Gee and Z. Y. Chen, Corros. Sci., 37 (1995): p. 2003.
6. S. I. Pyun, C. Lim and R. A. Oriani, Corros. Sci., 33 (1992): p.437.
7. A. A. Seys, M. J. Brabers, and A. A. Van Haute, Corrosion, 30 (1974): p.49.
8. Q. Yang, L. J. Qiao, S. Chiovelli and J. L. Luo, Corrosion, 54 (1998): p.628.
9. L. J. Qiao and J. L. Luo, Corrosion, 54 (1998): p.281.
10. R. Nishimura, H. Habazaki, A. Kawashima, K. Asami and K. Hashimoto, Materials Sci. and Eng., A134 (1991): p.1074.

Chapter 2. Literature Review

2.1. HYDROGEN IN METALS

2.1.1. Sources of Hydrogen in Metals

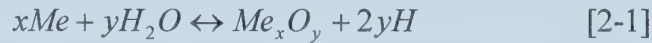
In 1864 Cailletet¹ discovered that when an iron specimen was immersed in dilute sulfuric acid a small amount of liberated hydrogen was absorbed by the metal. In 1922, Bodenstein² found that the quantity of atomic hydrogen entering into iron could be varied by application of a cathodic current. These two very simple observations demonstrate that hydrogen atoms generated may enter into the metallic lattice and permeate through the metal.

2.1.1.1. During Manufacturing Processes

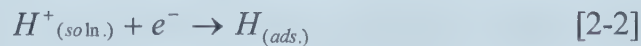
The entering of hydrogen in metals occurs during many manufacturing processes such as steel making and casting.³ Hydrogen can be introduced during cleaning, pickling, or electroplating and other surface treatment processes.^{4,5,6,7,8} Hydrogen is also absorbed into welds from contaminants and moisture in the welding arc during a welding operation and subsequently diffuses into the heat-affected zone (HAZ) in a metal.⁹

2.1.1.2. During Service

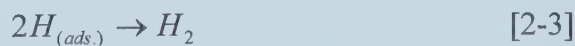
Hydrogen can be picked up during service. The most common source of hydrogen in metals is the atomic hydrogen liberated by the following reaction:



Probably the most insidious phenomenon which can result in hydrogen entry into metals is associated with corrosion.^{10,11} When a metal corrodes a loss of material occurs by anodic dissolution of the metal to form corrosion products. The electronically balancing cathodic reaction may involve the reduction of hydrogen ions producing hydrogen atoms. For example, in acids the cathodic reaction can be written as:¹²



The adsorbed hydrogen can either enter a metal in the atomic form or alternatively, combine to form molecular hydrogen gas and release from the metal surface:¹³



A frequently employed method of preventing the corrosion of steels in service is cathodic protection.¹⁴ This can be applied by the impressed current method or by

coupling to sacrificial anodes. In either case the objective is to cause a direct current flow to the surface of the protected structure to ensure that only cathodic reactions occur at the surface. Cathodic protection may involve hydrogen evolution and absorption. In some instances, dissociation of molecular hydrogen itself may also be a significant source of hydrogen. This is particularly true at high temperature.¹⁵

Hydrogen can also enter into metals in an environment containing sour gas such as H_2S . A pressure vessel encounters hydrogen absorption in a refinery environment containing H_2S .¹⁶

2.1.2. The Hydrogen Evolution Reaction and Hydrogen Absorption Reaction

The entry of hydrogen into metals is usually undesired because of the damage that hydrogen causes to the physical, chemical and mechanical properties of metals. In order to apply effective measures to prevent or decelerate the entry of hydrogen into metals, it is essential to understand the basic characteristics of the hydrogen evolution reaction (HER) and the hydrogen absorption reaction (HAR).

2.1.2.1. The Mechanism of HER

The mechanism of HER is discussed first because the hydrogen absorption reaction is a side reaction of HER. HER is a very simple reaction; it occurs in a number of consecutive steps, which are schematically illustrated in Figure 2-1.

In considering the steps occurring in an acid, these steps include:¹⁷ (1) transport of a hydrated proton (H_3O^+) to the double layer on a metal surface, (2) loss of the water of hydration shield in the vicinity of the double layer, (3) adsorption of the proton on the electrode surface, (4) discharge (electronation) of the proton to an absorbed hydrogen atom, (5a) chemical recombination of two adjacent hydrogen adatoms to form a hydrogen molecule, (5b) combination of an adatom and a proton to form a hydrogen molecule, (6)

desorption of H_2 , and (7) bubble formation due to coalescence of H_2 molecules, and evolution of bubbles.

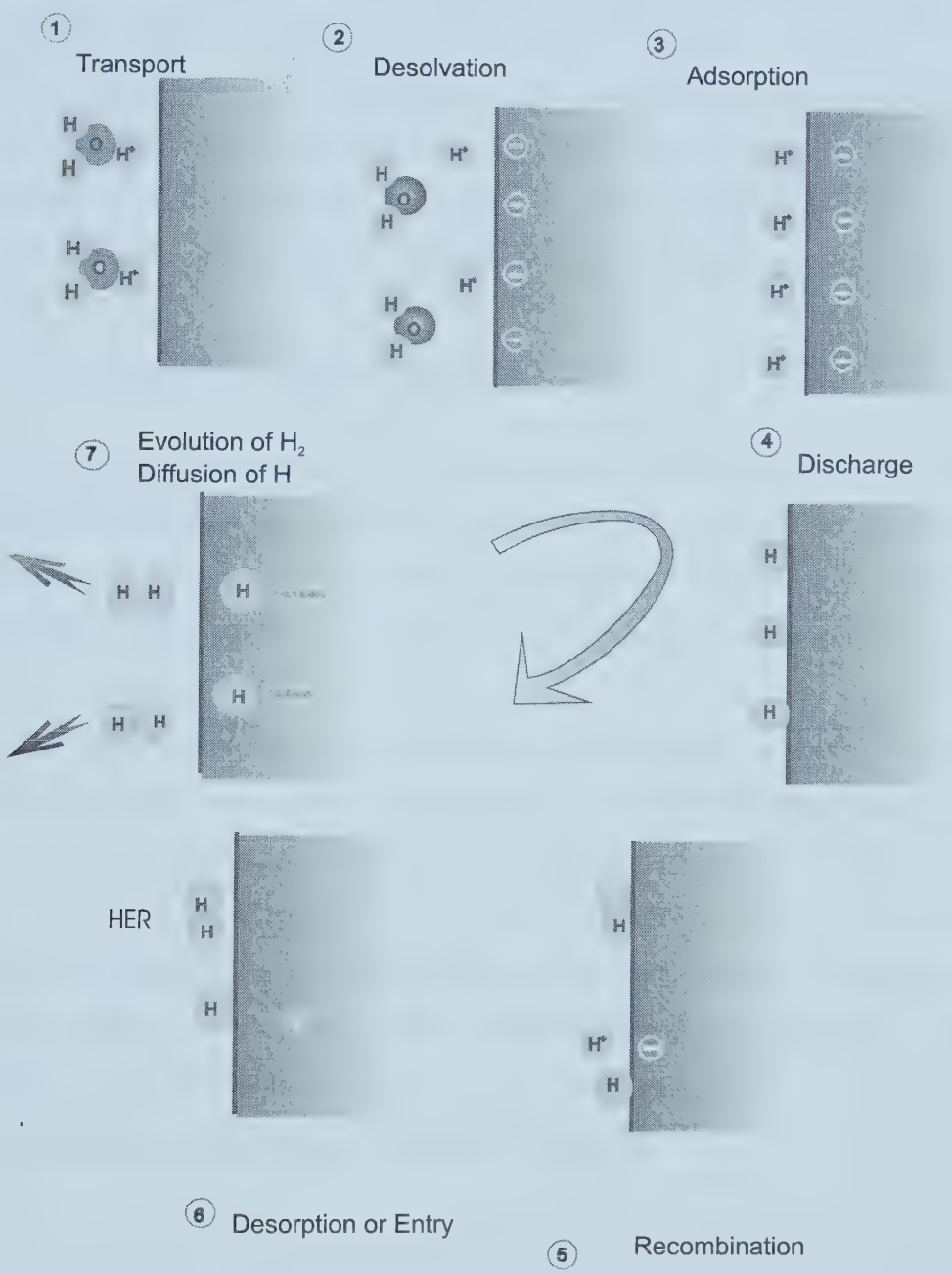


Figure 2-1. The consecutive steps of the hydrogen evolution reactions.¹⁷

Steps (1) and (7) are rarely rate limiting steps. In addition, steps (2) and (3) are thought not to affect the overall reaction rate. Therefore, the discharge step, one of the combination steps, 5a or 5b, and the desorption step, are steps of interest. The combination and desorption steps are usually combined because of the weak affinity for H_2 to chemisorb. Thus the HER occurs in two important steps: discharge followed by chemical or electrochemical combination. Either of these steps may be the rate-determining step or they may proceed in a lock-chain fashion (coupled reaction).

2.1.2.2. Controlling Factors of the HAR

From an experimental point of view, the extent of the HAR is controlled by:¹⁷ (1) the potential of the metal (and hence the current density); (2) the pH and composition of the solution; (3) the presence of certain species called promoters that catalytically favor hydrogen absorption; (4) the temperature and (5) the presence or absence of stress.

The solution composition can affect the hydrogen entry rate; the lower the pH, the higher is the entry rate. The anion sometimes alters the hydrogen absorption reaction. Hudson¹⁸ measured the corrosion rate and amount of hydrogen absorbed by a low carbon steel in studying the pickling of the steel in various acids. The acids used were H_2SO_4 , H_3PO_4 , HCl and HNO_3 . Very little hydrogen was absorbed during pickling in nitric acid despite a high corrosion rate. With regard to HCl , H_2SO_4 and H_3PO_4 , the hydrogen absorption rate at $38^\circ C$ is generally lower in phosphoric acid than the other two acids for a range of acid concentrations between 0.05 and 10 N.

2.1.2.3. The Role of Environmental Species --- Hydrogen Promoters and Inhibitors

2.1.2.3.1. Hydrogen Promoters

A number of species have the effects of increasing the kinetics of the hydrogen entry into metals. The generic terms “cathode poison” and “cathodic promoter” are applied to

these species because they poison the evolution reaction and therefore promote hydrogen absorption.

The species found to promote hydrogen entry are:¹⁷

1. Certain amounts and elemental forms of Group V-A and VI-A elements of the Periodic Table (Figure 2-2). These are phosphorus, arsenic, antimony (V-A), and sulfur, selenium, and tellurium (VI-A). The most effective promoters are the elements and compounds containing these elements.
2. The following anions: iodide (I^-) in acid solutions, cyanide (CN^-) in alkaline solutions,¹⁹ and rhodanide (CNS^-).
3. The following compounds of carbon: carbon sulfide (CS_2), carbon monoxide (CO), urea (CON_2H_4), and thiourea (CSN_2H_4).

V	VI	VII
N	O	F
P	S	Cl
As	Se	Br
Sb	Te	I
Bi	Po	At

Figure 2-2. Portion of the Periodic Table showing the location of promoter elements.¹⁷

There are also scant and inconsistent indications or assumptions in the literature^{20,21} as to the hydrogen promoting properties of mercury, lead, tin salts, and also of fluoride, bromide ions and aromatic hydrocarbon naphthalene, etc.

Smialowski and Szklarska-Smialowska²² were the first to postulate that hydride formation of a promoter was an essential step in the process of hydrogen entry, and promoter efficiency should be related to the binding force between M and H in the hydride. It was suggested²³ that hydrides with a binding force smaller than that possessed by the H₂ molecule (binding force constant 576 N/m) were efficient promoters.

The entry rate of hydrogen into metals depends on the concentration of the promoting compound in the electrolyte. In most cases, the highest efficiency of hydrogen promoters is observed at relatively low concentrations.²⁴ Because of hydrolysis and other secondary reactions, high concentrations often lead to the deposition of insoluble products on the surface that can inhibit the hydrogen entry.

2.1.2.3.2. Hydrogen Entry-Inhibiting Species

Some substances, when added to a solution, substantially reduce the entry rate of hydrogen. These are mainly polar organic compounds containing nitrogen, sulfur or oxygen. The organic nitriles, as a class, have this property.^{25, 26} These molecules probably adsorb on the surface thereby restricting the adsorption of protons. Dibenzyl sulfoxide²⁷ is reported to be an effective inhibitor of hydrogen entry.

Some strong oxidizing species tend to discourage the HAR. The weak absorption effects in nitric acid have been reported.¹⁸ The nitrate ions, especially at high concentrations, shift the potential in the noble direction which lowers the kinetics of the HER and consequently the HAR. Chromate is also believed to lower the absorption rate of hydrogen, and dissolved oxygen may act similarly.

2.1.3. Existing Forms and Locations of Hydrogen in Metals

2.1.3.1. Solid Solution of Hydrogen

Hydrogen dissolves atomically in all metals and is ionized, i.e., it gives its electron to the conduction band of the host metal. The concentration of hydrogen C_H dissolved in a metal at equilibrium with a hydrogen gas phase is generally describable in at least some range of temperature T and partial pressure of hydrogen P_{H_2} by Sievert's law:

$$C_H = \eta(T)P_{H_2}^{1/2} \quad [2-4]$$

where $\eta(T)$ is a temperature-dependent constant of proportionality.²⁸

Hydrogen dissolved interstitially in most metals causes a large lattice distortion. The kinds of data implying the large lattice distortion include internal friction, mechanical properties, and electrical resistivity. Consistent with its interstitial site occupancy, hydrogen diffuses with a high mobility in most metals. This is especially true in body centred cubic metals, for which the activation energies for hydrogen diffusion are typically of the order 4-20 kJ/mole (1-5 kcal/mole). Because of the larger interstices and close packing of host atoms in face centred cubic (fcc) and hexagonal close packed (hcp) metals, the mobilities of hydrogen are less in these metals than in bcc metals. Activation energies of the order of 20-60 kJ/mole (5-15 kcal/mole) are usually encountered in fcc and hcp metals.

2.1.3.2. Hydrogen-Defect Interactions

As mentioned by Interrante²⁹ at the first international conference on current solutions to hydrogen in steels, hydrogen is a problem in steel because it is highly mobile as an atom or a screened ion. They both can diffuse through the lattice and be transported by

the movement of dislocations. Hydrogen interacts with materials in many ways that involve the precipitation, grain boundaries, inclusions and other imperfections in the lattice. The interaction of hydrogen with defect traps is universally observed in metal-hydrogen systems. Some of the interactions are strong and influence properties significantly over a wide temperature range. However, even some of the comparatively weak interactions can have significant effects on properties at lower temperatures.

Suppose that hydrogen is dissolved in a metal and is partitioned between normal interstitial sites and other sites in which it is associated with a defect D to form a defect complex HD . This defect may be any point, line, surface or volume defect with which hydrogen can interact. In general, the complexes might be complicated ones, e.g., an H_mD_p complex consisting of m number of hydrogen atoms and p number of defects. Also, the interaction can be attractive or repulsive.

2.1.3.2.1. Hydrogen-Point Defect Interactions

There is considerable evidence that hydrogen atoms in many metals interact with each other, with vacancies and with other solutes, both interstitial and substitutional, but in most instances the best examples of these interactions come from the non-ferrous alloys.

2.1.3.2.2. Hydrogen –Dislocation Interactions

The unique nature of dislocation traps lies in the fact that they are mobile. Transport of hydrogen by dislocations can therefore be expected, providing the temperature is neither so high that the hydrogen has left dislocation sites, or so low that the hydrogen can not diffuse along the dislocations.

2.1.3.2.3. Hydrogen-Surface Interactions

Low angle grain boundaries can be described in terms of dislocation arrays of varying complexity which define a distinct internal interface. Consequently, one should expect

interactions with hydrogen of comparable magnitude to those determined or implied for dislocations and interfaces in general. The interactions are supported by autoradiography results³⁰ of the large segregation of hydrogen at dislocations, grain boundaries and other interfaces. Miodownik³¹ also found a correlation between hydrogen solubility and grain size (grain boundary area) in iron alloys.

Available data suggest³² that the grain boundaries are nominally as effective as dislocations in binding hydrogen, while the interfaces of internal voids, nitrides and carbides have larger binding energies. Thus, when dislocations contact such internal interfaces, the relative chemical potentials are such that hydrogen should strongly tend to drain into interface from the dislocation core.

The interaction between stacking faults and hydrogen is described as a short range adsorption-type process.³³ The interaction can also be presented as an effect of hydrogen on the electron/atom ratio and therefore the stacking fault energy. Miodownik³¹ proposed the additional role of stacking faults as active sites for hydride precipitation in materials with relatively low stacking fault energy.

2.1.3.2.4. Hydrogen-Volume Defect Interaction

Heterogeneities such as dislocations, impurity atoms, interfaces and voids have been considered as hydrogen traps. Figure 2-3 shows a schematic view of energy relations in gas-metal equilibrium, including trapping. E_s is the heat of the solid solution while E_b is the binding energy between hydrogen and defects.

A defect trap for hydrogen is well characterized if its binding energy E_b , its number density N_x and its specific saturability are known. Table 2-1 gives the values of E_b and N_x for a number of traps in ferrous alloys.³⁴

Most traps can be classified into three categories: weak traps with $E_b < E_s$, moderate traps with $E_b \sim E_s$ and strong traps with $E_b > E_s$.

Strong traps behave irreversibly in the sense that the rate of escape of hydrogen is relatively small. Moderate or weak traps have appreciable escape rates by comparison and act reversibly under the same experimental conditions.

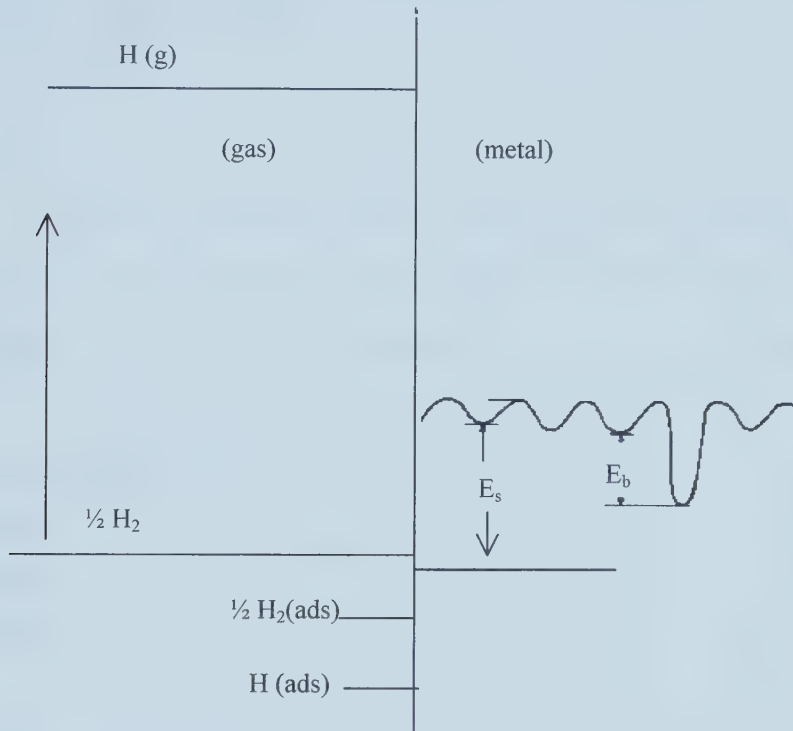


Figure 2-3. A schematic view of energy relations in gas-metal equilibrium, including trapping.³⁵

There are many ways that a defect which extends in three dimensions can interact with hydrogen or influence its behavior. Some effects of volume defects may involve the volume defects directly: (a) some defects can store hydrogen within the volume and (b) there may be various defects within the volume defect with which hydrogen can interact.

Hydrogen-void interactions remain important in two ways: (1) The matrix-void interface remains a potentially important adsorption-type trapping site for hydrogen. (2) Under conditions of high equilibrium pressures of hydrogen, voids may become heavily populated with hydrogen.

Mechanical strain offered by the matrix to second phases can account for the enhanced solubility of hydrogen. It can be explained that elastic and plastic work done on the matrix of a metal by the second phase precipitates can enhance the effective solubility of hydrogen in the metal.³⁶

Table 2-1. Hydrogen-Trap Interactions in Ferrous Alloys³⁴

Trap	E_b (kJ/mol)	N_x (no/m ³)
Interstitial solutes (N, C)	~ 3-15	10^{25}
Si atom	> 20	10^{27}
Ti atom	26	10^{27}
Vacancy	46	$<10^{23}$
- elastic stress field	20	10^{19} - 10^{26}
dislocation core (screw)	20-30	10^{19} - 10^{26}
dislocation core (mixed)	59	10^{19} - 10^{26}
1/2 H₂ (vapor/void)	29	---
Grain boundary	~59	10^{19} - 10^{23}
Free surface	70-95	10^{21}
AlN interface	65	10^{24} - 10^{25}
Fe₃C interface	84	10^{24} - 10^{25}
TiC interface	96	10^{24} - 10^{25}

2.1.4. Effects of Hydrogen on the Properties of Metals

2.1.4.1. Hydrogen Induced Cracking and Blistering

Several authors^{37,38,39} have investigated the generation of internal cracks and flaws by the introduction of large non-equilibrium amounts of hydrogen. Hydrogen was introduced into metals by cathodically electrolytic charging³⁷ or by gas-phase charging at high temperature, and subsequent quenching to a low temperature,³⁹ where the hydrogen solubility is much lower.

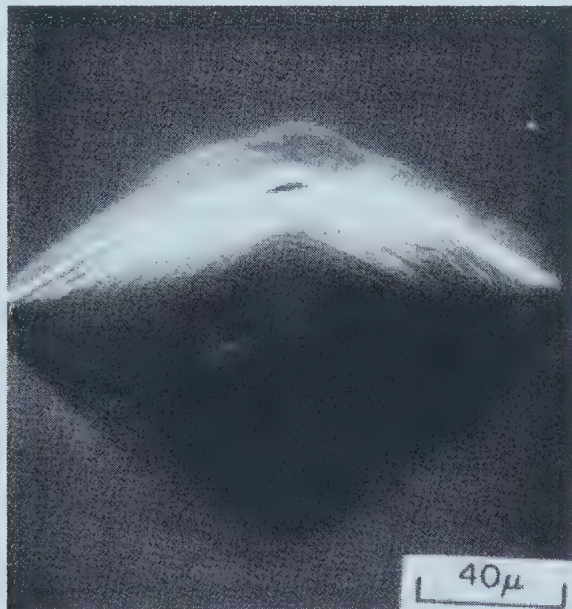


Figure 2-4. Hydrogen-induced surface blister in an iron single crystal.⁴²

This large amount of excess hydrogen can be accommodated in the following ways: a) outgassing through external surface; b) interaction with, and trapping by, lattice and grain boundary defects, and c) recombination of dissolved hydrogen to molecular hydrogen at internal sites. The associated internal stress increase will also locally increase the lattice hydrogen concentration.⁴⁰

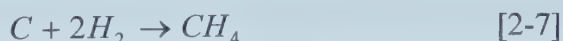
One of the sequences is the introduction of internal flaws, either intergranular or transgranular cracks^{37,39} or voids.⁴¹ Molecular hydrogen, resulting from recombination at the internal sites, aids the more direct role of dissolved hydrogen in promoting crack nucleation and growth. When these flaws are located near, and most effectively parallel to the external surfaces, surface blistering is often observed. The blisters are believed to form as a stress relief mechanism, which is related to the build-up of internal pressure in near-surface voids. Intense, highly localized slip produces large surface offsets, which become a macroscopic blister (Figure 2-4).⁴²

2.1.4.2. Hydrogen Attack

Hydrogen attack is a form of internal decarburization^{29, 43} associated with steels that are exposed to hydrogen at high temperature and pressure. It can be distinguished from hydrogen embrittlement by the fact that attack occurs above approximately 200°C and the material damage caused by it cannot be reversed with a low-temperature annealing treatment.

Hydrogen attack is caused by nucleation, growth, and coalescence of methane bubbles, primarily along the grain boundaries. The methane gas exerts internal pressure and forms fissures or enlarged pores in the metal.

The methane is produced by an internal reaction between carbon and hydrogen. The decarburization can be summarized by the following chemical steps in a hydrogen environment:



This phenomenon has been observed in both the petroleum and synthetic ammonia

industries for many years. Steels which are subjected to hydrogen attack undergo permanent internal damage resulting in a marked reduction in strength and ductility.

2.1.4.3. The Effects of Hydrogen on Corrosion Behavior

2.1.4.3.1. Effects of Hydrogen on Pitting Corrosion

The effects of hydrogen charging on austenitic stainless steels are: (1) increased anodic reactivity, (2) phase transformation from austenite to martensite, (3) a certain distortion of the metal, and (4) hydrogen embrittlement. Seys et al.,⁴⁴ thought that logically these effects were also to be expected in pitting corrosion. Hydrogen evolution in the pit causes secondary effects on the pitting corrosion process. A hydrogen-charged stainless steel is anodically more reactive. Hydrogen evolution mainly occurs at the pit bottom, the material around the pit is embrittled, and this decreases the material strength of the remaining metal. Hydrogen can induce transformation of austenite to martensite; however, the effect of this transformation in pitting corrosion is not clear. Hydrogen can have another effect on the secondary pit initiation. It was found that pitting corrosion preferentially initiated at dislocation barriers, such as twins, microtwins and slip lines. Dissolved hydrogen may pin the originally mobile dislocations, and can in this way create new initiation sites for pitting corrosion. This may be one of the reasons why many small pits are often found in the vicinity of a big pit.

Yashiro et al.⁴⁵ investigated the effect of permeated hydrogen on pitting behavior of Type 304 stainless steel using a Devanathan type cell. One side of the stainless steel sheet was galvanostatically charged with hydrogen, while the other side was subjected to pitting tests. The permeated hydrogen was found to enhance the pitting susceptibility. The pitting potential typically shifted to more noble values when the specimen was left standing in the solution, which suggested that the passive film became more stable. When the specimen was being charged, however, this shift in pitting potential was not observed (Figure 2-5). Thus, hydrogen appears to impede the aging process of the passive film, and thereby prevent the pitting susceptibility from becoming less pronounced with time.

Alternatively, aging may occur, but hydrogen would then have to enhance the pitting susceptibility so that the pitting potential changes very little. Hydrogen charging could shorten the induction periods for pitting, but has no effect on the critical pitting potential, which was obtained from the pitting potential vs. the square root of the potential scan rate plots. As found by Shibata and Takeyama,⁴⁶ a linear relationship between the critical pitting potential and the square root of the scan rate was observed. Extrapolation to zero scan rate gives the critical pitting potential. It was found that hydrogen charging did not affect the pitting potential. They concluded that the difference in pitting potential observed in dynamic polarization curves could be attributed to the difference in induction period, not in critical pitting potential. XPS analysis for the specimens partly hydrogen charged revealed that the hydrogen charged part was less enriched with chromium than the uncharged part. The XPS data also showed that the O 1s spectrum for the charged part indicated a large amount of OH^- , while the ratio of $\text{O}^{2-}/\text{OH}^-$ was higher at the uncharged part.

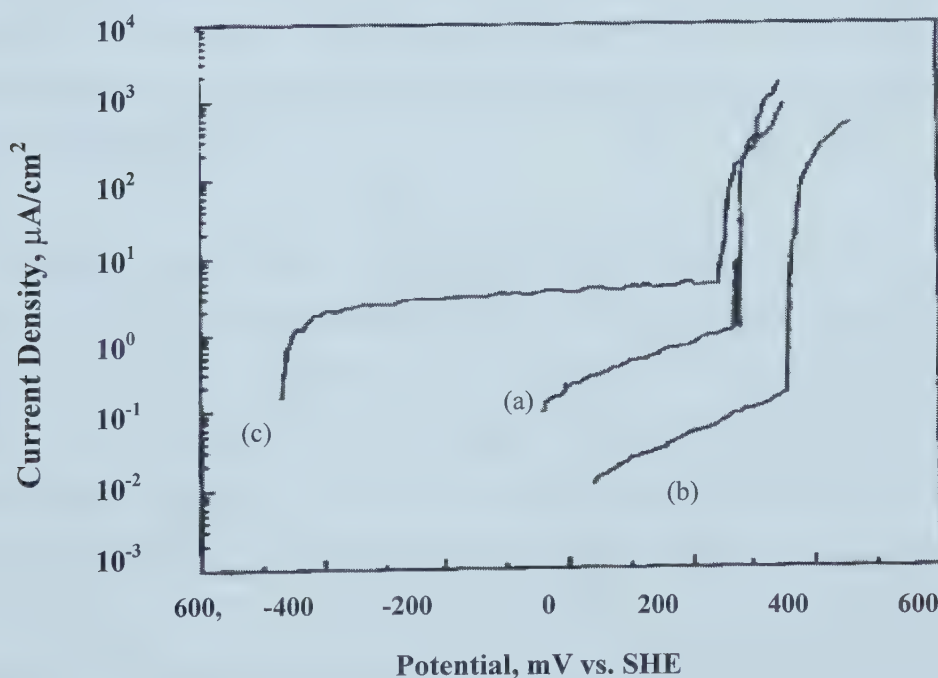


Figure 2-5. Effect of permeated hydrogen and aging of the passive film on anodic polarization curves for type 304 stainless steel. (a) just after the solution was heated to 343 K, (b) after 24 h of standing without hydrogen charging, (c) after 24 h of hydrogen charging. The solution used is 0.5 M NaCl + 0.1 M Na₂SO₄.⁴⁵

Pyun et al.⁴⁷ studied the pitting initiation behavior of a hydrogen-charged passive film on pure iron in 0.15 N $\text{Na}_2\text{B}_4\text{O}_7$ + 0.15 N H_3BO_4 solution using gas-phase hydrogen charging and an electrochemical detection technique. The metal sheet specimen separated a gas-charging compartment from an electrochemical compartment in the test apparatus. The pitting induction time was measured as a function of input hydrogen-charging pressure and of the time elapsed prior to the addition of chloride ions after cessation of hydrogen charging. The uncharged specimen did not show any change in anodic current density up to 3000 minutes after the addition of $5 \times 10^{-3} \text{M}$ Cl^- ions, whereas for the hydrogen-charged specimen there was a sudden increase in the anodic current density 30 minutes after the addition of the Cl^- ions. The pitting induction period increased with increasing waiting time before the addition of Cl^- ions, indicating that the resistance to pitting initiation increased as the hydrogen concentration in the passive film decreased because of the outgassing of hydrogen. The above results show that hydrogen present in the passive film reversibly affects the resistance to pitting initiation of the passive film. The authors thought that hydrogen reduced the resistance to pit initiation by chloride ions by increasing the OH^- and H_2O contents of the film, both of which can easily exchange with Cl^- .

Armacanqui and Oriani⁴⁸ conducted research to assess the effect that hydrogen injected into the passivating film on nickel had upon the pitting caused by chloride ions (Figure 2-6). It was observed that an increase in slope of the anodic current occurred some time after the chloride ions were added. Current fluctuations were observed usually after the change of slope, followed by a relatively sharp increase in the anodic current. The sharpness increases with increasing chloride concentration and also with the presence of hydrogen. It should be mentioned that hydrogen alone does not cause current fluctuations. The results for hydrogen-free films show that the pitting resistance increases with increasing age of the passivating film before adding chloride ions to the electrolyte. For hydrogen-bearing films, the significant variable controlling continuous pitting initiation is the time during which both chloride ions and hydrogen are present. The

authors indicated that the results in the paper favored the idea that the deleterious effect of chloride ions on pitting susceptibility of nickel resulted from an action within the film, as opposed to an effect of adsorption at the film-electrolyte interfaces.

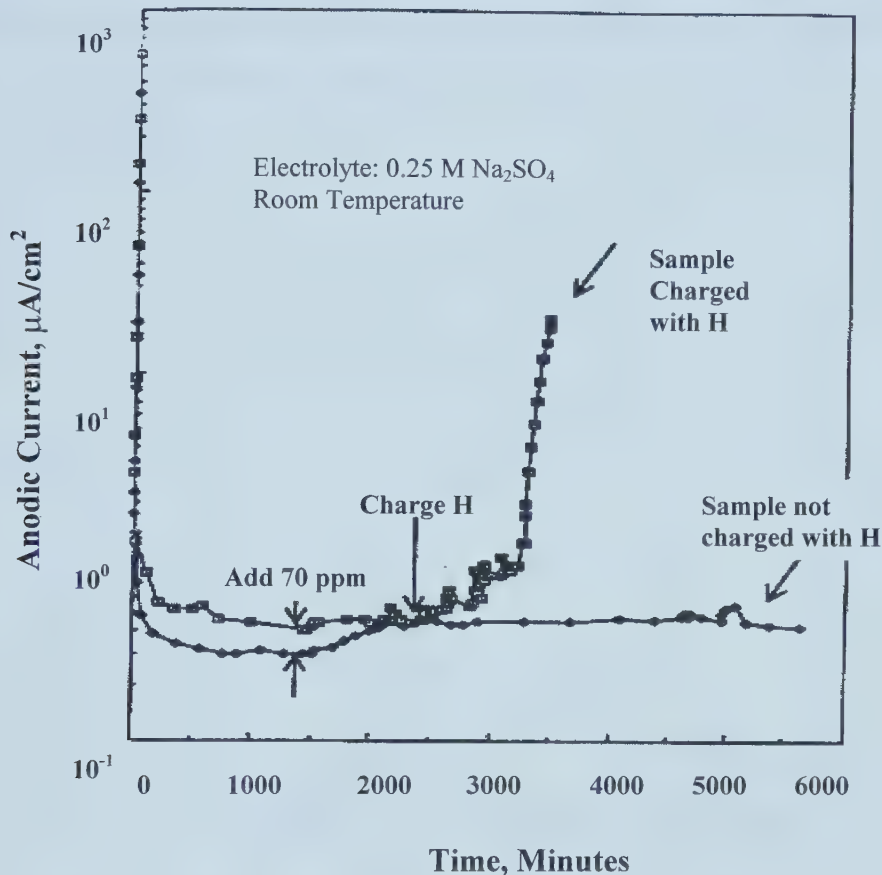


Figure 2-6. Effect of 70 ppm chloride ion in the electrolyte and of atomic hydrogen injected into the passivating film on nickel on the anodic current density at 400 mV (SCE).⁴⁸

2.1.4.3.2. Effects of Hydrogen on Intergranular and General Corrosion

The effect of dissolved hydrogen on intergranular and general corrosion of austenitic stainless steels was investigated by Hasegawa and Osawa.⁴⁹ Type 304 and 304L steels were hydrogen charged in hydrogen gas at 723K (Figure 2-7). In solution treated specimens, hydrogen charging has little effect on corrosion rate. The corrosion rate of hydrogen charged specimens sensitized at 923 K was greater than that of hydrogen-free

ones in a boiling Strauss solution and it increased with sensitizing time. In addition to Type 304 stainless steel, the corrosion behavior of Type 316, Type 321 and 20Cr-30Ni-Nb steels was studied. Similar to Type 304 steel, the corrosion rate of Type 316 steel increased with hydrogen charging, but the increment of corrosion rate of Type 321 and 20Cr-30Ni-Nb steels was not as remarkable as in Type 304 steel. Type 316 steel, as with Type 304 steel, precipitated carbide in the grain boundaries and thereby exhibited intergranular corrosion.

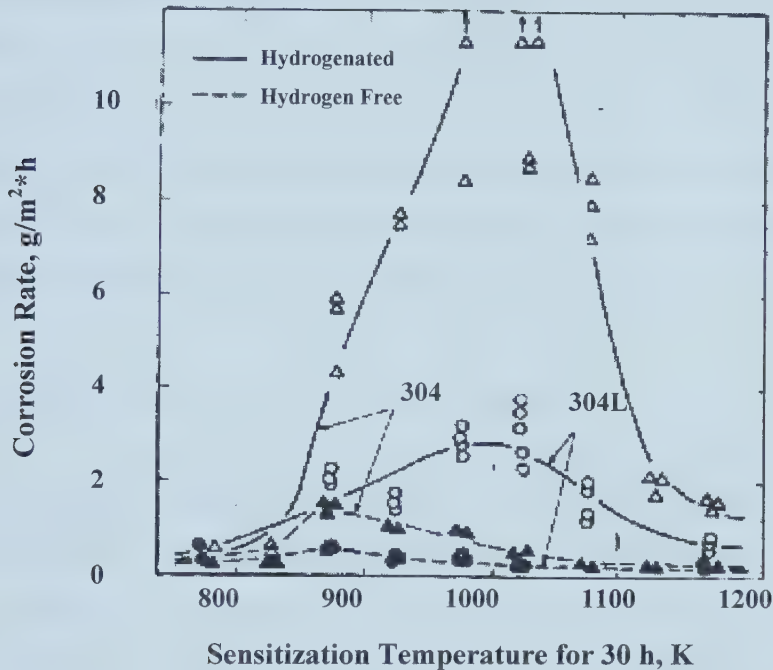


Figure 2-7. Change of intergranular corrosion rate in Strauss solution of Type 304 and Type 304L steels sensitized at 923 K and exposed to 27 MPa hydrogen at 723 K for 16 hours.⁴⁹

Type 321 and 20Cr-30Ni-Nb steels precipitated TiC and NbC, respectively, in the matrix and did not show any accelerated intergranular corrosion due to the hydrogen charging. The sensitization led to intergranular corrosion, and hydrogen charging accelerated this type of corrosion. The increase in the corrosion rate was interpreted to be caused by hydrogen charging instead of by an increase in the fraction volume of martensite in this case. An explanation of this phenomenon was made in terms of the

interactions between hydrogen and microdefects. A part of the dissolved hydrogen might be trapped and aggregated on the heterogeneous phases, such as carbide precipitates or martensite. This hydrogen aggregation seemed to be accompanied with a tangled dislocation by the strain energy release. These internal microdefects might impair the passivation characteristics, or be anodically active or be attacked selectively.

The effect of dissolved hydrogen in ferritic steels (soft iron and ferritic low alloy steel) on general corrosion was also investigated in acid solution by the same authors.⁵⁰ Weight losses of hydrogen-charged ferritic steels were markedly greater than those of hydrogen-free ones, and increased with increasing hydrogen content. Anodic polarization curves of hydrogen-charged specimens in H_2SO_4 solution exhibited an increase in the current density in the passive region in agreement with the corrosion data. Similar to the previous study,⁴⁹ it was suggested that this anomalous corrosion was caused by activated internal microdefects in the steels formed by hydrogen trapping.

2.1.4.3.3. Effect of Hydrogen on Anodic Dissolution

Kahaldeev⁵¹ studied the effect of hydrogen on the anodic behavior of a pure Cu single crystal in sulfate solution containing halide ions. The observation of the widened active dissolution region and changes in the Tafel slope indicated that hydrogen enhanced the anodic dissolution process. The effect of halides depended strongly on their concentrations in the solutions. Localized anodic dissolution was observed.

Qiao et al.⁵² studied the effect of hydrogen on the anodic behavior of 304 stainless steel in 1 N H_2SO_4 + 0.1 N HCl solution. The oxidized current increased with an increase in charging current density. The current increased nearly 30 times in the active and transpassive regions for a specimen charged at 50 mA/cm^2 for 25 hours, but increased only a little in the passive region. This increase in the polarization current (i_A) could be induced by two factors, i.e. i_M and i_H . It is possible that dissolved hydrogen might increase metal dissolution rate (i_M), on the other hand, hydrogen in the specimen could escape during the test, and then became oxidized under anodic potential (i_H). This would

result in an increase of polarization current i_A . ICP-AES (Inductively Coupled Plasma-Augur Electron Spectroscopy) was used to determine the ion concentrations of Fe, Cr and Ni dissolved in the solution. The dissolved ion concentrations, which correspond to the corrosion rate, increase with increases in the amount of hydrogen. The results strongly show that hydrogen could promote the anodic dissolution of 304 stainless steel in the transpassive region. The results of anodic behavior in the passive region indicated that the amount of dissolution was similar for the uncharged and charged specimens.

As revealed by Qiao and Luo,⁵³ hydrogen also enhanced the anodic dissolution rate of 310 stainless steel in the active and transpassive potential regions. ICP analysis provided the evidence that hydrogen in stainless steels hindered the enrichment of Cr at the metal surfaces and significantly weakened the capability for the passivity of stainless steels.⁵³

The effect of hydrogen on the passivity of iron-based (Fe-xCr-13P-7C, $x=5, 10, 15$) and nickel-based (Ni-15Cr-16P-4B) amorphous alloys has been investigated in a sulphuric acid solution at 303 K using the electrochemical method.⁵⁴ The final passive current for the iron-based and nickel-based amorphous alloys after 1h polarization tended to increase with charging time. It was found that the iron-based alloys had a critical charging time at which a black film was formed, while the nickel-based alloys had no critical charging time within the experimental charging time range. The black film, which was responsible for the inhibition of passivation, included a significant amount of phosphorus. However, before the critical charging time the existence of hydrogen in the amorphous alloys seemed to have only a limited effect on passivation. It was thought that the critical charging time might be associated with a critical hydrogen concentration in the amorphous alloys. The critical hydrogen concentration should be larger for the nickel-based amorphous alloy than for the iron-based amorphous alloys.

2.1.4.4. Hydrogen Embrittlement

Extensive research has been carried out to investigate hydrogen embrittlement. The

term hydrogen embrittlement is used to characterize any of the most common effects of hydrogen in metals at temperature near room temperature. These effects include the loss of ductility, decrease in true stress at fracture, loss of load carrying capacity, cracking and delayed cracking.

The mechanisms proposed to explain hydrogen embrittlement are numerous. These mechanisms are briefly listed as follows:

1. Pressure Theory

This theory was initially proposed by Zapffe and Sims.⁵⁵ It is assumed that hydrogen increases its concentration within the internal defects (such as voids and fissures), creating a large internal pressure which enhances void growth and crack formation. The pressure theory has been proved many times where externally applied loads are either low or non-existent, and the driving force needed for crack extension is provided by internal pressure.⁵⁶

2. Surface Energy Theory

Petch and Stables⁵⁷ proposed that the role of hydrogen was to adsorb on the free surfaces created by crack propagation, thereby decreasing the work of fracture and enhancing cracking. It has been demonstrated that plastic flow can occur, screening a sharp crack tip from intense stress concentrations but permitting some elastic stress concentration, and thus enabling the crack tip to advance in a brittle manner.^{58,59,60}

3. Enhanced Plastic Flow Theory

On the basis of electron microscopy evidence of plasticity at the crack tip, the enhanced plastic flow theory proposes that atomic hydrogen collects at the dislocations at the crack tip and enhances their mobility and the creation of new dislocations. The major effect of hydrogen is to promote the injection of dislocations at the crack tip. The

injection would cause crack propagation by an alternate sliding off of the crack tip.⁶¹

4. Hydride Formation Mechanism⁶²

The transition metals, notably titanium and zirconium, but not steel, can suffer hydrogen embrittlement by formation of a brittle hydride phase at the crack tip, cracking of the hydride, and crack arrest and deformation when the tip reaches the matrix phase, the sequence then repeating. Even in circumstances where the hydride phase is unstable, the hydride may be stable in the high stress region ahead of the crack.

5. Decohesion Model

The most widely accepted explanation of the embrittlement is a decohesion model proposed by Troiano⁶³ and modified by Oriani.⁶⁴ In this model hydrogen atoms diffuse ahead of a crack tip and accumulate in regions of high triaxial stress, particularly in grain boundaries and dislocations. Hydrogen alters the bonding between metal atoms, lowering the cohesive forces, producing microcracks ahead of the main crack, and allowing the crack to extend under tensile stress below the yield strength.

2.2. PASSIVITY OF METALS

2.2.1. Theory of Passivity and Breakdown of Passive Films

2.2.1.1. Definition of Passivity

Passivity results when certain metals and alloys form very thin protective films on their surfaces in a corrosive environment. Most commercially available corrosion resistant alloys depend on passive films for their resistance. According to Wagner,⁶⁵ passivity is a state of metal in which the rate of anodic dissolution or corrosion in a given environment is much less than the rate at a less noble potential or at some lower driving

force for the corrosion reaction. In this phenomenological definition, the mechanistic or structural nature of passivity was not explained. Uhlig⁶⁶ proposed two definitions of passivity:

- (1) A metal is passive if it substantially resists corrosion in a given environment resulting from marked anodic polarization.
- (2) A metal is passive if it substantially resists corrosion in a given environment despite a marked thermodynamic tendency to react.

2.2.1.2. Types of Passive Films

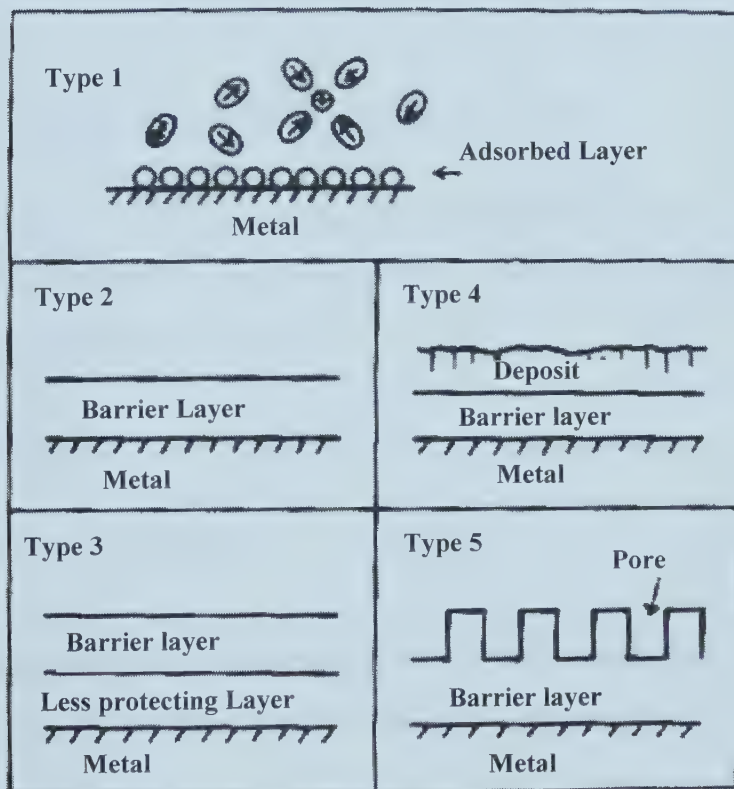


Figure 2-8. Five types of passive films.⁶⁷

The passive films on metals may be classified into five types⁶⁷ as shown in Figure 2-8: (1) The adsorption film consists of a monoatomic or multimolecular layer of oxygen or other species. (2) The barrier film of a three-dimensional oxide polymer layer forms sustaining a potential of $10^6 \sim 10^7$ V/cm. Generally, the barrier film thickness at steady state is a linear function of potential if the passivity-maintaining current is independent of potential. (3) The barrier film is formed on a less protecting layer. It seems that the existence of a non- or less protective layer between the metal and the passivating layer makes passivity unstable in an acid solution. (4) The barrier film is covered with a hydrated deposit layer and (5) the barrier layer is covered with a porous layer of the same composition. It seems that pore formation on barrier oxide films is determined by the mechanical properties of the films, as well as by kinetics of film growth and dissolution.

2.2.1.3. Compositions and Structures of Passive Films

Although at present it is accepted that passivation is a consequence of the presence of oxides on the surface, a large variety of theories have been proposed involving different structures and compositions.

2.2.1.3.1. Irons

1. Crystalline Oxide Model

This model explains passivation based on the formation of crystalline oxide on a metallic surface. In the case of iron the films are composed of $\gamma\text{-Fe}_2\text{O}_3$, $\text{Fe}_2\text{O}_3 \cdot n\text{H}_2\text{O}$ or Fe_3O_4 .

The crystalline oxide in many cases is assumed to have a spinel structure with permeability to ionic transport. The passive film usually contains hydrogen in addition to metal ions and oxygen, hydrogen being present in the form of protons, OH^- or water. The presence of Cl^- and SO_4^- increases the amount of bound water.

2. Sandwich Structure

This model is based on the fact that Fe^{3+} oxide, constituting the passive film, is thermodynamically unstable when in contact with metallic iron.⁶⁸ The sandwich oxide structure model was initiated by Nagayama and Cohen⁶⁹ by analogy with the oxidation of iron in air at high temperatures where the film is composed of an outer layer of $\alpha\text{-Fe}_2\text{O}_3$ and an inner layer of Fe_3O_4 . However, several studies indicate that the outer layer may be $\gamma\text{-Fe}_2\text{O}_3$.

2.2.1.3.2. Stainless Steels

The passive films formed on stainless steel are thinner than those formed on pure iron, showing more complex composition. The film structure and composition are still not well understood.

Various studies^{70,71,72} have postulated that the film structure is a duplex type of oxide with an inner layer enriched in chromium and an outer layer enriched in iron. The chemical form of chromium in the film is also not clear, the literature indicating species like Cr_2O_3 ,⁷³ CrO_3 ,⁷¹ CrO ,⁷³ $\text{Cr}(\text{OH})_3$ ⁷¹ and CrOOH ⁷⁴ and also mixed oxides such as $(\text{Fe}, \text{Cr})_2\text{O}_3$ and FeCr_2O_4 .⁷⁰

Several models have been postulated to describe the structure of the passive films on stainless steels.

1. Polymeric Hydrated Oxide Model

Okamoto and Shibata⁷⁵ have proposed a model for the structure of the passive layer. This model emphasizes the role of bound water in the film formation reaction.

In this model it has been assumed that the passive film is a hydrated oxide film having

a gel-like structure as shown in Figure 2-9(a).

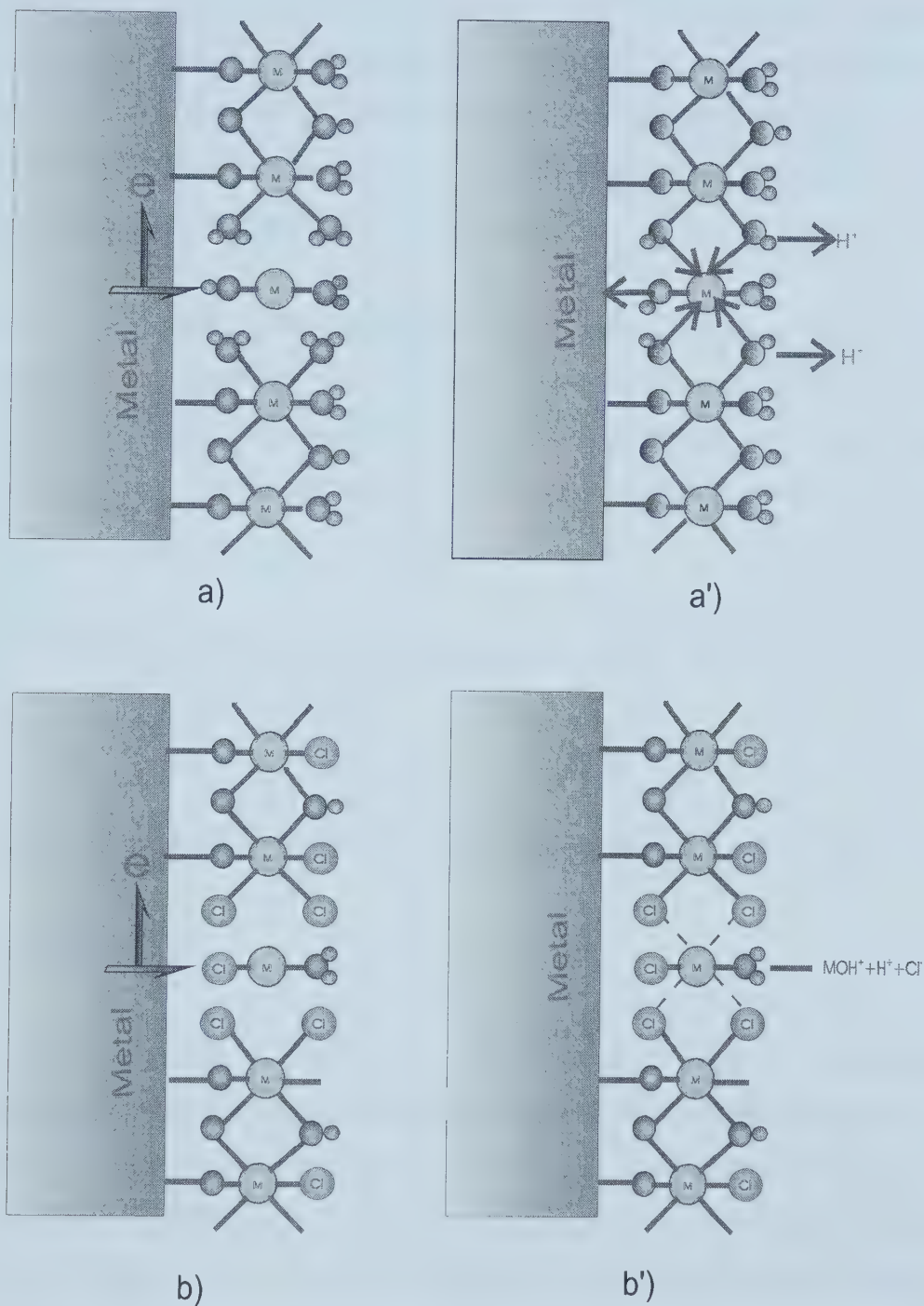
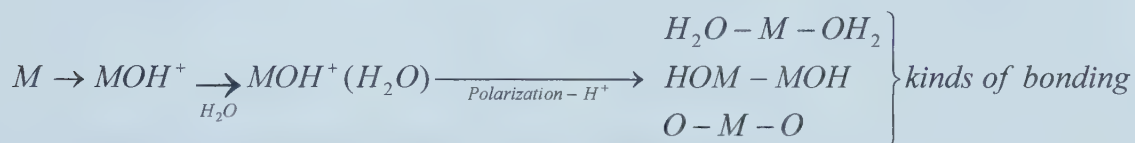


Figure 2-9. Polymeric Hydrated Oxide Model. (a) Dissolution of metallic ions leading to film formation; (b) Cl⁻ ions replace water molecules resulting in breakdown of the film.⁷⁶

The proton included in the film structure is extracted out by aging and anodic polarization. The metal ions produced by the anodic dissolution through an undeveloped part in the film from intermediates is denoted as MOH^+ . Then MOH^+ is captured by surrounding H_2O molecules and precipitates as a solid film in the undeveloped part, as shown in Figure 2-9(a'). The freshly formed film, still containing a large amount of bound water, changes to a less hydrated structure with time. Dehydration of the film during aging has been shown by other researchers.⁷⁷

At any stage of aging, the film might contain various forms of bridge connection between metal ions: there are three different bridges, $\text{H}_2\text{O}-\text{M}-\text{OH}_2$, $\text{HO}-\text{M}-\text{OH}$, $\text{O}-\text{M}-\text{O}$, depending on the degree of loss of protons. With loss of protons, the bridge changes to a perfect oxide ($\text{O}-\text{M}-\text{O}$) while the $\text{H}_2\text{O}-\text{M}-\text{OH}_2$ structure is more reactive.



This model was originally proposed for stainless steels, but can also be applied to iron.⁷⁸

2. Bipolar Model

Based on the results of RHEED and XPS obtained for AISI 304 stainless steel in H_2SO_4 solutions with and without NaCl and on the works of Sakashita and Sato⁷⁹ and also Brooks⁷¹, the model describes the film as a bipolar ionic rectifier composed of a Cr-rich inner layer and a Fe-rich outer layer. The inner layer, resulting from the direct reaction of Cr with water, is formed by Cr_2O_3 and $\text{Cr}(\text{OH})_3$ and is anion selective. The outer layer, rich in iron, incorporates SO_4^{2-} ions, which makes it cation selective.

When an anodic potential is imposed, a deprotonation reaction takes place in the internal layer, near the interface of the duplex film, resulting in the loss of protons to the

solution through the external layer (cation selective).

Since the inner layer is anion selective, the exit of metal cations from the substrate is difficult. As a consequence, the O^{2-} ions originating in the deprotonation reaction accumulate at the interface, then migrate towards the metal surface, and form a dehydrated oxide. The bipolar model is schematically illustrated in Figure 2-10.

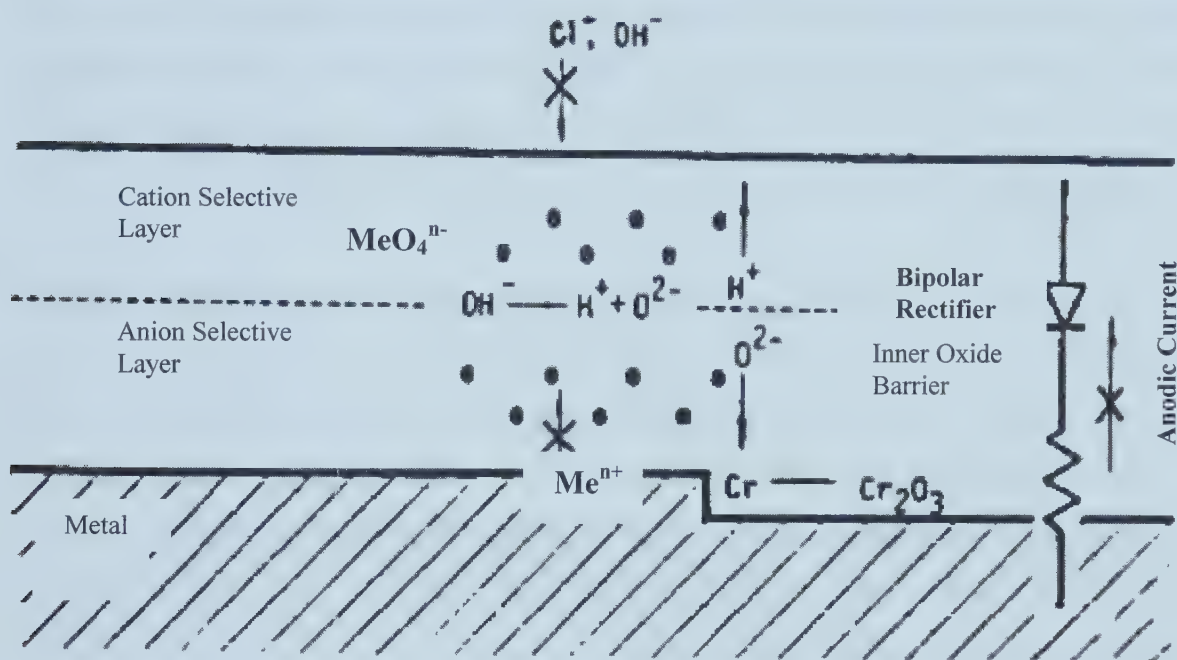


Figure 2-10. The bipolar model of a passive film.⁷¹

2.2.1.3.3. Presence of Hydrogen in Films

As a rule, passive films formed on metals and alloys in aqueous solutions contain hydrogen, in addition to metal ions and oxygen. Certain authors have claimed that hydrogen is present in the form of protons, OH^- , or water.^{80,81} Bloom and Goldenberg⁸² postulated that proton concentration increased with the distance from the metal surface. However, Alexandre et al.,⁸³ using optical emission spectroscopy, found hydrogen at the oxide/iron interface and in the outer layer of the film. The secondary ion mass

spectroscopy method revealed the presence of OH^- in the outer layer of film. Kudo et al.⁸⁴ found a uniform distribution of water over the film, but according to numerous authors, water is present primarily in the outer portion of the film, the inner part only containing a small amount of water.

The water content (or hydrogen) in the film seems to be potential dependent, but data regarding the precise relationship are contradictory. According to some investigators,⁸⁴ the content of water increases with increasing potential and film thickness, while others maintain that the opposite is true. Yolken⁸⁵ et al., found that a significantly smaller number of protons in anodic films grew at potentials below 0 V vs. SCE than they did at higher potentials. The presence of O and OH^- in the passive film is now well established.

In the Okamoto model,⁷⁵ the bound H_2O plays a dual function to help film formation or be replaced by aggressive ions. It is thought that the hydrated oxide passive films have a strong buffering ability to prevent film breakdown because of their good repairing action assured by the abundance of water molecules in the structure of the film. In contrast, a well developed oxide, which has lost protons, has less capacity to repair the film destroyed by Cl^- . Chloride ions that are adsorbed on the surface are thought to migrate to the film with the assistance of the electric field and replace the water molecules (Figure 2-9 b'). In this case, no repairing of the film occurs.

2.2.1.4. Theory of Passivation

Many passivity theories have been presented in the literature, all of which fall into the categories of adsorption theories or polyatomic three-dimensional oxide theories.

The formation of a thin film of monoatomic or polyatomic oxide on the surface exerts great effects on the double layer structure. As a result, a metal ion must move through the film via at least three consecutive reactions to dissolve: metal ion transfer from the metal phase into the surface film, ionic diffusion in the film, and metal ion transfer and hydration across the Helmholtz layer at the film/solution interface. This last reaction is in

fact that of the dissolution of the film and determines the rate of the over-all metal dissolution reaction in the steady state. The potential difference Φ_H across the Helmholtz layer at the film/solution interface is, in general, a complicated function of the potential difference Φ_M between the metal and the solution. It appears that the adsorption of a monatomic oxygen layer does decrease the potential difference Φ_H and hence does decrease the anodic dissolution rate, which in some cases may lead to passivation. The dissolution rate, however, will increase with increasing potential Φ_M unless the adsorbed layer grows to a polyatomic thickness.

The general theory also suggests that even if a passivating film exists, the passive dissolution current will increase, remain constant, or decrease depending on the relationship between the film thickness and the potential Φ_M ; a potential-independent dissolution current may result from a linear relation between L (film thickness) and Φ_M .

2.2.1.5. Theories of Breakdown of Passive Films

Existing theories of the breakdown of passive films or pitting corrosion can be roughly divided into two groups depending on the model of passivity considered.⁶⁸ Authors in favor of the adsorption theory of passivity believe that pitting is a result of competitive adsorption between oxygen and halide ions; others, who assume the necessity of the existence of tridimensional films for obtaining passivity, propose that some kinds of local breakdown of the films occur during pitting.

1. Adsorption Theory

Uhlig^{86,87} was the first to describe the formation of pits as a result of competitive adsorption of chloride ions and oxygen. Pits develop at sites where oxygen adsorbed on the metal surface is displaced by chloride ions. Supporting this theory, Lolotykin^{88,89} assumed that even during the dissolution of a passivated metal, irregular distribution of the current might exist on the surface, the latter never being quite homogeneous.

According to these concepts, the pitting potential is the potential value at which the adsorption of aggressive anions on the metal surface displaces the adsorbed passivating species. However, the above theory became unsatisfactory because recently it has become clear that passive films on metals and alloys are separate phases rather than chemisorbed layers.

2. Anion Penetration and Migration Theories

In these theories, the common point is that the breakdown of passive films is due to the penetration and migration of aggressive ions through the films. The penetration and migration of aggressive anions is fulfilled by diffusion via dislocations⁹⁰, grain boundaries and other imperfections⁹¹. Smaller ions more readily penetrate the lattice, so that Cl^- is more aggressive than Br^- or I^- .

3. The Mechano-Chemical Model

Hoar⁹² assumed that in contact with an aggressive electrolyte, the oxide film on a metal became mechanically stressed and damaged by pores and flaws as a result of changes in the interfacial forces. Hydrolysis of metal ions leads to acidification in the pores. The increased dissolution process results in the increased migration of halide ions such as Cl^- to the pit interiors, so that electrical neutrality can be maintained. This mechanism is autocatalytic because the increased acidity of anodic regions increases the dissolution rate. However in a non-aggressive electrolyte, healing of pores results not only in neutral but also in acidic solutions as the pores are filled with insoluble products. According to this theory, the formation of pits on passive metals is facilitated by the existence of weak sites (such as pores and flaws). There are two reasons for the increase of aggressiveness with increasing Cl^- concentration: (1) increased conductivity of the solution and (2) decreased migration of OH^- ions into and H^+ ions out of pores. It has been shown that internal flaws do exist in passive films on aluminum.⁹³ Kruger⁹⁴ completed the above model by suggesting that the pitting potential is the potential for the

adsorption of aggressive anions on the bare metal at the base of pores.

The contribution of the surface energy may be important. It has been found that halides decrease the solid/liquid surface energy.⁹⁵ The linear decrease of pitting potential with $\log [\text{Cl}^-]$ is assumed to rely on the following: (1) lowering of the solid/liquid surface energy, which lowers the stress for the brittle fracture of the film by flaws, (2) the decrease in the passive film strength and (3) the loss of adhesion between the film and the metal when fracture occurs and the electrolyte comes into contact with the metal.

Sato⁹⁶ suggested that passivity breakdown occurred as the film attained a thickness L , at which the mechanical stresses became critical as a result of the electrostriction pressure p (dielectric deformation resulting from the precipitating opposite charges by the electric field). The role of aggressive anions is thought to consist of their ability to reduce the surface forces that counteract electrostriction by adsorption. According to this concept, the pitting potential is the potential value above which p exceeds the compressive stress for a film breakdown.

4. The Point Defect Model for Pit Initiation

This model has been developed by Macdonald.^{97,98,99} In this model, it is thought that there are numerous point defects in a passive film. It is assumed that during film growth, anions diffuse from the film/solution (f/s) interface to the metal/film (m/f) interface. Cation diffusion results only in dissolution, and not in the growth of the passive film. A consequence of the diffusion of metal cations from the m/f to f/s interface is that cation vacancies are generated at the m/f interface. These vacancies tend to diffuse into the bulk lattice of the metal and hence disappear. However, when the cation diffusion rate (i. e., the metal vacancy generation rate) is greater than the rate of vacancy submergence into the bulk, the metal vacancies will start to accumulate and will form a void at the m/f interface. When the void grows to a critical size, the passive film suffers local collapse. This is the case without halide ions.

In the presence of halide ions, it is supposed that the film breakdown process occurs much more easily because halide ions in the solution are incorporated into the outermost layer of the passive film by occupying the oxygen vacancies in the film. This results in an increase in the concentration of cation vacancies. When the incorporation reaction of halide ions proceeds severely enough, the cation vacancies will pile up at the m/f interface, leading to localized breakdown. In this model, it must be assumed that the point defects are non-uniformly distributed through the passive film, i.e., that “weak sites” exist more within an agglomeration of defects than elsewhere.

5. Chemical Dissolution Theories

As is well known, a stable insoluble species would inhibit corrosion, while a transient, readily dissociable complex would accelerate corrosion. In the group of chemical dissolution theories, all models can be included that assume that metal dissolution occurs by transient complex formation. The first model of this kind was proposed by Hoar and Jacob.¹⁰⁰ This theory is formulated as follows. Three or four halide ions jointly “adsorb” on the oxide film surface around a lattice cation, with one next to a surface anion vacancy for preference. The transitional complex thus formed will be of high energy, and the probability of its formation is very slight. However once formed, the complex can readily and immediately separate from the oxide ions in the lattice, with the cations dissolving in the solution much more readily than non- or aquo-complexed cations present in the film surface in the absence of halide ions. Under the anodic field, another cation comes up through the film to replace the dissolved cation. The field at a constant potential increases at the “thinned” point of the film. However, arriving at the f/s interface, rather than forming a stabilizing oxide ion from water, the cation finds several halide ions so that once the catalytic process has begun, it has a strong probability of repeating itself and accelerating because of the increasing electrostatic field. Thus, once localized breakdown starts with the initial transitional complex, it accelerates “explosively”.

The theory of transitional complexes is popular for aluminum. A theory of the breakdown of the passive film is proposed by Foroulis and Thubrikar.¹⁰¹ According to this model, the breakdown occurs in two stages: (1). Cl^- ions adsorb on the oxide/solution interface under the influence of the electric field in competition with the adsorption of OH^- ions and water molecules on the hydrated oxide surface. (2). The formation of a soluble, basic chloride salt with the lattice cation on the hydrated oxide surface. This process of localized dissolution is likely, once initiated, to continue in an autocatalytic fashion until the oxide film is locally penetrated and dissolution of the substrate metal begins. Several authors^{102,103} have supported the above model.

The rest of the models include a localized acidification model,^{104,105} a thermodynamic theory of pitting,^{106,107} a depassivation-repassivation theory¹⁰⁸ and so on.

2.2.2. Electronic Properties of Passive Films

Passive films on iron, steels and nickel are semiconductor passive films. Because dissolution, film formation, and breakdown all involve the movement of electrons and ions from the metal surface through the passive film or from the solution into the film, electronic properties are a significant aspect of the nature of the passive film. Moreover, electron transfer reactions that occurs on surfaces with passive films depend strongly on the electronic properties of such films.

2.2.2.1. Band Structures^{109,110,111}

The electrons in a single atom occupy discrete energy levels. The Pauli exclusion principle permits each energy level to contain only two electrons. When N atoms came together to produce a solid, the Pauli principle still requires that only two electrons in the entire solid have the same energy. Each energy level broadens into a band. The band occupied by valence electrons is called the valence band, while an unfilled band is called the conduction band. Between the filled valence band and unfilled conduction band is the

forbidden band. The broadness of the forbidden zone (energy gap E_g) can be used to characterize the type of conductivity (Figure 2-11). E_g is smaller (<0.2 eV) for a metal, and lies in the 0.2 to 2 eV range for a semiconductor and is greater than 2 eV for an insulator.

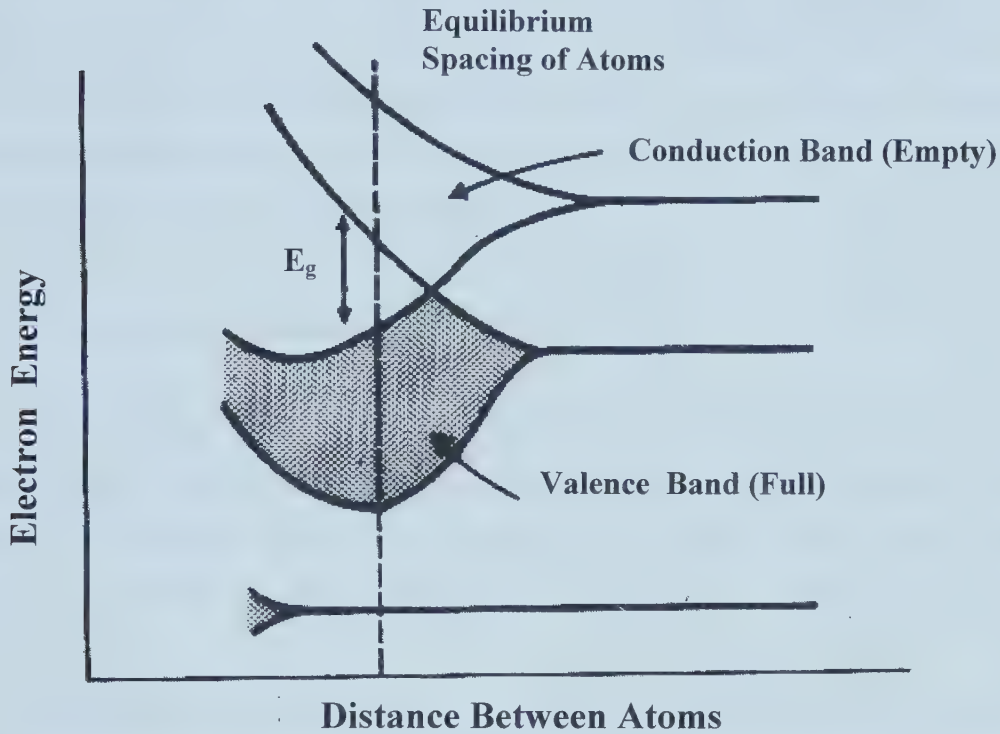


Figure 2-11. A schematic diagram of the band structure.¹¹²

A very important physical parameter in the band structure is the Fermi energy E_f . For a metal in ground state, E_f is the energy at which half of the possible energy levels in the solid are actually occupied by electrons. The Fermi distribution $f(E)$ gives the probability that a particular energy level E in the band is occupied by an electron:

$$f(E) = \frac{1}{1 + \exp\left(\frac{E - E_f}{kT}\right)} \quad [2-8]$$

where k is Boltzmann's constant (8.63×10^{-5} eV/K) and E is the electron energy. At absolute zero, the probability $f(E)$ that an electron has an energy less than or equal to E_f is 1; the probability $f(E)$ that an electron has an energy E greater than E_f is 0.

For semiconductor at higher temperatures, some electrons enter energy levels in the conduction band. The excited electrons leave behind unoccupied energy levels, or holes in the valence band. When an electron moves to fill a hole, another hole is created from the original electron source; consequently the holes appear to act as positively charged electrons and can carry an electrical charge.

2.2.2.2. Intrinsic Semiconductors

A semiconductor in which holes and electrons are created by thermal excitation across the energy gap is called an intrinsic semiconductor. Holes and electrons which are created in this manner are often referred to as intrinsic charge carriers and the conductivity arising from such carriers is sometimes termed intrinsic conductivity.

There are only a very small numbers of electrons that contribute to the conduction of electric current in intrinsic semiconductor materials. Also the behavior of an intrinsic semiconductor cannot be accurately controlled since slight variations in the temperature change the conductivity.

2.2.2.3. Extrinsic Semiconductors

Impurities and imperfections in a crystal often give a rise to localized energy levels within the band gap. If an electron or a hole occupies one of these levels, (a) it is localized –it no longer has a wave function extending through the crystal, and (b) it has an energy level in the gap. In most semiconductor devices, a considerably high number of charge carriers are present. They are introduced by intentionally doping, i.e., adding a small number of impurity atoms to the material, so that an extrinsic semiconductor can be produced. The conductivity of an extrinsic semiconductor depends primarily on the

number of impurity, or dopant atoms and temperature. Conductivity is therefore controllable and stable. If there are more electrons than holes in materials containing a type of impurity, such materials are termed n-type semiconductors. The terminology arises from the fact that most of the charged carriers are negative electrons. The extra electrons in the n-type semiconductor enter an energy level in a donor state just below the conduction band. Since the extra electrons are not tightly bound to the atoms, only a small increase in energy E_d is required for an electron to enter the conduction band (Figure 2-12 b).

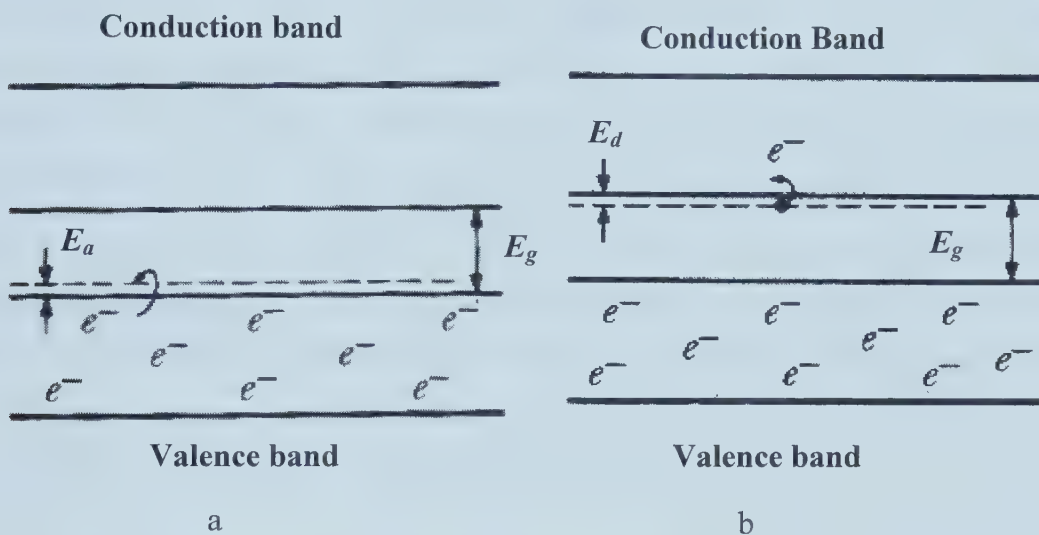


Figure 2-12. The band structures of p-type (a) and n-type (b) semiconductors.

The energy gap controlling the conductivity is now E_d rather than E_g . The Fermi energy is between the donor level and the conduction band edge for the n-type semiconductor at low temperature. For a p-type semiconductor, most of the charge carriers are holes. In a p-type semiconductor, the holes can act as acceptors of electrons. The hole sites have a somewhat higher than normal energy and create acceptor levels of possible electron energies just above the valence band. An electron must gain an energy of only E_a in order to create a hole in the valence band (Figure 2-12b). The Fermi energy is between the acceptor level and the valence band edge for the p-type semiconductor at low temperature. The component of electrical conductivity arising from the impurity

atoms is called extrinsic conductivity, and a substance whose charge carriers originate primarily from the impurity atoms is called an extrinsic semiconductor.

2.2.2.4. Effects of Defects

Some types of defects in a solid that have importance in the study of electrode reactions are vacancies, interstitials, dislocations, and grain boundaries.

A vacancy is a missing atom in the crystal. Anion vacancies are donors while the cation vacancies are acceptors. Consider a strong ionic oxide, where the valence electrons are in an orbital close to the oxygen ions. In order to remove a neutral metal atom from the solid and form a cation vacancy, leaving the region of the imperfection neutral, electron(s) must be taken from the neighbouring oxygen ion(s). However, the oxygen ions are still there with only slightly perturbed orbitals, and electrons can be accepted by these orbitals. The cation vacancy thus can be identified as an acceptor. In order to remove a neutral oxygen atom from the solid and form a neutral anion vacancy, two electrons (formerly on the O^{2-}) must be left behind with no valence orbital to accommodate them. The anion vacancy thus acts as a donor.

An interstitial atom is one that is squeezed between the atoms of a normal crystal. If such an interstitial atom tends to give up electrons, it will be an active donor. If it tends to accept electrons, in principle, it can be active acceptor. However the latter case is rarely found in nature. Dislocations and grain boundaries are also bulk defects that are of great importance in the behavior of the solution/solid interface. Both may provide energy levels in the gap.¹¹³

2.2.2.5. Correlation between the Electronic Properties and Corrosion Behavior of Passive Films

The electronic data of the passive film can be represented by the potentials E_{CB} and E_{VB} of the band edges, the band gap energy (E_g), a flat band potential (U_{FB}) and a donor

or acceptor concentration (N). The flat band potential is a characteristic potential of the junction where the bands are flat throughout the solid. The band structure model can be applied as a first approximation. We then can examine the influence of potential (U) on the potential distribution within the oxide film. The most characteristic situations are shown in Figure 2-13 for an n-type semiconductor film: the formation of an accumulation layer (b) during cathodic polarization, a depletion layer (a), and an inversion layer (c) in the case of anodic polarization. In the case of insulators, the model of linear potential drop can be applied to a good approximation. $\Delta\phi_{SC}$ in Figure 2-13 is the potential difference across the space charge layer.

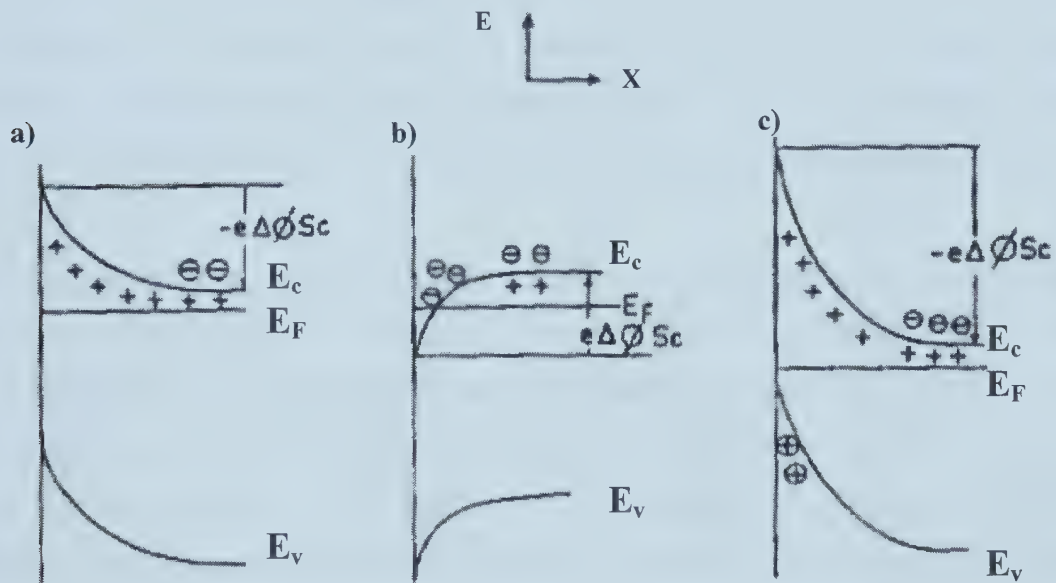


Figure 2-13. Types of space charge layers on n-type semiconductor: (a) depletion layer, (b) accumulation layer and (c) inversion layer.¹¹⁴

Bianchi et al.¹¹⁵ made the first attempt to correlate the electronic properties of oxide passive films with pitting susceptibility. To characterize the properties of oxide films formed on 19Cr-10Ni stainless steel by oxidation in air, they measured polarization curves in 0.5 M Na_2SO_4 + 0.1 M $\text{K}_3\text{Fe}(\text{CN})_6$ + 0.1 M $\text{K}_4\text{Fe}(\text{CN})_6$ solution.

The relationship between susceptibility to pitting and the anodic transfer coefficient (α_A) was as follows: lower α_A values for the oxide film (n-type passive film) promoted higher pitting susceptibility, while higher α_A values for the oxide film (p-type conductor) promoted lower susceptibility. The highest susceptibility to pitting was obtained for steel specimens oxidized at 300°C.

A similar study was performed by Szklarska-Smialowska and Janik-Czacher¹¹⁶ on low carbon steel oxidized in air at 100 to 400°C. Electrochemical measurements indicated that all films were n-type films. Nevertheless, the effect of oxidation temperature on susceptibility of oxide films to local breakdown was similar to that found by Bianchi et al.¹¹⁵ The highest susceptibility was for films at 250°C. From these results, the authors concluded that the type of conductivity does not control susceptibility of the oxide films to local breakdown, which depends primarily on the porosity of the film.

In the above tests, the conductivity types were all determined by measuring polarization curves (Bianchi's method). However, experimental data gathered to date does not permit definite conclusions to be drawn regarding the part played by the type of conductivity and by other electronic features in the overall electrochemical process of passive film deterioration. It seems that the higher conductivities of n-type oxides are associated with higher pit densities occurring on the surface of a given metal after corrosion.

2.3. ELECTROCHEMICAL METHODS TO STUDY PASSIVITY AND BREAKDOWN OF PASSIVE FILMS

2.3.1. Measurements of Polarization Curves

Polarization curves can be measured using controlled current methods and controlled potential methods. Because current is a single function of potential, the controlled

potential procedures are preferred. Among the controlled potential procedures, the potentiodynamic method of changing the potential continuously at a constant rate is the most commonly used method. Generally speaking, the anodic current increases rapidly after the potential reaches the critical pitting potential U_b (also called breakdown potential). From the polarization curve, the pitting potential can be determined from the curve as the potential above which the current will quickly increase. The difference between the conventional polarization curve and a cyclic polarization curve is as follows. For a cyclic polarization curve, after breakdown when a given anodic current density has been reached, the potentiodynamic scan is reversed in the negative direction. A hysteresis is observed in which the return polarization curve follows an active path, compared with the initial one. A potential can be determined where the reversed (backward) current intersects the forward passive current. This potential was called the protection potential, U_{prot} , by Pourbaix.^{117,118} It is generally accepted that pitting will be initiated very rapidly when the potential is above U_b , and if the potential is more negative than U_{prot} the pre-existing pits will be repassivated and stop growing. When the potential is between U_b and U_{prot} (metastable pitting stage), existing pits may grow but new pits can not initiate. These two parameters are often used to evaluate the susceptibility of alloys to pitting corrosion. The more noble U_b and U_{prot} are, the more resistant is the alloy to pitting. An alloy that is completely resistant to pitting shows no hysteresis, whereas susceptible alloys show significant hysteresis.¹¹⁹ It should be mentioned here that U_b and U_{prot} are strongly dependent on the experimental procedure such as scan rate.

2.3.2. Electrochemical Impedance Spectroscopy¹²⁰

The response of corroding electrodes to small amplitude alternating potential signals of widely varying frequency has been analyzed by electrochemical impedance spectroscopy (EIS). EIS can determine in principle a number of fundamental parameters relating to electrochemical kinetics and has been the subject of vigorous research.

The time-dependent current response $I(t)$ of an electrode surface to a sinusoidal alternating potential signal $V(t)$ has been expressed as an angular frequency (ω) dependent impedance $Z(\omega)$, where

$$Z(\omega) = V(t) / I(t) \quad [2-9]$$

$$t = \text{time}$$

$$V(t) = V_o \sin \omega t \quad [2-10]$$

$$I(t) = I_o \sin(\omega t + \theta) \quad [2-11]$$

and θ = phase angle between $V(t)$ and $I(t)$.

Various processes at the surface absorb electrical energy at discrete frequencies, causing a time lag and measurable phase angle, θ , between the time-dependent excitation and the response signals. These processes can be simulated by resistive-capacitive electrical networks.

The impedance, $Z(\omega)$, may be expressed in term of real, $Z'(\omega)$, and imaginary, $Z''(\omega)$, components.

$$Z(\omega) = Z'(\omega) + Z''(\omega) \quad [2-12]$$

The impedance behavior of an electrode may be expressed in Nyquist plots of $Z''(\omega)$ as a function of $Z'(\omega)$ or in Bode plots of $\log|Z|$ and $\log \theta$ versus frequency f in cycles per second (Hz), where $\omega = 2\pi f$.

Electrochemical impedance spectroscopy retains all the advantages of traditional direct-current (dc) methods. It is sensitive, can be conducted *in situ*, and often does not require artificial accelerating factors for testing, such as increased temperature and concentration. However, data interpretation may be ambiguous and difficult. Nevertheless, the added dimension of frequency can provide essential mechanistic information, which would be otherwise unavailable from dc measurements.

2.3.3. Electrochemical Methods to Study Electronic Properties of Passive Films

2.3.3.1. Mott-Schottky Method

The most commonly used method to study the electronic properties is the so-called Mott-Schottky analysis. The Mott-Schottky relation describes the potential dependence of the space charge capacity of a semiconductor electrode under depletion condition. Assuming that the solid state properties of the passive film determine its capacitance behavior and the Mott-Schottky relation is applicable, information on the conductivity type (n or p type) and on the donor or acceptor concentration and distribution can be obtained. According to the Mott-Schottky theory,^{121,122,123,124} the space charge-capacitance of a semiconductor (C_{sc}) is given by the following equations:

$$\frac{1}{C_{CS}^2} = \frac{2}{\epsilon\epsilon_o qN} \left(U - U_{FB} - \frac{kT}{q} \right) \quad \text{for an n-type passive film} \quad [2-13]$$

$$\frac{1}{C_{CS}^2} = \frac{2}{\epsilon\epsilon_o qN} \left(U_{FB} - U + \frac{kT}{q} \right) \quad \text{for a p-type film} \quad [2-14]$$

where ϵ denotes the dielectric constant, ϵ_o the vacuum permittivity, q the charge of the electron, N the charge carrier concentration. U the applied potential, U_{FB} the flatband potential, that is, the characteristic potential of the junction where the bands are flat

throughout the solid, and the term kT/q is 25 mV at room temperature. The quantity U_{FB} is related to the Fermi level of the semiconductor by the relationship:¹²⁵

$$E_F = - |e| U_{FB} \quad [2-15]$$

In a plot of $1/C^2$ vs. U (Mott-Schottky plot), n-type semiconductors have a straight-line section with a positive slope while p-type semiconductor have a negative slope. The concentration of donors for an n-type semiconductor, N , can be determined from the slope. The intersection at $1/C^2=0$ gives the flatband potential U_{FB} (more precisely $U_{FB} - kT/q$ for p-type or $U_{FB} + kT/q$ for n-type semiconductors). The thickness of the space charge layer is given approximately by the Debye length in the semiconducting film:

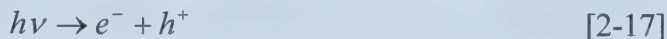
$$d_{SC} = \left(\frac{\epsilon \epsilon_o kT}{q^2 N_D} \right)^{\frac{1}{2}} \quad [2-16]$$

for an n-type material.

2.3.3.2. Photoelectrochemical Measurement

Photoeffects in electrochemical systems have been recognized for a long time, and a phenomenon where an additional current can be stimulated by irradiation with light, the Bequerel effect, is named after its discoverer. Photoelectrochemistry with semiconductor electrodes has undergone enormous advancement during the last 20-25 years, which has been largely due to the effort of searching for materials for liquid junction solar cells.^{126,121,127} The application of photoelectrochemistry to the study of passive films is based on the recognition that even very thin films contain their own specific properties. Consequently, photoelectrochemistry can be used as an *in situ* technique to characterize passive films with their optical and electronic properties.

A photoelectrochemical reaction on a passive metal electrode can be described in the following simplified way. If light with a suitable energy $h\nu$ is absorbed by the passive film, electrons can be excited from occupied electronic states into unoccupied ones,



As a consequence, the charge distribution in the film is changed, which can result in a current at constant potential or a potential change at constant current.

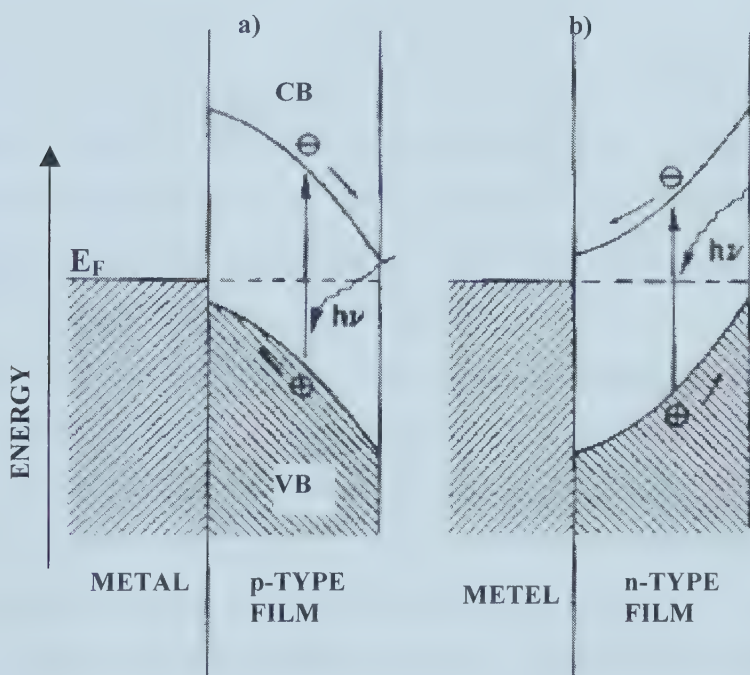


Figure 2-14. Schematic representation of illuminated p-type (a) and n-type (b) passive films under depletion conditions.¹²⁸

Depending on the properties of a passive film with respect to its conduction type, different energetic conditions can be distinguished for an n-type or p-type semiconducting or an insulating film. Figure 2-14 gives a schematic representation for crystalline films without, as yet, considering any effects caused by absorption that involves localized states.¹²⁸ Under the conditions of a depletion layer built up at the film-electrolyte

interface in a semiconducting film, the electron-hole pair is separated in the electric field of the space charge layer. The condition of a depletion layer is the one where the photoeffect can be observed. In the case of a p-type semiconducting passive film (Figure 2-14a) the electron migrates to the surface, where it can react with an unoccupied (acceptor) state in the electrolyte which is represented by an oxidizing species. The hole flows to the backside contact: the resulting current is cathodic. For an n-type film (Figure 2-14b), the situation is reversed. The hole migrates to the surface, reacting with an unoccupied (donor) state while the electrons move to backside contact: the photocurrent is anodic.

For amorphous or highly disordered films, effects caused by absorption that involves localized states should be considered. If the photoexcitation involves localized states or after excitation the electron-hole pair thermalizes into localized states, the occurrence of the photocurrent requires the removal of the carriers from their respective traps. Figure 2-15¹²⁹ shows a schematic representation of photoexcitation processes involving localized states. Processes 1 and 2 indicate excitation from the extended (in the band) to localized states and localized to extended states, respectively. If the localized state is close to the surface and the field is not too high, an electron also has a finite probability of direct escape to the electrolyte (Process 3). This latter process presents a tunneling process through the potential barrier against the field and is thought to be the cause of cathodic steady-state photocurrents that dominate the photo-response at low overpotentials.

The use of in-situ techniques seems preferable owing to unavoidable modifications of passive layers during removal of the electrode from the corrosion environment. Hence photoelectrochemical measurements have been extensively performed to study the electronic properties of passive films formed on various metals and alloys.^{130,131,132,133,134} Photoelectrochemical measurements have been used to measure the flat potential U_{FB} ¹³⁵ and band gap energy.^{136,137} Some researchers have used this technique to identify whether a passive film is amorphous¹³⁶ or crystalline.¹³⁸ The disorder degree (or disorder energy)

of a highly disordered passive film can be obtained by measuring the photocurrent spectra.¹³⁰

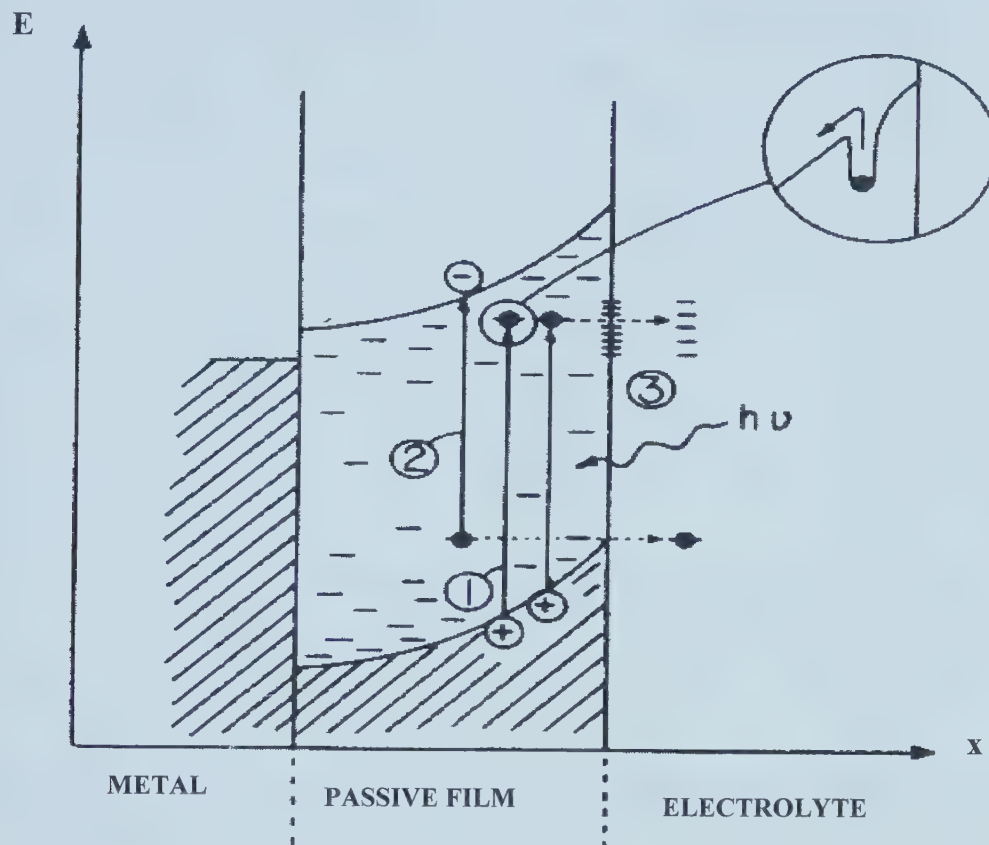


Figure 2-15. Schematic representation of photoexcitation process in a passive film: (1) extended to localized states; (2) localized states to extended states and (3) photoexcitation into a localized state followed by electron tunneling into the electrolyte.¹²⁹

Photoelectrochemical imaging has been suggested as a good tool to illustrate defects, the spatial variation of composition, and the microstructure of passive films. It offers the possibility of studying *in situ*, and in a continuous way, the corroding surfaces correlating the defects of passive films with the possible sites where film breakdown and pitting corrosion occur.

2.3.3.3. Polarization Measurement (Bianchi's Method)

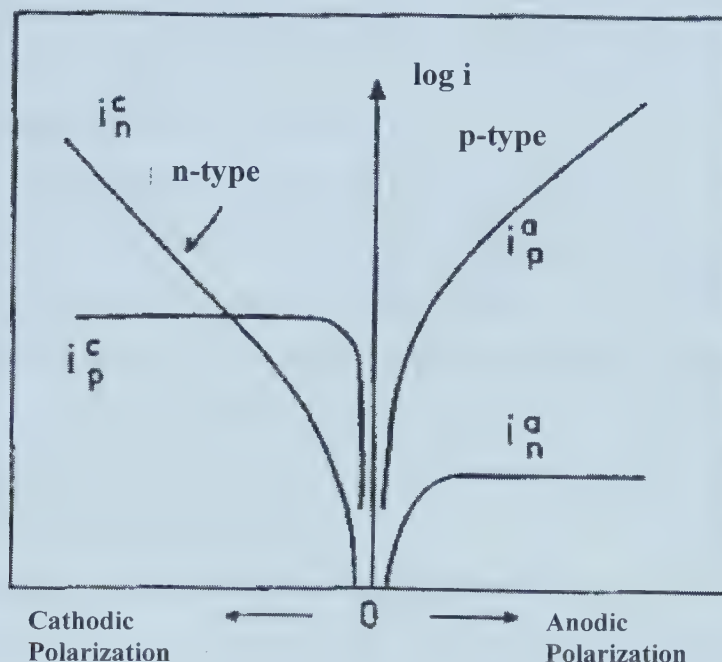


Figure 2-16. Typical current density curves for partial electron-transfer currents in the conduction band and in the valence band.¹¹⁵

According to Bianchi et al.,¹¹⁵ the semiconducting properties of oxide films were evaluated by anodic and cathodic polarization measurements in a $\text{Fe}(\text{CN})_6^{3-}/\text{Fe}(\text{CN})_6^{4-}$ redox system. In a redox reaction, electron transfer processes at a semiconductor electrode occur only at energy levels in the range of the conduction or of the valence band. Generally the mechanism of a redox reaction with positive normal potential in the electrochemical redox reaction scale is associated with the valence band, whereas the mechanism of a redox reaction with more negative normal potential is associated with the conduction band. The n-type or p-type oxide films can be differentiated by the evaluation of the anodic and cathodic transfer coefficients (Figure 2-16). Small α_A values and $\alpha_A \leq \alpha_C$ correspond to n-type films, whereas greater α_A values and $\alpha_A \geq \alpha_C$ correspond to p-type films.

REFERENCES

1. L. Cailletet, *Comptes Rendus*, 58, (1864): p.327.
2. M. Bodenstein, *Zeitschrift für Electrochemi.*, 28, (1922): p.517
3. F. Fitzgerald, “Hydrogen in Steelmaking and Casting”, Hydrogen in Steel, Spring Residential Conference, The Institution of Metallurgists, 14-16 April, (1982): p.1.
4. J. A. Kargol and L. D. Paul, “The Influence of Microstructure, Purity and Cadimum Coatings on H Behavior in High Strength Steels”, Current Solution to Hydrogen Problems in Steels, C. G. Interrante and G. M. Pressouyre, Eds., American Society for Metals, Metals Park, OH, (1982): p.91.
5. C. A. Zapffe and M. E. Maslem, *Plating*, 37, (1950): p. 366.
6. J. J. DeLuccia and D. A. Berman, “An Electrochemical Technique to Measure Diffusible Hydrogen in Metals (Barnacle Electrode)”, Electrochemical Corrosion Tests, ASTM STP 727, F. Mansfeld and U. Bertocci, Eds., American Society for Testing and Materials, Philadephia, (1981): p.256.
7. J. Crousier and T. Casanova, “Hydrogen Absorption during Zinc Plating on Steel”, No. 208, Volume II, EUROCORR’97, Trondheim, Norway, (1997): p. 477.
8. B. N. Popov, G. Zheng and R. E. White, *Corros. Sci.*, 36 (1994): p. 2139.
9. P. H. M. Hart, “Hydrogen in Steel – its Significance for Welding”, Hydrogen in Steel, Spring Residential Conference, The Institution of Metallurgists, 14-16 April, (1982): p.93.
10. J. Postlethwaite and M. Onofrei, *Corrosion*, 35 (1979): p.185.
11. R. B. Hamzah and M. J. Robinson, *Corros. Sci.*, 27 (1987): p. 971.
12. S. A. Bradford, *Corrosion Control*, Van Nostrand Reinhold, New York, (1992).
13. H. C. Cotton and F. A. Golightly, “Hydrogen Pick-up in Service”, Hydrogen in Steel, Spring Residential Conference, The Institution of Metallurgists, 14-16 April, (1982): p.119.

14. R. P. Hu, P. Manolatos, M. Jerome, M. Meyer and J. Galland, *Corros. Sci.*, 40 (1998): p.619.
15. P. Marer and D. P. Dautovich, "Hydrogen Entry into Alloys from High Temperature Water", *Hydrogen in Metals*, Vol. 6, Elmsford, New York, Pergamon Press Inc., (1977): paper 4A10.
16. S. M. Wilhelm and D. Abayarathna, *Corrosion*, 50 (1994): p. 152.
17. R. D. McCright, "Effects of Environmental Species and Metallurgical Structure on the Hydrogen Entry into Steel", *Stress Corrosion Cracking and Hydrogen Embrittlement of Iron Base Alloys*, R. W. Staehle, J. Hochmann, R. D. McCright and J. E. Slater, eds., NACE-5 (1977): p.306.
18. R. M. Hudson, *Corrosion*, 20 (1969): p. 247.
19. W. Beck, A. L. Glass and E. Taylor, *J. Electrochem. Soc.*, 112 (1965): p. 53.
20. T. P. Radhakrishnan and L. L. Shreir, *Electrochimica. Acta*, 11 (1966): p. 1007.
21. T. A. Bagotskaya, *Russ. J. Phys. Chem.*, 36 (1962): p. 2667.
22. M. Smialowski and Z. Szklarska-Smialowska, *Rocz. Chem.*, 29 (1955): p.85.
23. M. Smialowski, *Hydrogen in Steel*, Pergamon Press, (1962).
24. T. Zakroczymski, "Entry of Hydrogen into Iron Alloys from the Liquid Phase", *Hydrogen Degradation of Ferrous Alloys*, R. A. Oriani, J. P Hirth and M. Smialowski, eds., Noyes Publications (1985): p. 215.
25. J. O'M Bockris, J. McBreen, and L. Nanis, *J. Electrochem. Soc.*, 112 (1965): p.1025.
26. F. Matsuda and T. C. Franklin, *J. Electrochem. Soc.*, 112 (1965): p.767.
27. G. Trabanelli, F. Zucchi, G. Gullini and V. Carassiti, *Brit. Corro. J.*, 4 (1969): p.212.
28. R. B. McLellan, *Phase Stability in Metals and Alloys*, P. S. Rudman, J. Stringer and R. I. Jaffee, eds. McGraw-Hill, New York (1967): p.393.
29. C. G. Interrante, "Basic Aspects of the Problems of Hydrogen in Steels", *Current Solutions to Hydrogen Problems in Steels*, C. G. Interrante and G. M. Pressouyre, Eds., ASM, (1982): p.3.
30. J. P. Laurent and G. Lapasset, *Int. J. Appl. Radiation and Isotopes*, 24 (1973): p. 213.
31. A. P. Miowdownnik, "The Interaction of Hydrogen with Dislocations, Stacking Faults

- and Other interfaces”, Stress Corrosion Cracking and Hydrogen Embrittlement of Iron Base Alloys, J. Hochmann and R. W. Staehle, Eds., NACE, Houston, (1973): p. 272.
32. J. P. Hirth, *Met. Trans.*, 11A (1980): p.861.
33. R. Gibala, “Hydrogen-Defect Interactions in Iron-base Alloys”, Stress Corrosion Cracking and Hydrogen Embrittlement of Iron Base Alloys, J. Hochmann and R. W. Staehle, Eds., NACE, Houston, (1973): p. 244.
34. R. Gibala and D. S. DeMiglio, “Hydrogen in Iron and Steels: Interactions, Traps and Crack Paths”, Hydrogen Effects in Metals, I. M. Bernstein and A. W. Thompson, Eds., The Metallurgical Society of AIME, New York, (1981): p. 113.
35. H. H. Johnson and R. W. Lin, “Hydrogen and Deuterium Trapping in Iron”, Hydrogen Effects in Metals, I. M. Bernstein and A. W. Thompson, Eds., The Metallurgical Society of AIME, New York, (1981): p. 3.
36. N. Paton, B. Hickman and D. Leslie, *Met. Trans.*, 2 (1971): p.2791.
37. I. M. Bernstein, *Met. Trans.*, 1 (1970): p. 3143.
38. I. M. Bernstein and B. B. Rath, *Met. Trans.*, 4 (1973): p.1545.
39. A. S. Teteman and W. D. Robertson, *Trans. AIME*, 224 (1962): p.775.
40. G. C. Smith, “Effect of Hydrogen on Nickel and Nickel-Base Alloy”, Hydrogen in Metals, I. M. Bernstein and A. W. Thompson, Eds., ASM, Metal Parks, (1974): p.485.
41. A. S. Teteman and W. D. Robertson, in *Fundamental Aspects of Stress Corrosion Cracking*, R. W. Staehle, Ed., NACE, Houston, (1969): p. 446.
42. I. M. Burnstein, R. Garber and G. M. Pressouyre, “Effect of Dissolved Hydrogen on Mechanical Behavior of Metals”, *Effect of Hydrogen on Behavior of Materials*, A. W. Thompson and I. M. Bernstein, Eds., AIME, (1976): p. 37.
43. P. G. Shewmon, “Hydrogen Attack of Carbon Steel”, *Effect of Hydrogen on Behavior of Materials*, A. W. Thompson and I. M. Bernstein, Eds., AIME, (1976): p.59.
44. A. A. Seys, M. J. Brabers, and A. A. Van Haute, *Corrosion*, 30 (1974): p.49.
45. H. Yashiro, B. Pound, N. Kumagai and K. Tanno, *Corros. Sci.*, 40 (1998): p.781.
46. T. Shibata and T. Takeyama, *Corrosion*, 33 (1977): p.243.

47. S. I. Pyun, C. Lim and R. A. Oriani, *Corros. Sci.*, 33 (1992): p.437.
48. M. E. Armacanqui and R. A. Oriani, *Corrosion*, 44 (1988): p.696.
49. M. Hasegawa and M. Osawa, *Corrosion*, 36 (1980): p.68.
50. M. Hasegawa and M. Osawa, *Corrosion*, 39 (1983): p.115.
51. G. V. Kahladeev, *Zh. Priklad. Khim.*, 51 (1978): p. 2728.
52. L. J. Qiao, W.Y. Chu, C. M. Hsiao and H. Huang, the 10th ICMC, paper 11.9.
53. L. J. Qiao and J. L. Luo, *Corrosion*, 54 (1998): p.281.
54. R. Nishimura, H. Habazaki, A. Kawashima, K. Asami and K. Hashimoto, *Materials Sci. and Eng.*, A134 (1991): p.1074.
55. C. A. Zapffe and C. E. Sims, *Trans. AIME*, 145 (1941): p. 225.
56. C. D. Beachem, "Electron Fractographic Support for a New Model for Hydrogen-Assisted Cracking", *Stress Corrosion Cracking and Hydrogen Embrittlement of Iron Base Alloys*, R. W. Staehle, J. Hochmann, R D. McCright and J. E. Slater, Eds., NACE, Houston, (1977): p.376.
57. N. J. Petch and P. Stables, *Nature*, 169 (1952): p.842.
58. R. Thompson, *J. Mater. Sci.*, 13 (1978): p.128.
59. J. P. Hirth, "SCC and HE from the Viewpoint of the Defect Solid State", *Stress Corrosion Cracking and Hydrogen Embrittlement of Iron Base Alloys*, R. W. Staehle, J. Hochmann, R D. McCright and J. E. Slater, Eds., NACE, Houston, (1977): p.1.
60. C. J. McMahon, Jr. and V. Vitek, *Acta Met.*, 27 (1979): p. 507.
61. S. P. Lynch, *Metals Forum*, 2 (1979): p.189.
62. S. Gahr, M. L. Grossbeck and H. K. Birnbaum, *Acta Met.*, 25 (1977): p. 125.
63. A. R. Troiano, *Trans. ASM*, 52 (1960): p.54.
64. R. A. Oriani, *Ber. Bunsenges Phys. Chem.*, 76 (1972): p. 848.
65. C. Wagner, *Corros. Sci.*, 5 (1963): p. 751.
66. H. H. Uhlig, "History of Passivity, Experiments and Theories", *Passivity of Metals*, R. Frankenthal and J. Kruger, Eds., Electrochemical Society, Princeton, New Jersey, (1978): p. 1.
67. N. Sato, "Passivity of Metals and Passivating Films", *Passivity of Metals*, R.

- Frankenthal and J. Kruger, Eds., Electrochemical Society, Princeton, New Jersey, (1978): p. 29.
68. Z. Szklarska-Smialowska, Pitting Corrosion of Metals, published by NACE, Houston, Texas, 1986.
69. M. Nagayama and M. Cohen, J. Electrochem. Soc., 109 (1962): p. 781.
70. V. Mitrovic-Scepanovic, B. MacDougall and M. J. Graham, Corros. Sci., 24 (1984): p. 479.
71. A. R. Brooks, C. R. Clayton, K. Doss and Y. C. Lu, J. Electrochem. Soc., 133 (1986): p. 2459.
72. G. Lorang, M. Da Cunha Belo and J. P. Langeron, J. Vac. Sci. Technol. A, 5 (1987): p.1213.
73. D. A. Harrington, A. Wieckowski, S. D. Rosaaco, B. C. Schardt, G. N. Salaita, A. T. Hubbard and J. B. Lumsden, Corros. Sci., 25 (1985): p.849.
74. C. R. Clayton, K. Doss and J. B. Warren, "Structure and Stability of the Anodically Formed Films on 304 Stainless Steel in Sulfuric Acid", Passivity of Metals and Semiconductors, M. Froment, Eds., Elsevier Science Publishers, Amsterdam (1983): p. 585.
75. G. Okamoto and T. Shibata, "Passivity and the Breakdown of Passivity of Stainless Steel", Passivity of Metals, R. Frankenthal and J. Kruger, Eds., Electrochemical Society, Princeton, New Jersey, (1978): p. 646.
76. G. Okamoto, Corros. Sci., 13 (1973): p. 471.
77. W. P. Yang, D. Costa and P. Marcus, J. Electrochem. Soc., 141 (1994): p. 111.
78. T. Pou, O. Murphy and V. Young and J.O'M. Bockris, J. Electrochem. Soc., 131 (1984): p. 1243.
79. M. Sakashita and N. Sato, Corros. Sci., 17 (1977): p. 473.
80. G. Reinhard and F. Schreider, Proc. 2nd Int. Corros. Conf., Praha (1975): p.319.
81. N. Sato, T. Noda and K. Kudo, Electrochim. Acta., 19 (1979): p. 471.
82. M. G. Bloom and L. Goldenberg, Corros. Sci., 5 (1965): p. 623.
83. B. Alexandre, R. Berneron, J. C. Charbonnier, R. Namdar-Irani and L. Nevot,

- Memories Scient. Rev. Met., 78 (1981): p. 483.
84. K. Kudo, T. Shibata, G. Okamoto and N. Sato, Corros. Sci., 8 (1968): p.809.
85. H. T. Yolken, J. Kruger, J. P. Calvert, Corros. Sci., 8 (1968): p. 103.
- 86 H. H. Uhlig, J. Electrochem. Soc, 97 (1950): p. 215C.
87. H. Böhni and H. H. Uhlig, J. Electrochem. Soc., 113 (1969): p.906.
88. Ya. M. Lolotykin, J. Electrochem. Soc., 108 (1961): p. 209.
89. Ya. M. Lolotykin, Corrosion, 19 (1963): p. 261t.
90. K. G. Weil and D. Menzel, Z. Elektrochem., 63 (1959): p.669.
91. T. P. Hoar, D. C. Mears, and G. P. Rothwell, Corros. Sci., 5 (1965): p.279.
92. T. P. Hoar, Trans. Faraday Soc., 45 (1949): p. 683.
93. J. C. Richardson and G. C. Wood, J. Electrochem. Soc., 120 (1973): p. 193.
94. J. Kruger, "Chemical Breakdown of Passivity", Passivity and Its Breakdown on Iron and Iron Base Alloys, R.Staehle, H. Okada, Eds., NACE, Houston, Texas, (1976): p.91.
95. J. Yahalom and A. Poznansky, "Surface Energy and the Stability of the Passive Layer", Passivity of Metals, R. Frankenthal and J. Kruger, Eds., Electrochemical Society, Princeton, New Jersey, (1978): p. 328.
96. N. Sato, Electrochimi. Acta, 19 (1971): p. 1683.
97. C. Y. Chao, L. F. Lin and D. D. Macdonald, J. Electrochem. Soc., 128 (1981): p.1187.
98. L. F. Lin, C. Y. Chao and D. D. Macdonald, J. Electrochem. Soc., 128 (1981): p.1194.
99. D. D. Macdonald, J. Electrochem. Soc., 139 (1992): p.3434.
100. T. P. Hoar and W. R. Jacob, Nature (London), 216 (1967): p. 1209.
101. Z. A. Foroulis and M. J. Thubrikar, J. Electrochem. Soc., 122 (1975): p.1296.
102. S. Dallek and R. T. Foley, J. Electrochem. Soc., 123 (1976): p. 1775.
103. T. H. Nguyen and R. T. Foley, J. Electrochem. Soc., 126 (1979): p. 1885.
104. J. R. Galvele, J. Electrochem. Soc., 123 (1976): p. 464.
105. J. R. Galvele, J. B. Lumsden and R. W. Staehle, J. Electrochem. Soc., 125 (1978): p.

- 1204.
106. K. J. Vetter, *Ber. Bunsenges. Phys. Chem.*, 69 (1965): p. 589.
107. K. J. Vetter, *Ber. Bunsenges. Phys. Chem.*, 69 (1965): p. 683.
108. B. MacDougall, *J. Electrochem. Soc.*, 126 (1979): p. 919.
109. R. E. Hummel, *Electronic Properties of Materials*, 2nd edition, Springer-Verlag, (1992).
110. J. P. McKelvey, *Solid State and Semiconductor Physics*, Harper & Row Publishers Inc., (1966).
111. D. A. Askeland, *The Science and Engineering of Materials*, 2nd Edition, Chapman & Hall, (1991).
112. D. R. Askeland, *The Science and Engineering of Materials*, PWS publishers, Boston (1984).
113. J. N. Hobstetter, *Semiconductors*, N. B. Hannay, Eds., Reinhold, New York (1959): p. 508.
114. M. Da Cunha Belo, "Photoelectrochemistry: Theoretical Basis", *Electrochemical and Optical Techniques for the Study and Monitoring of Metallic Corrosion*, M. G. S. Ferreira and C. A. Melendres, Eds., NATO ASI Series, Kluwer Academic Publishers, (1989): p. 191.
115. G. Bianchi, A. Cerquetti, F. Mazza and S. Torchio, *Corros. Sci.*, 12 (1972): p.495.
116. Z. Szklarska-Smialowska and M. Janik-Czachor, *British Corros. J.*, 4 (1969): p.138.
117. M. Pourbaix, *Corro. Sci.*, 6 (1966): p.239.
118. M. Pourbaix, *Corro. Sci.*, 19 (1979): p.431.
119. Standard Method G61-86, *Annual Book of ASTM Standards*, ASTM, Philadelphia, 3.02 (1988): p. 254.
120. D. A. Jones, *Principles and Prevention of Corrosion*, MacMillan Publishing Company, (1991).
121. S. R. Morrison, *Electrochemistry at Semiconductor and Oxidized Metal Electrodes*, Plenum Press, New York (1980).
122. W. Schottky, *Z. Phys.*, 113 (1939): p.367.

123. N. F. Mott, Proc. R. Soc. London, A171 (1939): p. 27.
124. M. Da Cunha Belo, "Photoelectrochemistry: Application to the Study of Passive Films", Electrochemical and Optical Techniques for the Study and Monitoring of Metallic Corrosion, M. G. S. Ferreira and C. A. Melendres, Eds., NATO ASI Series, Kluwer Academic Publishers, (1989): p. 219.
125. S. Piazza, C. Sunseri and F. Di Quarto, AIChE Journal, 38, (1992): p. 219.
126. Yu. Ya. Gurevich, Yu. V. Pleskov and Z. A. Rotenberg, Photoelectrochemistry, Consultants Bureau, New York (1980).
127. A. Heller (Ed.), Semiconductor Liquid-Junction Solar Cells, The Electrochemistry Society, Princeton, New Jersey (1977).
128. U. Stimming, Electrochim. Acta, 31 (1986): p. 415.
129. P.C. Searson, R. M. Latanision and U. Stimming, J. Electrochem. Soc., 135 (1988): p.1358.
130. A. Di Paola, D. Shukla and U. Stimming, Electrochim. Acta, 6 (1991): p. 345.
131. A. Di Paola, F. Di Quarto and C. Sunseri, Corros. Sci., 26 (1986): p. 935.
132. K. Azumi, T. Ohtsuka and N. Sato, J. Electrochem. Soc., 133 (1986): p.1326.
133. F. Di Quarto, S. Piazza and C. Sunseri, Corros. Sci., 31 (1990): p. 721.
134. U. Stimming, "Properties of the Passive Film on Iron Electrode by Capacity and Photocurrent Measurements", Passivity of Metals and Semiconductors, M. Froment, Ed., Elsevier Science Publishers, Amsterdam (1983): p.477.
135. S. M. Wilhelm and N. Hackerman, J. Electrochem. Soc., 128 (1981): p.1668.
136. J. W. Schultze, U. Stimming and J. Weise, Ber. Bunsenges Phys. Chem., 86 (1982): p.276.
137. L. M. Castillo and L. M. Peter, J. Electroanal. Chem., 146 (1983): p. 377.
138. H. S. Waff and K. Park, Physics Letters, 32A (1970): p. 109.

Chapter 3. Topic Selection and Experimental Approaches

3.1. TOPIC SELECTION

Stainless steels exhibit excellent general corrosion resistance due to the formation of a thin, hydrated, oxidized and chromium-rich passive film.¹ Stainless steels are widely used in very aggressive corrosive environments and they encounter very severe localized corrosion. The corrosion resistance of stainless steels is often determined by their susceptibility to a local breakdown of passive films. Studies of the passivity and breakdown of passive films are extremely important for stainless steels and have drawn a considerable attention among corrosion scientists.

Stainless steels are classified as ferritic, austenitic, duplex, martensitic and precipitation hardening stainless steels according to their microstructures. Austenitic stainless steels are the most widely used in industry. The addition of nickel to iron-chromium alloys stabilizes the face-centered cubic austenite phase and improves corrosion resistance synergistically with chromium. Austenitic stainless steels are widely used for architectural trim in industrial and marine atmospheres, in the food-processing industry, in the pulp and paper industry, in electric power plants for turbine blades and vanes, heat exchangers, condenser tubing and flue-gas desulfurization equipment. Austenitic stainless steels have been used frequently to contain industrial chemicals and to handle process streams containing water and H_2S in the oil and gas industry. Because of their wide applications, Types 304 and 310 austenitic stainless steels have been chosen as the test materials in this research.

Corrosion-generated hydrogen affects the corrosion process itself. Corrosion promoted by hydrogen becomes a serious factor in the reliability of the structures as a result of the development and construction of oil refineries, chemical and power plants dealing with hydrogen-containing reducing gases. Unfortunately, as indicated in the literature review, the effects of hydrogen on corrosion behavior are still not clear.

As Armacanqui and Oriani² have indicated, more extensive investigation of hydrogen in passive films may produce valuable insights into the mechanisms of passive film breakdown. It is necessary to obtain information about the effects of hydrogen on the compositions and structures (including electronic structures) of passive films. However, this information is not available in the published literature. Hence “the effects of hydrogen on the passivity and corrosion related behavior of austenitic stainless steels” has been selected as the topic of this thesis.

3.2. APPROACH METHODS

In order to study the effects of hydrogen on the passivity and corrosion related behavior of stainless steels, hydrogen was introduced into the specimens. The methods commonly used for hydrogen introduction include charging in hydrogen gas and charging

electrochemically. Electrochemical charging is economical and is easy to control. The amount of hydrogen entering a specimen can be controlled by changing the current density or the charging time.

It is well known that hydrogen can induce martensitic transformation and surface cracking. It is important to know under what conditions the phase transformation and cracking can occur, and whether the surface phase transformation and cracking can greatly affect the corrosion behavior. To reveal these aspects, the critical charging conditions for martensitic transformation and surface cracking will be investigated in Chapter 5. X-ray diffraction techniques together with optical metallographic methods are used to determine the new phases. The amount of martensite has been calculated. The relationship between martensite, surface cracking and the anodic dissolution rate will be studied.

There are some indications that the electronic properties of the passive films may play an important role in the film breakdown mechanism.^{3,4,5} In order to fully understand the mechanisms of the breakdown processes, it is necessary to investigate the electronic properties of the passive films. As indicated in Chapter 2, the Mott-Schottky method and the photoelectrochemical technique are the favorite *in situ* measurements. These two techniques will be applied to reveal the effects of hydrogen on the electronic and structural properties. The conducting type of the passive films, the carrier concentration, the bandgap energy, the flatband potential and the disorder degree of the films will be obtained through these measurements. The information will be used to clarify how hydrogen can affect the passivity and breakdown processes.

The main focus will be on the effects of hydrogen on the passivity and breakdown processes. A standard immersion test will be used to investigate the effects of hydrogen on the pitting susceptibility. As is well known, the halide ions, especially chloride ions, play an important role in the breakdown of passive films. To understand how hydrogen can affect the film breakdown, it is necessary to know whether hydrogen and chloride ions have a synergistic effect. The effects of hydrogen and chloride ions on the

breakdown potential will be obtained by measuring polarization curves. The effects of hydrogen and chloride ions on the anodic current density will also be investigated. A constant passivating potential will be applied to the specimens and the current response to the application of the potential and the addition of chloride ions is recorded. From the current response, the effect of hydrogen on the critical concentration of chloride ions for film breakdown will be measured. Considering the existence of internal and external stresses on the components in practice, an investigation of the effect of stress and hydrogen on the breakdown processes will be included in this research. The impedance technique will also be used to measure the polarization resistance and double layer capacitance.

Based on the results obtained, the effects of hydrogen on the passivity of stainless steels will be discussed. Future work will be recommended at the end of this thesis.

REFERENCES

1. D. A. Jones, Principles and Prevention of Corrosion, published by Macmillan Publishing Company, (1991): p. 514.
2. M. E. Armacanqui and R. A. Oriani, Corrosion, 44 (1988): p.696.
3. P. Schmuki and H. Böhni, J. Electrochem. Soc., 139, (1992): p. 1908.
4. N. Sato, J. Electrochem. Soc., 129, (1982): p. 255.
5. P. Schmuki and H. Böhni, Werkst. Korros., 42 (1991): p. 203.

Chapter 4. Experimental

4.1. EXPERIMENTAL MATERIALS

The commonly used types 304 (UNS-S30400) and 310 (UNS-S31000) stainless steels were chosen as the materials in the study of effects of hydrogen on passivity and corrosion related behavior. These materials used were membranes in the annealed condition, as received. They are 0.2 mm and 0.1 mm thick, respectively. Both steels are austenitic steels due to the presence of a high concentration of nickel, an austenite-stabilizing element. 310 stainless steel has a higher concentration of nickel, and consequently has a higher austenitic stability than 304 stainless steel. The chemical compositions of these two steels are listed in Tables 4-1 and 4-2.

Chemicals used in this research were of analytical reagent grade unless otherwise specified. Deionized water was used to prepare solutions.

Table 4-1. Chemical Compositions (wt%) of UNS-S30400 Stainless Steel

Element	C	Mn	Si	Cr	Ni
Percentage, %	0.072	1.43	0.57	18.24	8.06
Element	Mo	Cu	S	P	Fe
Percentage, %	0.16	0.07	0.0088	0.048	Balance

Table 4-2. Chemical Compositions (wt%) of UNS-S31000 Stainless Steel

Element	C	Mn	Si	P	S	Ni	Cr	Mo
Percentage, %	0.064	1.760	0.696	0.021	0.017	18.40	23.50	0.148
Element	Cu	V	Nb	Ti	Al	Co	W	Fe
Percentage, %	0.156	0.073	0.020	0.090	0.010	0.059	0.056	Balance

4.2. EXPERIMENTAL EQUIPMENT

An Accumet 950 pH/ Ion meter made by Fisher Scientific was used to measure the pH values of the solutions. To introduce hydrogen into specimens, a Hewlett-Packard Harrison 6200B DC power supply was used to provide constant current.

A Gamry Corrosion Measurement System CMS100 was used to conduct potentiodynamic, cyclic potentiodynamic and potentiostatic tests. The AC impedance tests and Mott-Schottky measurements were carried out using a Solatron SI 1287 Electrochemical Interface and 1255B Frequency Response Analyzer. A Potentiostat/Galvanostat Model 273 made by EG & G Princeton Applied Research and a Model SR 810 lock-in amplifier made by Stanford Research Systems were used for the photoelectrochemical measurements.

To examine and analyze the surface of specimens, an optical microscope and a Hitachi S-2700 Scanning Electron Microscope (SEM) were used. The video images were printed out, or saved in the computer using Snappy software. The changes in microstructures were detected using a Philips X-ray Diffractometer.

4.3. EXPERIMENTAL SET-UP

4.3.1. Surface Preparations

Before hydrogen charging, the specimens were wet ground down to 600 grit using SiC paper, then cleaned and rinsed with deionized water, degreased with acetone and dried using a compressed air stream. All the specimens were prepared under the same conditions except for those used for the microstructure observations.

An electrochemical polish was given to the specimens for microstructure observations by applying a constant current density of 780 mA/cm^2 for 5 minutes in 37% H_3PO_4 +

56% glycerin + 7% H₂O solution at 110°C. The specimens acted as the anode while a Pt mesh served as the cathode.

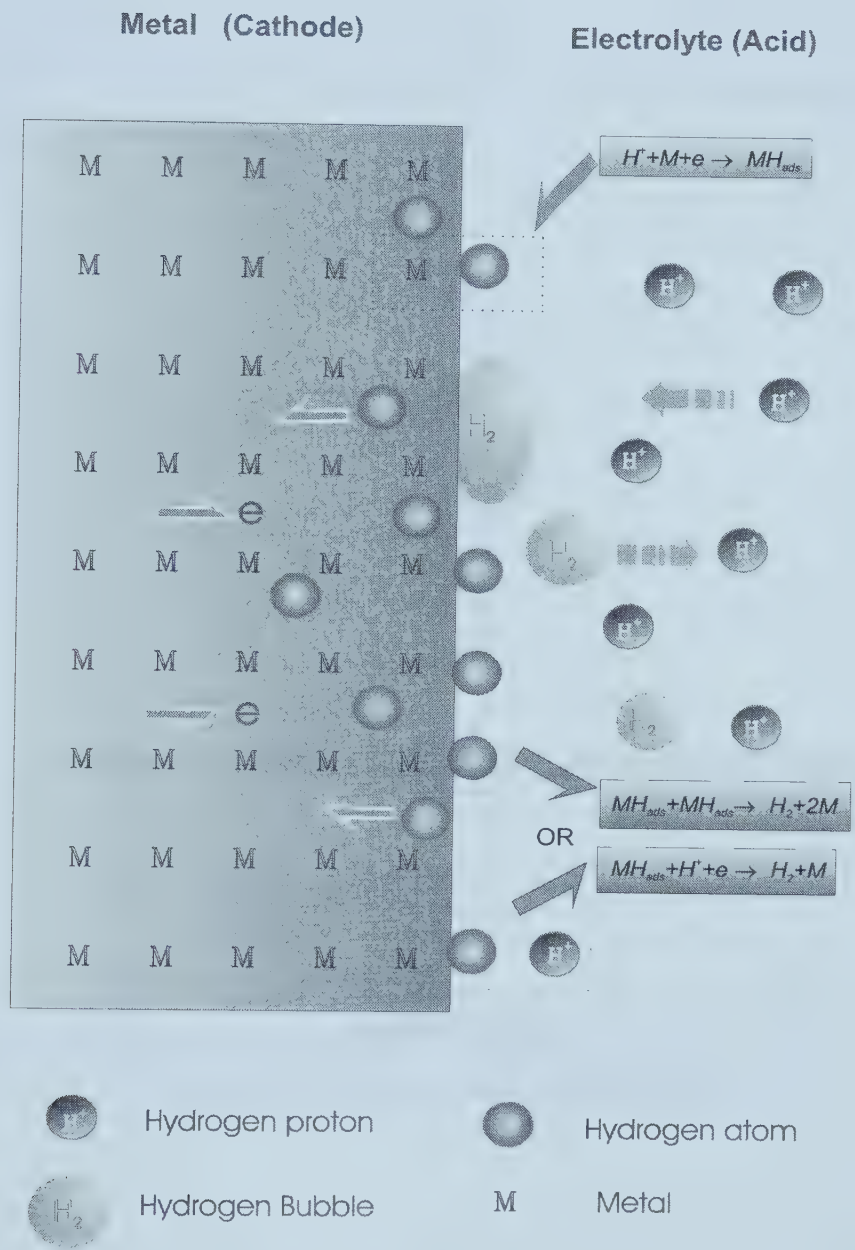


Figure 4-1. A schematic of the reactions and processes involved in cathodically charging in an acid.

4.3.2. Hydrogen Charging

In order to study the effects of hydrogen on the passivity and corrosion related behavior of stainless steels, hydrogen was introduced into the specimens by cathodically charging at a constant current density.

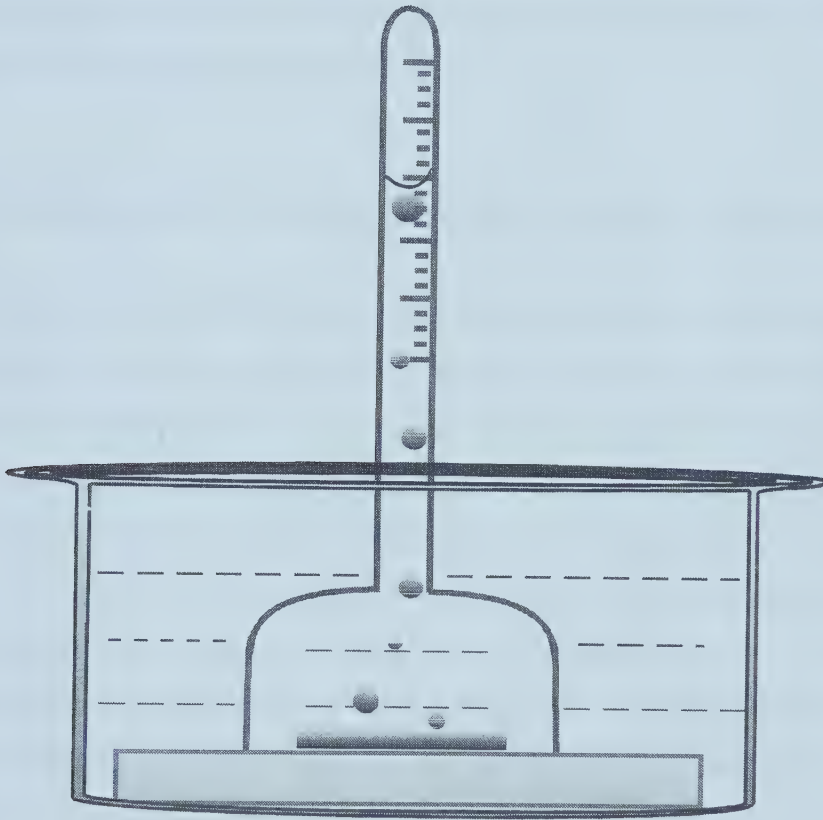


Figure 4-2. Setup for measurements of diffusible hydrogen in specimens.

During the hydrogen charging, a specimen acted as a cathode. The anode used was a U-shaped platinum net with a size of 2.5 X 3.75 mm. During charging, the anode was parallel to each surface of the specimen to guarantee a uniform distribution of current during the charging. The distance between the net and the surface of the specimen was 2mm. A 0.5 M H_2SO_4 + 250 ppm As_2O_3 solution was chosen as the charging electrolyte. As_2O_3 acted as a hydrogen recombination poison, which promoted the absorption of hydrogen by the specimens.¹ The reactions and processes involved in cathodically hydrogen charging in an acid are shown in Figure 4-1. To introduce different amount of hydrogen into specimens, the specimens were hydrogen charged at different current densities for different charging periods.

4.3.3. Measurements of Amount of Diffusible Hydrogen in Specimens

It is important to reveal the effects of charging conditions on the amount of hydrogen in the charged specimens. However, it is very difficult to measure the amount of hydrogen in the metals directly. In this research, the amount of diffusible hydrogen was measured indirectly. The diffusible hydrogen in a charged specimen was measured by collecting the escaped hydrogen after charging at room temperature. After charging, the specimens were immediately transferred into a special upside-down glass cup that was filled and sealed with silicone oil. The setup is shown in Figure 4-2. The volume of hydrogen released from the charged specimens was measured for 24 hours and the hydrogen mass was calculated using the ideal gas equation. This method was originally proposed to measure the diffusible hydrogen in weldments.²

4.3.4. Detection of Phase Transformations by X-ray Diffraction Analysis and Optical Metallographic Observation

To investigate the effects of hydrogen charging on the phase transformation, before the tests, the specimens were initially annealed for 1 hour at 1050°C in argon and water quenched to room temperature. The carbide particles, if they existed in the specimens,

would dissolve into austenite phase during the heating. The fast cooling prevented the re-precipitation of the carbide. Therefore after heat treatment, the specimens had 100% austenite.

An optical microscope was used to observe changes in the microstructures and surface cracks. One set of specimens was etched in a 0.5 M H₂SO₄ + 0.1 M HCl solution at 1.05 - 1.1 V (vs. SCE) for 2-5 minutes. The etched specimen acted as the anode and a platinum net as the counter electrode.

The phases and phase amounts were determined by X-ray diffraction (XRD) analyses, employing Cu K_α radiation with the diffraction angle θ scanned through 20 to 45°. Any phase transformation was identified by the appearance of new reflections. The percentage of each phase component in a multiphase specimen was determined from the relative intensities of diffraction peaks by the direct comparison method.³ As suggested by Bentley and Smith,⁴ the integrated intensity of a diffraction line, I_i , can be expressed as:

$$I_i = KR_iV_i \quad [4-1]$$

where K is a constant for a given experimental condition, independent of the diffracting substance; R_i is a structure factor related to the intensity; V_i is the volume of the phase exposed to the X-ray beam.

The volume of a certain phase, V_i , in a multiphase specimen can be expressed as $\frac{I_i}{KR_i}$, and the volume fraction of this phase $\frac{V_i}{\sum_i V_i}$, can be calculated from the following equation:

$$\frac{V_i}{\sum_{i=1}^n V_i} = \frac{\frac{I_i}{R_i}}{\sum_{i=1}^n \frac{I_i}{R_i}} \quad [4-2]$$

where n is the number of phases present in the specimen.

In this study the average values of $\frac{I_i}{R_i}$ obtained from several peaks for each phase were used to calculate the phase percentages. The peaks used in the quantitative evaluation, together with the R_i values calculated from the data of Cullity³ are given in Table 4-3. The lattice parameters of the phases were determined with Bragg's law and the crystallographic relationships between lattice parameters and interplanar spacing d .

Both metallographic and X-ray diffraction analyses were used to determine the critical charging conditions for martensite transformation.

Table 4-3. X-Ray Diffraction Peaks Used in the Quantitative Determination of Phase Components

Reflection	d (Å)	Diffraction Angle (2θ)*	R_i values ^{3, 4}
$\{111\}_\gamma$	2.070	43.75	212
$\{200\}_\gamma$	1.792	50.96	95
$\{220\}_\gamma$	1.267	74.94	52
$\{110\}_{\alpha'}$	2.028	44.69	279
$\{200\}_{\alpha'}$	1.434	65.05	40
$\{211\}_{\alpha'}$	1.171	82.36	79
$\{10\bar{1}1\}_\epsilon$	1.935	46.96	188
$\{10\bar{1}2\}_\epsilon$	1.500	61.86	24
$\{10\bar{1}3\}_\epsilon$	1.163	83.07	30

* Cu K_α radiation

4.3.5. Immersion Tests

ASTM Practice G48 Method A⁵ was used to evaluate the pitting susceptibility of both charged and uncharged specimens. The immersion test was carried out at 22 °C. For 310 stainless steel, the solution consisted of 100 g reagent grade $\text{FeCl}_3 \cdot 6\text{H}_2\text{O}$ and 900 ml of distilled water. The time elapsed between the end of the charging period and the beginning of the measurement was kept constant at 5 minutes. One of the specimens was taken out of the solution after each immersion period and observed with an optical microscope. The surface morphological pictures were taken through a video camera and printed out using a video printer. Some of the pictures were saved into files using Snappy software. The pit density, size and the percentage of the apparent surface area occupied by pits were statistically measured. For each specimen, at least eight to ten fields were used to obtain accurate statistical results.

4.3.6. Electrochemical Measurements

4.3.6.1. The Typical Three-Electrode Cell

For the electrochemical measurements, the typical three-electrode cell was used. In this cell, the test specimen acted as a working electrode with a saturated calomel electrode (SCE) as a reference electrode and a Pt net as counter electrode. The cell used for most of the electrochemical measurements is shown in Figure 4-3. Figure 4-4 shows details about the specimen holder.

The reference electrode was placed outside the cell, and the potential of the working electrode was measured through a salt bridge probe with respect to the reference electrode. The salt bridge has two roles: (1) to reduce the liquid junction potential and (2) to prevent or to reduce the mutual contamination of the cell solution and the reference electrode solution. There are various ways to make a salt bridge. In this research, a salt bridge with agar gel was used. To make this salt bridge, a saturated KCl solution with

2~3% agar was heated to dissolve the agar, which was then used to fill a glass tube. After cooling, an immobile gel formed inside the tube. The diameter of the glass tube close to the working electrode (the specimen) was made gradually thinner to become a Luggin capillary. The tip of the capillary was placed very close to the specimen to reduce the potential drop due to the ohmic electrolyte resistance of the solution between the capillary and the specimen.

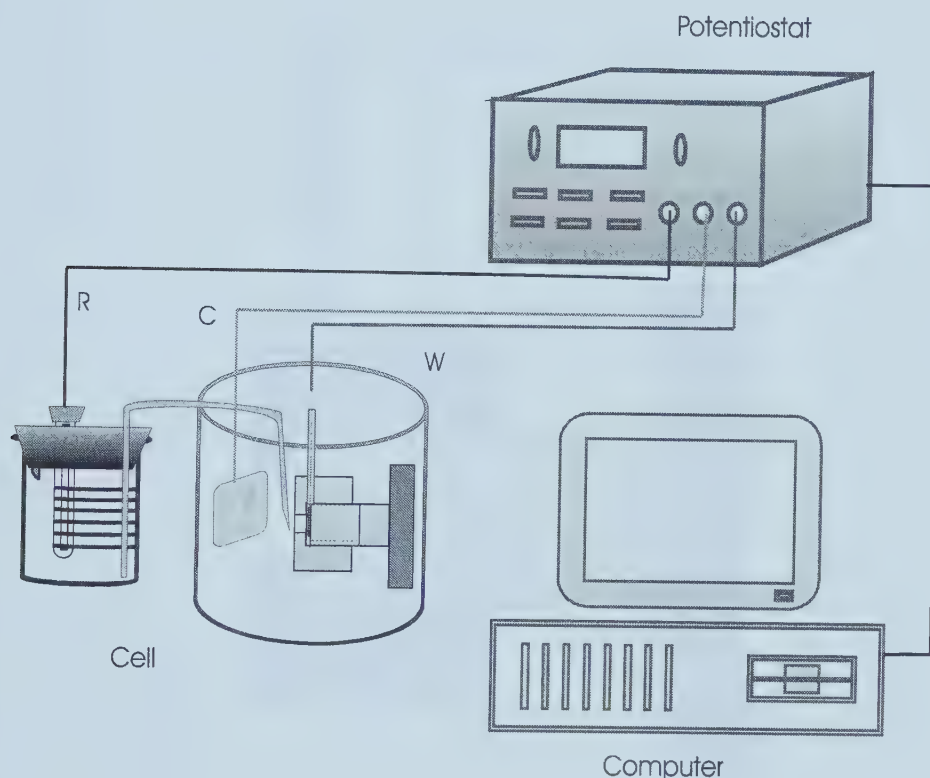


Figure 4-3. Setup for most of electrochemical measurements.

Counter electrodes (auxiliary electrodes) must be made of materials that are inert to the electrolyte, even under strong anodic polarization.⁶ Platinum is often the choice. Due to the rising precious metal prices, a less expensive, lower mass/area alternative is the platinum net spot welded to platinum wire which is sealed into a glass tube with epoxy.

In this research, all potentials were presented with respect to the SCE. All the electrochemical measurements were carried out in solutions open to the air.

The electrolytes used for most of electrochemical measurements were 0.02M H_3BO_3 + 0.005M $\text{Na}_2\text{B}_4\text{O}_7 \cdot 10\text{H}_2\text{O}$ (pH 8.45) borate buffer solutions containing sodium chloride (NaCl) of various concentrations.

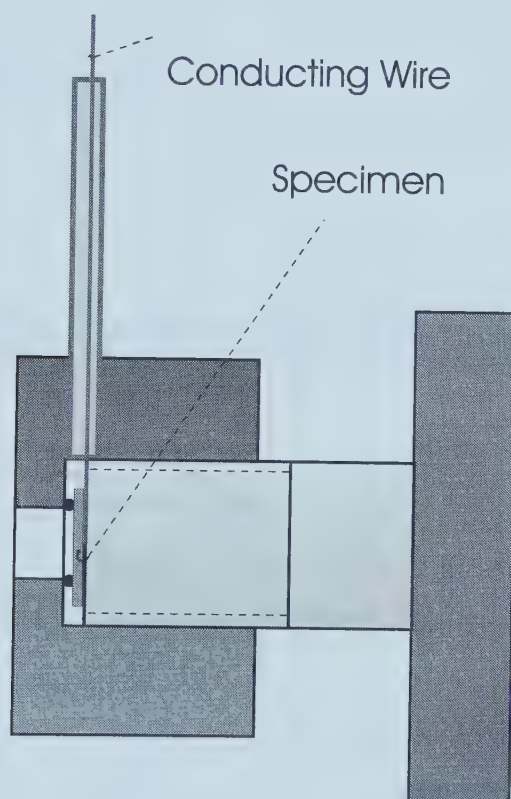


Figure 4-4. The details of the specimen holder.

4.3.6.2. Potentiodynamic Polarization and Cyclic Potentiodynamic Polarization (CPP) Measurements

Potentiodynamic polarization curves are measured with an initial potential of -0.3 V vs. open circuit potential and a scan rate of 0.33 mV/s at 22 °C.

The cyclic potentiodynamic polarization (CPP) technique is widely used for examining the pitting susceptibility. Measurements were performed in a borate buffer solution containing 200 ppm NaCl at 22°C. The initial potential was -0.5 V vs. SCE. The scan rate was 1 mV/second. The scan was first made in the anodic direction with the reverse scan beginning when the current reached 200 $\mu\text{A}/\text{cm}^2$.

4.3.6.3. Potentiostatic Measurements

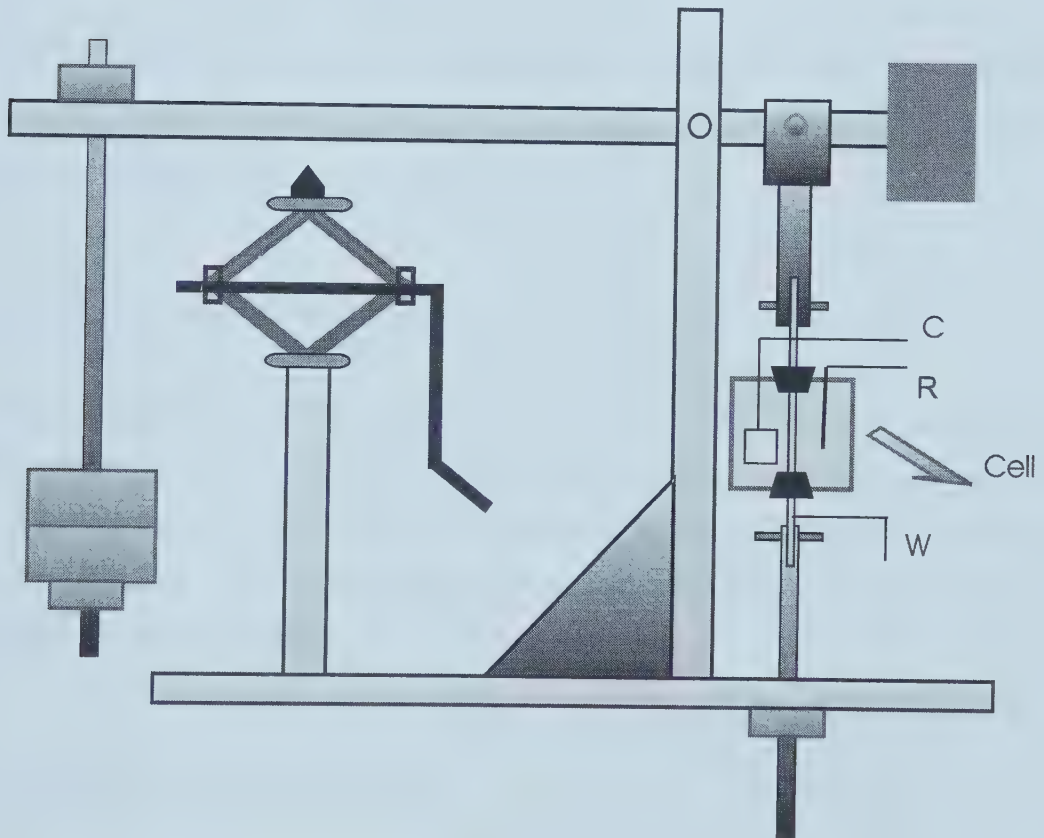


Figure 4-5. Setup for the electrochemical measurements of stressed specimens

To investigate the effects of hydrogen and chloride ions on the stability of passive films and measure the critical chloride concentration for the breakdown of passive films, a constant potential was applied to the specimens in the chloride-free buffer solution. After passivation for 10 minutes, NaCl of various concentrations was added to the solution. The current responses to the application of the constant potential and the addition of chloride ions were recorded. The total testing time for each current response measurement was 1 hour. A sudden increase of anodic current was considered to be the result of the breakdown of the passive film. The time interval between the addition of chloride ions and this current increase was defined as the initiation time for the film breakdown.

To study the effects of stress on the breakdown of passive films on charged and uncharged specimens, a constant tensile load was applied to the specimens through the device shown in Figure 4-5.

4.3.6.4. AC Impedance Measurements

For the AC impedance measurements, the frequency range of the AC signal was 10 KHz to 5 mHz and the DC potential was 0.1 V vs. SCE while an AC voltage signal was superimposed on the DC potential. The amplitude of the AC signal was 10mV peak-to-peak in this research. The impedance data were collected with a Gamry CMS 300 Electrochemical Impedance System.

4.3.6.5. Mott-Schottky Measurements

To characterize the electronic properties of passive films, Mott-Schottky plots were determined for each passive film by measuring the capacitance of the passive film as a function of potential at a rate of 12.5 mV/step (1.5 mV/s) in the anodic direction. An AC voltage signal of frequency 1000Hz and 10 mV peak-to-peak in magnitude was applied

to the system. The values of capacitance were calculated from the imaginary part of the impedance, using an equivalent series RC circuit.

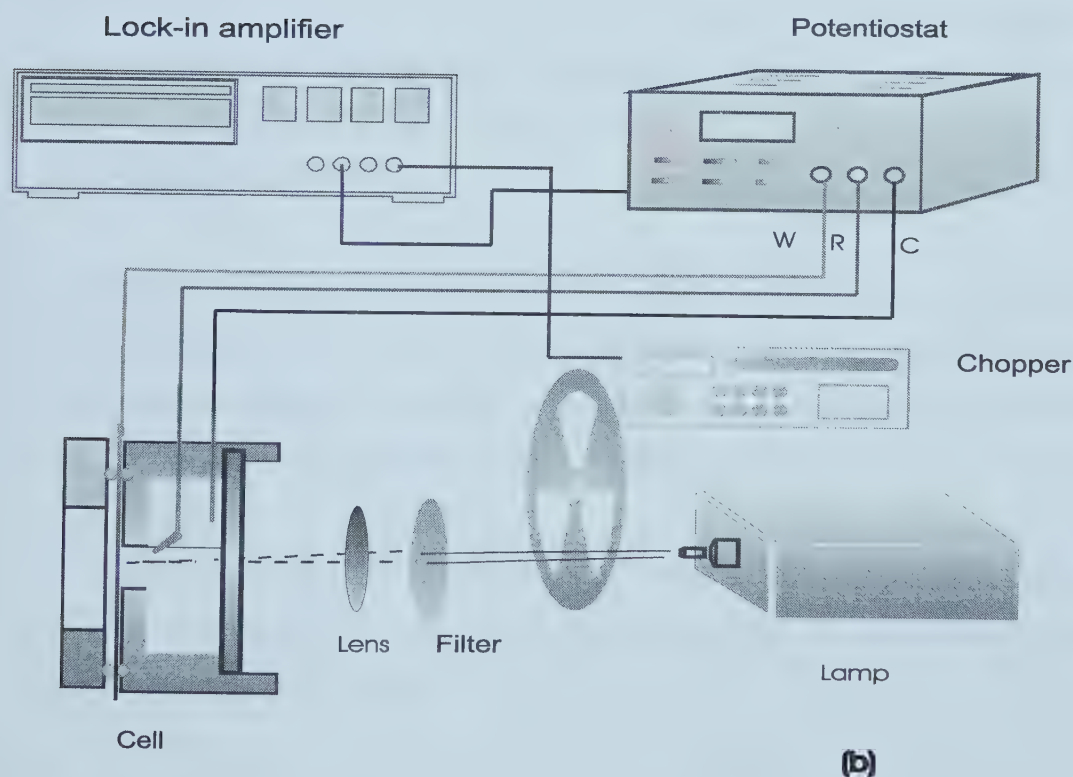
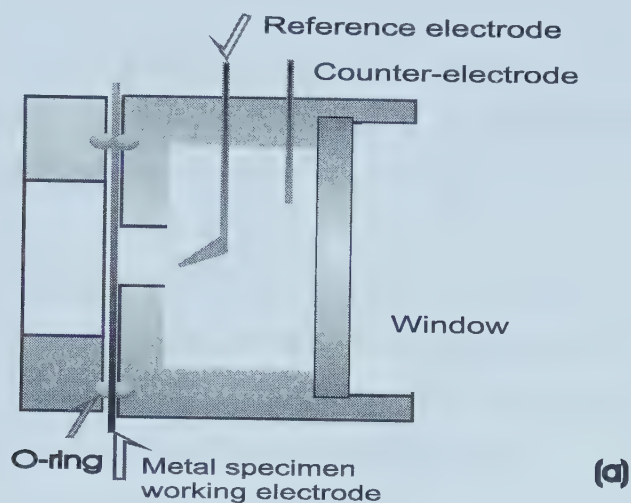


Figure 4-6. The electrochemical cell for the photoelectrochemical measurement (a) and the experimental setup (b).

4.3.6.6. Photoelectrochemical Measurements

The setup for the photoelectrochemical measurements is shown in Figure 4-6. The specimens were first passivated in the solution at 0.7 V, and then the photoelectrochemical responses were measured. The photocurrent measurements were performed in the same solution on the illuminated specimens.

A polychromatic light source was used in this research. The advantage of the polychromatic source is its high intensity and its spectrum covering a wide range of wavelengths.⁷ A 150 W Xenon arc lamp acted as a light source. The incident light was chopped at a frequency of about 30 Hz by a light chopper.

Photocurrent spectra were acquired by focusing chopped monochromatic light onto the specimens, scanning the wavelength in the range of 340 to 600 nm and measuring, under potentiostatic conditions, the photocurrent response. In order to illuminate the electrode surface, the cell had a quartz window and the electrolyte was 8 mm thick to avoid light spot degradation.

Photocurrents were measured as functions of the wavelength of the incident light and the electrode potential. In most cases, photocurrents are fairly small requiring methods with a superior signal-to-noise ratio. A lock-in amplifier was used in this research. In this case, the frequency control of the chopper sends a signal, f_1 , to the lock-in amplifier.

In order to obtain intensity corrected spectra, the intensity vs. wavelength curve of the light source (calibration curve) has to be determined. A silicon diode was used as a detector to measure this curve.

Except specially indicated, lines in most of the figures in this thesis will be plotted for the guide of eye.

REFERENCES

1. T. Zakroczymski, Hydrogen Degradation of Ferrous Alloys, A. Oriani, J. P. Hirth and M. Smialowski, Eds., Noyes Publications, Park Ridge, New Jersey (1985): p.225.
2. E. F. Nippes and D. J. Ball and W. J. Gestal, Jr., Welding Journal, (1981): p.50-S.
3. B. D. Cullity, Elements of X-ray Diffraction, Addison-Wesley, Reading, MA (1978): p. 407.
4. A. P. Bentley and G. C. Smith, Metall. Trans. A, 17A (1986): p.1593.
5. "Standard Test Methods for Pitting and Crevice Corrosion Resistance of Stainless Steels and Related Alloys by Use of Ferric Chloride Solution", G 48-92, Annual Book of ASTM Standards, 03.02, ASTM, PA, (1997): p.181.
6. Denny A. Jones, Principles and Prevention of Corrosion, Macmillan Publishing Company, New York, 1991.
7. U. Stimming, Electrochimica Acta, 31, (1986): p.415.

Chapter 5. Hydrogen-Induced Martensitic Phase Transformation, Surface Cracking and Anodic Dissolution

It is well accepted that hydrogen can induce a martensitic transformation in Type 304, 310, 316 and 321 stainless steels.^{1,2,3,4,5,6} The preferential dissolution of martensite would result in an increase in the anodic dissolution⁷ and facilitate the formation of active paths for stress corrosion cracking propagation.⁸ Hydrogen-induced martensite also has some effects on pitting corrosion.⁹ Published research reveals that martensite formation is detected in connection with hydrogen embrittlement.^{10,11} Martensite transformation is also responsible for surface cracking.¹² Therefore, hydrogen-induced martensite could play an important role in corrosion and stress corrosion cracking processes. In previous reports,^{1,2,4,7} almost all the results were obtained by charging the specimens with very

high cathodic current densities ($\geq 50\text{mA/cm}^2$). It is doubtful that such a high current density would be obtained in practice. Therefore, it is very important to investigate the critical charging conditions for hydrogen-induced martensite transformation.

The objectives of this research are to find the critical charging current density for certain charging times or a critical charging time for certain charging current densities and to find the threshold charging current density below which no martensite transformation would occur. Based on the critical charging conditions, a relationship between martensite transformation, surface cracking and corrosion behavior will be established.

5.1. EFFECTS OF CHARGING PARAMETERS ON THE AMOUNT OF HYDROGEN IN TYPE 304 STAINLESS STEEL

In this research, hydrogen was introduced into specimens by cathodically charging at a constant current density for a period. The amount of hydrogen was changed by varying the charging current density or the charging time. It is necessary to reveal how the change in charging current density or charging period affects the amounts of hydrogen in the specimens.

5.1.1. Hydrogen Release Curves

The amounts of hydrogen in specimens were measured indirectly by measuring the diffusible hydrogen which escaped from the specimens during a certain length of time.

Figure 5-1 shows the amount of hydrogen vs. release time curves of the specimens charged at 10 mA/cm^2 for different charging times. It is observed that hydrogen escapes very quickly at the beginning and then slows down. At first, the amount of released hydrogen follows the following equation with respect to the release time:

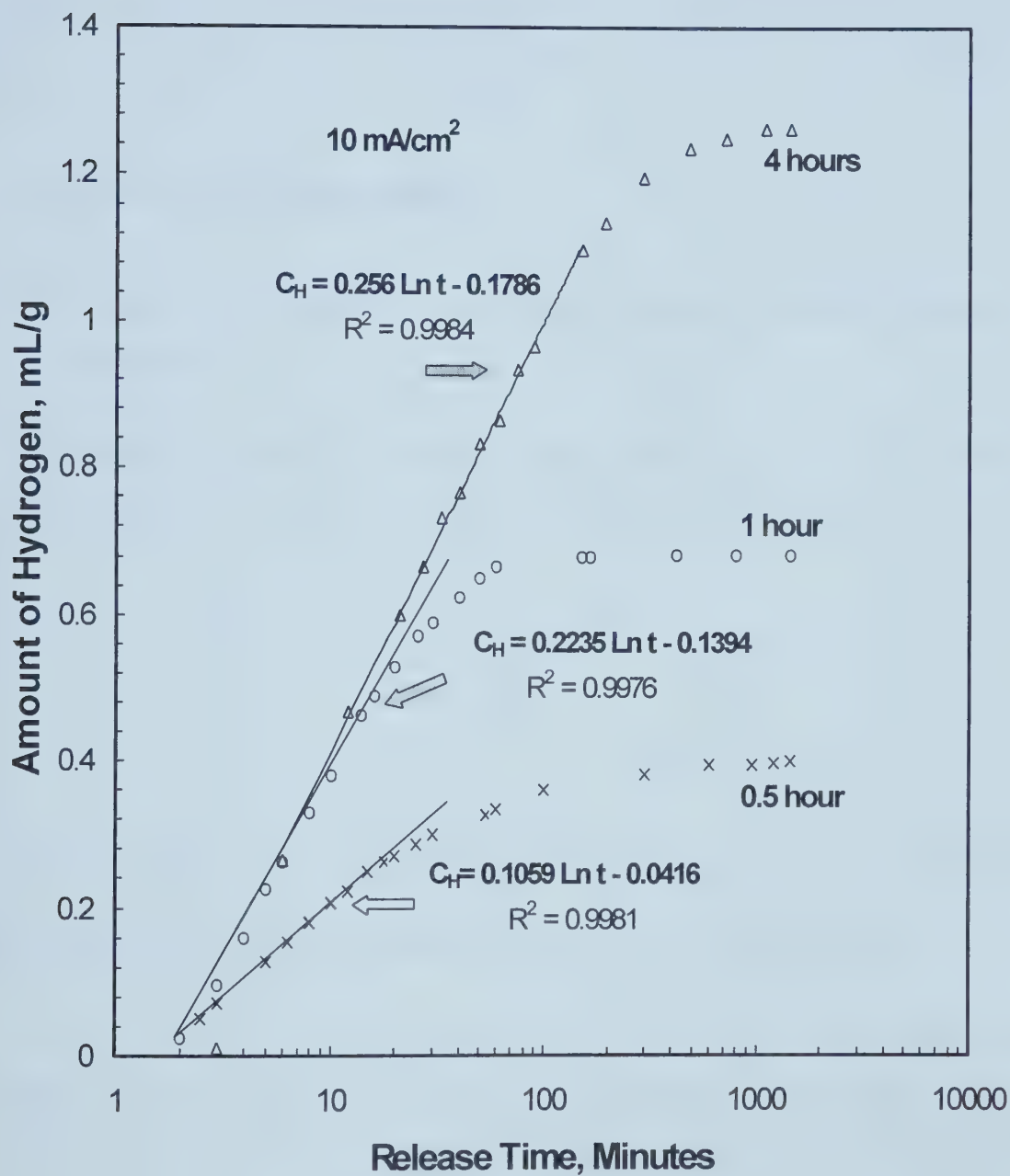


Figure 5-1. The amount of hydrogen vs. release time curves of the specimens charged at 10 mA/cm^2 for different charging time as indicated in the figure.

$$C_H = a_H \ln t + b \quad [5-1]$$

where C_H is the amount of hydrogen (ml/g) released from the specimen and t is the release time.

5.1.2. Kinetics of Hydrogen Release

In Figure 5-1 where the time axis is on a logarithmic scale, a straight-line section on each curve is observed.

The equations for the trend lines of the linear sections are shown in the same figure. R-squared values are also presented in Figure 5-1. R-squared values indicate the goodness of fit:

$$R^2 = 1 - \frac{SSE}{SST} \quad [5-2]$$

where $SSE = \sum (Y_i - \hat{Y}_i)^2$ and $SST = (\sum Y_i^2) - \frac{(\sum Y_i)^2}{n}$. Y_i and \hat{Y}_i are experimental and fitted data, respectively. n here is the number of the experimental data for fitting.

The optimum of R^2 value is 1 when the regression line fits the experimental data perfectly. The closer R^2 is to 1, the better the regression line fits the data. The R-square values in this case are very close to 1 (> 0.997), which indicates the fits are quite good.

The slope of the linear section changes with the charging time and the curves deviate from the straight lines after a certain period.

Figure 5-2 shows this change in slope for the specimens charged at 10 mA/cm², demonstrating that the slope increases with increasing charging time. Also it can be

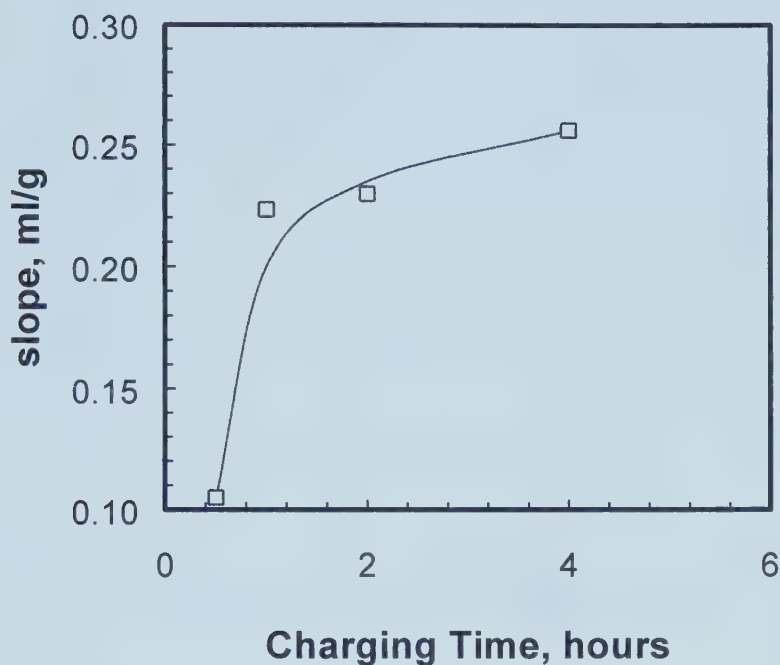


Figure 5-2. The change in the slope of the straight-line section of hydrogen release curves with charging time. The charging current density is 10 mA/cm².

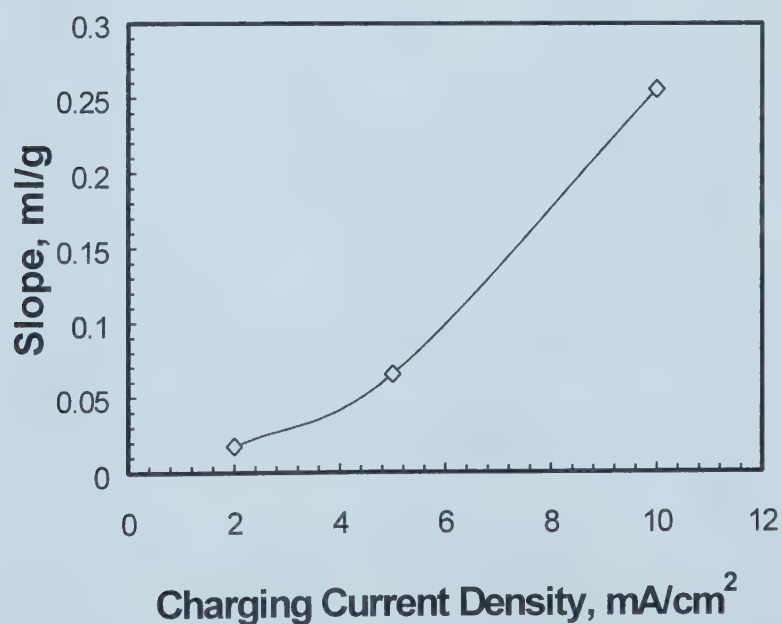


Figure 5-3. The change in the slope of the straight-line section of hydrogen release curves with the charging current density. The charging time is 4 hours.

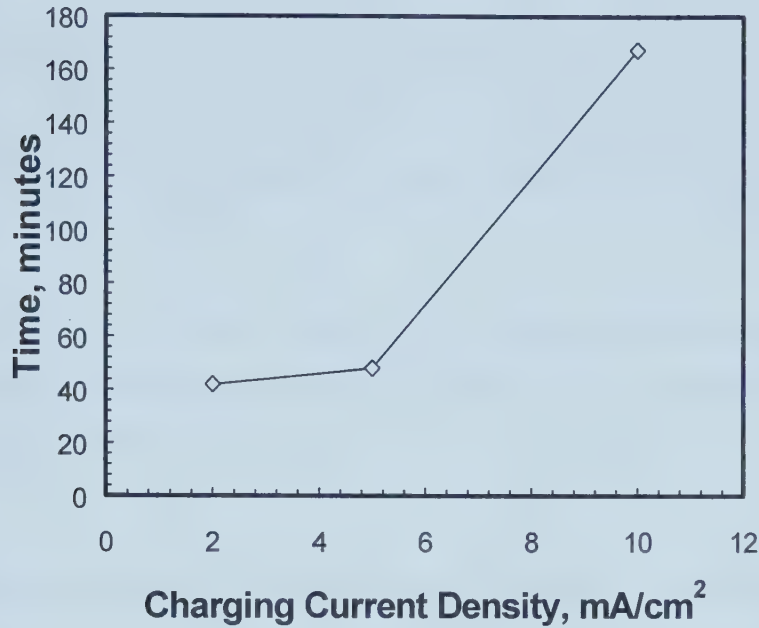


Figure 5-4. The time at deviation from the linear section in the hydrogen release curves changes with charging current density. The charging time is 4 hours.

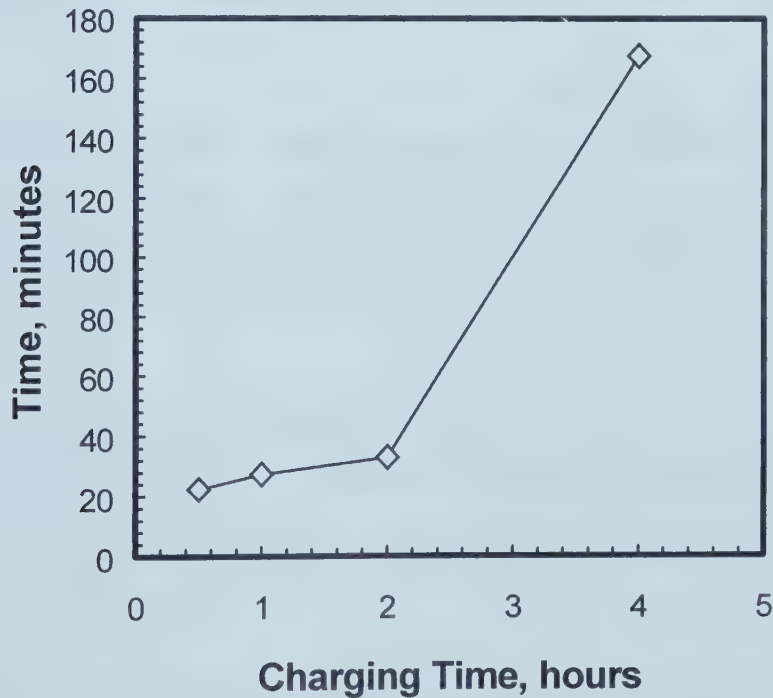


Figure 5-5. The time at deviation from the linear section in the hydrogen release curves changes with charging time. The charging current density is 10 mA/cm².

observed (Figure 5-3) that for the specimens charged for the same time, the slope increases with charging current density. The increase in the slope indicates a higher hydrogen release rate from the specimens charged at higher current densities or for longer charging times.

The time at which a serious deviation from the straight-line section begins increases with the charging current density (Figure 5-4) or the charging time (Figure 5-5). This is similar to the trend observed for the slope.

5.1.3. Effects of Hydrogen Charging Parameters on the Amount of Hydrogen in the Specimens

Changing the hydrogen charging parameters can change the amount of hydrogen in the specimens. Figure 5-1 shows that most of hydrogen was released in the first couple of hours.

Using the amount of the released hydrogen during a period of 1440 minutes to approximately represent the entire amount of hydrogen and converting mL/g to ppm (10^{-3} mg/g), the effects of hydrogen charging parameters on the amount of hydrogen are shown in Figure 5-6.

It should be pointed out here that the amount of the ‘residual’ or trapped hydrogen is much less than the amount of the diffusible hydrogen.¹³ Therefore, we can use the amount of the diffusible hydrogen to approximately represent the total amount of hydrogen in the specimens.

It is shown that the longer the hydrogen charging time or the higher the charging current density, the more hydrogen is introduced into the specimens. This provides the basis for this research to use the hydrogen charging parameters to represent the relative amount of hydrogen in the specimens.

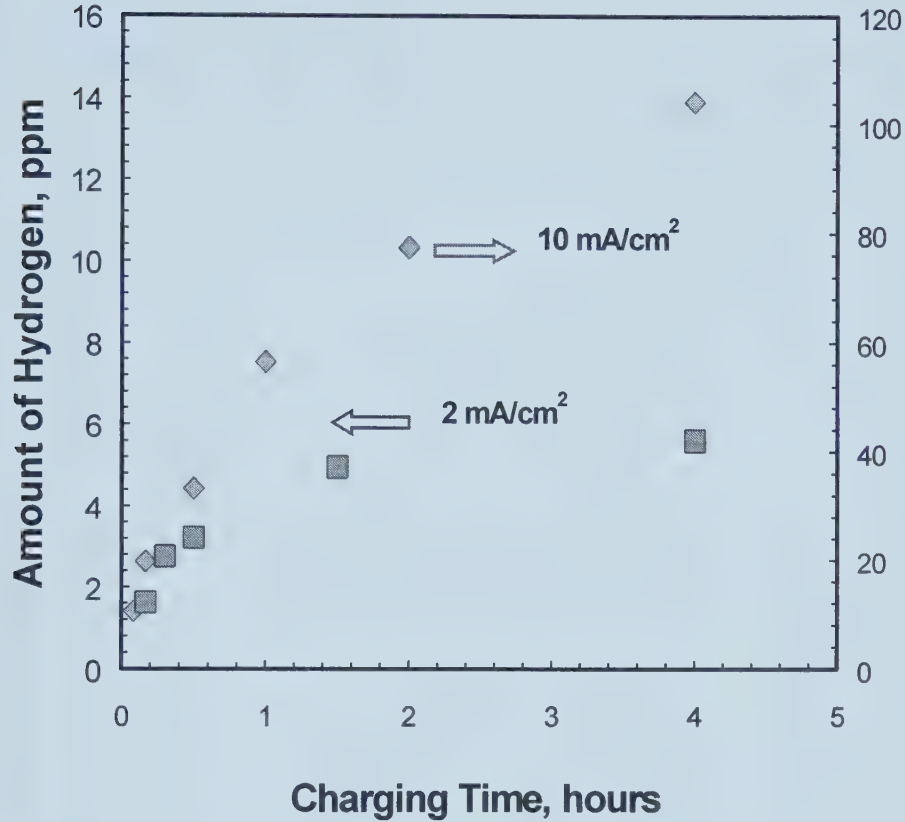


Figure 5-6. The amount of hydrogen released from the specimens charged at 10 mA/cm² for 24 hours at room temperature.

5.2. EFFECTS OF CATHODIC CHARGING ON PHASE TRANSFORMATION OF TYPE 304 STAINLESS STEEL

5.2.1. X-Ray Diffraction (XRD) Analyses

XRD spectra for the uncharged specimen and specimens charged at 20 mA/cm² for various times are shown in Figure 5-7.

The charged specimens used for X-ray diffraction were aged at room temperature for 24 hours after charging.

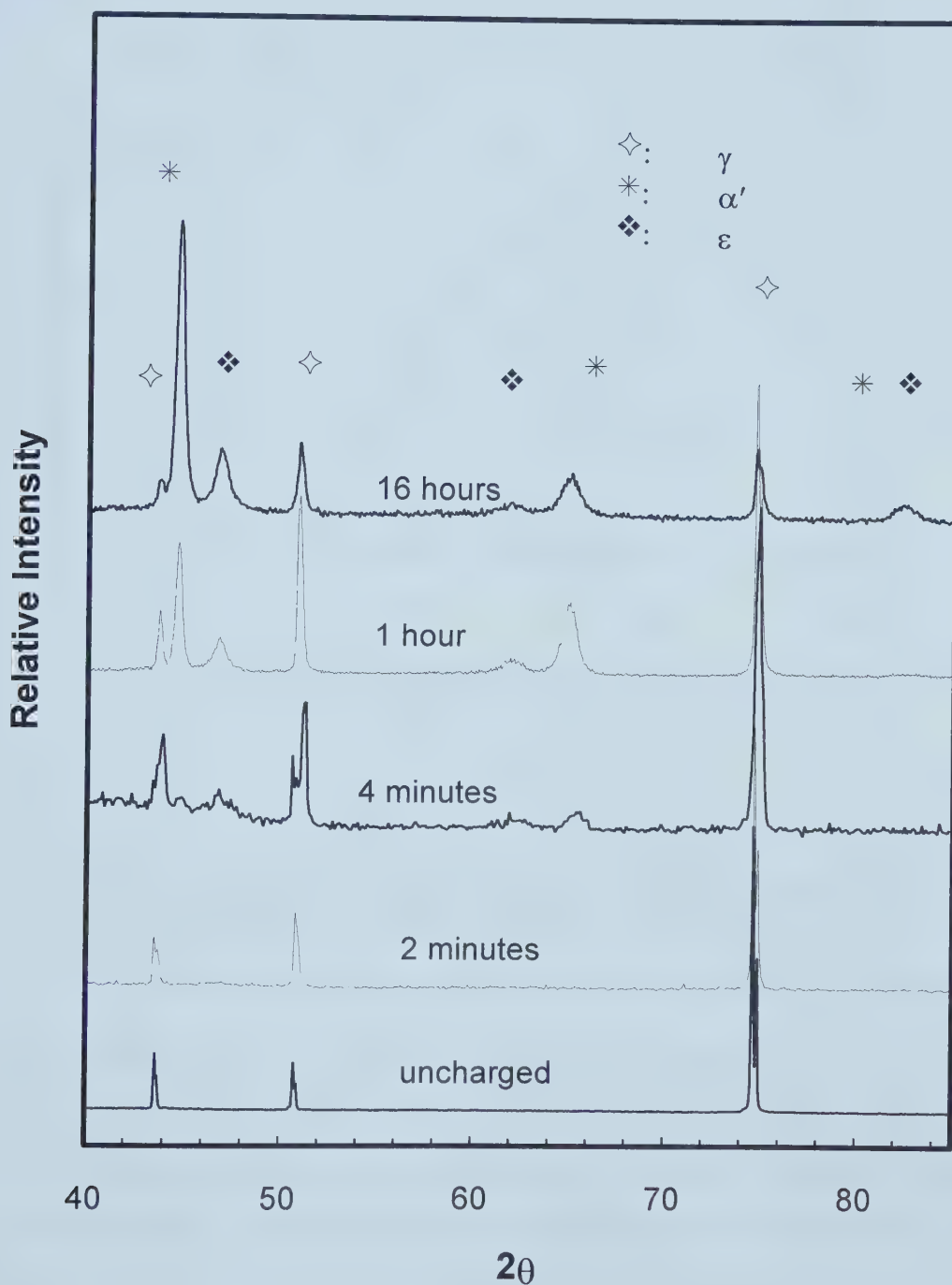


Figure 5-7. XRD spectra of the uncharged specimen and specimens charged at 20 mA/cm^2 for different charging periods.

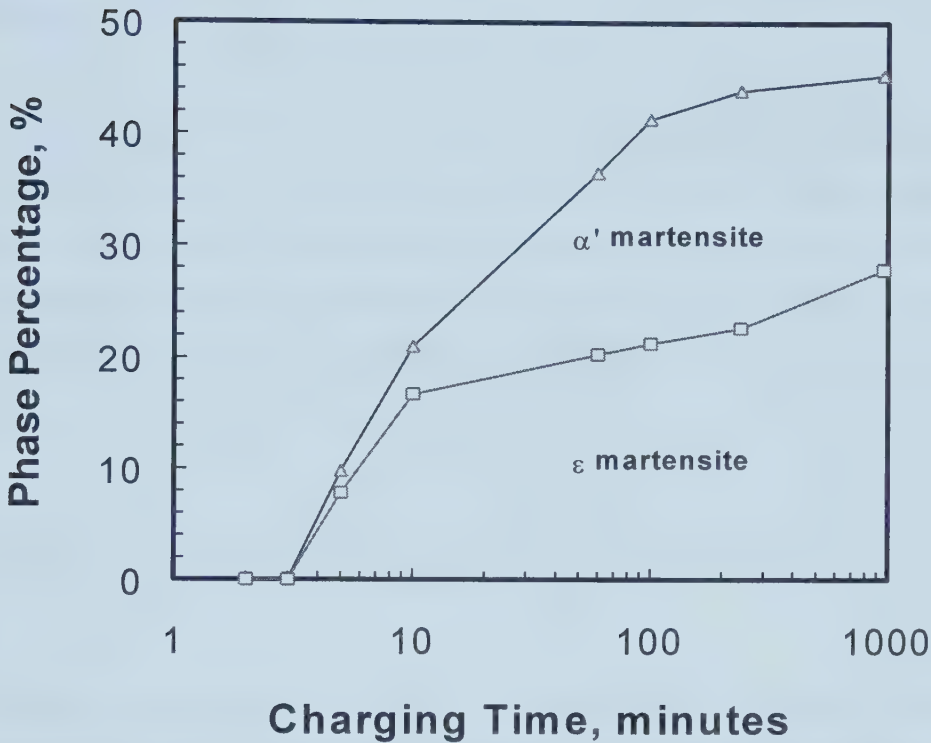


Figure 5-8. Changes in martensite volume percentage with charging time for the specimens charged at 20 mA/cm^2 . The measurements were performed after the specimens were aged at room temperature for 24 hours.

From the XRD analyses, it is shown that only the austenite phase, γ , (f.c.c structure) exists for the uncharged specimens and the lattice constant a is $3.593 \cdot 10^{-10} \text{ m}$. New reflections observed for the specimens after hydrogen charging can be indexed as belonging to ϵ and α' martensites. α' martensite has a b.c.c structure with lattice parameter $a = 2.868 \cdot 10^{-10} \text{ m}$ which nearly equals that of α' martensite formed by deformation ($a = 2.865 \cdot 10^{-10} \text{ m}$)¹⁴. The ϵ martensite has a close-packed hexagonal structure and the lattice parameters measured in this work were $a = 2.541 \cdot 10^{-10} \text{ m}$ and $c = 4.080 \cdot 10^{-10} \text{ m}$ ($c/a = 1.606$), both being about 5%~6% less than those immediately after severe hydrogen charging ($a = 2.66$

$\ast 10^{-10}$ m and $c = 4.35 \ast 10^{-10}$ m)³ and very close to the reported parameters for ϵ martensite formed by plastic deformation ($a = 2.531 \ast 10^{-10}$ m, $c = 4.137 \ast 10^{-10}$ m).¹⁵ This fact suggests that ϵ martensite formed during hydrogen charging is changed to hydrogen-free ϵ phase during aging.

The percentages of martensite phases present in the uncharged and charged specimens are shown in Figure 5-8. For the specimens charged at 20 mA/cm², when charging time is less than 3 minutes, only γ phase exists in the metals. For the specimens charged longer than 4 minutes, the percentages of both α' and ϵ martensite phases increase with an increase in the charging time. For the specimen charged for 16 hours, after aging, the total amount of martensites ($\alpha' + \epsilon$) can be up to about 70%.

5.2.2. Metallographic Observations Immediately after Charging

Five minutes after being charged the specimens were immediately etched and then observed using an optical microscope. Figure 5-9 shows the photomicrographs of the uncharged specimen and the specimens charged at 20 mA/cm². For the uncharged specimen, only one phase (austenite) exists (Figure 5-9 (a)). Grain boundaries and annealing twin bands are clearly visible. For the specimens charged at 20 mA/cm² for less than 3 minutes, no new phase is observed (Figure 5-9 (b)). After charging for more than 3 minutes martensite is observed (see the short straight lines inside of the frame in Figure 5-9 (c)), and the amount of martensite increases with an increase in the charging time (Figure 5-9 (d)). Because α' martensite has not been observed immediately after hydrogen charging,¹² these martensite platelets should be ϵ martensite. Martensite platelets are parallel to each other, but do not cross twin boundaries. This indicates that martensite platelets grow along certain crystallographic directions.

5.2.3. Critical Charging Conditions for Martensite Transformation

From Figure 5-9, it is observed at a certain charging current density, that there is a

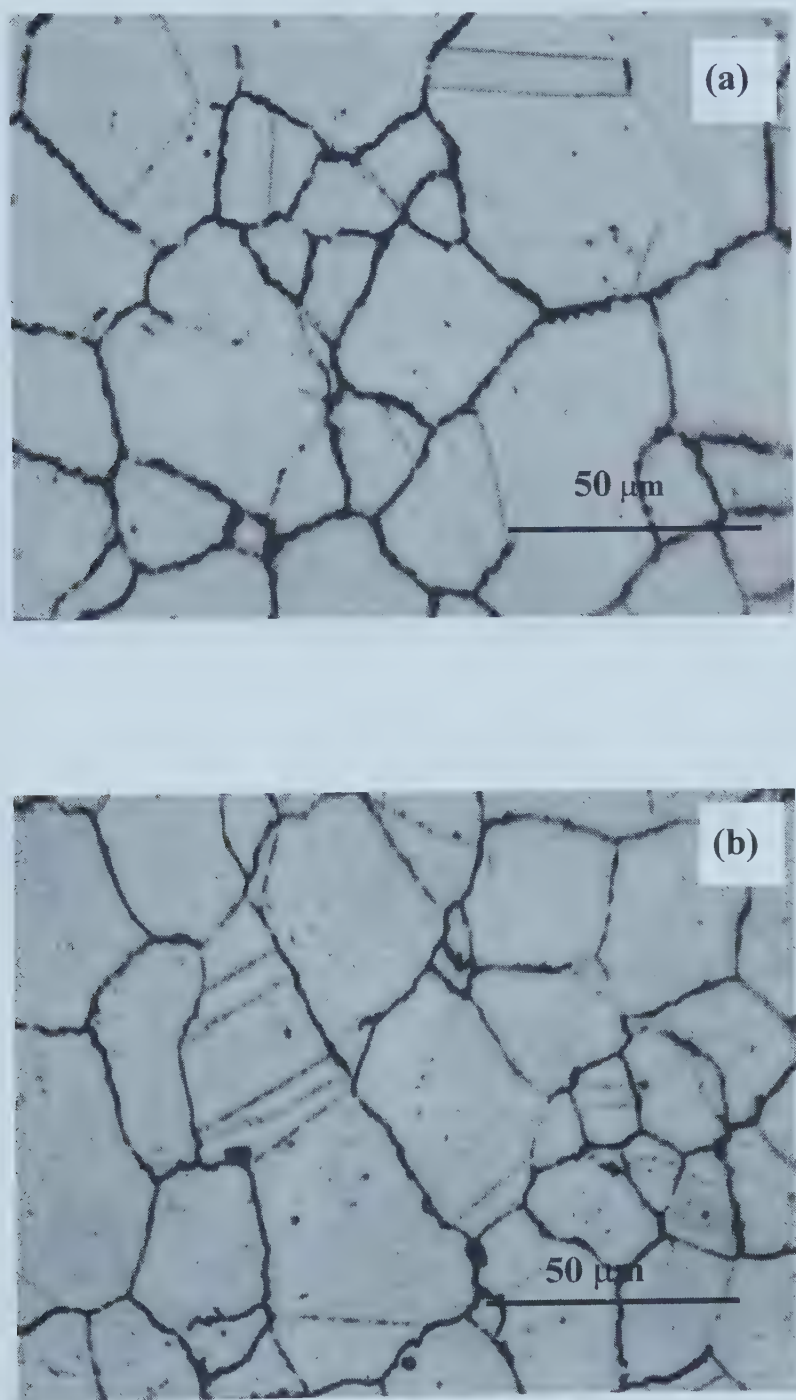


Figure 5-9.--- continued

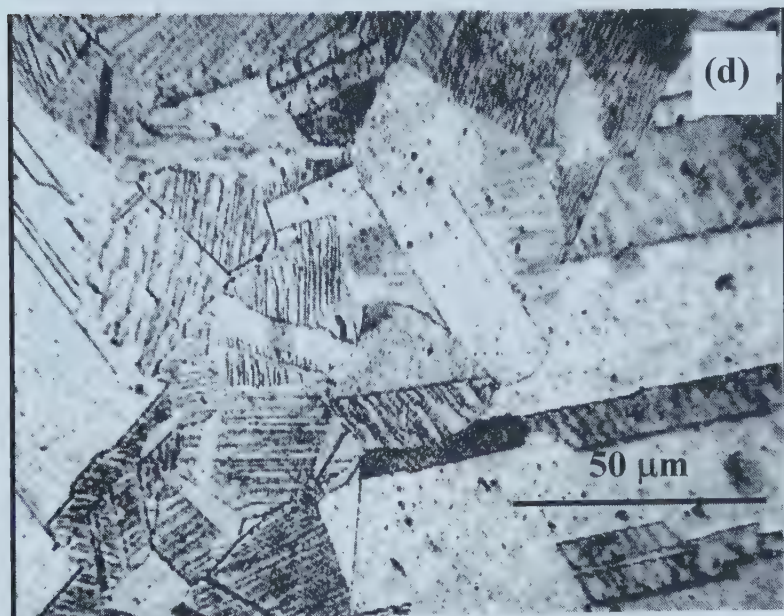
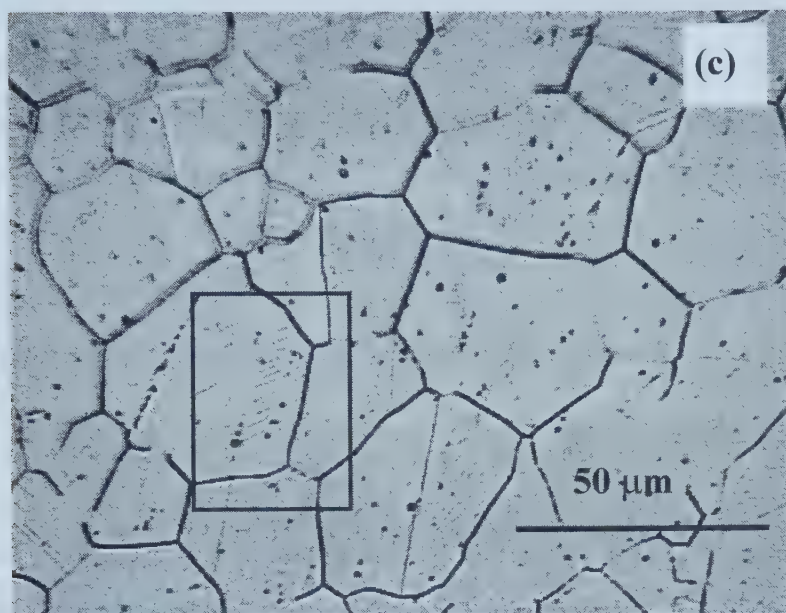


Figure 5-9. The optical micrographs of the uncharged specimen (a), and the specimens charged at 20 mA/cm² for 2 minutes (b), 7 minutes (c) and 30 minutes (d). The photos were taken immediately after charging and etching.

critical charging time for the martensite transformation. The specimens are charged at various current densities for different periods. After charging, the surfaces were observed in an optical microscope and examined by the X-ray diffraction to detect the martensite transformation. Surface relief (see the arrow in Figure 5-10) can be observed on the surfaces if the martensite transformation occurs (Figure 5-10). The solid line in Figure 5-11 presents the critical charging conditions for the martensite transformation. To study the effect of grain size on the martensite transformation, one extra set of differently annealed (1100°C for 2 hours) specimens were used. The average grain sizes of the specimens annealed at 1050°C for 1 hour and at 1100°C for 2 hours are $34\mu\text{m}$ and $56\mu\text{m}$ respectively.

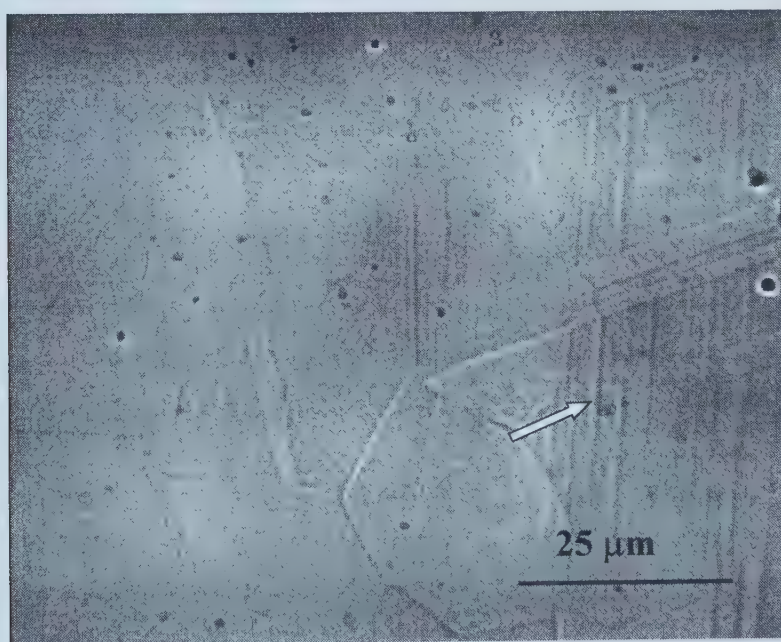


Figure 5-10. Surface relief observed immediately after hydrogen charging. The specimen was charged at 20 mA/cm^2 for 15 minutes. Surface relief indicates the crystallographic direction of martensite.

For a certain period of charging time there is a critical cathodic charging density. The martensite transformation only occurs when the charging current density is higher than the

critical charging current density. When the charging period increases, the critical charging current density decreases. In other words, for a certain cathodic charging current density, the martensite transformation occurred when the charging time exceeded the critical time. When the charging current density increases, the critical charging time decreases.

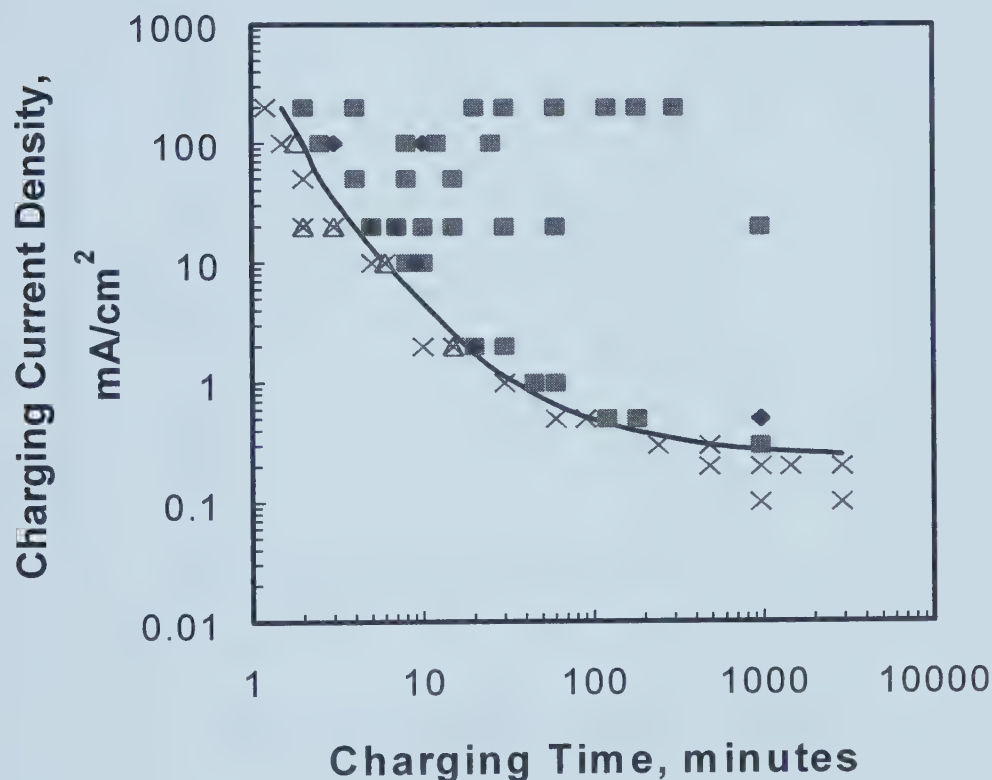


Figure 5-11. The critical charging conditions for hydrogen induced martensite transformation.. X: 1050°C, 1 hour annealed specimen, austenite; Δ: 1100°C, 2 hours annealed specimen, austenite; ■ : 1050°C, 1 hour annealed specimen, austenite and martensite; ◆: 1100°C, 2 hours annealed specimen, austenite and martensite.

Figure 5-11 also shows that grain size plays no obvious role on the critical charging conditions. When the charging current density is lower than 0.2 mA/cm^2 , no martensite transformation is found no matter how long the specimen has been charged. This charging current density is defined as the threshold charging current density, which indicates the stability of austenite.

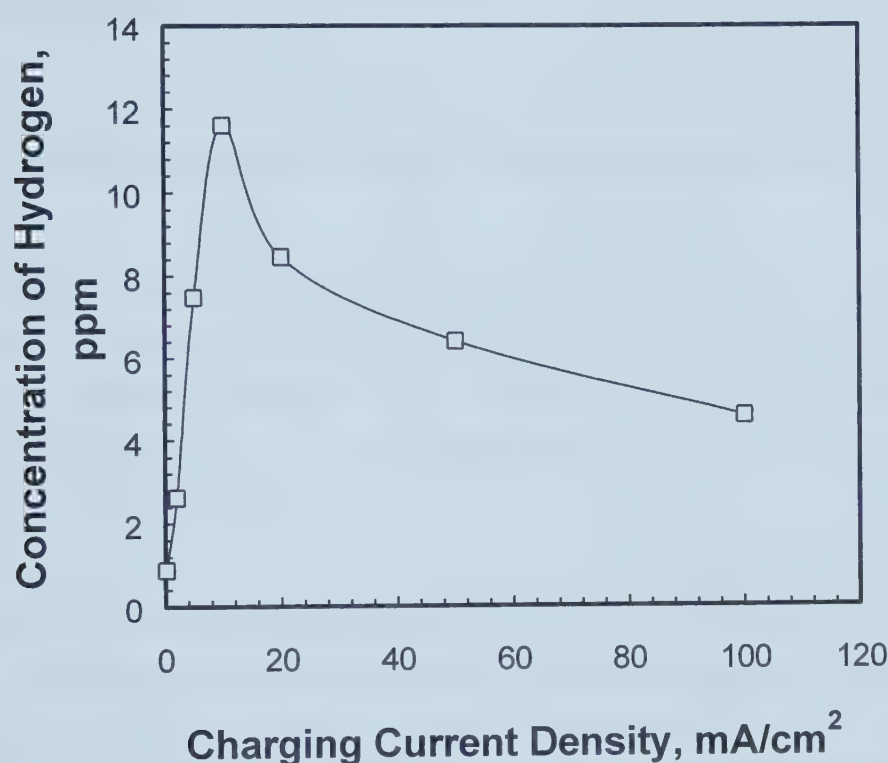


Figure 5-12. The concentrations of hydrogen corresponding to the critical charging conditions for martensite transformation.

It is reasonable to expect that the charging current density threshold is higher for the more stable austenitic stainless steel. For the system investigated in this work, the threshold charging current density is 0.2 mA/cm^2 . The solid line in Figure 5-11 represents the boundary conditions for martensite transformation. If the point representing a certain charging condition (i.e., charging current density and time) lies above this line, martensite transformation will occur, otherwise no martensite will be present in the specimen. The total concentrations of diffusible hydrogen corresponding to

the critical charging conditions are displayed in Figure 5-12. The average hydrogen concentration at a critical charging condition increases with charging current density at first, but when the charging current density is higher than 10 mA/cm^2 , it begins to decrease.

5.3. EFFECTS OF HYDROGEN ON SURFACE CRACKING OF TYPE 304 STAINLESS STEEL

5.3.1. In Situ Observation of Surface Cracking Process during Aging

To identify the surface crack growth process during aging, after being charged the specimens were immediately observed using an optical microscope without etching. The changes in the surface morphologies in a fixed field were monitored continuously for 6 hours. No surface cracks were observed during aging for the charged specimens for which no martensite was detected.

Figure 5-13 shows the photomicrographs of the specimen charged at 20 mA/cm^2 for 12 hours at the different aging times. Six minutes after charging a few cracks are observed (Figure 5-13a). As the time passed, the existing cracks propagate in both length and depth directions. At the same time additional cracks initiate on the surface. This indicates that surface cracks mainly develop during the aging (outgassing) stage instead of during cathodic charging. The surface cracks form and grow mainly during the first 1-2 hours, from then on neither the number nor length of cracks change very much. As indicated before, the hydrogen outgassing is very quick during the first couple of hours, and then slows down. This result shows that crack formation and growth might be related to the hydrogen outgassing process.

5.3.2. Critical Charging Conditions for Surface Cracking

The critical conditions for surface cracking are shown in Figure 5-14.

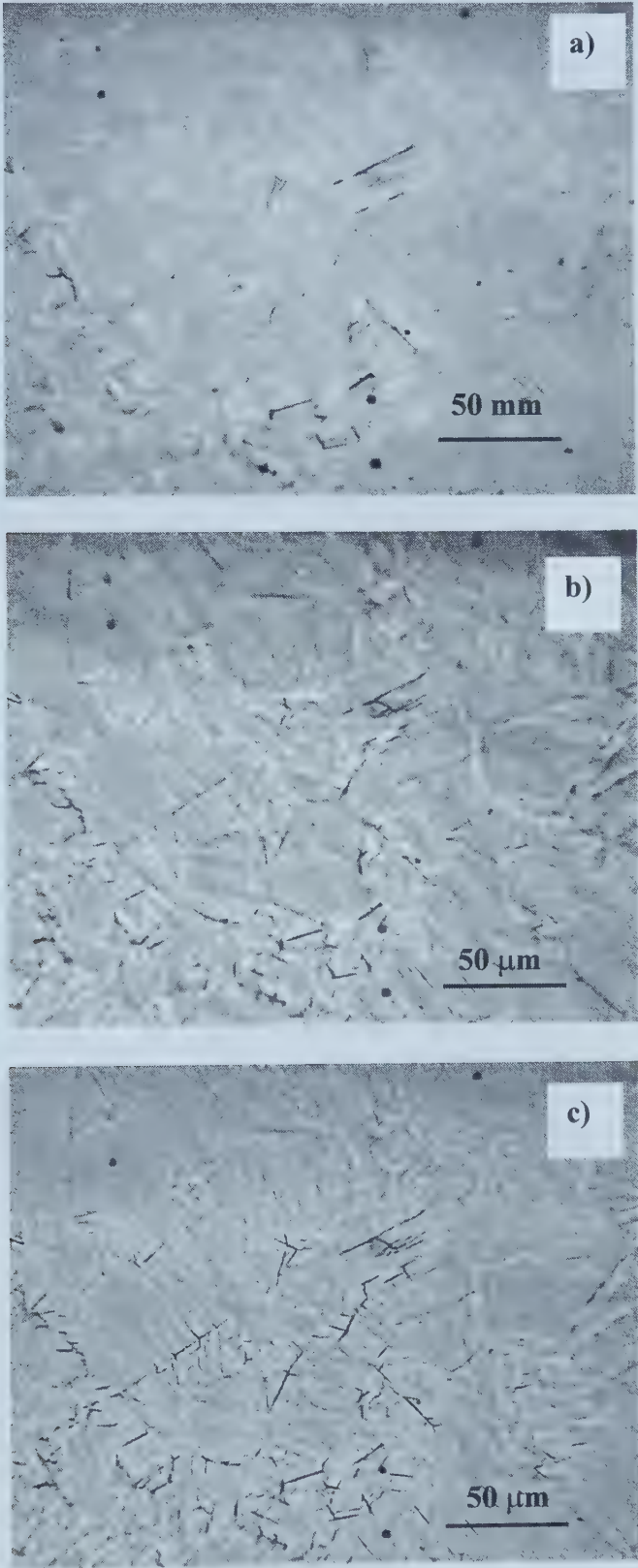


Figure 5-13. --- continued.

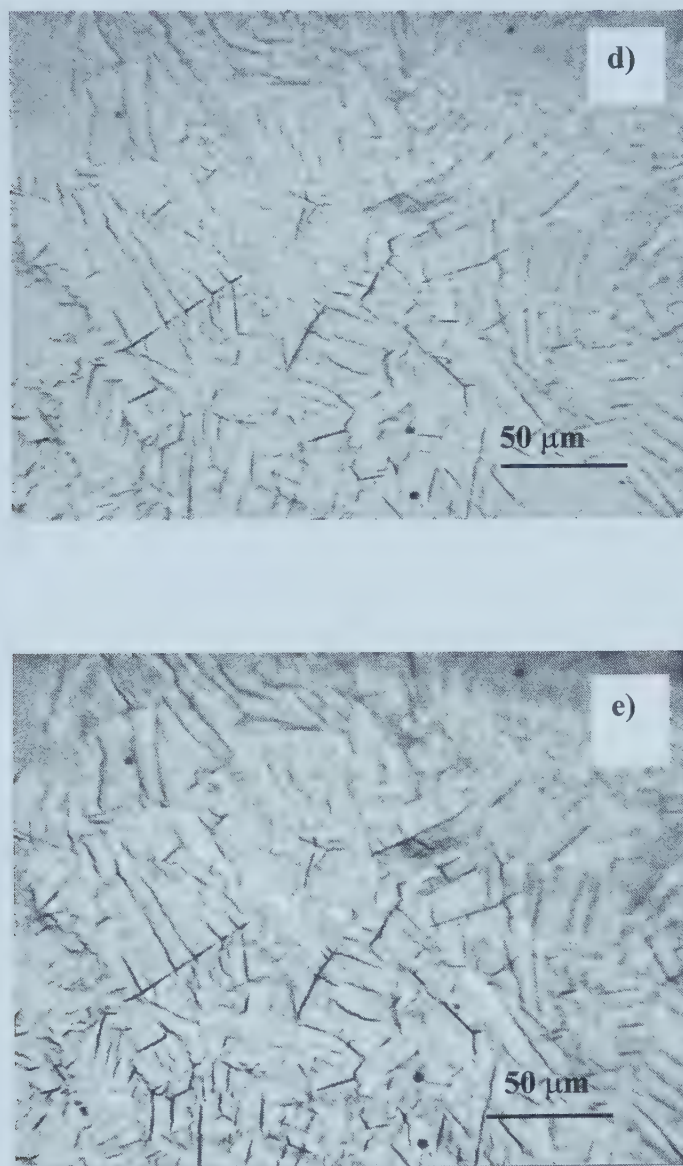


Figure 5-13. The *in-situ* observation of surface cracking during aging after the specimen was charged at 20 mA/cm^2 for 12 hours. Aging time: (a) 6 minutes; (b) 15 minutes; (c) 60 minutes; (d) 240 minutes; and (e) 360 minutes.

The critical charging time for surface cracking at a given charging current density (solid line) is longer than that for martensite transformation (dashed line). No surface cracks are observed during aging for the specimens on which no martensite phase is detected.

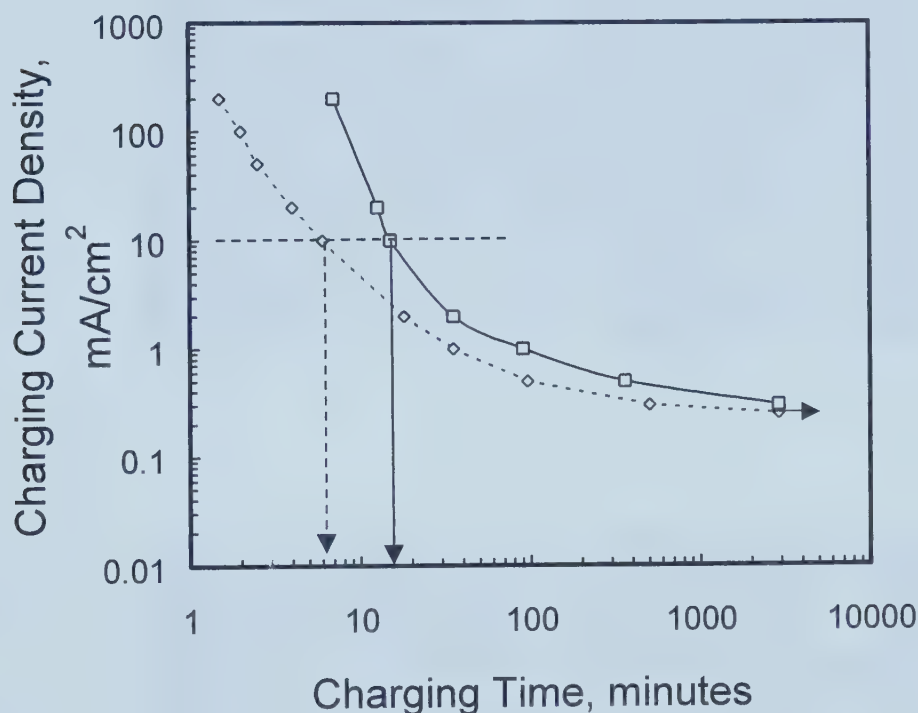


Figure 5-14. The critical charging conditions for surface cracking. The dashed line represents the critical charging conditions for martensite transformation.

5.3.3. Surface Cracking Sites

Figure 5-15 shows the different surface cracking sites. Some cracks are along grain or twin boundaries as indicated by arrows A and B respectively in Figure 5-15. They are straight and parallel to each other. These cracks grow through ϵ martensite or along ϵ/γ

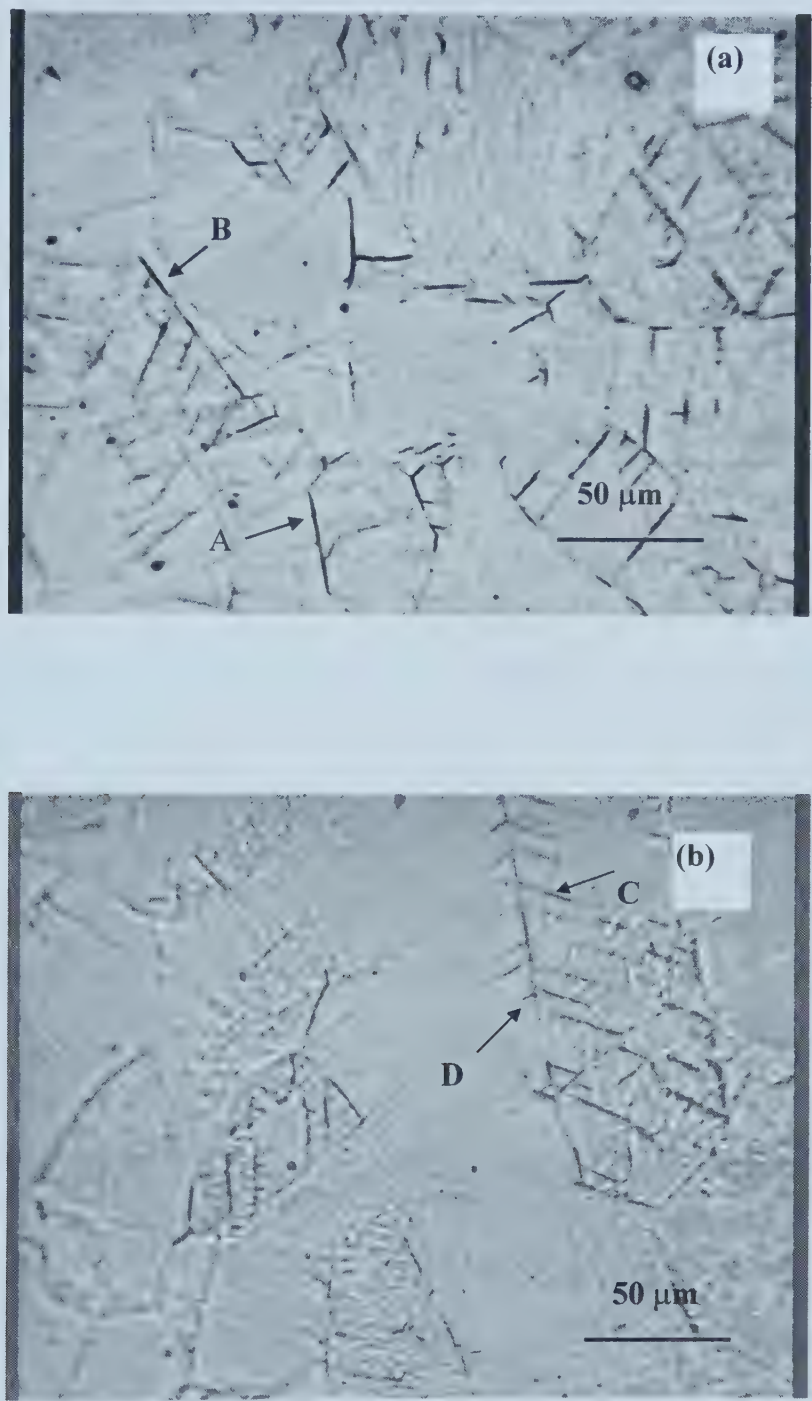


Figure 5-15. The surface cracking sites. The photos were taken from the specimen charged at 20 mA/cm² for 4 hours and aged for 4 hours.

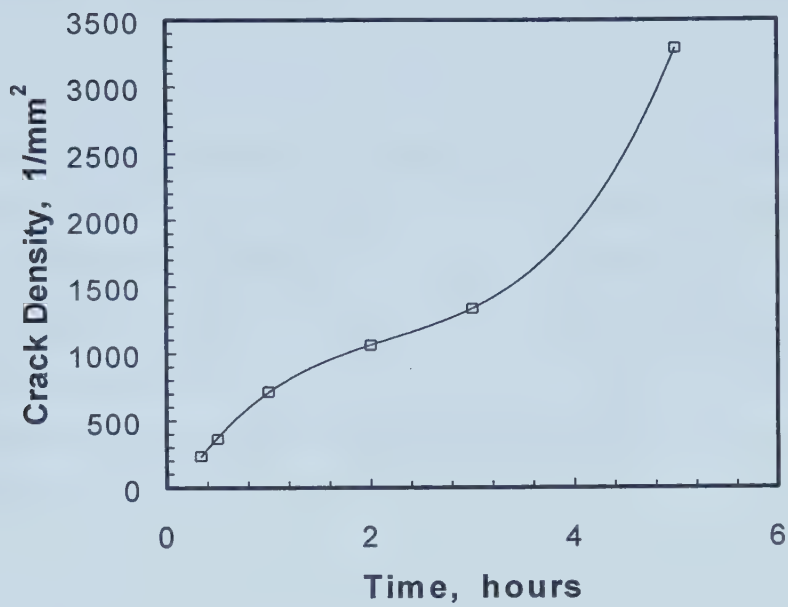


Figure 5-16. The crack density vs. charging time curve of specimens charged at 200 mA/cm². Crack densities were measured after aging for 4 hours.

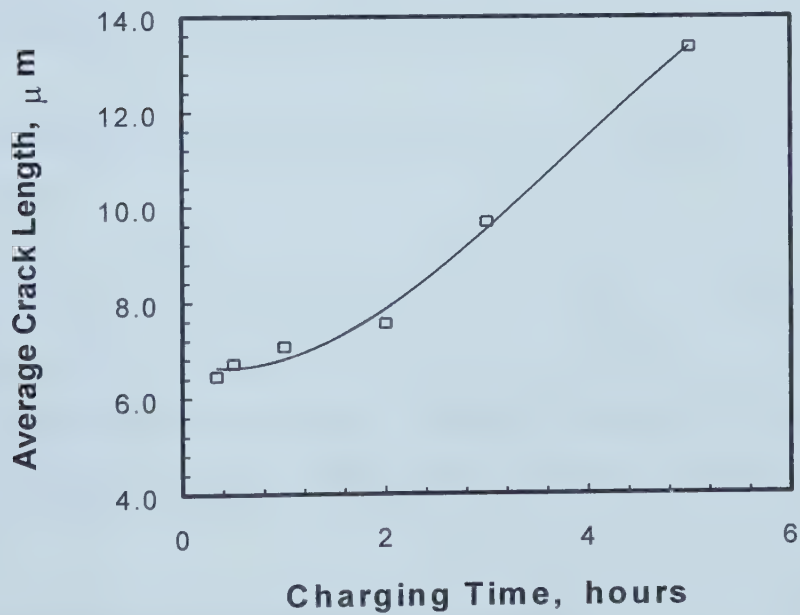


Figure 5-17. The average crack length vs. charging time curve for the specimens charged at 200 mA/cm². Crack lengths were measured after aging for 4 hours.

interface intersections of ϵ martensite and twin boundaries (arrow D in the Figure 5-15).

Figures 5-16 and 5-17 present the curves of crack density and average crack length vs. charging time, respectively, for the specimens charged at 200 mA/cm^2 . The crack length and density were measured after aging for 4 hours. If the curve in Figure 5-16 is extrapolated, the charging time corresponding to $0/\text{mm}^2$ is 10 minutes. This value is larger than the critical charging time of martensite transformation for a specimen charged at 200 mA/cm^2 as shown in Figure 5-11. This result confirms the fact that no cracks exist on the charged specimens on which no martensite transformation is detected. Both the crack density and average crack length increase with the charging time.

After aging for 4 hours, one set of the charged specimens was etched. A typical photomicrograph is shown in Figure 5-18. Comparing Figure 5-18 with Figures 5-9 and 5-15, it is clear that some shallow and parallel lines are etched out. Some patterns shown in the black frame in Figure 5-18 are not observed in Figures 5-9 and 5-12. These new lines in Figure 5-18 must correspond to the α' martensite laths. The appearance of these new patterns also indicates that surface cracking is not spatially related to α' laths.

5.4. RELATIONSHIP BETWEEN MARTENSITE TRANSFORMATION AND CORROSION

To investigate the relationship between martensite and corrosion properties, a corrosion test was carried out in $0.5 \text{ M H}_2\text{SO}_4 + 0.1 \text{ M HCl}$ solution. A constant potential of 1.2 V vs. SCE , which is higher than the transpassive potential of the materials in the solution, was applied to the uncharged and charged specimens for 10 minutes. Weight loss was measured.

5.4.1. Effects of Hydrogen Charging on Weight Loss

The weight loss curve is shown in Figure 5-19. The weight losses of the specimens charged at 2 mA/cm^2 for less than 25 minutes are low. Weight losses are high when the

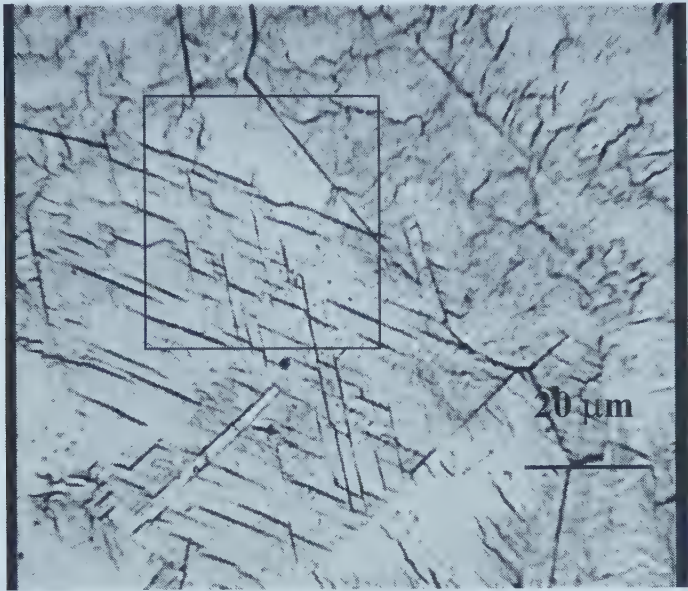


Figure 5-18. The photomicrograph of a specimen charged at 20 mA/cm² for 16 hours, aged for 4 hours and then etched.

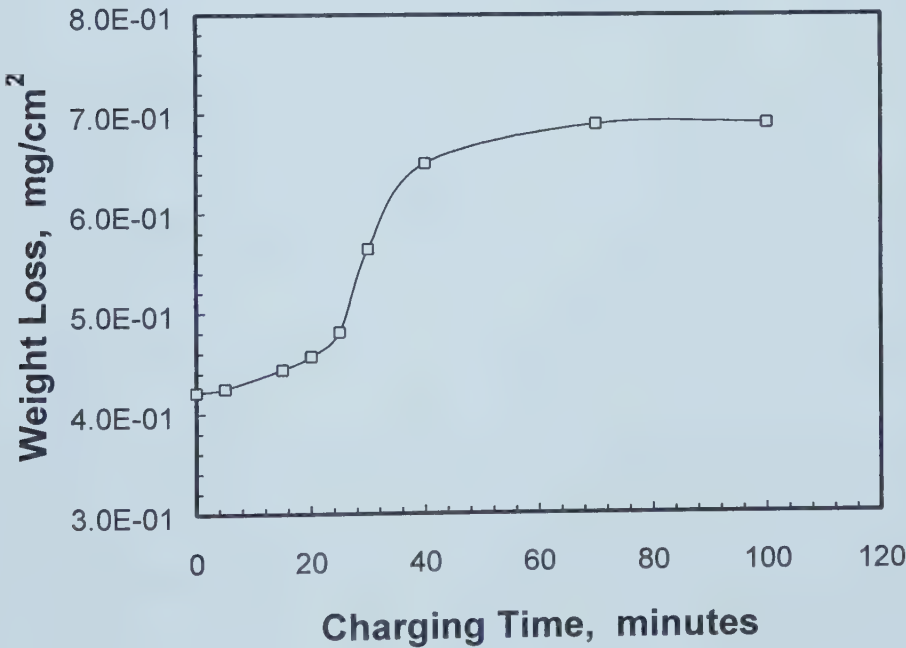


Figure 5-19. The weight loss vs. charging time curve. The specimens were polarized 1.2V vs. SCE for 10 minutes in 0.5 M H₂SO₄ +0.1 M HCl solution. The specimens had been charged with hydrogen at 2 mA/cm² for different times.

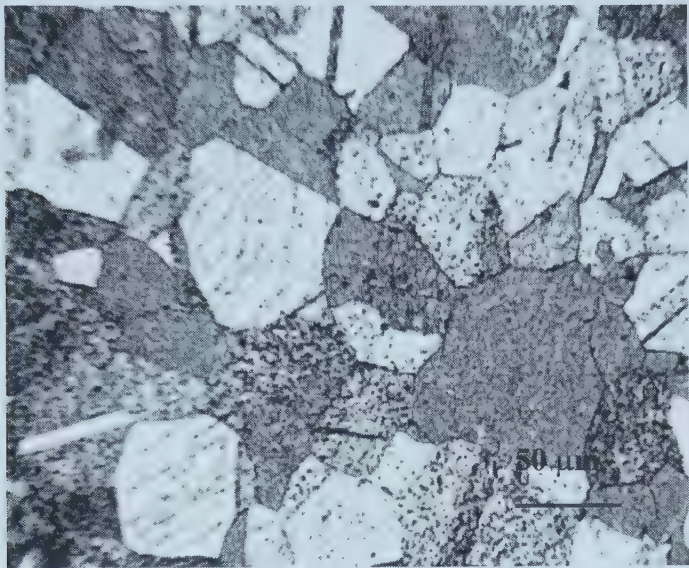


Figure 5-20. The corroded surface of the specimen charged at 2 mA/cm^2 for 40 minutes. The specimen was corroded at 1.2 V vs. SCE for 1 minute in a 0.5 M $\text{H}_2\text{SO}_4 + 0.1 \text{ M HCl}$ solution.

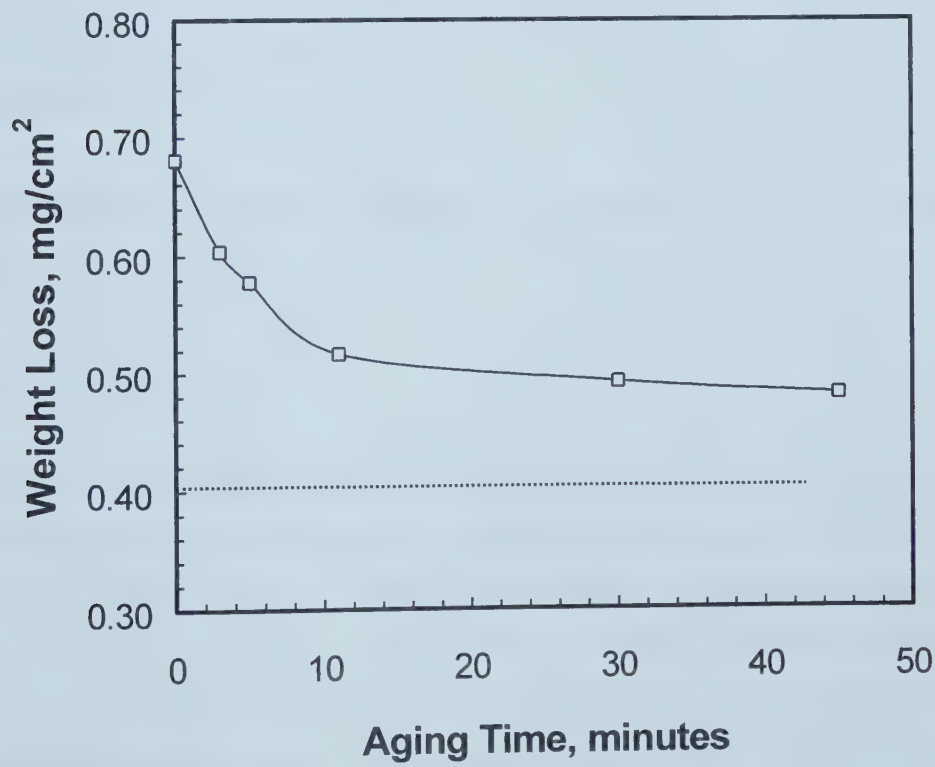


Figure 5-21. Weight loss vs. aging time curve. The specimens were hydrogen charged at 2 mA/cm^2 for 1 hour, aged and then corroded in a 0.5M $\text{H}_2\text{SO}_4 + 0.1 \text{ M HCl}$ solution at 1.2 V vs. SCE for 10 minutes.

specimens are charged for more than 30 minutes. The optical observations of the corroded surfaces reveal that the obvious increase in weight loss is due to the preferential dissolution of martensite phases (Figure 5-20). From Figure 5-11 it can be seen that the critical charging time for a charging current density of 2 mA/cm^2 is about 20 minutes. When charging time is slightly greater than the critical time, the amount of martensite is not high enough to lead to a great increase of the weight loss. This is the reason why the obvious increase of weight loss occurs at a time later than the critical charging time for the martensite transformation.

5.4.2. Effects of Aging on Weight Loss after Hydrogen Charging

Figure 5-21 shows the change in weight loss with the aging time of the specimens charged at 2 mA/cm^2 for 1 hour. The dotted line represents the weight loss of the uncharged specimen. The weight loss decreases with an increase in aging time. It decreases dramatically in the first 10 minutes, then slows down. The weight loss of the charged specimen after aging for 45 minutes is still well above the weight loss (dashed line) of the uncharged specimen.

5.5. HYDROGEN-INDUCED SURFACE CRACKING ON 310 STAINLESS STEEL

5.5.1. X-ray Spectra

The X-ray spectra for the specimens of 310 stainless steel charged at 20 mA/cm^2 are shown in Figure 5-22. From the spectra, it can be observed that no martensite is found even when the charging time is 1.5 hours. Only austenite is observed. Comparing with the X-ray spectra of specimens of 304 stainless steel, the critical charging time for martensite transformation for 310 stainless steel should be much longer than that for 304 stainless steel, indicating that the 310 stainless steel exhibits a higher austenitic stability.

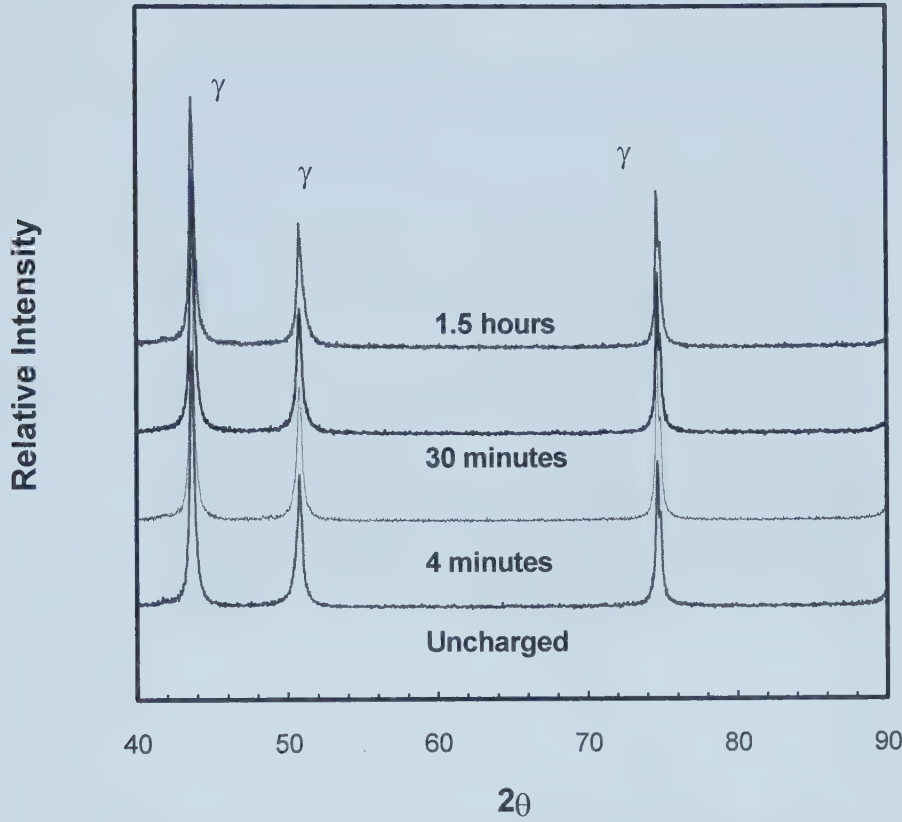


Figure 5-22. The X-ray diffraction spectra of uncharged 310 stainless steel specimen and specimens charged at 20 mA/cm² after 24 hours' aging.

5.5.2. Surface Cracking

The surfaces of the charged specimens were observed after aging for at least 4 hours. Figure 5-23 shows the surface morphologies of the specimens charged at 20 mA/cm² for different charging times. It can be observed that as more hydrogen (the longer charging time in this case) was introduced into specimens, the number of cracks increased. The cracks appear to initiate at grain and twin boundaries. SEM was also applied to observe the surface; an SEM micrograph is shown in Figure 5-24. A “mud cracking pattern” can be observed.

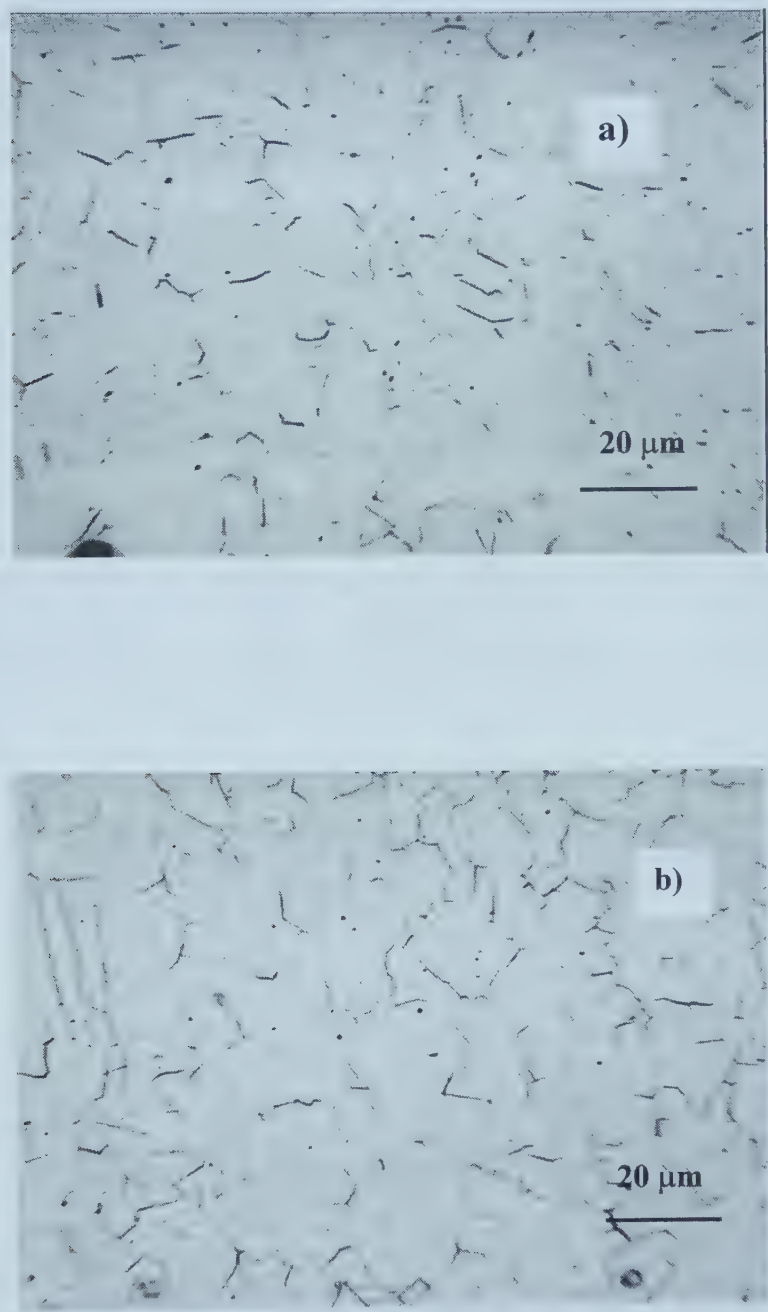


Figure 5-23. --- continued

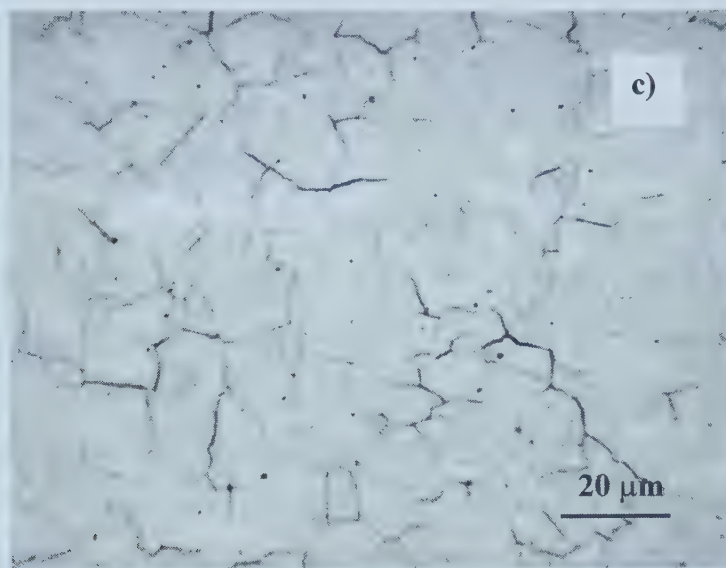


Figure 5-23. The surface morphologies of specimens of 310 stainless steel charged at 20 mA/cm^2 for different charging times: (a) 75 minutes, (b) 5 hours and (c) 16 hours. The specimens were observed after aging for at least 4 hours.

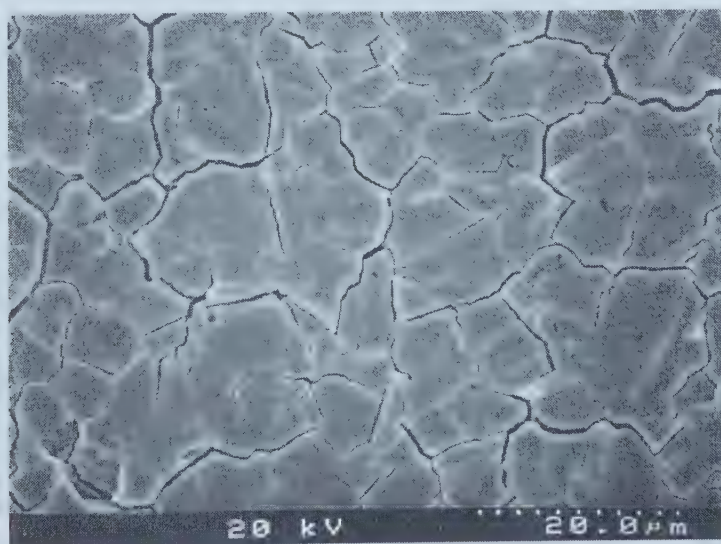


Figure 5-24. SEM surface morphology of a specimen of 310 stainless steel charged at 20 mA/cm^2 for 16 hours. The specimen was observed after aging for longer than 4 hours.

5.6. DISCUSSION

Introduction of hydrogen into specimens by means of a cathodic charging method can result in a considerable amount of phase transformation at the surface. The combined influence of the hydrogen itself and the stresses arising from the high concentration gradient of hydrogen at the surface result in a considerable reduction in the stability of austenite, particularly with respect to the formation of ϵ phase.

It has been suggested³ that hydrogen can raise the martensite start temperature (M_s) and the highest temperature for martensite transformation by deformation (M_d) for ϵ martensite transformation, and therefore reduce the stability of austenite. Because the hcp phase may form from the fcc structure by the motion of Shockley partial dislocations on $\{111\}$ planes leaving behind stacking fault arrays, many researchers have surmised that the ϵ phase may be associated with the stacking faults in the parent austenite and these stacking faults may be the nucleation sites for the martensite transformation.¹⁶ During the initial stage of cathodic charging, many stacking faults form in austenite.¹ This suggests that dissolved hydrogen can lower the stacking fault energy of austenitic stainless steels^{17,18} and such reduction can promote the formation of ϵ martensite.¹⁹

The stress level in the surface layer can also contribute to the reduction in driving force required for the transformation from austenite to martensite.²⁰ The small lattice diffusivity of hydrogen in austenite results in the high hydrogen concentration gradients beneath the surface with the high concentration at the surface. It is reported that the high surface concentration of about one H atom to one metal atom can be established at the surface.³ The volume expansion associated with the uptake of this high hydrogen concentration at the surface will lead to high stresses in the metal lattice.²¹ The high concentration of hydrogen at the surface together with the high stress resulting from inhomogeneous distribution of hydrogen in the lattice can lead to martensite transformation.

This type of stress-assisted martensite transformation involves the spontaneous nucleation and growth of martensite in plate form (ϵ martensite platelets).²¹ A large amount

of tiny martensite plates nucleate at grain and twin boundaries. Because these boundaries can act as hydrogen traps,²² the hydrogen concentration in these regions is higher than other regions and stress concentrations can possibly occur at grain and twin boundaries.²³ It is reported that during the $\gamma \rightarrow \epsilon$ transformation, a contraction of 1% in the direction of the c-axis of ϵ martensite takes place,²⁴ producing a tensile stress state perpendicular to the ϵ/γ interface. This tensile stress promotes diffusion and thus may influence the segregation of hydrogen to the ϵ/γ interface. Therefore ϵ martensite can absorb more hydrogen than austenite.²⁵ Local stress concentrations together with local high hydrogen concentrations make these boundaries the sites for preferential nucleation of martensite.^{26,27}

The most interesting result of this study is that there is a critical charging condition to induce martensite. As mentioned above, the concomitant presence of a high concentration of hydrogen and stress at a surface is the prerequisite for martensite transformation. It needs sufficient time and charging current density to build up this high hydrogen concentration and high stress at the surface. Otherwise the driving force required for the $\gamma \rightarrow \epsilon$ transformation cannot be reached. This is the reason why there is a critical charging condition and threshold charging current density for martensite formation.

Aging after hydrogen charging results in a number of significant structural changes as hydrogen is released from the specimens. During the aging process outgassing of hydrogen is expected mainly through the external surfaces. The hydrogen concentration at the surface drops immediately to zero, while a considerable hydrogen concentration still exists several microns below the surface.²⁸ As the ϵ phase loses hydrogen to form hydrogen-free ϵ martensite, the surface contracts¹² which results in a high tensile stress at the surface. Because the formation of α' martensite from close-packed structures is accompanied by volume expansion (approximately 1.5%- 3.5% volume expansion by calculation), the tensile stress and lack of constraint at the surface can facilitate this transformation. It is reported that the formation of α' martensite in 304 stainless steel occurred after aging for a period of time sufficient to allow a decrease in hydrogen concentration, and thus a change in the stress state.³

Surface cracking is never observed in specimens in which hydrogen-induced martensite transformation is not detected for type 304 stainless steel. Cracks are observed on the specimens which are hydrogen charged longer than the critical charging time for the phase transformation. Martensite transformation is not the necessary condition for surface cracking on type 310 stainless steel. Few cracks are present on the surface immediately after charging, and the severity of cracking increases as hydrogen is lost during aging. Surface cracking mainly occurs during aging rather than during charging. This is in agreement with the expectation of high compressive stress during charging and tensile surface stress during aging. Because most cracks are found at the high hydrogen concentration sites (grain boundaries, twin boundaries and ϵ/γ interfaces), the hydrogen-induced cracking should be associated with hydrogen effusion from supersaturated sites.

The results of the corrosion tests reveal that preferential dissolution of martensite causes the obvious increase in weight loss and the weight loss is less with an increase in aging time. The high dissolution rate of martensite results from the highly defective nature of martensite and the high hydrogen concentration in it.

5.7. SUMMARY

The results in this chapter clearly exhibit the effects of cathodic hydrogen charging on phase transformation and surface cracking of stainless steels. It is revealed in this chapter that cathodic hydrogen charging can induce martensite transformation and surface cracking. There are critical charging conditions for the martensite transformation and surface cracking. The critical charging periods both for martensite transformation and surface cracking decrease with charging current density. For type 304 stainless steel, surface cracking is closely related to martensite transformation. No cracks can be found on the specimens without martensite transformation. The critical charging period is longer for the surface cracking than for the martensite transformation. However, the martensite transformation is not a necessary condition for the surface cracking of 310 stainless steel. In-situ observations after hydrogen charging show that surface cracking mainly occurs during aging after charging rather than during charging. The surface

cracking develops very quickly in the first couple of hours. Martensite transformation can obviously affect the anodic dissolution. The weight loss increases with charging time. However, the obvious increase of weight loss occurs at a time later than the critical charging time for the martensite transformation. The weight loss decreases with the aging time.

REFERENCES

1. Kazuyoshi Kamachi, Muneo Oka and Mutsumi Touge, *New Aspects of Martensitic Transformation*, published by The Japan Institute of Martensitic Transformation, Kobe (1976): p.309.
2. D. Eliezer, *Hydrogen Effects in Metals*, Ed. by I. M. Bernstein, Anthony and W. Thompson, Warrendale, PA: TMS-AIME, (1980): p. 565.
3. N. Narita, C. J. Altstetter and H. K. Birnbaum, *Metall. Trans. A*, 13A (1982): p.1355.
4. C. M. Hsiao and W. Y. Chu, *Hydrogen Effects in Metals*, Ed. by I. M. Bernstein, Anthony and W. Thompson, Warrendale, PA: TMS-AIME, (1980): p.255.
5. S.C. Chen, M. Gao and R. P. Wei, *Scripta Metall. Mater.*, 28 (1993): p.471.
6. S.C. Chen, M. Gao and R. P. Wei, *Metall. Trans. A*, 27A (1996) p.29.
7. L. J. Qiao and J. L. Luo, *Corrosion*, 54 (1998): p. 281.
8. Z. Fang, Y. Wu, R. Zhu, B. Cao and F. Xiao, *Corrosion*, 50 (1994): p.873.
9. A. A. Seys, M. J. Brakers and A. A. Van Haute, *Corrosion*, 30 (1974): p.47.
10. P. D. Hicks and C. J. Alstetter, *Metall. Trans. A*, 23A (1992): p.237.
11. D. Hardie and D. Dong, *Brit. Corro. J.*, 29 (1994): p.156.
12. A. P. Bentley and G. C. Smith, *Metall. Trans. A*, 17A (1986): p.1593.
13. T. Boniszewski, D. Mckeown, D. S. Taylor and J. C. Lochhead, *Metal Construction*, 18 (1986): p.309.
14. R. Reed, *Acta Met.*, 10 (1962): p. 865.
15. H. M. Otte, *Acta Met.*, 5 (1957): p. 614.
16. J. Breedis and W. Robertson, *Acta. Met.*, 11 (1963): p. 547.
17. M. Whiteman and A. Troiano, *Phy. Stat. Sol.*, 7 (1964): p.109.

18. M. L. Holzworth and M. R. Louthan, Jr., *Corrosion*, 24 (1968): p. 110.
19. S. Jani, M. Marek , R. F. Hochman and E. L. Meletis, *Metall. Trans. A*, 22A, (1991): p. 1453.
20. P. G. Maxwell, A. Goldberg and J.C. Shyne, *Metall. Trans.*, 5 (1974): p.1305.
21. P. Rozenak, L. Zevin and D. Eliezer, *J. Mater. Sci. Letters*, 2 (1983): p. 63.
22. R. Gibala and D. S. DeMiglio, *Hydrogen Effects in Metals*, Ed. by I. M. Bernstein, Anthony and W. Thompson, Warrendale, PA: TMS-AIME (1980): p.113.
23. M. Tokizane, *New Aspects of Martensitic Transformation*, published by The Japan Institute of Martensitic Transformation, Kobe (1976): p. 345.
24. S. M. Hannula, *Scripta.Metall.* 17 (1983): p. 510.
25. J. Ovejero Garcia, J. Chene and M. Aucouturier, *Proc. 2nd J.I.M Int. Symp. on Hydrogen in Metals*, Trans. Japan Inst. of Metals, 21 (1980): p. 525.
26. M. Kato and T. Mori, *Proc. 2nd J.I.M Int. Symp. on Hydrogen in Metals*, Trans. Japan Inst. of Metals, 21 (1980): p. 525.
27. O. N. C. Uwakweh and J. -M. R. Génin, *Metall. Trans. A*, 22A (1991): p.1979.
28. R. C. Frank, J. E. Baker and C. J. Altstetter, *Metall. Trans. A*, 13A (1982): p. 581.

Chapter 6. Effects of Hydrogen on Electronic Properties of Passive Films

The presence of a stable passive film on the surface of a stainless steel explains the good corrosion resistance in various corrosive environments. Passive films on iron and ferrous alloys are considered to be semiconductor films. To understand the corrosion behavior of stainless steels, it is a prerequisite to know the electronic properties of passive films. The most common *in situ* methods for studying the electronic properties of passive films are photoelectrochemistry and Mott-Schottky analyses. Photoelectrochemistry has proved to be a valuable technique for the characterization of passive films. The photoelectrochemical response is considered to be sensitive to the structural properties of the film and its composition. Literature shows that the electrochemical research on passive films has mainly been carried out on passive films in different media without hydrogen. Only G. Razzini et al.,

have published some excellent work studying the hydrogen diffusion process¹ into a metal and hydrogen induced damage² by using scanning photoelectrochemical microscopy (SPCM) technique. In this study, the effects of hydrogen on the electronic properties of passive films will be investigated using the Mott-Schottky method and photoelectrochemical measurements.

6.1. ELECTRONIC PROPERTIES OF PASSIVE FILMS MEASURED BY THE MOTT-SCHOTTKY METHOD

6.1.1. Effect of Hydrogen on the Electronic Properties of Passive Films on Type 310 Stainless Steel

After passivation at 0.1 V vs. SCE in a borate buffer solution for 1 hour, the electrode capacitances of uncharged and charged specimens were measured. As shown in Figures 6-1 and 6-2, the capacitance, C , vs. potential, U , curves of both uncharged and charged specimens exhibit a hysteresis. The appearance of the hysteresis indicates that the passive films on stainless steels are highly defective.³ Compared with the uncharged specimen, the charged specimen had a more obvious hysteresis loop. This difference between charged and uncharged specimens probably indicates that hydrogen can increase the degree of disorder in passive films. In other words, hydrogen in a passive film can cause an increase in defect concentration.

Figure 6-3 shows the Mott-Schottky plots ($1/C^2$ vs. U) for the uncharged and charged specimens measured in the borate buffer solution. Mott-Schottky plots are based on the Mott-Schottky relation, which describes the potential dependence of the space charge capacity of a semiconductor electrode under depletion conditions. For n-type semiconductors, it can be expressed as:⁴

$$C^{-2} = \frac{2}{eN\epsilon\epsilon_o} \left(U - U_{FB} - \frac{kT}{e} \right) \quad [6-1]$$

where ϵ is the relative dielectric constant of the semiconductor, ϵ_o the vacuum permittivity, k the Boltzmann constant, T the absolute temperature, e the electron charge, U the electrode

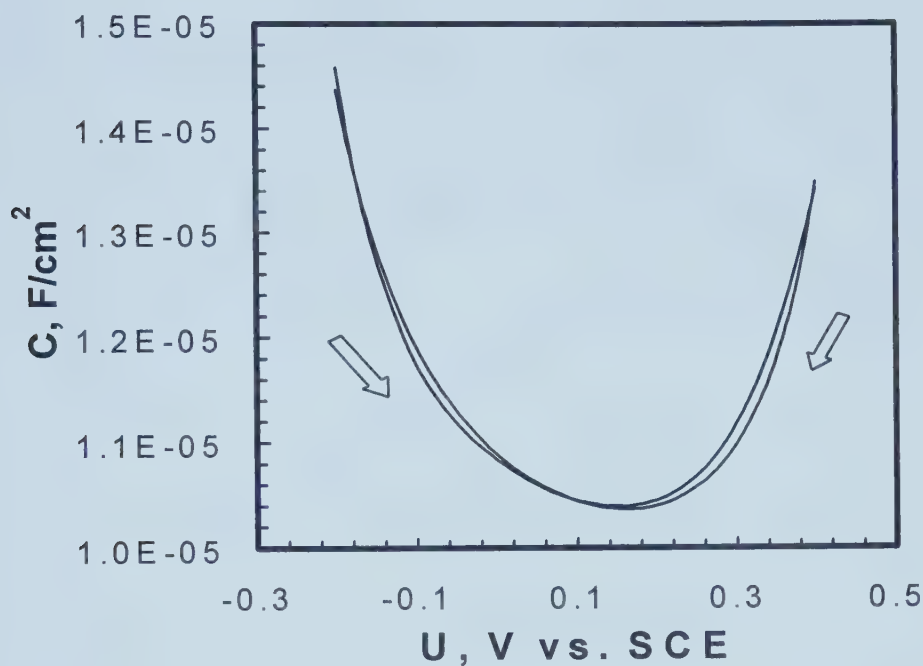


Figure 6-1. The capacitance, C , vs. potential, U , curves of the uncharged 310 SS specimen.

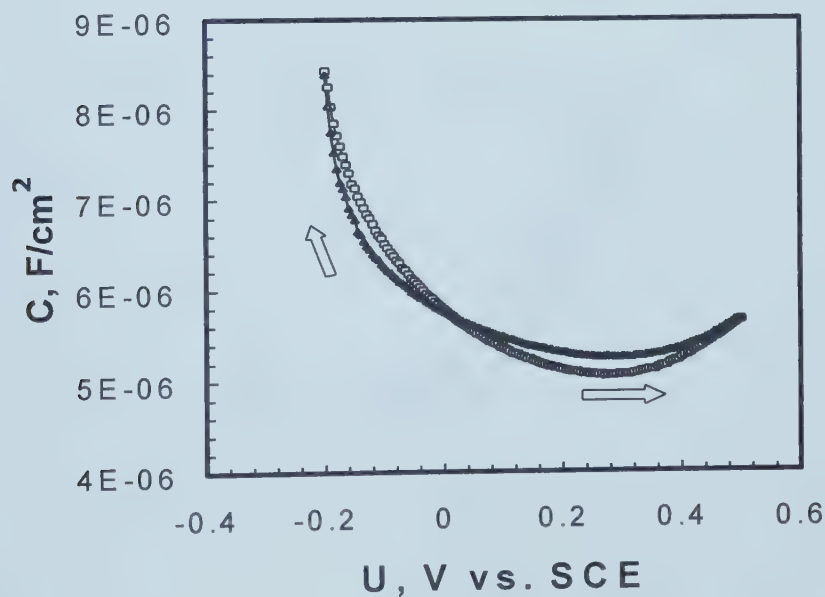


Figure 6-2. The capacitance vs. potential curve of the 310 SS specimen charged at 2 mA/cm^2 for 30 minutes.

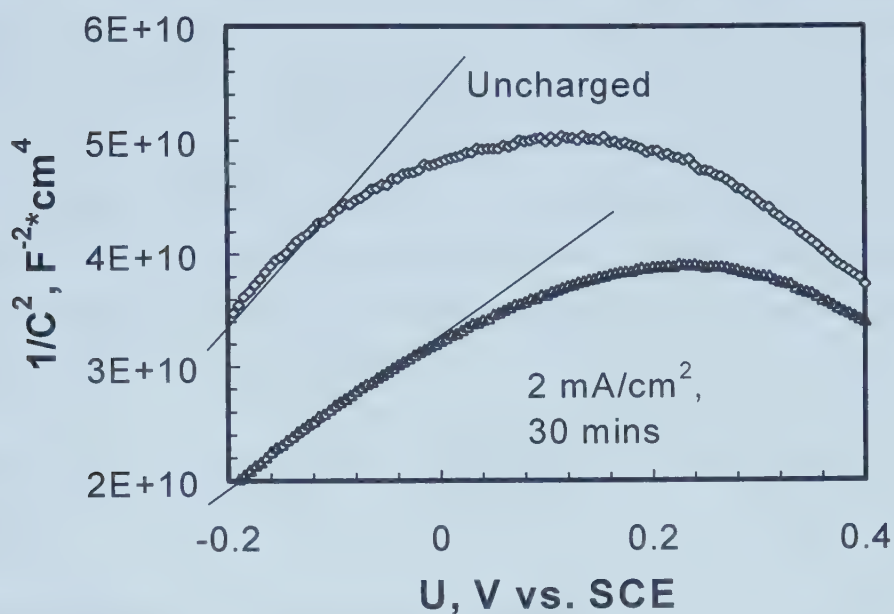


Figure 6-3. The $1/C^2$ vs. U plots of the uncharged and charged 310 SS specimens.

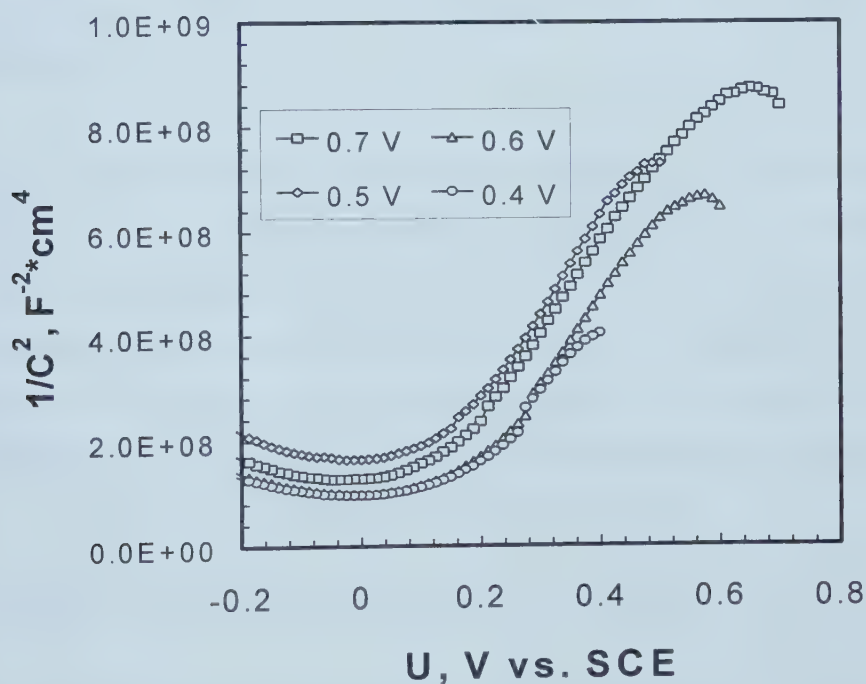


Figure 6-4. Mott-Schottky plots of uncharged 304 stainless steel, pre-passivated at different potentials for 120 minutes in 0.5M H_2SO_4 solution. The impedance was measured at 1000 Hz at 0.0125V/step.

potential, and U_{FB} the flat band potential. In a $1/C^2$ vs. U plot (Mott-Schottky plot), n-type semiconductors have a straight-line section with a positive slope. The concentration of deionized donors for an n-type semiconductor, N , can be determined from the slope, assuming the dielectric constant of the passive film on stainless steels to be 15.6^5 and that hydrogen will not affect this constant. At the lower potentials, straight lines are obtained. The positive slopes indicate the passive films on stainless steel are n-type semiconductors. The decrease in the slope for the charged specimen, according to the equation, indicates that hydrogen can increase the donor concentration.

6.1.2. Effect of Hydrogen on Electronic Properties of Passive Films on Type 304 Stainless Steel

6.1.2.1. Mott-Schottky Plots Measured in 0.5 M H_2SO_4

Mott-Schottky plots of uncharged specimens passivated at various potentials for 120 minutes are shown in Figure 6-4. The positive slopes of the straight-line sections indicate that the passive films are n-type passive films. The variation in passivation potentials does not appear to affect the slope.

Figures 6-5 and 6-6 show the effects of hydrogen charging on the Mott-Schottky plots of the specimens passivated at different polarization potentials. The most interesting result observed is that hydrogen charging can decrease the slope. The decrease in this slope represents an increase in the donor concentration. Figure 6-7 summarizes the effects of hydrogen and passivating potential on the donor concentration. The donor concentrations of the charged specimens are always higher than those of the uncharged ones. The polarization potential seems to have no obvious effect on the donor concentration.

6.1.2.2. Mott-Schottky Plots Measured in the Cl^- Free Borate Buffer Solution

The Mott-Schottky plots were also measured in the borate buffer solution. Figure 6-8 presents the results of the specimens passivated at 0.1 V for 2 hours. It can be observed that passive films on 304 SS also exhibit an n-type semiconductivity. The hydrogen charging can change the slope of the straight-line sections, and hence change the donor concentration. The

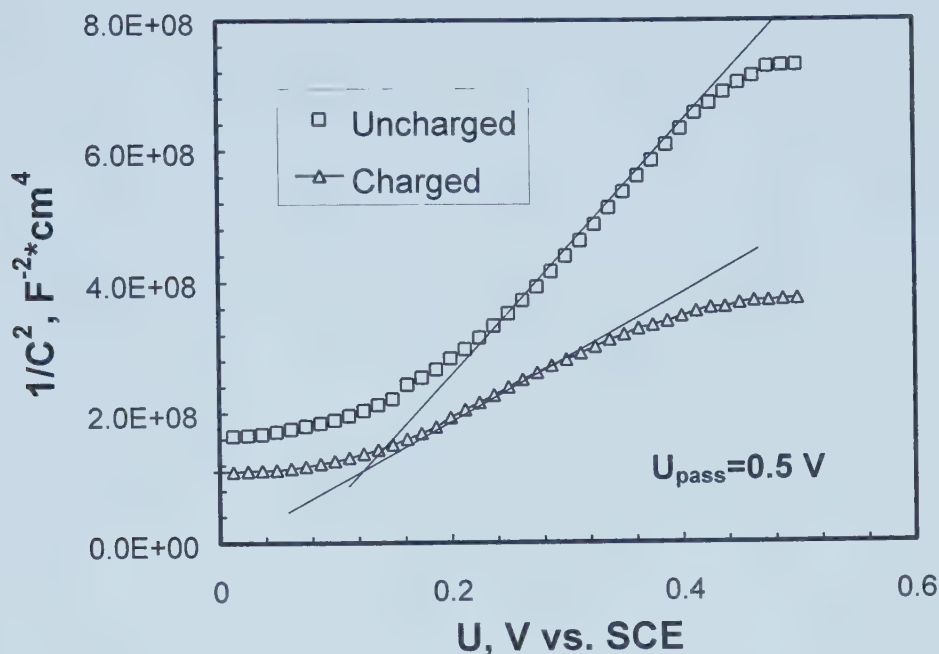


Figure 6-5. Mott-Schottky plots of the uncharged and charged 304SS specimens, passivated at 0.5 V for 120 minutes in the 0.5M H₂SO₄ solution. The impedance was measured at 1000 Hz at 0.0125V/step.

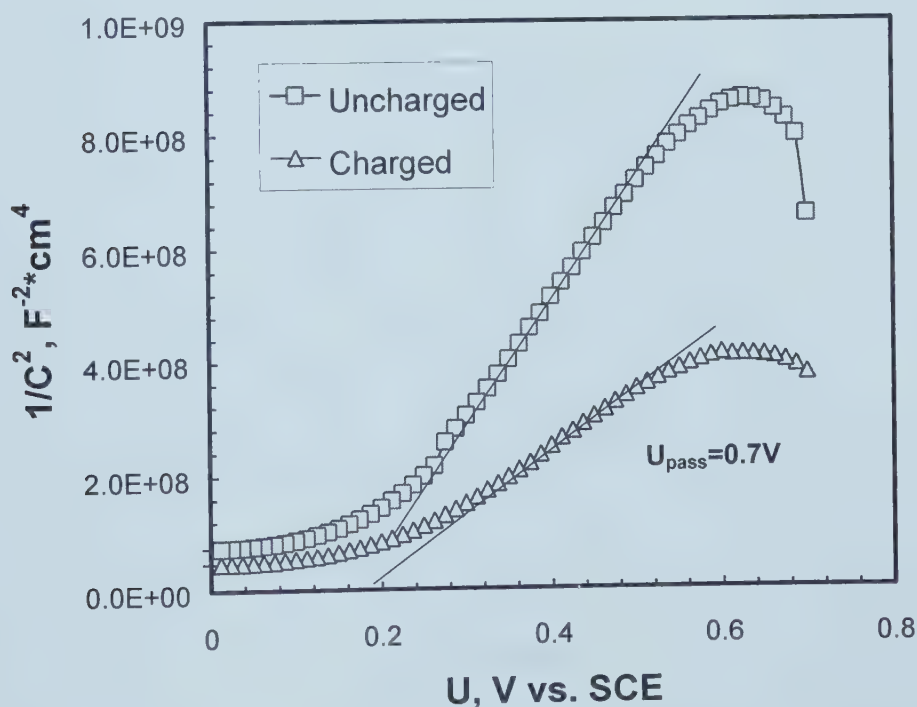


Figure 6-6. Mott-Schottky plots of the uncharged and charged 304SS specimens, passivated at 0.7 V for 120 minutes in the 0.5M H₂SO₄ solution. The impedance was measured at 1000 Hz at 0.0125V/step.

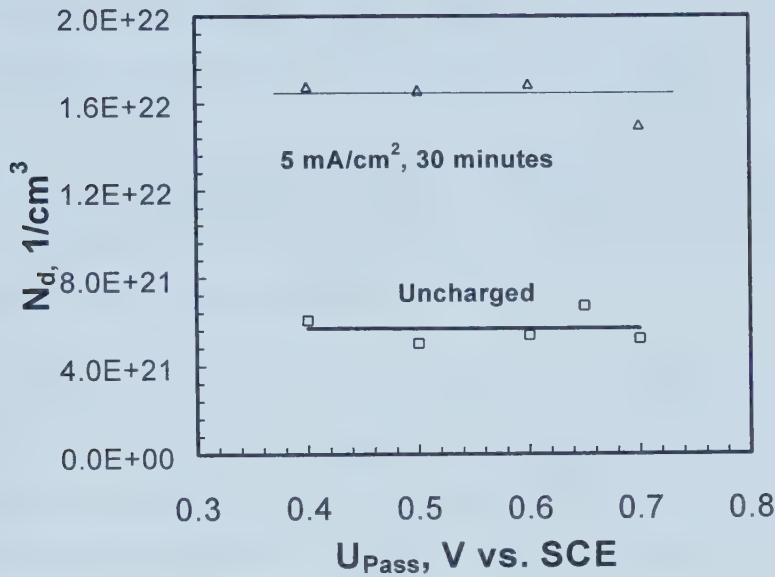


Figure 6-7. The changes in donor concentrations of the charged and uncharged Type 304 stainless steel with passivating potential. The specimens were passivated at constant potentials for 2 hours before the measurements.

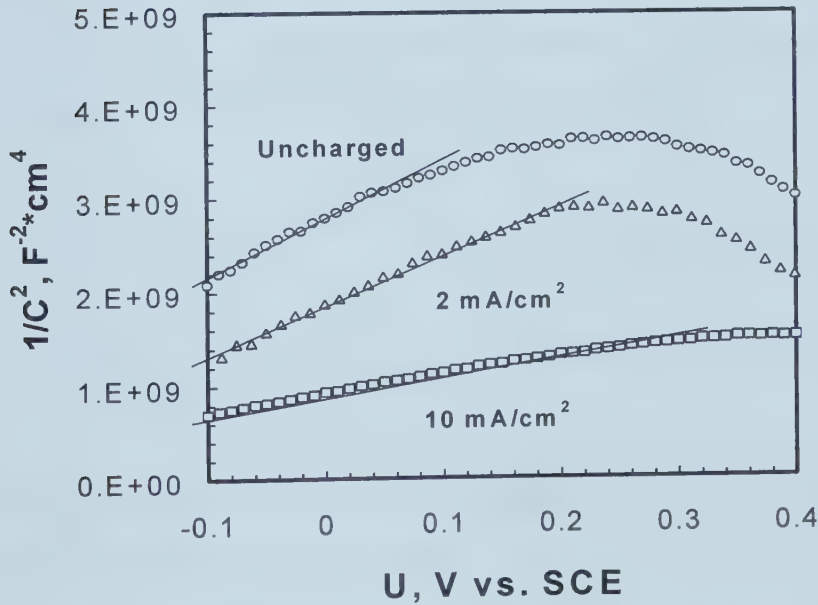


Figure 6-8. Mott-Schottky plots of the uncharged and charged specimens in Cl⁻ free solution. The specimens were passivated at 0.1 V for 2 hours before the measurements.

change in the donor concentration with the charging current density is shown in Figure 6-9. Again hydrogen can increase the donor concentration in the passive films.

A similar situation happens on the specimens passivated at 0.5 V for 2 hours. Figures 6-10 and 6-11 present the Mott-Schottky plots and corresponding donor concentration vs. charging current density curves, respectively.

A typical Mott-Schottky plot obtained for a passive film formed on the charged specimen passivated at 0.7 V is illustrated in Figure 6-12. Two linear sections can be observed with a break at a critical potential U_c . The positive sign of the slopes of the linear sections indicates that the passive film formed on the charged specimens exhibited an n-type character.

Nonlinearity on Mott-Schottky plots has been reported.⁶ There are several explanations for this phenomenon. The theory of Myamlin and Pleskov⁷, based on the existence of a deep level, is the most widely accepted. According to this theory, the critical potential at which the break takes place is explained as the critical electrode potential for the ionization of the deep donor in the space charge layer. Assuming a dielectric constant of the passive film on stainless steel as 15.6,⁵ the concentration of the donors can be calculated from the two slopes S_1 and S_2 , as defined in Figure 6-12, by using the following equations:

$$S_1 = \frac{2}{\epsilon\epsilon_o e N_{D1}} \quad \text{for } U < U_c \quad [6-2-a]$$

$$\text{and} \quad S_2 = \frac{2}{\epsilon\epsilon_o e (N_{D1} + N_{D2})} \quad \text{for } U > U_c \quad [6-2-b]$$

where N_{D1} is the density of the donor with an energy level closer to the conduction band and N_{D2} the density of the donor at the deep level.

The same treatment applied to the present data shows that the densities of the donors are charging-current-density dependent (Figure 6-13). With an increase in charging current density, the densities of both donors at two levels (N_{D1} and N_{D2}) increase exponentially, following the empirical equations:

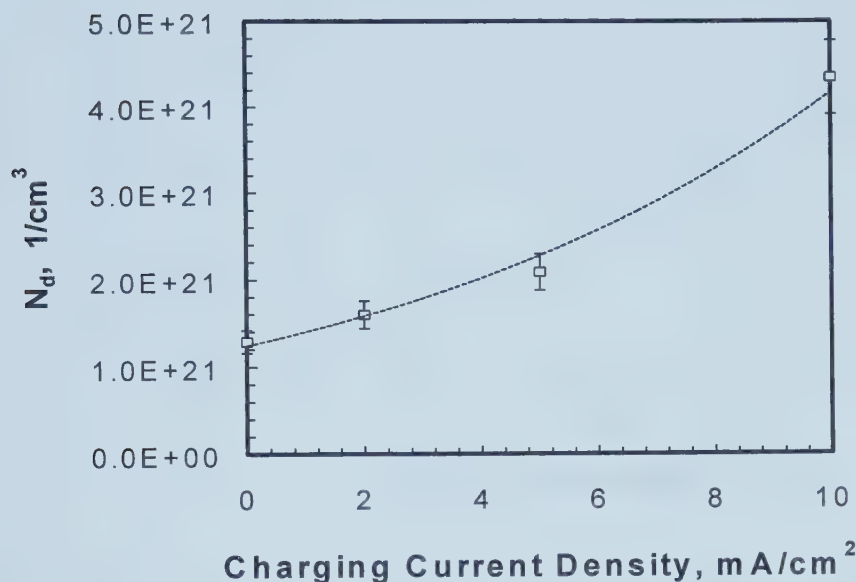


Figure 6-9. The change in donor concentration with hydrogen current density. The charging time is 30 minutes. The specimens were passivated in the chloride-free borate buffer solution at a potential of 0.1 V vs. SCE for 2 hours.

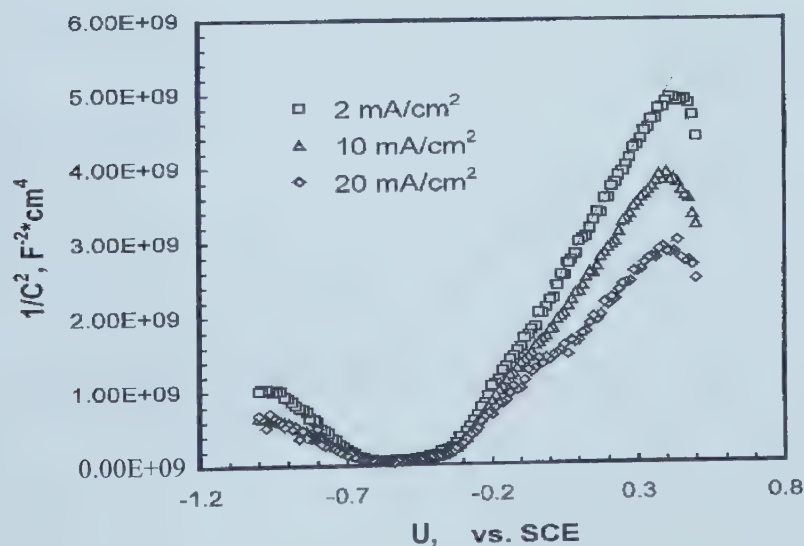


Figure 6-10. Mott-Schottky plots of the uncharged and charged specimens (charging time: 30 minutes) in the Cl⁻ free solution. The specimens were passivated at 0.5 V for 2 hours before the measurements.

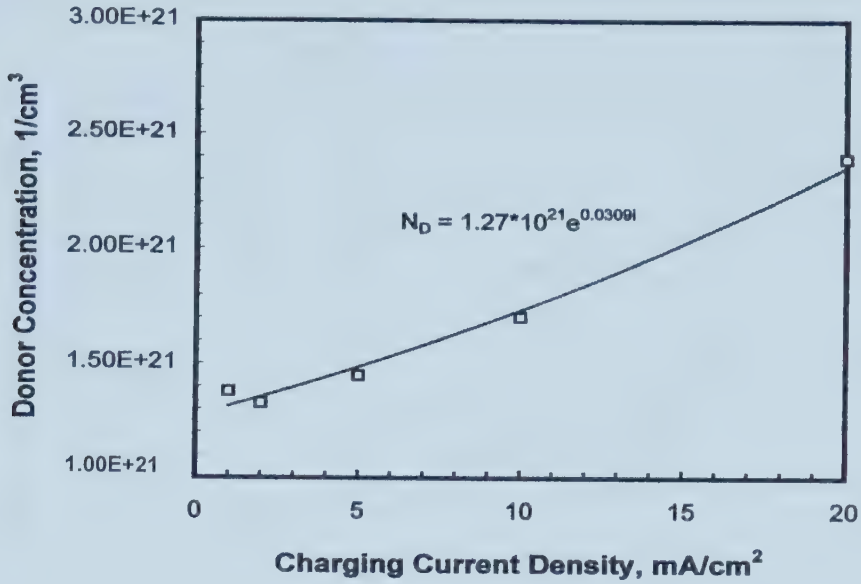


Figure 6-11. The change in the donor concentration with the charging current density. The specimens were passivated at 0.5 V for 2 hours before the measurements.

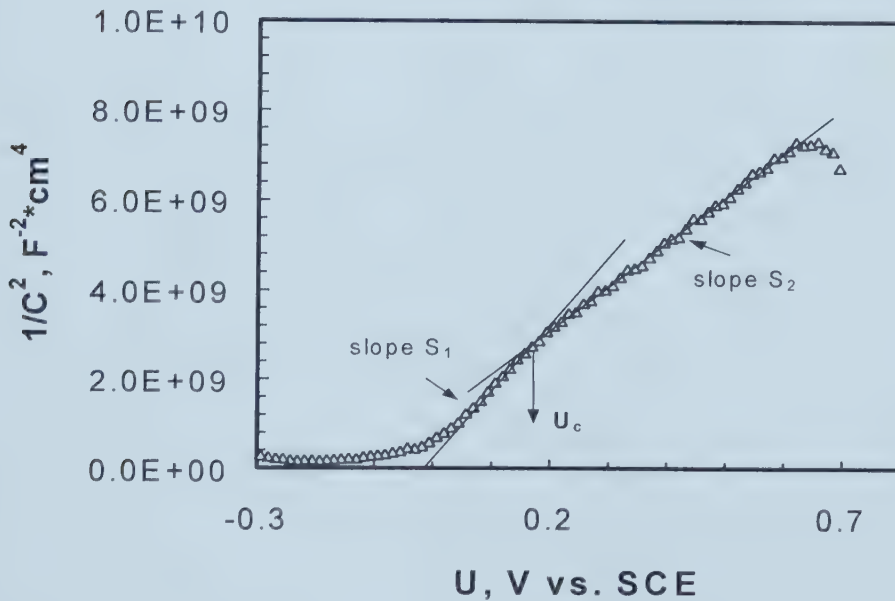


Figure 6-12. Mott-Schottky plot of type 304 stainless steel. The specimen had been hydrogen charged at 5 mA/cm² for 1 hour, and then passivated at 0.7 V for 2 hours.

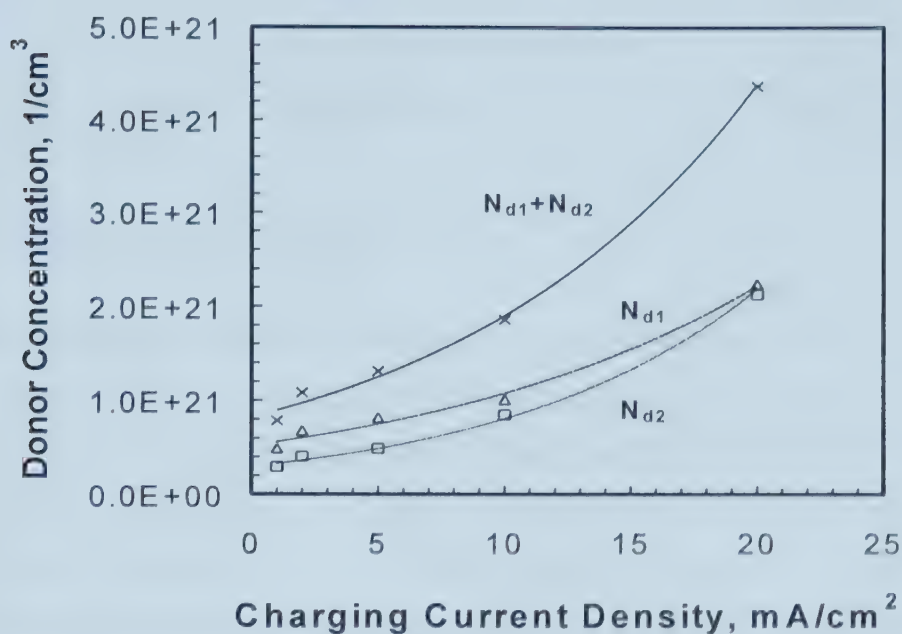


Figure 6-13. The donor concentrations vs. charging current density plot.

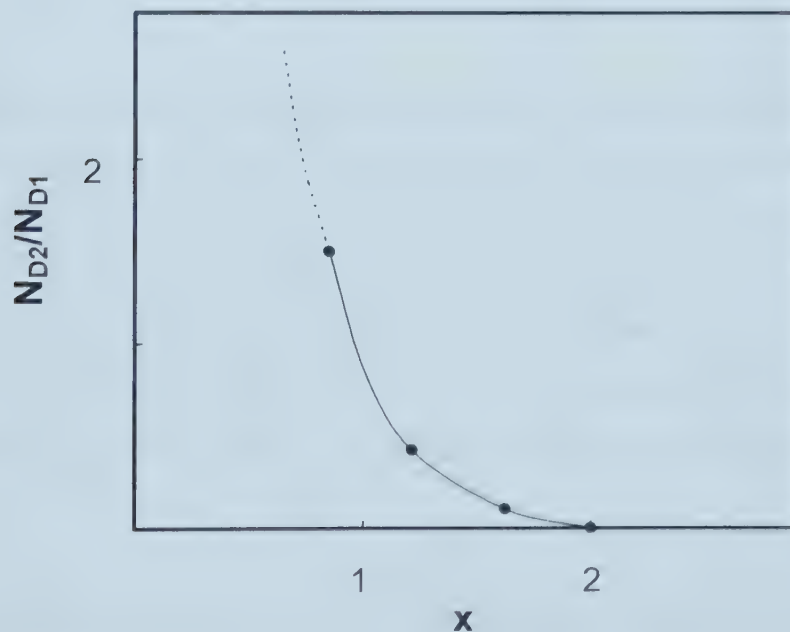


Figure 6-14. Influence of the degree of Cr^{3+} substitution in $(\text{Fe}^{2+}\text{Fe}^{3+}_{2-x}\text{Cr}^{3+}_x)(\text{O}^{2-})_4$ on the donor ratio N_{D2}/N_{D1} .⁸

$$N_{D1} = 5.2 * 10^{20} \exp(7.2 * 10^{-2} i) \quad [6-3-a]$$

and
$$N_{D2} = 3.0 * 10^{20} \exp(9.9 * 10^{-2} i) \quad [6-3-b]$$

where i is the charging current density.

A possible reason for the nonlinearity may lie in modification of the passive film due to hydrogen. Simoes et al.⁵ found that an inverse spinel structure made of Cr-substituted magnetite had two donor levels. The general formula of passive films formed on stainless steel was proposed as $(\text{Fe}^{2+}\text{Fe}^{3+}_{2-x}\text{Cr}^{3+}_x)(\text{O}_4)^{2-}$ with $0 < x < 2$ by Gillot and Rousset.^{8, 9} With the data published by these authors, it was found that N_{D2}/N_{D1} increases as x decreases (Figure 6-14).⁸ From Equation [6-3-a] and [6-3-b], the ratio of N_{D2}/N_{D1} can be derived as:

$$\frac{N_{D2}}{N_{D1}} = 5.7 * 10^{-1} \exp(2.7 * 10^{-2} i) \quad [6-4]$$

N_{D2}/N_{D1} increases with the charging current density, therefore x decreases with the charging current density. According to our experimental N_{D2}/N_{D1} data and Figure 6-14, x decreases from 1.16 to 0.98 when the charging current density increases from 1 to 20 mA/cm² (Figure 6-15). This indicates that hydrogen in the passive film may cause a decrease in chromium concentration in the film formed at high potential. The electro-oxidation reaction oxidation of Cr^{3+} to the soluble CrO_4^{2-} occurs at high potential.¹⁰ Whether hydrogen can promote this reaction is still unknown. Further research is needed to fully understand this phenomenon.

6.1.2.3. Mott-Schottky Plots Measured in the Cl⁻ Containing Borate Buffer Solution--- Effects of Cl⁻ on the Donor Concentration

The Mott-Schottky plots, C^{-2} vs. U , for the charged specimens in the borate buffer solutions containing different $[\text{Cl}^-]$ are shown in Figure 6-16. The specimens were passivated

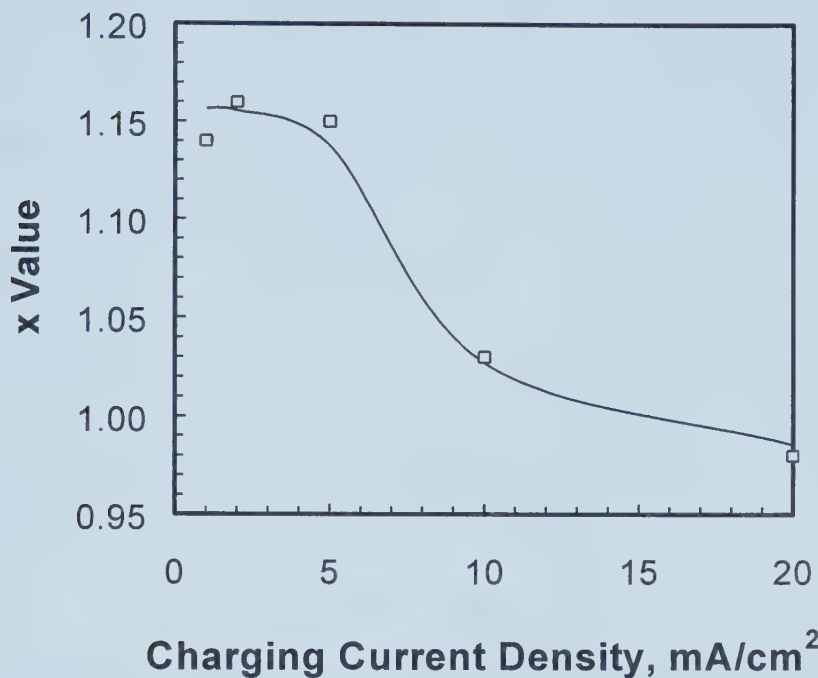


Figure 6-15. x value vs. charging current density plot.

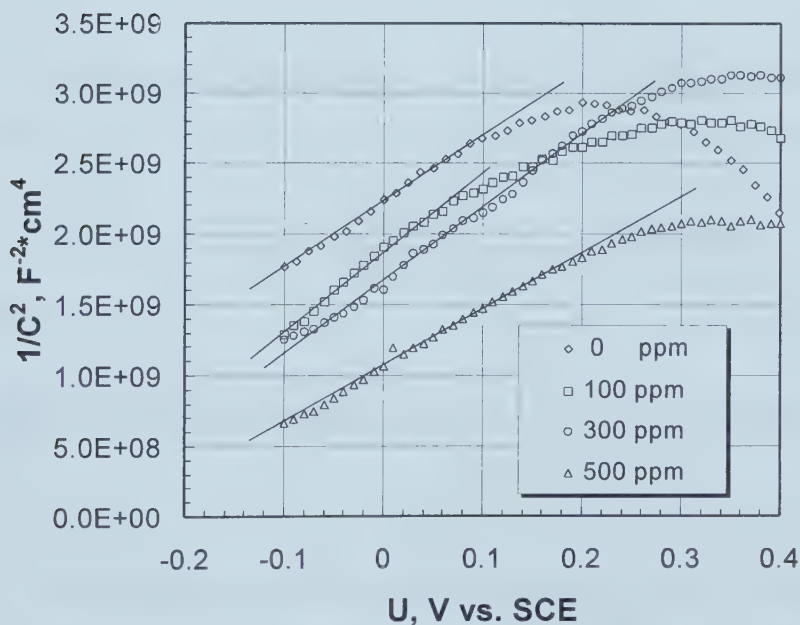


Figure 6-16. Mott-Schottky plots of 304 SS specimens charged at 5 mA/cm² for 30 minutes. The specimens were passivated at 0.1 V vs. SCE for 2 hours in borate buffer solution containing different [Cl⁻].

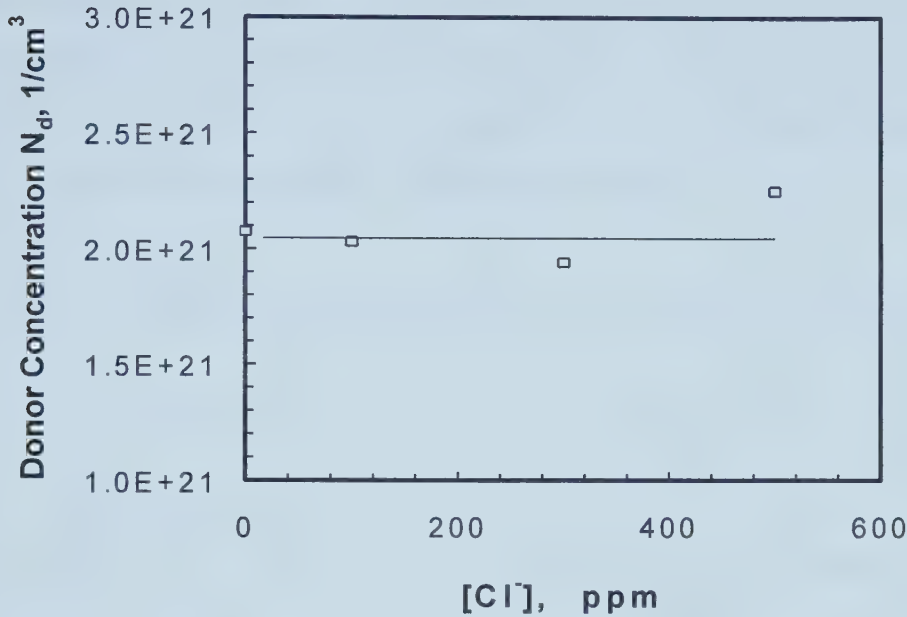


Figure 6-17. The change in donor concentration with $[\text{Cl}^-]$. The specimens were charged at 5 mA/cm^2 for 30 minutes, then passivated in the borate buffer solutions containing different $[\text{Cl}^-]$ for 2 hours.

at 0.1 V for 2 hours before the measurements. Positive slopes indicate that the passive films exhibit typical n-type semiconductivity. The donor concentrations were calculated. Figure 6-17 shows the change in the donor concentration with $[\text{Cl}^-]$ for the specimens charged at 5 mA/cm^2 for 30 minutes. Unlike hydrogen, Cl^- ions have no obvious effect on the donor concentration.

6.1.2.4. Effects of Hydrogen-Induced Martensite and Surface Cracking on Mott-Schottky

Plots

To check whether hydrogen induced-martensite and surface cracking can affect the electronic properties, the charging condition of 20 mA/cm^2 and 2 hours was chosen to guarantee the formation of martensite and surface cracking. After charging, the charged specimen was baked at 50°C for 72 hours to bake the hydrogen out of the specimen. To keep the experimental conditions the same, the uncharged specimen was also baked at the same

temperature for the same time. The Mott-Schottky plots were measured in the borate buffer solution after the specimens were cathodically reduced at -0.3 V vs. open circuit potential for 1000 seconds. The measured Mott-Schottky plots shown in Figure 6-18 indicate that the surface martensite and cracks do not significantly affect the electronic properties, such as the type of semiconductivity and the donor concentration.

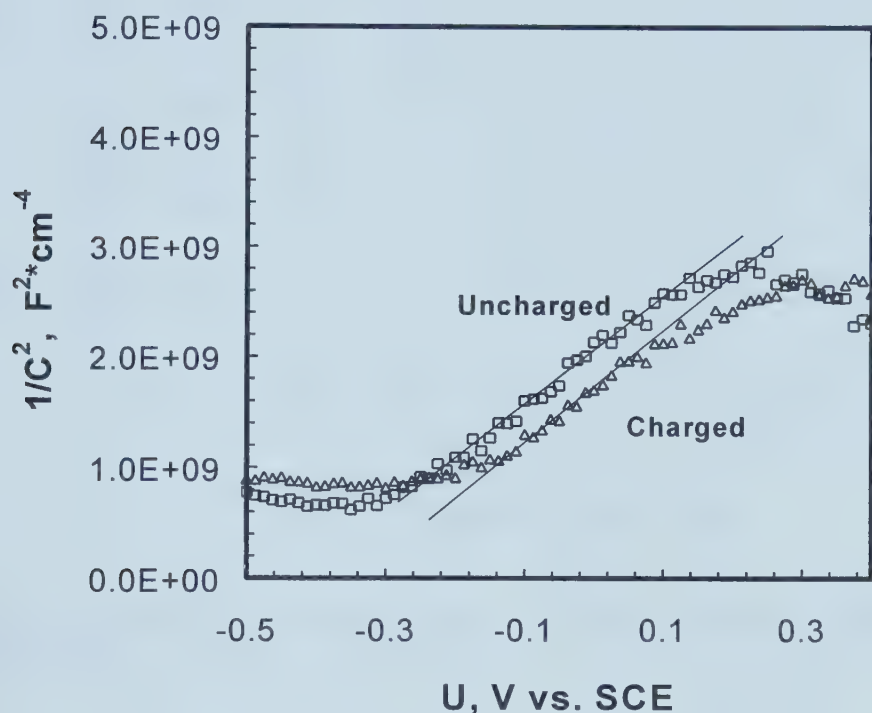


Figure 6-18. Mott-Schottky plots of the uncharged specimen and the specimen charged at 20 mA/cm² for 2 hours. The specimens were baked at 50°C for 72 hours before the measurements.

6.2. PHOTOELECTROCHEMISTRY MEASUREMENTS

6.2.1. Variation of the Light Intensity Source with Wavelength

The variation of light intensity with the wavelength was measured with a silicon diode. The light intensity spectrum is shown in Figure 6-19. The light intensity changed greatly with

the wavelength. To eliminate the effect of light intensity on the photocurrent, the photocurrent spectra are corrected by being divided by the light intensity at the same wavelength in the following sections.

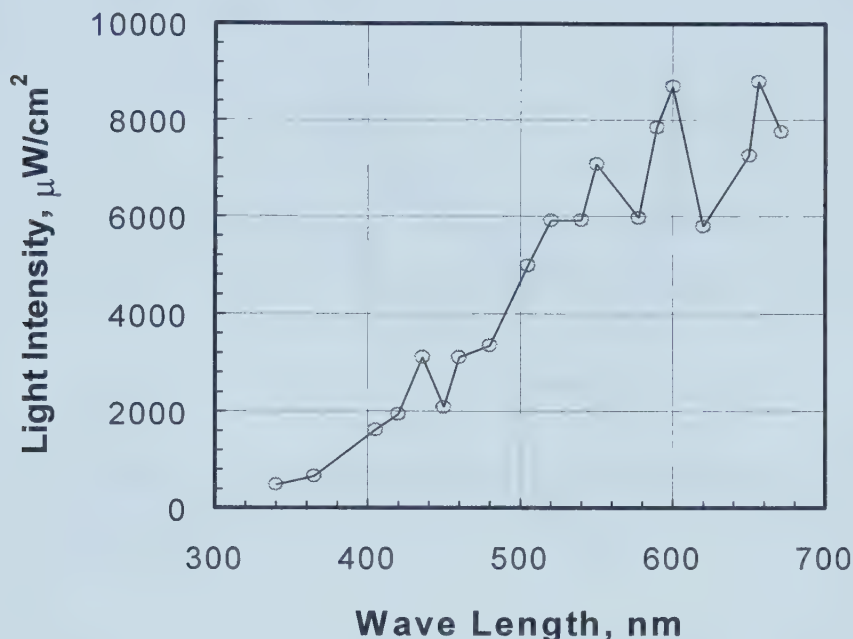


Figure 6-19. The variation of light intensity with the wavelength measured with a silicon diode.

6.2.2. Photocurrent Spectra

Figure 6-20 shows the photocurrent action spectra of the uncharged specimen at four different potentials. It reveals an attenuated but measurable photoresponse down to relatively low photon energies (long wavelengths). This kind of behavior has been observed for many amorphous semiconductors, and is known as the Urbach tail. Such a tail, which results in a sub-gap response, can be due to surface or localized states.

The optical gap values of the passive film were determined from an analysis of the photocurrent spectra. The following equation has been used assuming proportionality between the measured photocurrent and the optical absorption coefficient:

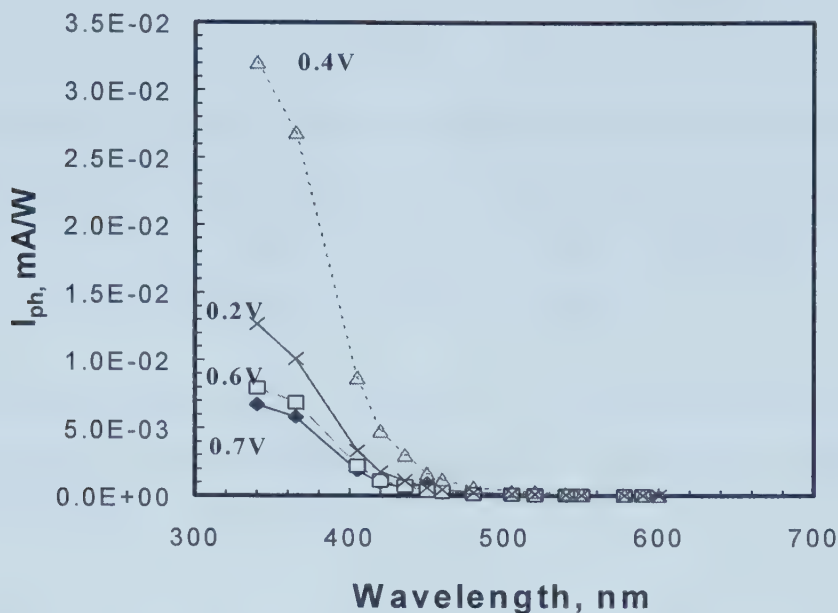


Figure 6-20. Photocurrent action spectra of uncharged 310 stainless steel. Photocurrent was measured in the borate buffer solution at different potentials.

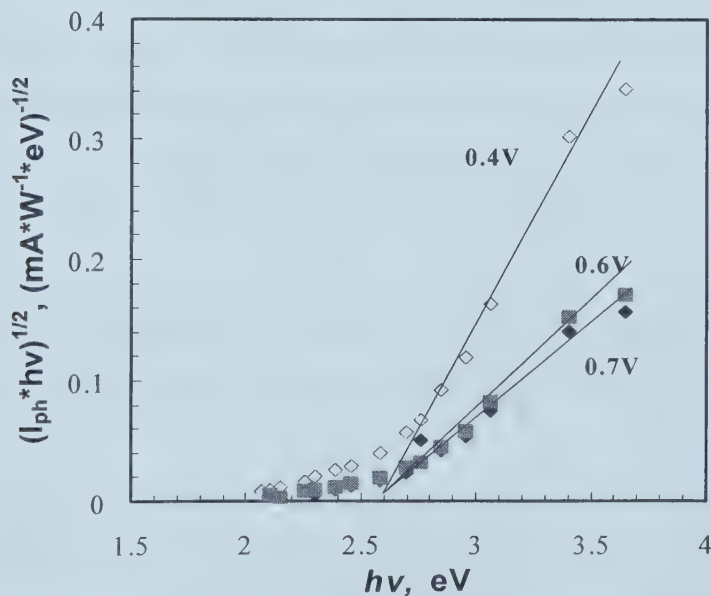


Figure 6-21. Plot of $(I_{ph} \cdot hv)^{0.5}$ vs. photon energy for the uncharged specimens passivated at 0.7V for 3.5 hours. Photocurrent is measured in borate buffer at different measuring potentials.

$$i_{ph} \cdot h\nu = (h\nu - E_g^{opt})^n \quad [6-5]$$

where E_g^{opt} is the band gap energy and n describes the type of transition between the valence band and conduction band in a crystalline material. For a direct transition, $n=1/2$ while for an indirect transition $n=2$. In amorphous materials, the same equation has been found as an empirical relation with n having different values, but predominantly 2.

An analysis according to equation [6-5] was applied to the photocurrent data measured at different electrode potentials. Plots of spectral data according to equation [6-5] yield straight lines for $n=2$, which indicates an indirect transition.

The plots of $(I_{ph}h\nu)^{0.5}$ vs. photon energy for the uncharged specimen are shown in Figure 6-21. From the intercept, the optical gap of the passive film can be determined, which in this case is 2.6 eV.

The action spectra for the specimens charged at 5 mA/cm² and 10 mA/cm² are shown in Figures 6-22 and 6-23 respectively. With increasing electrode potential, the photocurrents in these two cases first increase and then decrease. The photocurrent was the highest at 0.6V. The corresponding plots of $(I_{ph}h\nu)^{0.5}$ vs. $h\nu$ are presented in Figures 6-24 and 6-25. The optical gaps of the passive film were 2.56 and 2.54 eV respectively.

Figure 6-26 presents the change in the optical gap with the charging current density. From the plot, it is obvious that hydrogen charging has very little effect on the optical gap.

Hydrogen could affect the amplitude of photoresponse. Figure 6-27 shows the change in photocurrent with charging current density. In the both cases of exposure to 365 and 460 nm monochromatic lights, photocurrent increased with charging current density.

The Urbach tail can be characterized by a logarithmic dependence of the photocurrent on photon energy, frequently obeying the following relationship^{11, 12}:

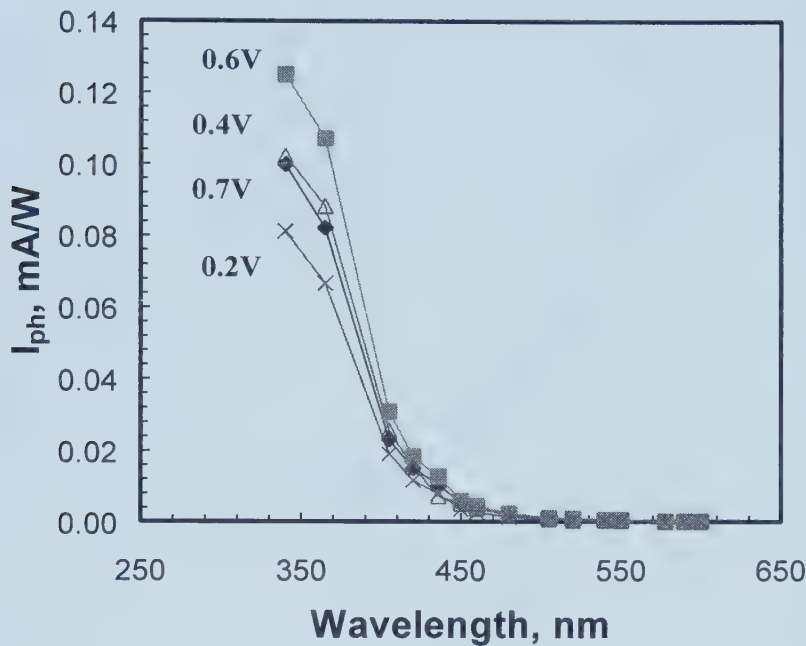


Figure 6-22. Photocurrent action spectra of 310 SS charged at 5 mA/cm^2 for 5 hours, and passivated at 0.7V for 3.5 hour, then photocurrent was measured in the borate buffer solution at different measuring potentials.

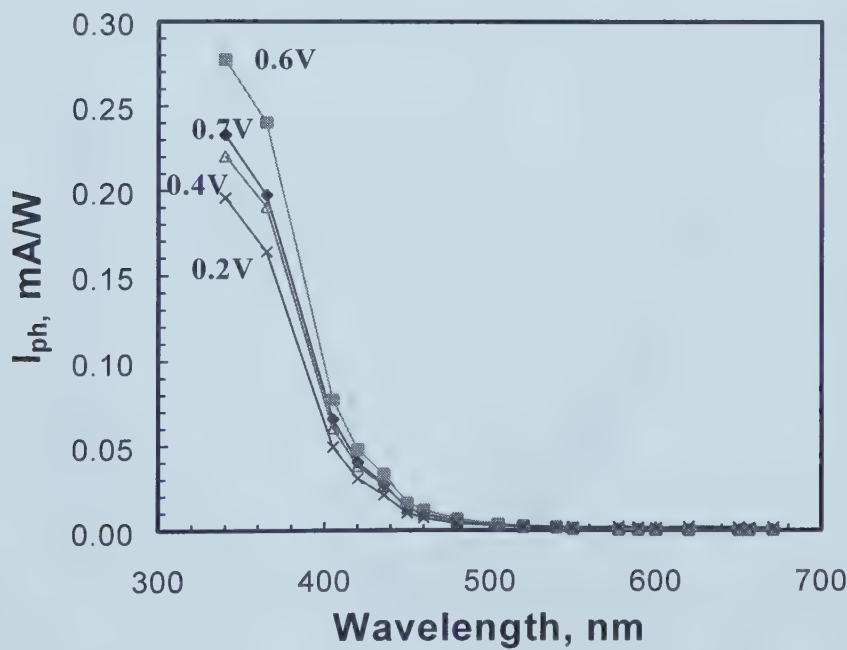


Figure 6-23. Photocurrent action spectra of 310 SS charged at 10 mA/cm^2 for 5 hours and passivated at 0.7 V for 3.5 hours. Photocurrent was measured in the borate buffer solution at different measuring potentials.

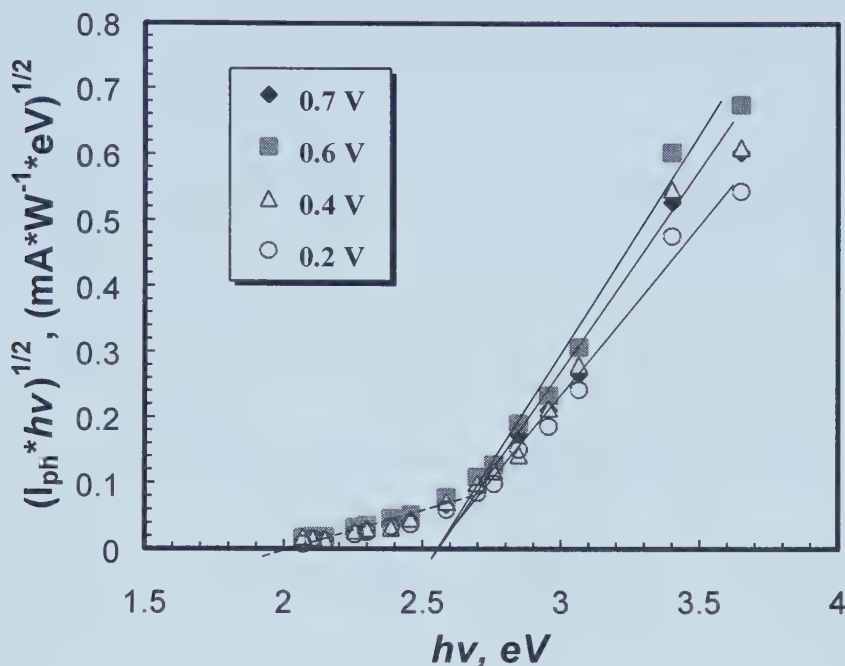


Figure 6-24. Plot of $(I_{ph} \cdot hv)^{0.5}$ vs. photon energy for 310 SS charged at 5 mA/cm^2 for 5 hours, passivated at 0.7V for 3.5 hours. Photocurrent was measured in the borate buffer solution at different measuring potentials.

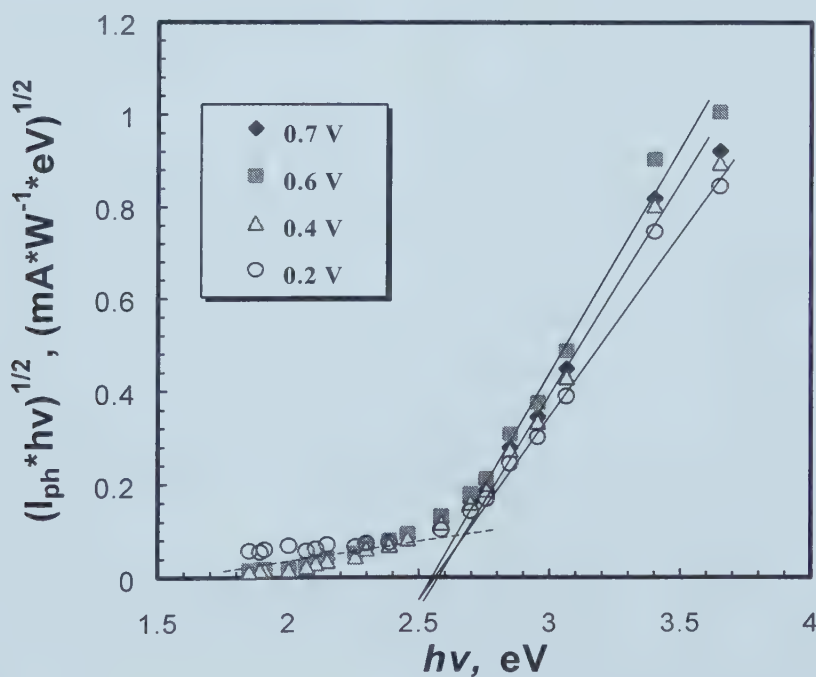


Figure 6-25. Plot of $(I_{ph} \cdot hv)^{0.5}$ vs. photon energy for 310 SS charged at 10 mA/cm^2 for 5 hours and passivated at 0.7V for 3.5 hours. Photocurrent was measured in the borate buffer solution at different measuring potentials.

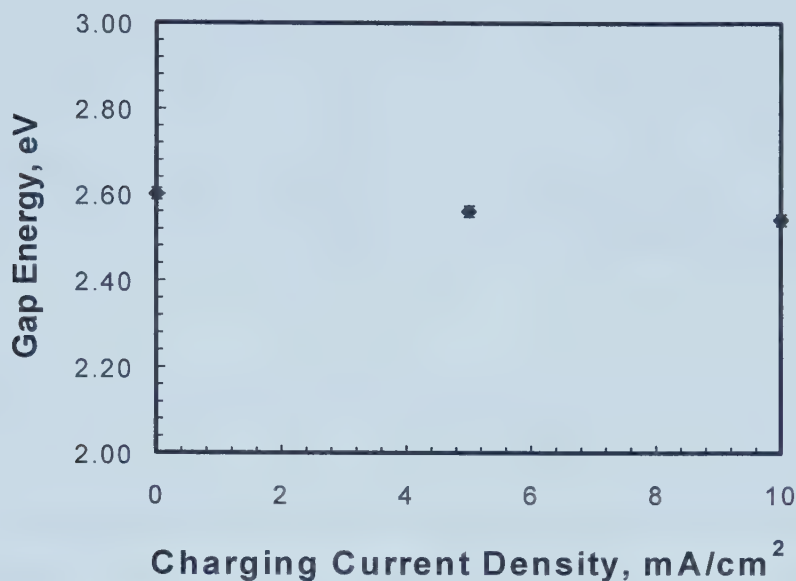


Figure 6-26. The change in the gap energy with the charging current density.

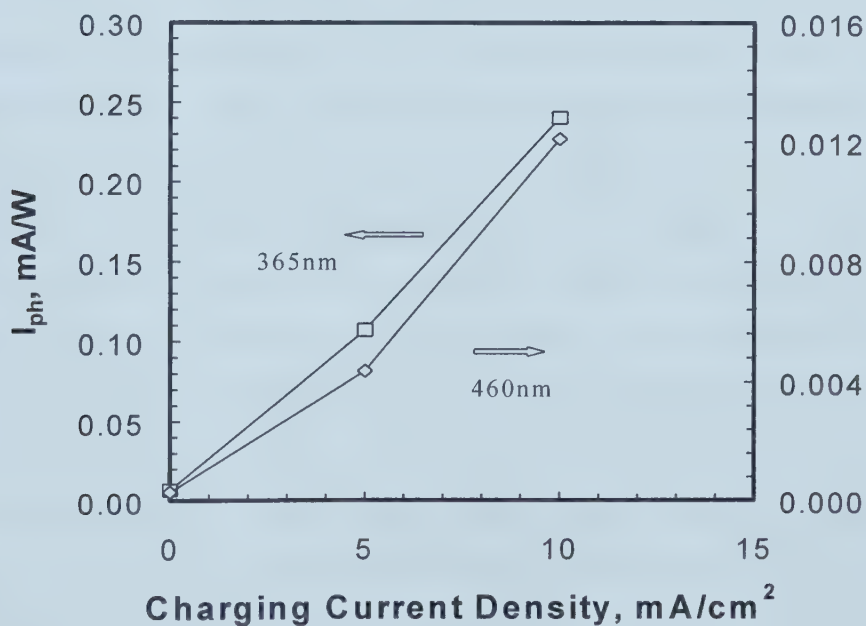


Figure 6-27. The changes in photocurrent with charging current density. Specimens were passivated at 0.7V for 3.5 hours. Photocurrent was measured in the borate buffer solution at 0.6 V.

$$\alpha = \alpha_0 \exp[\gamma(h\nu - E_g^{opt}) / kT] \quad [6-6]$$

where α is the optical absorption coefficient, $h\nu$ is the photon energy, E_{opt} = optical gap, k = Boltzmann's constant (8.620×10^{-5} eV/K) and T is the temperature in Kelvin. α_0 and γ are constants.

I_{ph} is assumed to be proportional to the optical absorption constant α .¹³ The $\log(I_{ph})$ vs. $h\nu$ plots (Urbach plots) of the uncharged and charged specimens according to equation [6-6] are shown in Figures 6-28, 6-29 and 6-30. The result reveals that the photocurrent spectra at the bandedge follows this type of relationship. The constant γ can be calculated from the Urbach slope:

$$\gamma = 2.303 \text{ slope} \times kT \quad [6-7]$$

The Urbach plots of the charged and uncharged specimens measured at 0.7 V are presented in Figure 6-31. From Figure 6-31, it was observed that the slope, and therefore γ , decreased with the charging current densities. The average calculated value of γ for the uncharged specimens was 0.146. This is in the same order of magnitude as amorphous semiconductors by photoelectrochemical measurement.^{14,15,16} Mott and David¹² assumed that a higher slope (higher γ) indicated an ideal amorphous network with few defects and voids. Dunstan¹⁷ proposed that the factor $1/\gamma$ could be used to describe the degree of disorder. According to this proposal, Stimming et al.^{18,19} showed that the disorder degree of ion-implanted hafnium oxide films increased with increasing implantation concentration. The change in the disorder energy kT/γ with charging current density is shown in Figure 6-32. An increase in kT/γ with charging current density indicated that hydrogen permeated into the passive film could increase the disorder degree of the film.

6.2.3. Potential Dependence of Photocurrent

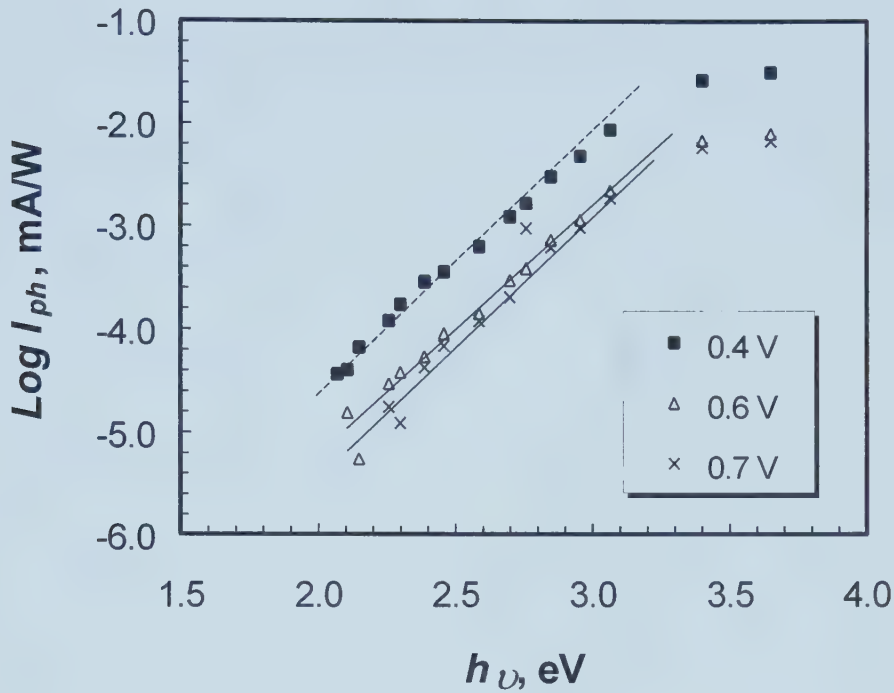


Figure 6-28. $\text{Log } I_{ph}$ vs. $h\nu$ plots of the uncharged specimens as derived from photocurrent spectra measured at different potentials.

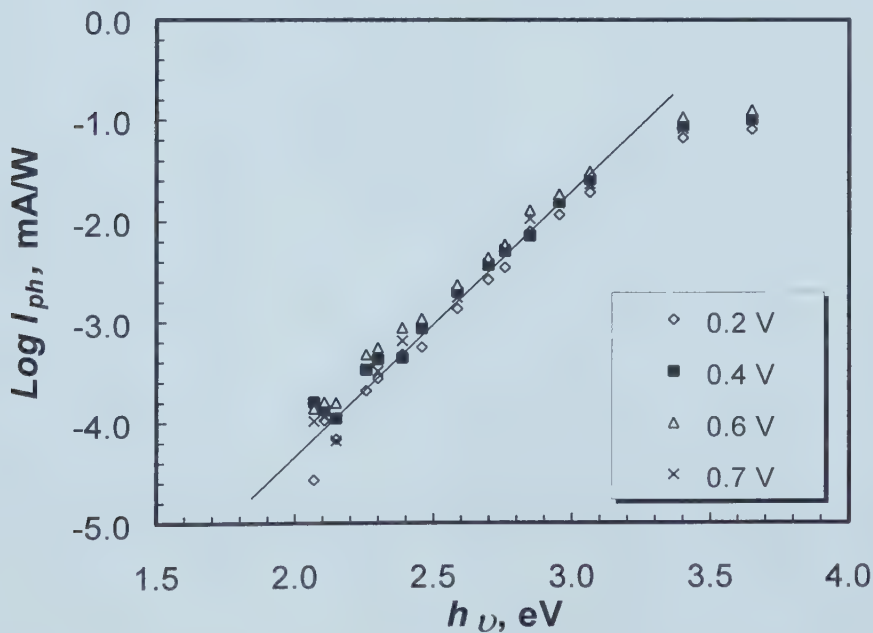


Figure 6-29. $\text{Log } I_{ph}$ vs. $h\nu$ plots as derived from photocurrent spectra measured at different potentials. The samples were charged at 5 mA/cm^2 for 5 hours, then passivated at 0.7 V for 3.5 hours in the borate buffer solution.

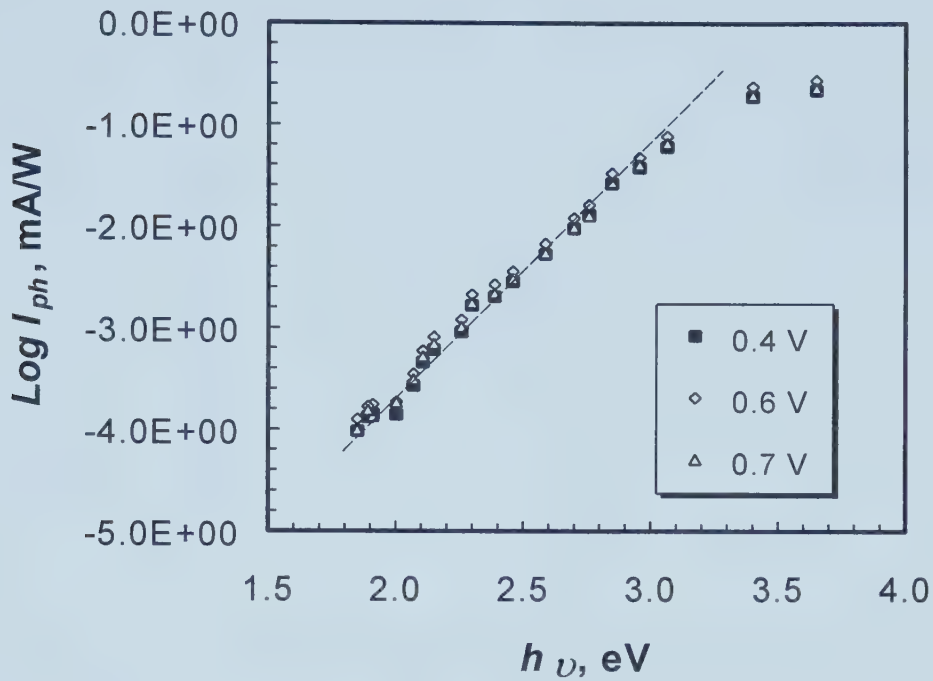


Figure 6-30. $\text{Log } I_{ph}$ vs. $h\nu$ plots as derived from photocurrent spectra measured at different potentials. The samples were charged at 10 mA/cm^2 for 5 hours, then passivated at 0.7 V for 3.5 hours in the borate buffer solution.

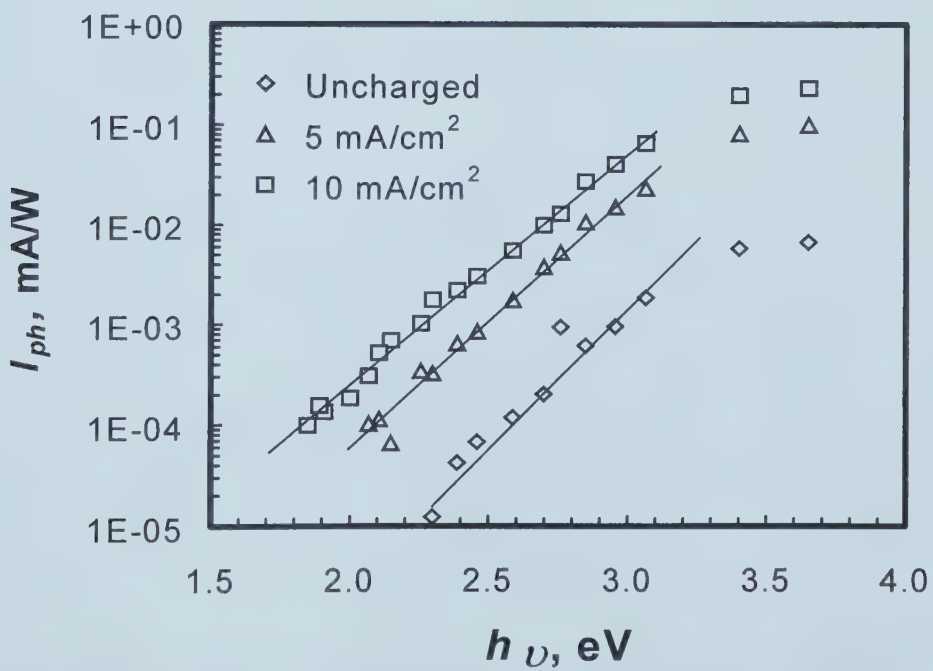


Figure 6-31. The photocurrent vs. photon energy curves of the uncharged and charged specimens.

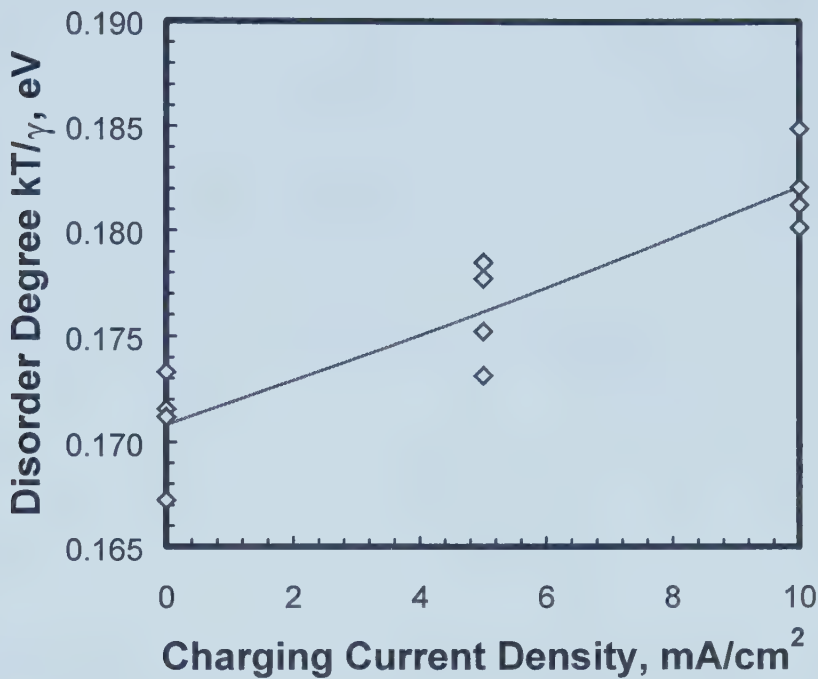


Figure 6-32. The change in disorder energy (kT/γ) with charging current density.

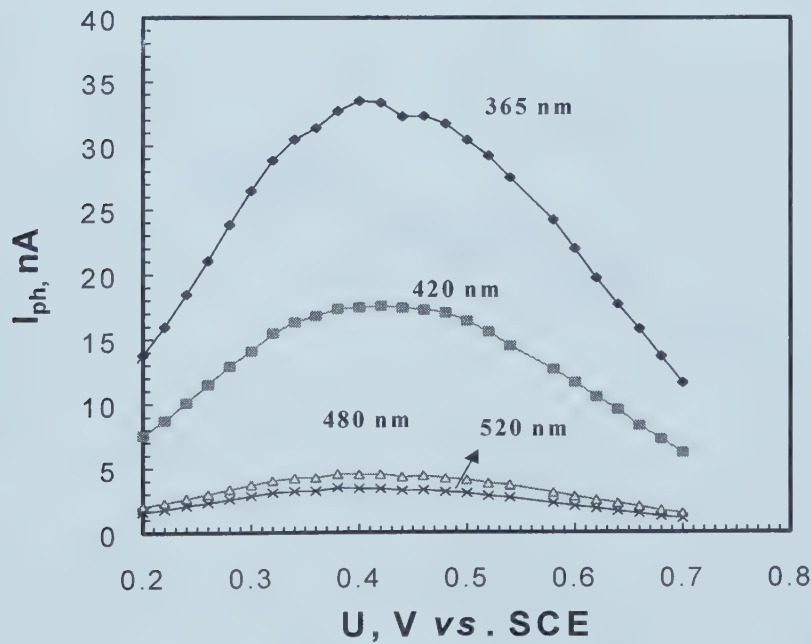


Figure 6-33. Plots of I_{ph} vs. potential for the uncharged specimen. The specimen was passivated at 0.7V for 3.5 hours in the borate buffer solution before the photocurrent was measured.

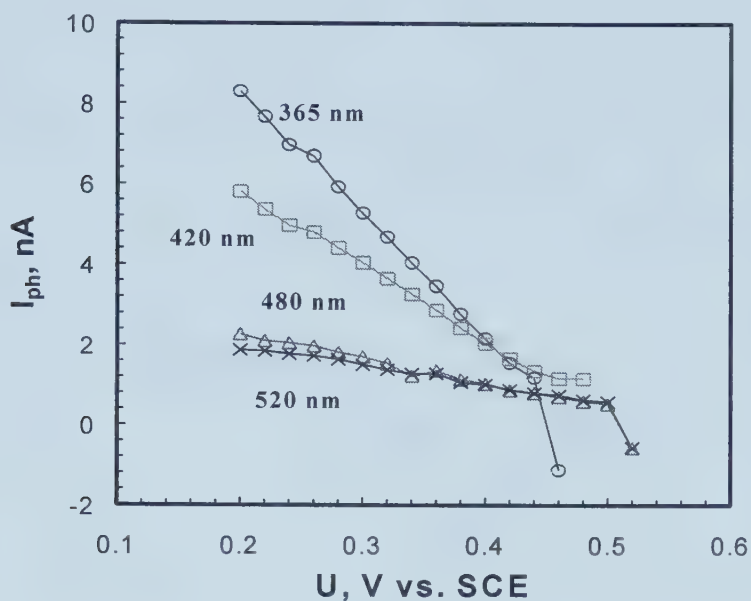


Figure 6-34. Potential dependence of photocurrent of 310 SS charged at 5 mA/cm^2 for 5 hours and passivated at 0.7V for 3.5 hours in the borate buffer solution. Specimens were illuminated with monochromatic lights.

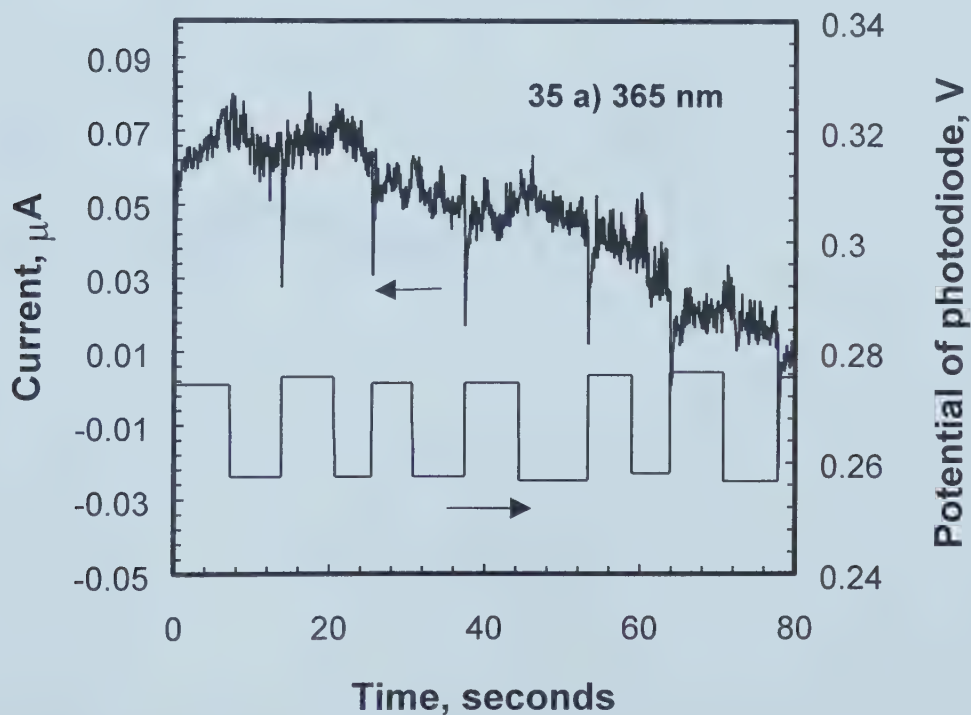


Figure 6-35. --- continued

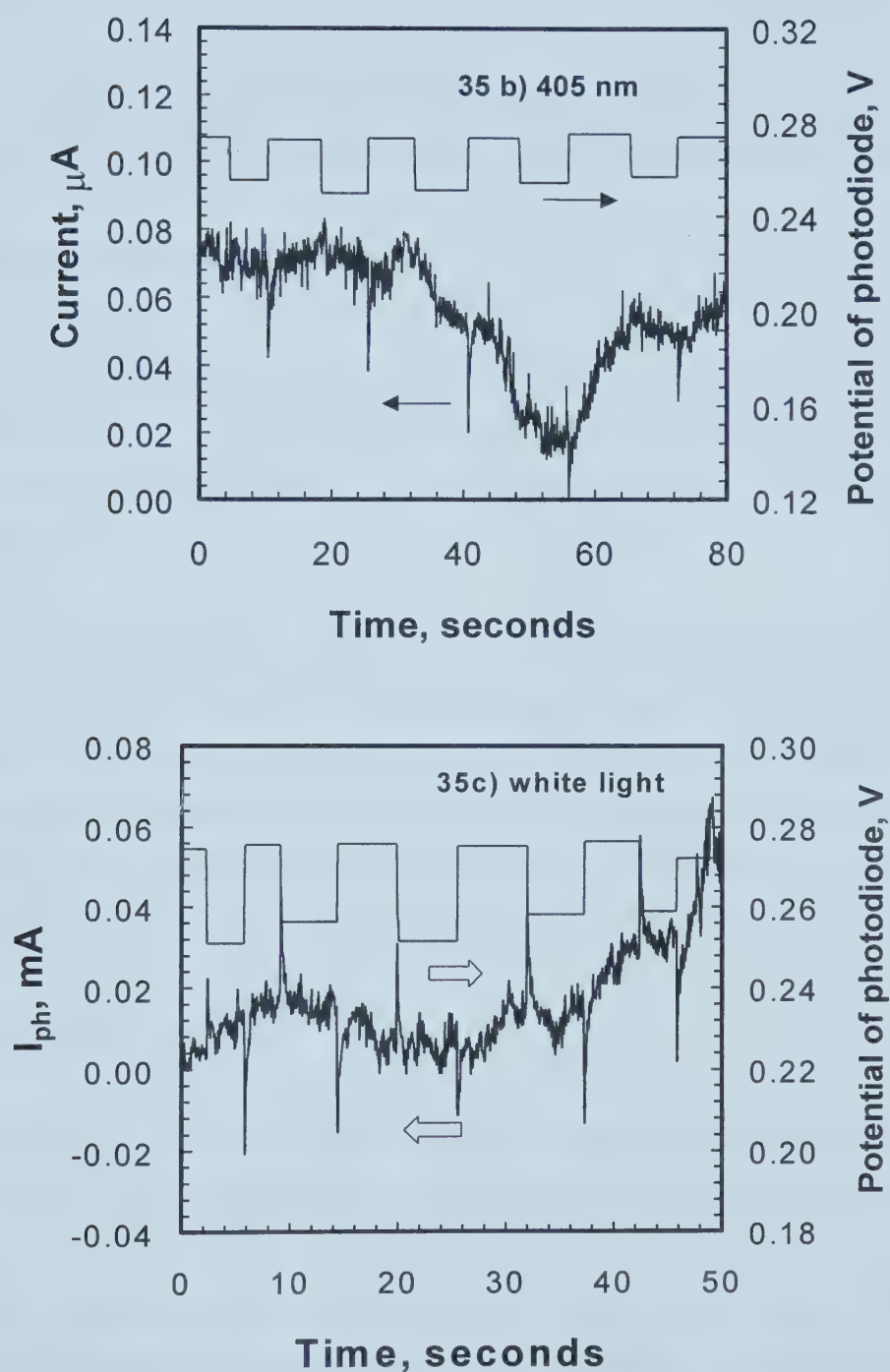


Figure 6-35. Photocurrent transients of uncharged samples obtained at 0.6 V under monochromatic illumination [(a) and (b)] and white light (c).

Figure 6-33 shows the I_{ph} vs. potential plots for the uncharged specimen at different wavelengths. The photocurrent first increased and then decreased with the applied potential.

The I_{ph} vs. potential plots for the specimen charged at 5 mA/cm^2 for 5 hours are given in Figure 6-34. The photocurrent decreased with the applied potential in the measured range.

6.2.4. Photocurrent Transients

Usually the lock-in technique is used to measure the spectral distribution because of small photocurrents. A drawback, however, is that transient effects and possible changes in sign of the photocurrent are difficult to detect. For this reason, direct current measurements were performed.

Figure 6-35 shows the direct photocurrent responses of the passive films of uncharged specimens to 365 nm, 420 nm and white light. The specimens were passivated at 0.7 V for 6 hours, and the photocurrent was measured under a potential of 0.6 V. A sharp cathodic peak appeared when the electrode was illuminated, and the photocurrent decayed fairly quickly to a steady state value. When light stopped illuminating, a sharp anodic peak appeared for the white light while no anodic peak appeared for the two monochromatic lights.

6.3. DISCUSSION

Passive films on metals are often insulators or semiconductors. The results of Mott-Schottky measurements demonstrate that the passive films on stainless steels exhibit semiconductive properties. The positive slopes of Mott-Schottky plots indicate the passive films shows n-type semiconducting characteristics. Photoelectrochemistry, which produces electrochemical reactions due to stimulation by incident light, can reflect the optical and electronic properties of the surface film. The chemical composition and structural properties of the film are reflected in optical and electronic properties, and consequently can be investigated with photoelectrochemistry.

Electronic transitions between the valence and conduction bands in a crystalline semiconductor correspond to the minimum energy difference, E_g , between the lowest minimum in the conduction band and the highest maximum in the valence band. If these two points lie on the same point in momentum space, the transition is direct; if they do not overlap, then the transitions are indirect and are only possible when phonon assisted (Figure 6-36a and b). In sufficiently pure crystals the indirect transitions are usually less probable than direct ones. In contrast, in relatively heavily doped semiconductors the probability of the indirect transitions is relatively larger due to the interactions between electrons and defects (such as impurities) (Figure 6-36 c).²⁰ The photocurrent spectra for highly disordered semiconductors have been observed to follow a behavior similar to that observed for indirect transitions in crystalline semiconductors near the band edge. In our research, it is found that the passive films on stainless steels follows the indirect transition pattern.

Mott-Schottky methods demonstrate that hydrogen can increase the donor concentration. According to the physics of semiconductors, one of the possible reasons is the increase in the concentration of oxygen vacancies. When the oxide MO contains a vacancy in its oxygen sublattice, the valence electrons of excess atom M are captured by oxygen vacancies that behave as effective positive charges, creating an additional coulombic field. This field perturbs the periodicity of the potential energy of the oxide.²¹ The excess electrons occupy energy levels lying below the conduction band, which are called donor levels.

The dependence of the photocurrent on wavelength reveals structureless spectra with Urbach tails. This type of spectrum indicates that the passive film is highly disordered.¹⁴ The appearances of the hysteresis on capacitance vs. potential curves confirm that passive films formed on stainless steels are highly disordered films. An electron at an atomic site around a defect in the material finds itself in a different environment from that found at another site. The defects in the passive films are registered as localized states. It has been found for highly disordered films (with larger disorder energy kT/γ) that the density of states-function extends largely into the bandgap region of the material.²² This introduces a high number of localized states. Highly disordered semiconductors are characterized by a high density of states localized between valence and conducting bands. A schematic representation of the band

structure of n-type passive films with localized states is shown in Figure 6-37.²³ The most interesting result found in this research is that hydrogen can increase the degree of disorder of passive films, which indicates a higher density of the localized states in the gap.

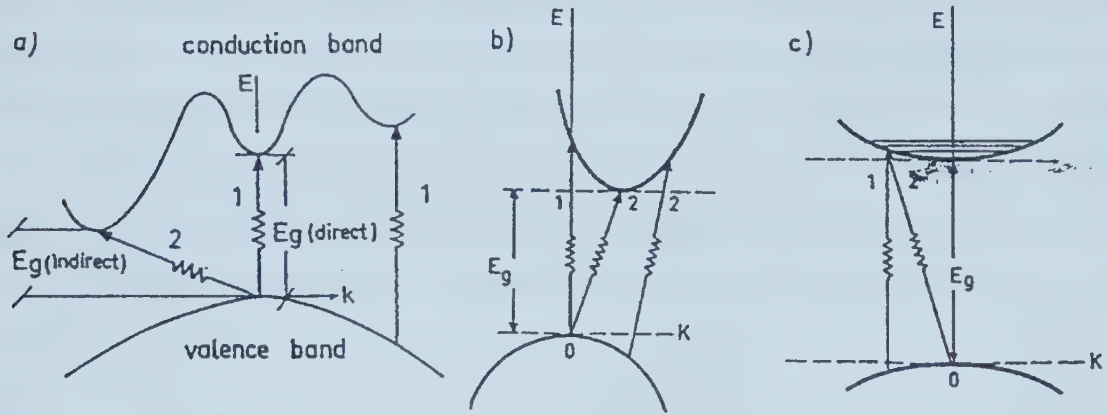


Figure 6-36. Schematic representation for direct (1) and indirect (2) optical transitions from the valence band to the conduction band: (a) maxima and minima of the bands coincident; (b) maxima and minima of the bands non-coincident; (c) optical transitions when some of the electron levels in the conduction band are occupied (n-type semiconductor).²⁰

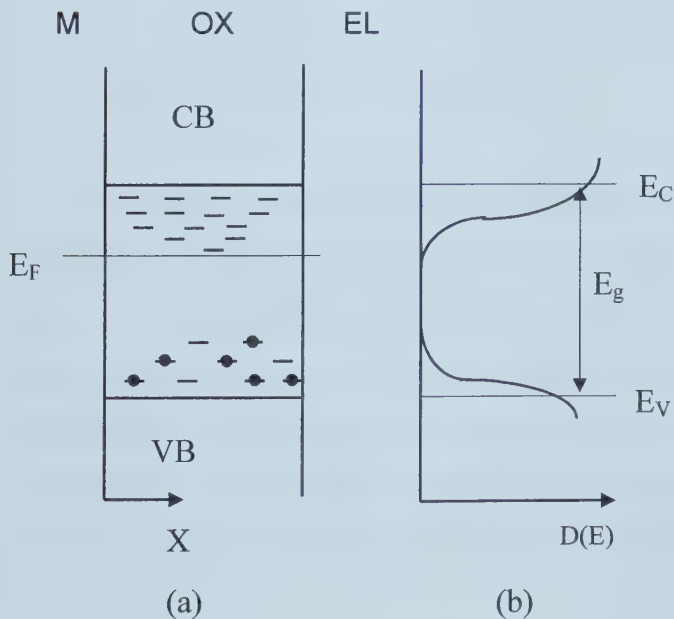


Figure 6-37. The schematic representations of electron band structure with localized states of an n-type passive film (a) and possible density of state distribution in the band gap (b) at $U=U_{FB}$.²³

The photoprocess involves localized states. Thus the rate-determining step in the photoexcitation process is probably the removal of the photoexcited carrier from its respective trap. This can be an electron as well as a hole. These processes include the excitation from localized states to extended states and extended states to localized states. If the localized state is close to the surface and the field is not too high, an electron has a finite possibility of direct escape to the electrolyte. This latter process represents a tunneling process through the potential barrier against the field and is thought to be the cause of the cathodic photocurrent. The fact that this behavior is apparent after prolonged polarization suggests a change in the surface structure of a passive film with time. Appearance of the cathodic photocurrent has been reported for the films formed on iron¹⁵ and stainless steels^{14,24}.

Schmuki and Böhni²⁵ revealed that the passive films on stainless steels had a highly defective electronic structure. The higher their resistance to pitting corrosion, the less they possess localized states situated deeper in the bandgap. Deep localized states may occur at the sites where the structure of the film is heavily distorted and hence such a point may act as a nucleation site for pitting corrosion. Similar to the hydrogen effect on a silicon crystal,²⁶ it is possible that a high density of hydrogen in the passive film generates strong distortions and structural defects which could create deep levels in the bandgap. This might be the reason why hydrogen can promote pitting corrosion.

Hydrogen in passive films is considered to be present as a charged species (proton)^{27,28} because passivating oxides have an ionic bonding character, and also because passive films support a strong electric field. Hydrogen can penetrate into the passive film from the metal side and ionize. Hydrogen can improve the photocurrent response of the passive films; this improvement is partly due to the photo-oxidation of hydrogen atoms. The photoresponse is proportional to the hydrogen concentration in the metals. This phenomenon has also been observed in anodically polarized iron and nickel loaded with hydrogen and illuminated.

6.4 SUMMARY

Mott-Shottky measurements reveal that the passive films on stainless steels are n-type

semiconductor films. Hydrogen charging can increase the donor concentration of the passive films, but chloride ions have no obvious effect on it. Hydrogen, however, has no obvious effect on the flatband potential.

The occurrences of the hysteresis in capacitance vs. potential curves and the Urbach tails in photocurrent spectra indicate that the passive films formed on the stainless steels are highly disordered. From the Urbach tails, the disorder degree of the passive films was calculated. Hydrogen in a passive film increased the disorder energy of the film, which means that hydrogen can make passive films more defective. Hydrogen can increase the magnitude of the photocurrent.

REFERENCES

1. G. Razzini, S. Maffi, G. Mussati and L. Peraldo Bicelli, *Corros. Sci.*, 37 (1995): p.1131.
2. G. Razzini, S. Maffi, G. Mussati, L. Peraldo Bicelli and G. Mitsi, *Corros. Sci.*, 39 (1997): p.613.
3. A.D. Paola, *Electrochim. Acta*, 203 (1989): p. 34.
4. Y. V. Pleskov and Y. Y. Gurevich, *Semiconductor Photoelectrochemistry*, Chap. 3, Consultants Bureau, New York, (1986).
5. A. M. P. Simoes, M. G. S. Ferreira, B. Rondot and M. da Cunha Belo, *J. Electrochem. Soc.*, 137, (1990): p. 82.
6. J. Schoonman, K. Vos, and G. Blasse, *J. Electrochem. Soc.*, 128, (1981): p. 1154.
7. V. A. Myamlin and Y. V. Pleskov, "Semiconductor Photoelectrochemistry", Chap. 3, Plenum Press, New York (1967).
8. B. Gillot and A. Rousset, *J. Solid State Chem.*, 65, (1986): p. 322 .
9. B. Gillot and A. Rousset, *C. R. Acad. Sci. Paris, Series II*, 293, (1981): p. 23.
10. M. U. MacDonald and D. D. MacDonald, *J. Electrochem. Soc.*, 132 (1985): p. 555.

11. J. Tauc, Optical Properties of Solids, Ed. By F. Abeles, Elsevier, Amsterdam (1972): p. 277.
12. N. F. Mott and E. A. Davis, Electronic Processes in Non-crystalline Materials, Clarendon Press, Oxford (1979).
13. U. Stimming, Electrochem. Acta, 31 (1986): p. 415.
14. A. Di Paola, D. Schukla and U. Stimming, Electrochimica Acta, 36 (1991): p.345.
15. P. C. Searson, R. M. Latanision and U. Stimming, J. Electrochem. Soc., 135 (1988): p.1358.
16. B. Danzfuss, J. W. Schultze and U. Stimming, J. Electroanal. Chem., 164 (1984): p. 89.
17. D. J. Dunstan, J. Phys. C, 16 (1983): p. L567.
18. B. Dunzfuss, J. W. Schultze, and U. Stimming, Principles of Electrode Reactions, Ed. by J. W. Schultze, Dechema Monographs, 102 (1986): p. 465.
19. U. Stimming, Nucl. Instr. Meth. B, 23 (1987): p. 505.
20. M. Da Cunha Belo, "Photoelectrochemistry: Theoretical Basis", Electrochemical and Optical Techniques for the Study and Monitoring of Metallic Corrosion, M. G. S. Ferreira and C. A. Melendres, Kluwer Academic Publishers, Dordrecht, Netherlands, (1989): p.191.
21. Z. M. Jarzebski, Oxide Semiconductors, Pergamon Press, (1973).
22. V. Halpern, Philos. Mag. B, 49 (1984): p. L57.
23. M. H. Dean and U. Stimming, Corros. Sci., 29 (1989): p.199.
24. A. Di Paola, F. Di Quarto and C. Sunseri, Corro. Sci., 26 (1986): p.935.
25. P. Schmuki and H. Böhni, J. Electrochem. Soc., 139 (1992): p.1908.
26. P. de Mierry, A. Etcheberry, R. Rizk, P. Etchegoin and M. Aucouturier, J. Electrochem. Soc., 141, (1994): p.1539.
27. R. Ruetschi and R. Giovanoli, J. Electrochem. Soc., 135 (1988): p. 2663.
28. R-H Song, S. I Pyun and R. A. Oriani, Electrochimica Acta, 36 (1991): p.825.

Chapter 7. Effects of Hydrogen on the Passivity and Breakdown of Passive Films

In this chapter, immersion tests, measurements of polarization curves, the AC impedance technique and other measurements are used to investigate the effects of hydrogen on the passivity and breakdown of passive films. The anodic current density, pit density, pit size, protection and pitting potentials and other relevant parameters are measured to evaluate the effects.

The essential condition for film breakdown is the presence of one of the specifically acting anions in the solution particularly Cl^- , Br^- or I^- .¹ The breakdown of a passive film is observed most often in the presence of chloride ions. This is due to not only their greater aggressiveness, but also the wider distribution of chlorides in nature, that is, the greater chance of their being present in aggressive media, including many technically

employed solutions. It is critically important to discover whether there is a hydrogen-enhanced effect of chloride ions on the breakdown of passive films. However, to date no research has been carried out on this aspect. This enhanced effect will be investigated in this chapter.

Aggressive anions can stimulate the breakdown of passive films or development of pitting corrosion only if they are present in the solution with a concentration greater than a certain critical concentration of aggressive anions.^{2,3} As would be expected, this critical concentration of the aggressive anions depends on the nature of the metal or alloy, its heat treatment and the state of its surface.⁴ Hydrogen charging should change this critical concentration for the breakdown of passive films. Therefore, the effects of hydrogen on the stability of the passive films on stainless steels can be evaluated through the change in this critical concentration.

The critical chloride concentration is obtained by measuring the current responses of specimens under a constant passivating potential to additions of various amounts of chloride ions. In practice, components often serve under stressed conditions. However, all the research regarding effects of hydrogen on breakdown/pitting process are carried out in unstressed conditions. It is useful, from both the practical and theoretical aspects, to study the effect of hydrogen on specimens upon which an external stress is applied. Effects of external stress on this critical chloride concentration are also measured in this chapter.

7.1. IMMERSION TESTS

7.1.1. Methods to Measure the Pit Density, Size and the Percentage of the Apparent Surface Area Occupied by Pits

The pit density, size and percentage of the apparent surface area occupied by pits were statistically measured. For each specimen at least eight randomly selected fields were used in order to obtain more accurate statistical results.

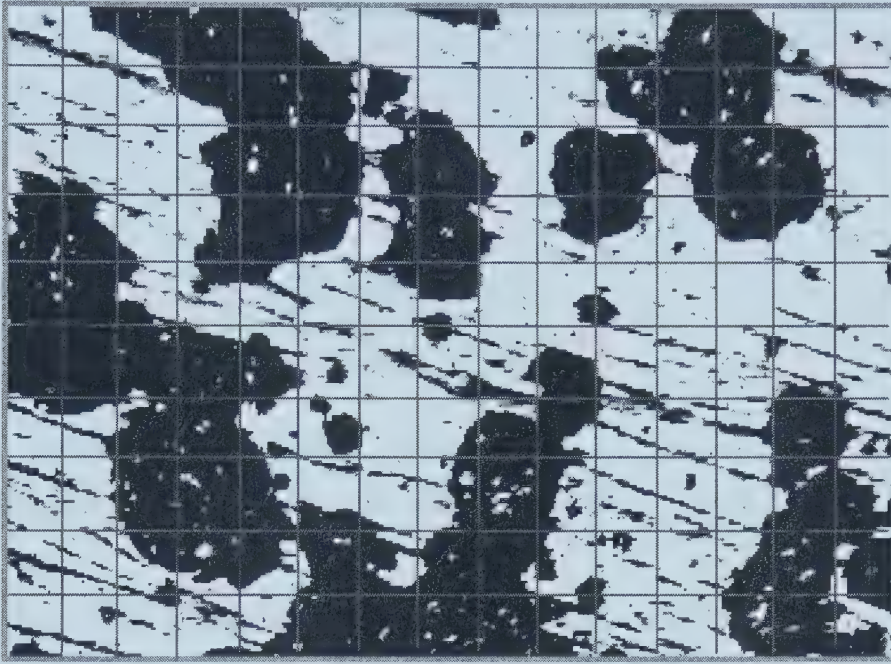


Figure 7-1. A 10 by 15 grid is marked on each video print to measure the apparent area percentage occupied by pits.

The pit density (P_{den}) is the number of pits per unit area, which can be expressed as:

$$P_{den} = \frac{n_{pit}}{A} \quad [7-1]$$

where n_{pit} is the number of pits appearing in an area A . The pit density is used to quantitatively evaluate the effects of hydrogen on pit initiation. The size of a pit is measured as a pit diameter, assuming the shape of the pit is circular. The diameter of each pit is measured along three different directions and the corresponding average diameter is calculated.

The apparent area percentage occupied by pits is measured by quantitative metallography. A 10 by 15 grid is marked on each video print (Figure 7-1) and the number (n_{g-p}) of the units of grid, more than 50% of whose area is occupied by pits, is counted. The apparent area percentage occupied by pits can be calculated according to the following equation:

$$A_p = \frac{n_{g-p}}{n_{g-t}} \times 100\% \quad [7-2]$$

where n_{g-t} is the total number of the units of the grid. The 10 by 15 grid suffices for this application, because the magnification can be adjusted for a particular pit morphology.

7.1.2. Results of Immersion Tests for 310 Stainless Steel

7.1.2.1. Effects of Hydrogen on Pitting Initiation

Hydrogen was introduced into specimens by charging at different current densities before the immersion tests. The hydrogen charging time was 24 hours. No pit was found even after 144 hours of immersion for the uncharged specimens. For the specimens charged at 0.1 mA/cm², pits did not appear until 80 minutes of immersion. Pit density, however, reached approximately 60/mm² after only 2 minutes of exposure for the specimens charged at 2 mA/cm². These results indicate that hydrogen in a stainless steel greatly facilitates pitting initiation.

The change in the pit initiation time with charging current density is summarized in Table 7-1.

Figure 7-2 shows the morphologies of the specimens charged at 2 mA/cm² for 24 hours and immersed for different periods. It is obvious that both density and size of pits

increase as the immersion time increases.

Table 7-1. The change in the pitting initiation time with the charging current density. The charging time is 24 hours.

Charging Current Density	Initiation Time
Uncharged	> 6 days
0.1 mA/cm ²	~ 70 minutes
2 mA/cm ²	< 2 minutes

Figure 7-3 shows the pitting morphologies of specimens charged at different current densities, after immersion of 20 minutes. These micrographs clearly reflect the promoting effects of hydrogen on pitting susceptibility. Both pit density and pit size of the specimen charged at 2 mA/cm² were much higher than those charged at 0.5 mA/cm². Most of the pits were very shallow. Pit overlaps were observed when pit density was very high as shown in Figure 7-3 (c). It was found that numerous pits initiated around nonmetallic inclusions (mainly sulfide) and precipitates (such as aluminum nitride). EDS was used to identify the inclusions and precipitates.

Figure 7-4 presents the changes in pit density with immersion time. It shows that an increase in hydrogen charging current density leads to an increase in pit density. The

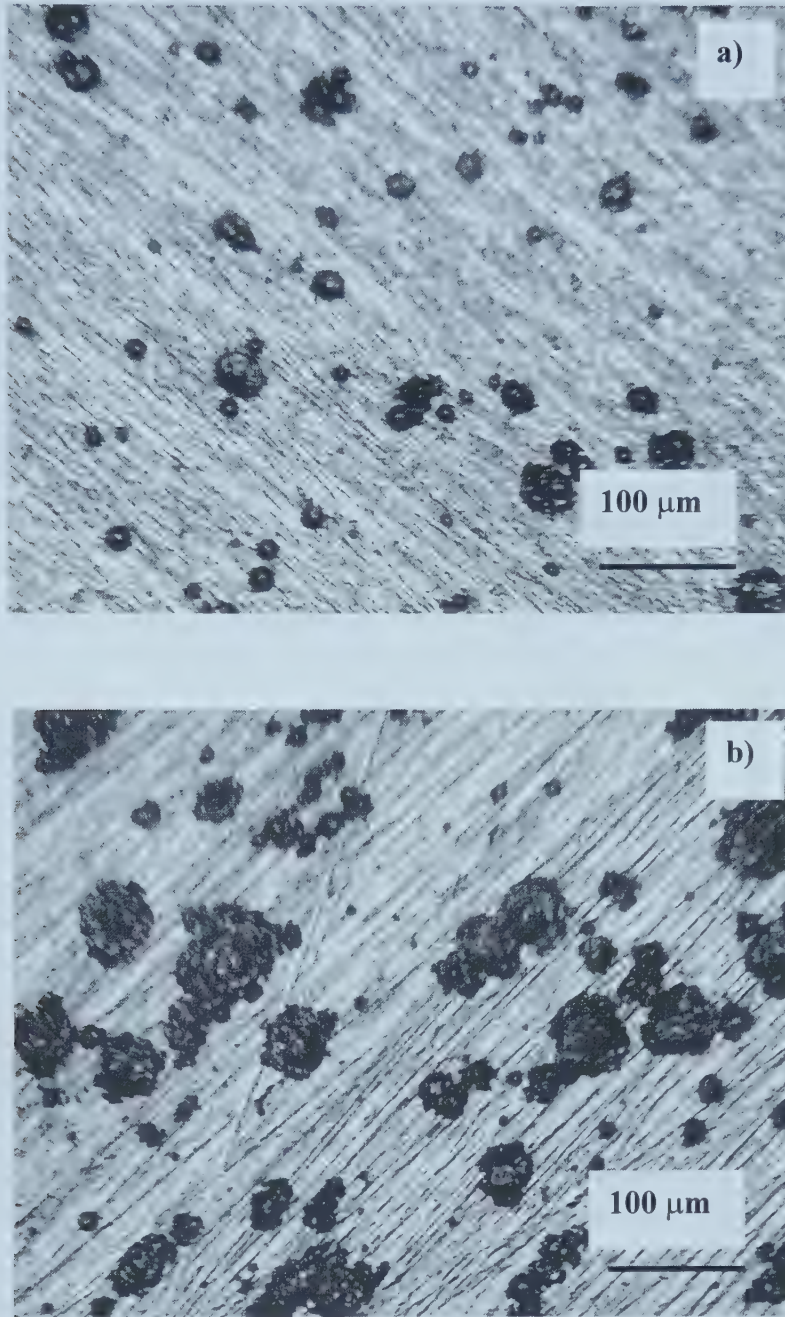


Figure 7-2 --- continued.

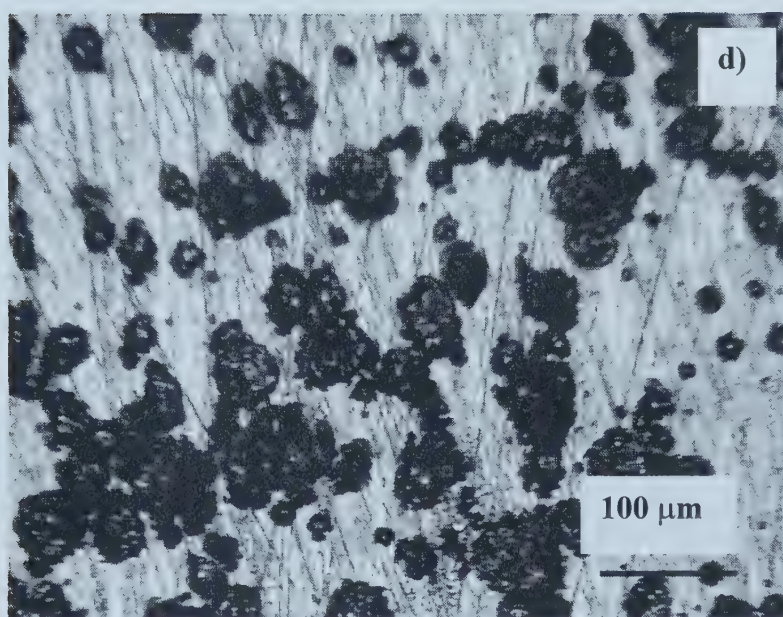
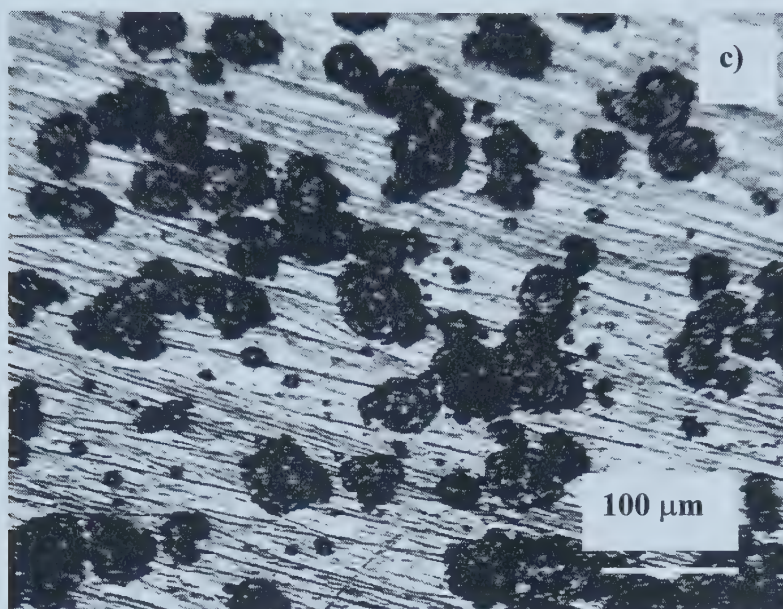


Figure 7-2. The morphologies of the 310 specimens after immersion for different periods in 6% FeCl_3 solution: a) after immersion for 5 minutes, b) after 20 minutes, c) after 60 minutes and d) after 100 minutes. The specimens were charged at 2 mA/cm^2 for 24 hours.

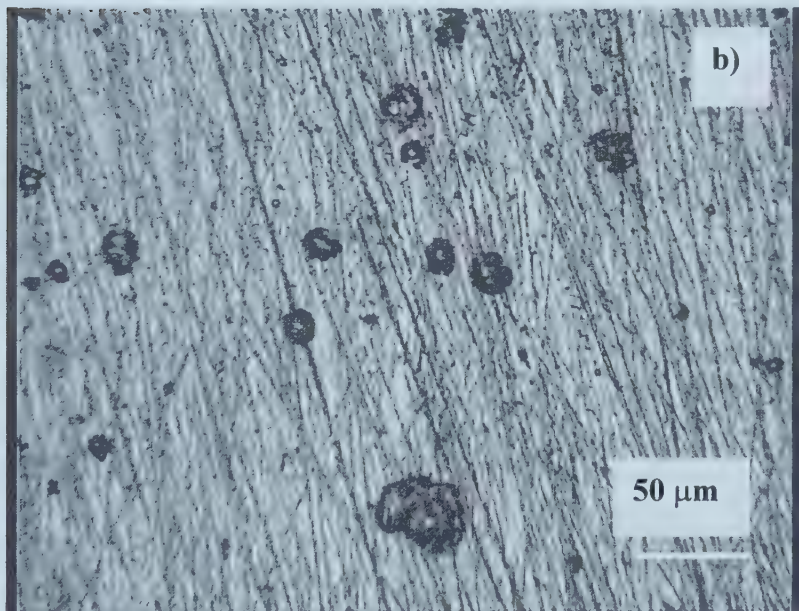
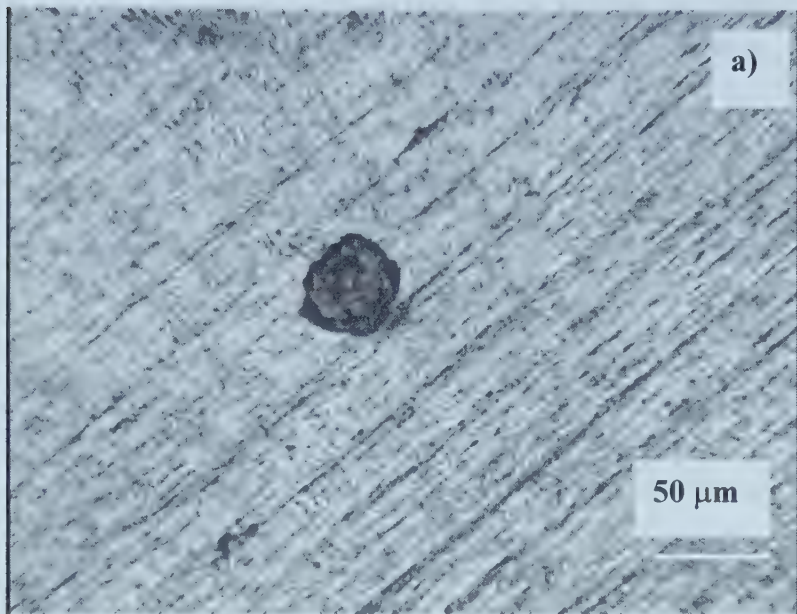


Figure 7-3 --- continued.

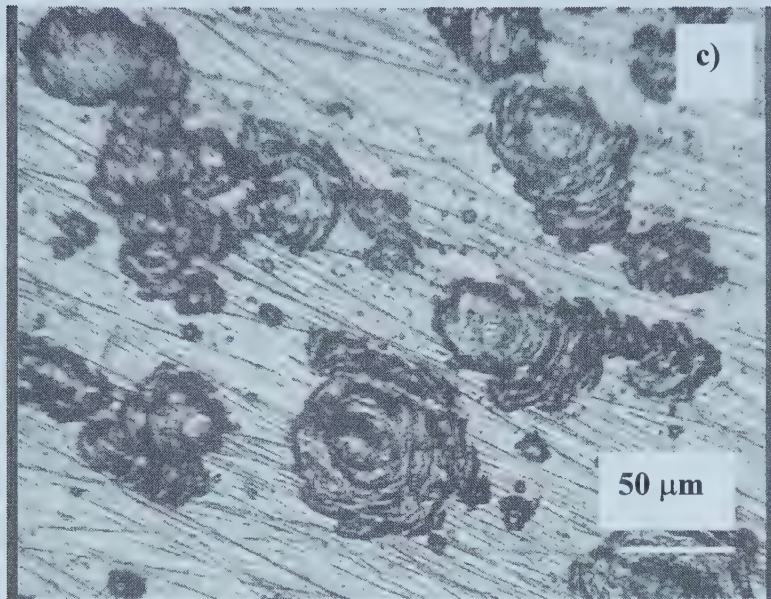


Figure 7-3. Pitting morphologies for the specimens charged at: (a) 0.1 mA/cm², after 80 minutes of immersion; (b) 0.5 mA/cm², after 20 minutes of immersion; (c) 2 mA/cm², after 20 minutes of immersion. The charging time is 24 hours.

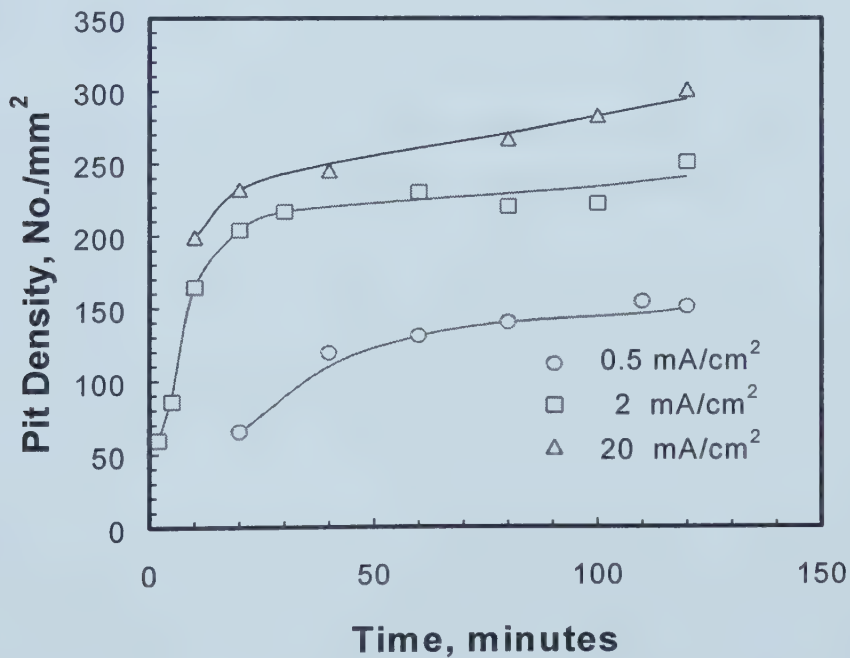


Figure 7-4. Pit density vs. immersion time. The charging time is 24 hours.

pit density for the specimen charged at 20 mA/cm^2 was the highest while the pit density of the specimen charged at 0.5 mA/cm^2 was the lowest among the specimens charged at three different charging current densities. In an 80 minute immersion test, the pit densities for the specimens charged at 0.5, 2 and 20 mA/cm^2 were 140, 220 and $267/\text{mm}^2$, respectively, while for the specimen charged at 0.1 mA/cm^2 the pit density was only $2.9/\text{cm}^2$ after 72 hours of immersion. It was also found that pit density increased with immersion time. The pit density increased rapidly during the first 10 minutes of the immersion test, then the pit density increased slowly. However, the pits were still developing.

7.1.2.2. Effects of Hydrogen on Pit Growth

Hydrogen promotes not only pit initiation but also pit growth. Figure 7-5 shows histogram plots of pit size distribution of specimens charged at 2 mA/cm^2 after being immersed for different immersion periods. The pits are distributed at different surface sites with percentages of pits low at the small and large size ends of the plots but high in the middle. The contours are skewed bell-shaped. The maximum percentage appears at a certain pit size for each immersion time. It can be observed that the pit size corresponding to the maximum percentage increases with the immersion time. If Figure 7-5 is transformed to the percentage of pits with the size $< X$ vs. X plots (Figure 7-6), it becomes easy to observe the effect of immersion time on pit size. The dotted line corresponds to a percentage of 50%. The X values of the interceptions between this dotted line and experimental curves increase with the immersion time, which indicates that pits tend to grow to large sizes with an increase in immersion time.

Figure 7-7 shows the pit size distribution histogram plots together with fitted curves for 0.5, 2 and 20 mA/cm^2 charged specimens, after 20 minutes of exposure. The pit diameter corresponding to the peak of the fitted curve increased with the hydrogen charging current density. It shifted from about $30 \mu\text{m}$ for the specimens charged at 0.5 mA/cm^2 to $55 \mu\text{m}$ for the specimens charged at 20 mA/cm^2 . Figure 7-8

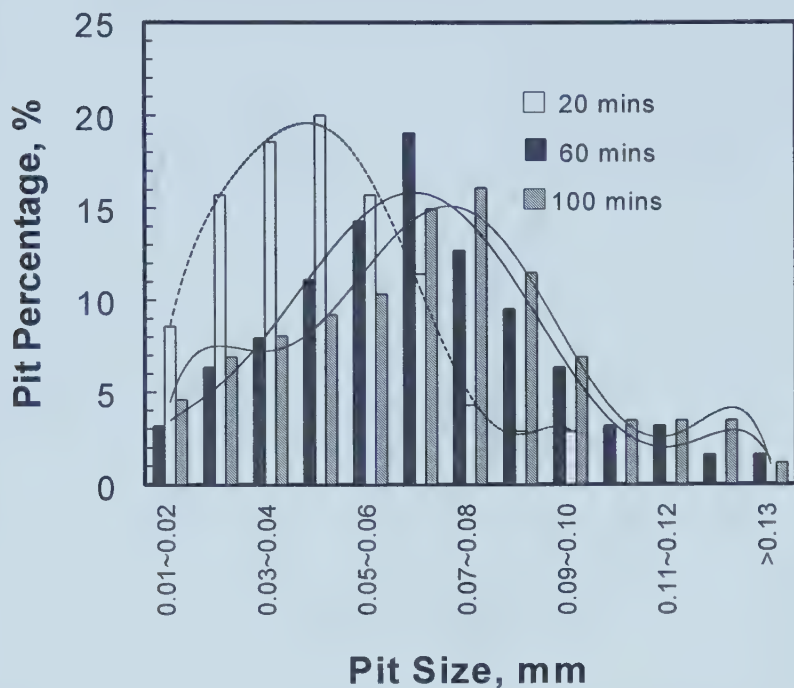


Figure 7-5. The histogram plots of pit size distribution of the 310 specimens charged at 2 mA/cm^2 for 24 hours after being immersed for different immersion periods.

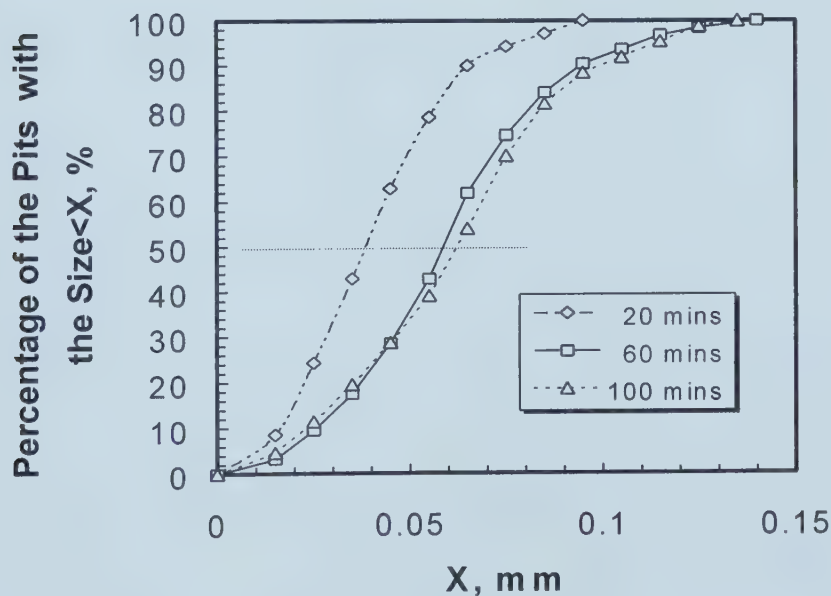


Figure 7-6. The percentage of pits with a size $< X$ vs. X plots of the 310 specimens charged at 2 mA/cm^2 for 24 hours after being immersed for different immersion periods.

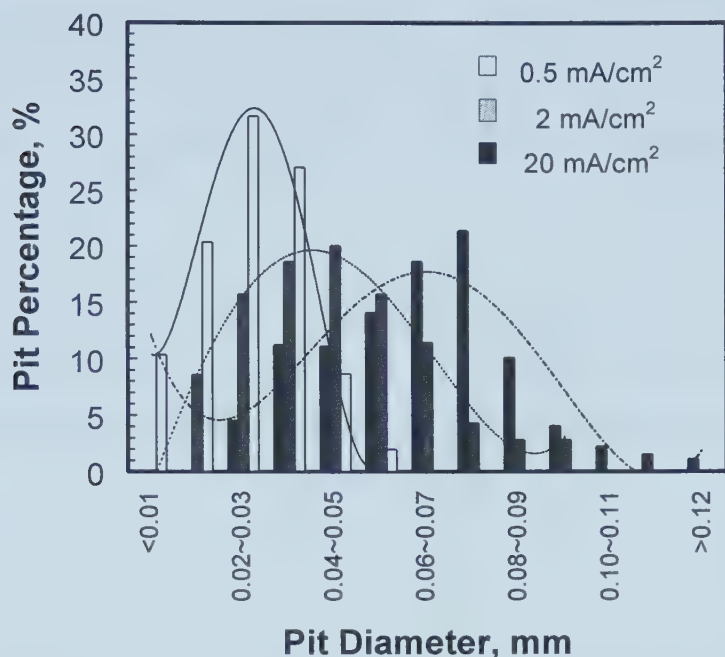


Figure 7-7. Pit diameter distribution histogram plots for the charged 310 specimens after 20 minutes of immersion. Solid and dashed lines are fitted curves. The charging time is 24 hours.

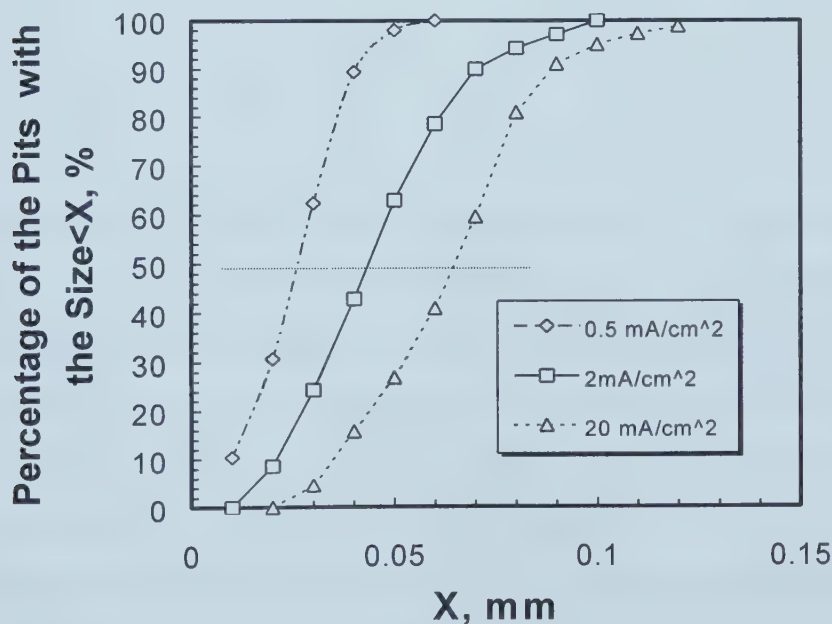


Figure 7-8. The percentage of pits with a size $< X$ vs. X plots of the 310 specimens charged at different current densities for 24 hours after being immersed for 20 minutes.

presents the percentage of pits with the size $< X$ vs X curves for the different charged specimens. Similar to Figure 7-6, the dotted line corresponds to the percentage of 50%. The X values of interceptions between this dotted line and experimental curves increase with the charging current densities, which indicates that hydrogen promotes the pit growth.

Figure 7-9 shows the change in the average pit diameter (D_a) with immersion time. The arithmetic mean method was used to get the average pit diameter value. D_a increased linearly with the logarithm of immersion time. This linear relation can be expressed as:

$$D_a = \alpha_D \ln t + \beta_D \quad [7-3]$$

where t is the immersion time, α_D and β_D are the constants which are related to the film properties, solution and temperature.

From Equation [7-3], the pit radial growth rate R_p can be derived as:

$$R_p = \frac{dD_a}{dt} = \frac{\alpha_D}{t} \quad [7-4]$$

R_p is proportional to the reciprocal of the immersion time. At a given exposure time, the larger the constant α_D , the higher the pit radial growth rate. Therefore the change in the constant α_D can be used to evaluate the effect of hydrogen on pit growth. The equations for the fitted lines are presented in Figure 7-9. The values of α_D are 9.587, 11.013 and 12.35, respectively, for the 0.5, 2 and 20 mA/cm² charged specimens. The fact that hydrogen increases the α_D value indicates that hydrogen can promote pit growth. R-squared values are also presented in Figure 7-9. The R-square values in this case are very close to 1, which indicates a good fit.

The apparent percentage of the surface area occupied by pits (A_p) can also reflect the

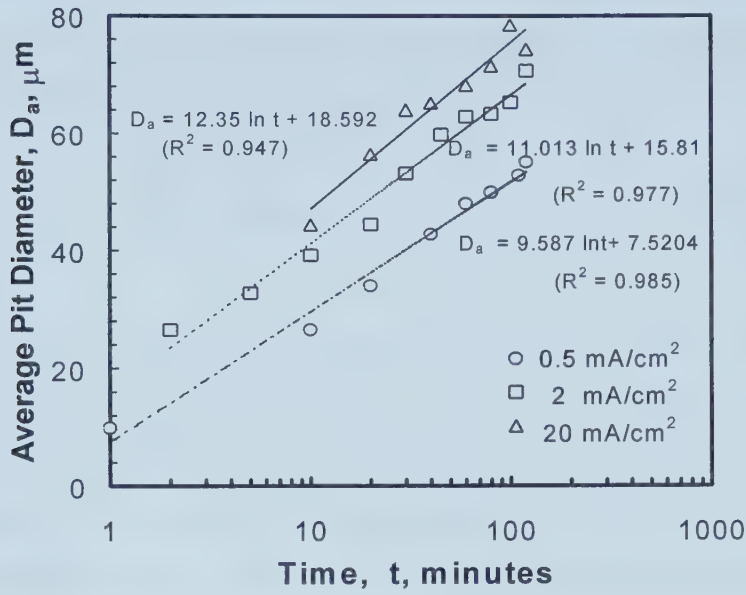


Figure 7-9. The change in average pit diameter with immersion time. The R-squared values for the best-fit lines are given in the brackets.

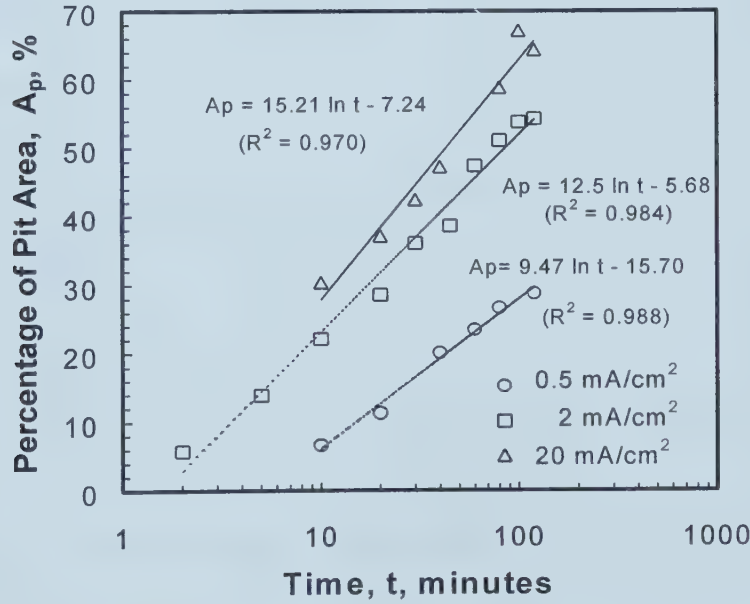


Figure 7-10. The change in the percentage of apparent pit area with immersion time. The R-squared values for the best-fit lines are given in the brackets.

pitting susceptibility. Figure 7-10 shows the change in A_p with immersion time. Similar to the average pit diameter, the apparent area percentage of pits increased linearly with the logarithm of immersion time:

$$A_p = \alpha_p \ln t + \beta_p \quad [7-5]$$

where α_p and β_p are the constants. The constant α_p increased with an increase in hydrogen charging current density. It increased from 9.47 to 15.21 when the charging density increased from 0.5 to 20 mA/cm². At the same exposure time the A_p for the specimens charged at higher current densities is larger than that for those charged at lower current densities. This reinforces the conclusion that hydrogen accelerates pit growth.

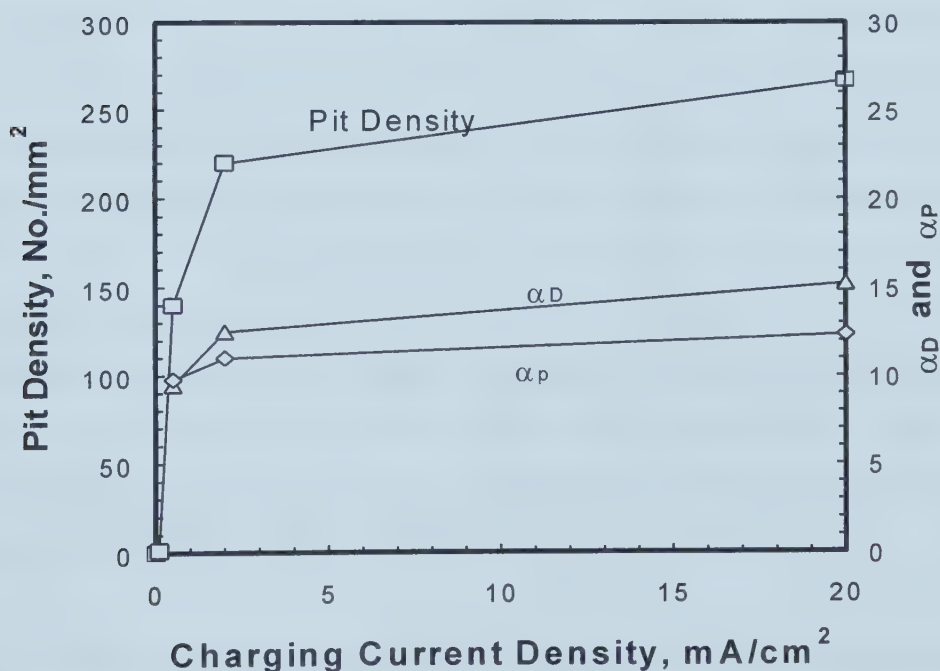


Figure 7-11. Changes in the pit density, α_D and α_p with hydrogen charging current densities, after 120 minutes of immersion.

The change in pit density, α_d , and α_p with hydrogen charging current density are shown in Figure 7-11. It was found that an increase in hydrogen content could affect the pitting susceptibility greatly when hydrogen charging current density was lower than 2 mA/cm². When hydrogen charging current density was higher than 2 mA/cm², the effect of hydrogen on pitting corrosion reached a relatively stable value.

7.1.2.3. Effects of Inclusions on the Pitting Corrosion

From the above results, it is found that pits prefer to initiate around inclusions. Upon pickling the surface in HNO₃-HF solution, a marked reduction of inclusions, such as (Mn, S) inclusions, can be observed.⁵ The surfaces of some specimens were chemically treated in 10% HNO₃ + 2% HF pickling solution for 20 minutes at 50 °C. The number of inclusions was counted by optical microscopy. In order to make the optical microscopic observation easier, the surface was electrochemically polished by applying a constant current density of 780 mA/cm² for 5 minutes in 37% H₃PO₄ + 56% glycerin + 7% H₂O solution at 110°C before pickling. Small holes left on the surface due to the dissolution of inclusions during pickling look dark and make the counting the number of inclusions difficult. Therefore, after pickling, the surface was slightly electrochemically polished (for 1 minute) to remove the holes. Figure 7-12 shows the effect of pickling on the reduction in inclusions. It is clear that pickling can greatly reduce the number of inclusions on the surface. The density of inclusions decreases from 304/mm² for the unpickled specimens to 161/mm² for the pickled ones. Electrochemical polishing was only applied to the specimens for the inclusion number counting.

After pickling, some of the specimens were charged with hydrogen and were then immersed in 6% FeCl₃ solution. The procedure was the same as the previous section. Figure 7-13 shows the changes in pit density with immersion time for both unpickled and pickled specimens, hydrogen charged at 2 mA/cm² for 24 hours. At any immersion time, the pit densities for the pickled specimens were always much lower than those for the unpickled ones. After immersion for 120 minutes, the pit density for the

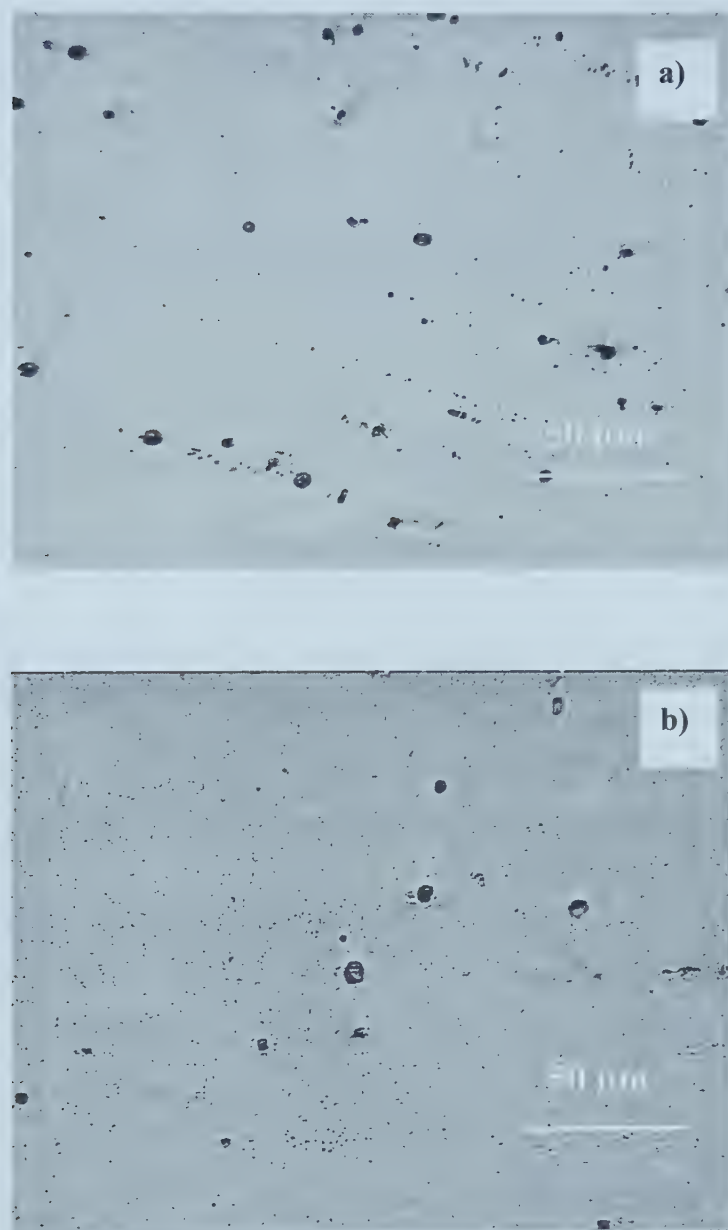


Figure 7-12. The effects of pickling on the density of inclusions on the surface: a) unpickled specimen and b) specimen pickled in 10% HNO_3 + 2% HF for 10 minutes at 50 °C.

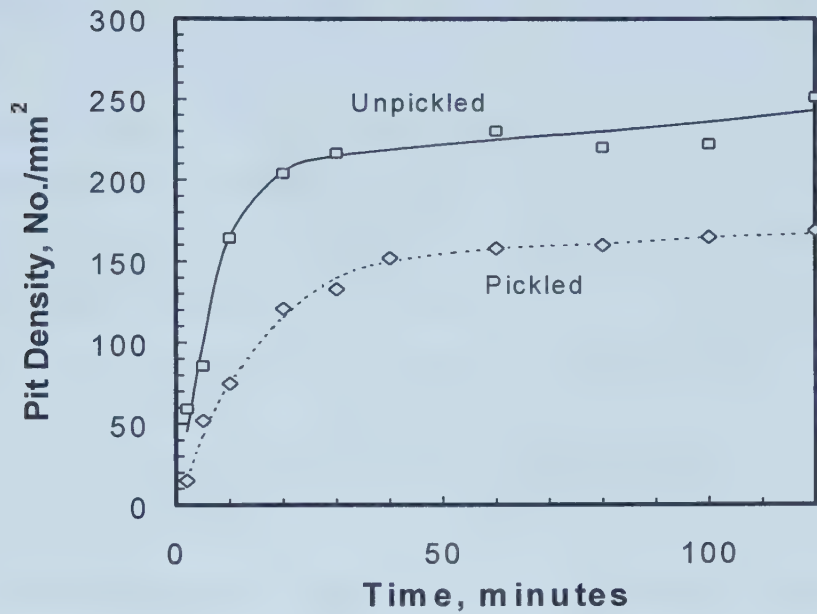


Figure 7-13. Pit density vs. immersion time of the unpickled and pickled 310 specimens charged at 2 mA/cm² for 24 hours.

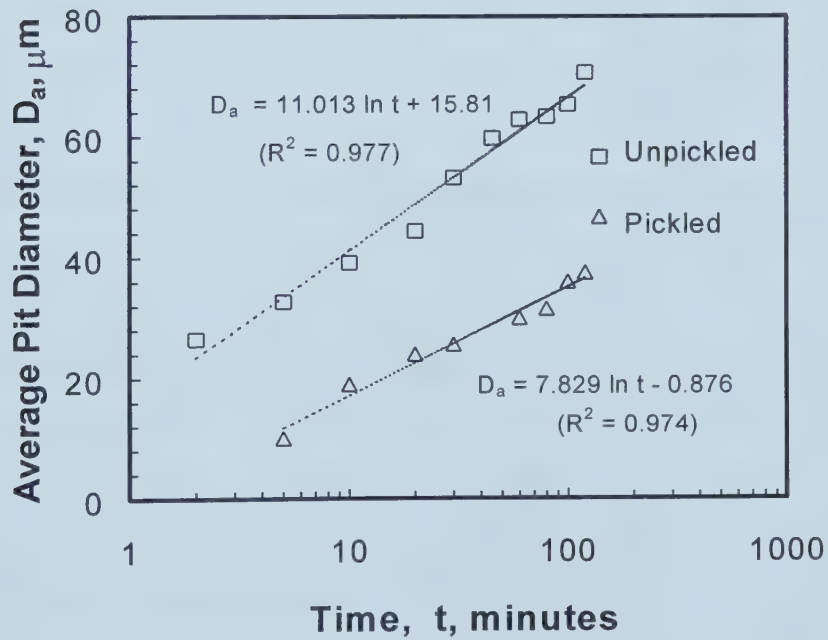


Figure 7-14. Change in the average pit diameter with immersion time for the pickled and unpickled 310 specimens charged at 2 mA/cm² for 24 hours. The R-squared values for the best-fit lines are given in the brackets.

unpickled one was $248/\text{mm}^2$ while it was $170/\text{mm}^2$ for the pickled specimen. Figure 7-14 shows the change in the average pit diameters with immersion time, for the unpickled and pickled specimens charged at $2 \text{ mA}/\text{cm}^2$. The average pit diameter of specimens, increases linearly with immersion time, with a slope ($7.829 \text{ }\mu\text{m}$) for the pickled specimens lower than that for the unpickled ones ($11.013 \text{ }\mu\text{m}$). These results show that pickling reduces the pit initiation sites and the pit growth rate. The surface morphologies of the pickled specimens after the immersion test are shown in Figure 7-15. Even after pickling, some pits are still found to initiate at the sites of inclusions.

7.1.3. Results of Immersion Tests of 304 Stainless Steel

Immersion tests were carried out in 6% FeCl_3 solution at room temperature. Some of the specimens were charged with hydrogen at various current densities for 2 hours. Specimens were removed from the solution after exposure for 30 minutes and it was found that the uncharged specimen had the lowest pit density ($2.07/\text{cm}^2$). With an increase in charging current density, the pit density had an obvious increase. The pit density increased to $792/\text{mm}^2$ for the specimen charged at $2 \text{ mA}/\text{cm}^2$ for 2 hours. Compared with the results for 310 SS, even though the charging time is much shorter in this case, the pit density is higher for 304 SS. This clearly indicates that for the specimens charged with hydrogen, 310 SS has a lower pitting susceptibility than 304 SS.

It appeared that 6% FeCl_3 solution was too aggressive for the 304 SS so a less aggressive solution (3.5% NaCl + 1% FeCl_3) was used. The specimens were charged at different current densities for 16 hours, and were then exposed to the solution for 2 hours. The change in pit density with the charging current density is shown in Figure 7-16. The pit density increased with the charging current density. The pit density increased rapidly when the charging current density was less than $2 \text{ mA}/\text{cm}^2$.

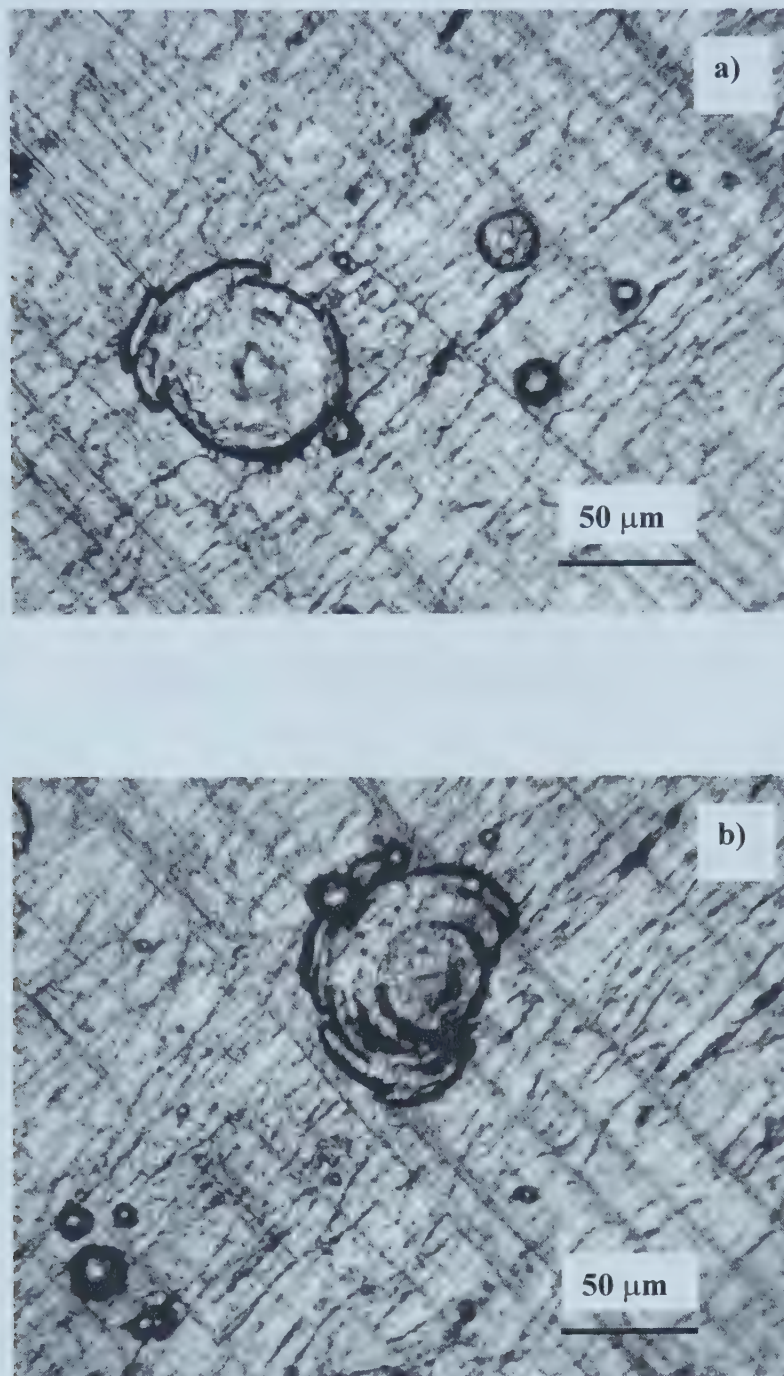


Figure 7-15. The surface morphology of the pickled 310 specimen which was charged at 2 mA/cm^2 for 24 hours. The specimen was immersed in 6% FeCl_3 solution for 80 minutes.

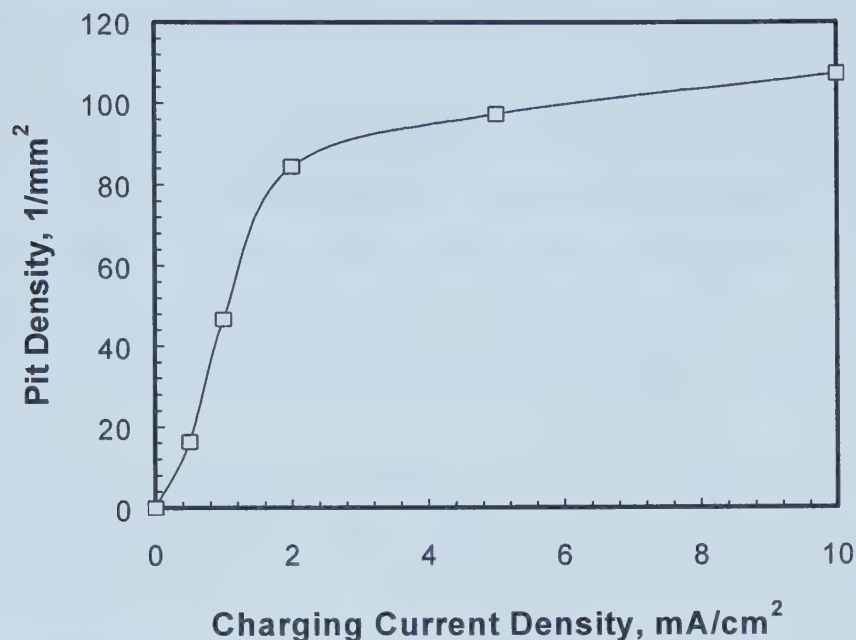


Figure 7-16. The pit density vs. charging current density plot. The 304 stainless steel samples were hydrogen charged at different current densities for 16 hours, then immersed in 3.5 % NaCl + 1% FeCl₃ solution for 2 hours.

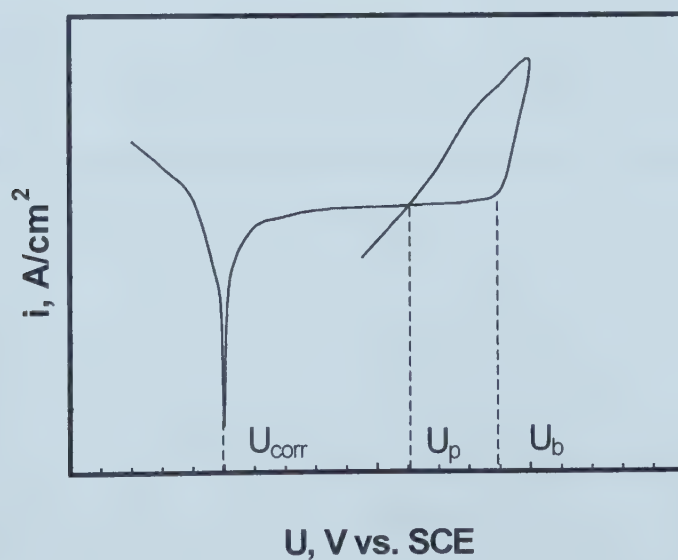


Figure 7-17. The schematic representation of the cyclic potentiodynamic polarization curve.

7.2. STATISTICAL INVESTIGATIONS OF EFFECTS OF HYDROGEN ON PITTING, PROTECTION AND CORROSION POTENTIALS

Two pitting parameters are determined from a cyclic potentiodynamic polarization curve (Figure 7-17): pitting potential U_b and protection potential U_p . U_b denotes the potential at which pits initiate on the forward scan so that the current increases abruptly. U_p is the potential at which the pits are repassivated during the reverse scan, at which point the current goes below the passive current values of the forward scan.

It is generally accepted that pitting will be initiated very rapidly when the potential is above U_b . If the potential is more negative than U_p , pre-existing pits will repassivate and stop growing.⁶ When the potential is between U_b and U_p (metastable pitting stage), existing pits may grow but new pits cannot initiate.

It has been recognized that the scattering of corrosion data, especially for localized corrosion cannot be avoided. For quantitative analysis, it is important to estimate reliable parameters by means of a statistical approach.^{7,8}

The cyclic potentiodynamic polarization (CPP) technique is widely used for examining the pitting susceptibility. Specimens of Type 304 stainless steel were charged at various current densities for 30 minutes. Measurements were performed in a borate buffer solution containing 200 ppm NaCl at 22°C.

7.2.1. Results

Figures 7-18, 7-19 and 7-20 present the distribution plots of pitting, protection and corrosion potentials on normal probability paper. Very good straight

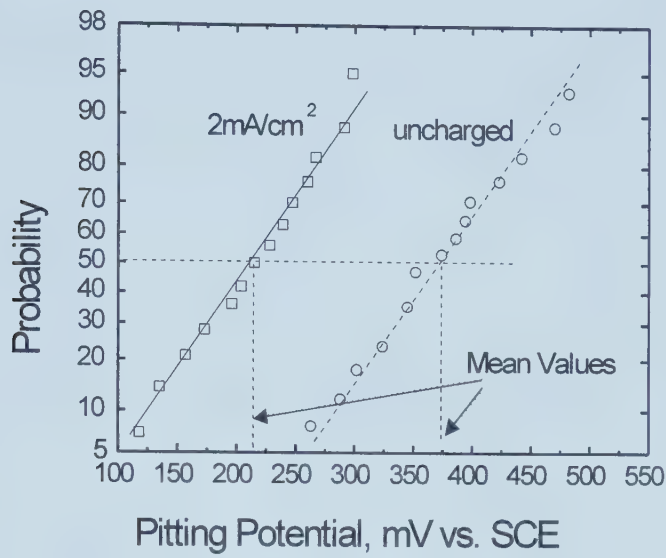


Figure 7-18. The normal distribution plots of pitting potentials for the charged and uncharged 304 samples. The charging time was 30 minutes.

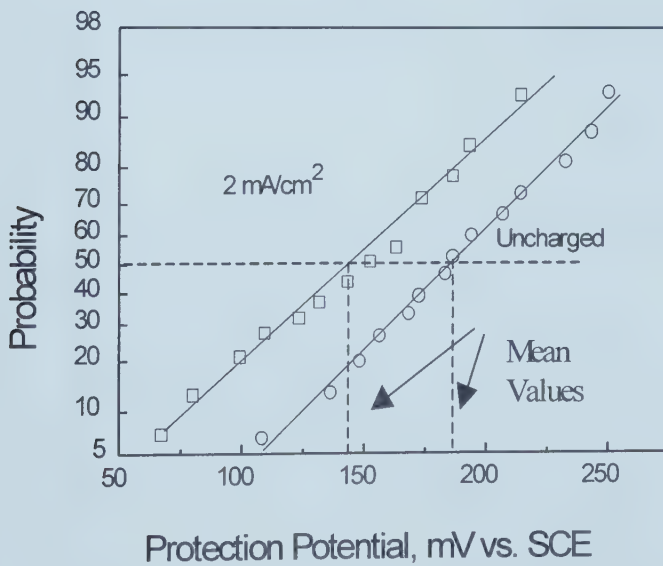


Figure 7-19. The normal distribution plots of protection potential for the charged and uncharged 304 specimens. The charging time was 30 minutes.

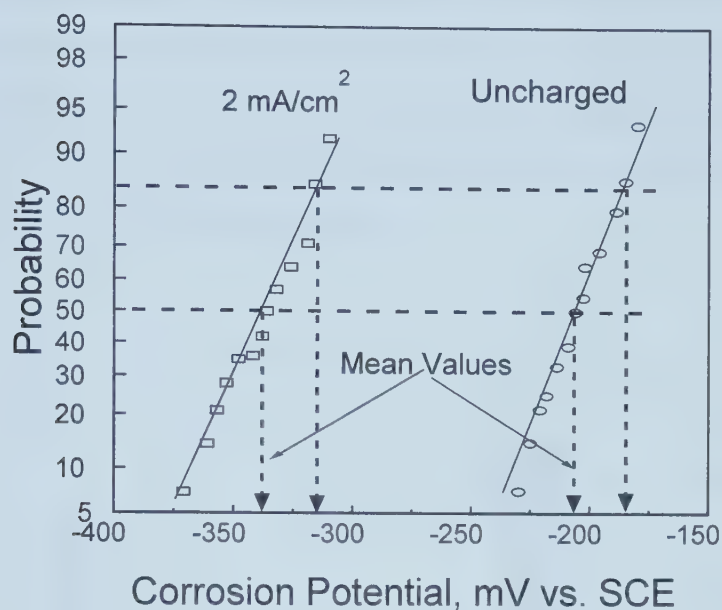


Figure 7-20. The normal distribution plots of corrosion potential for the uncharged and charged 304 specimens. The charging time was 30 minutes.

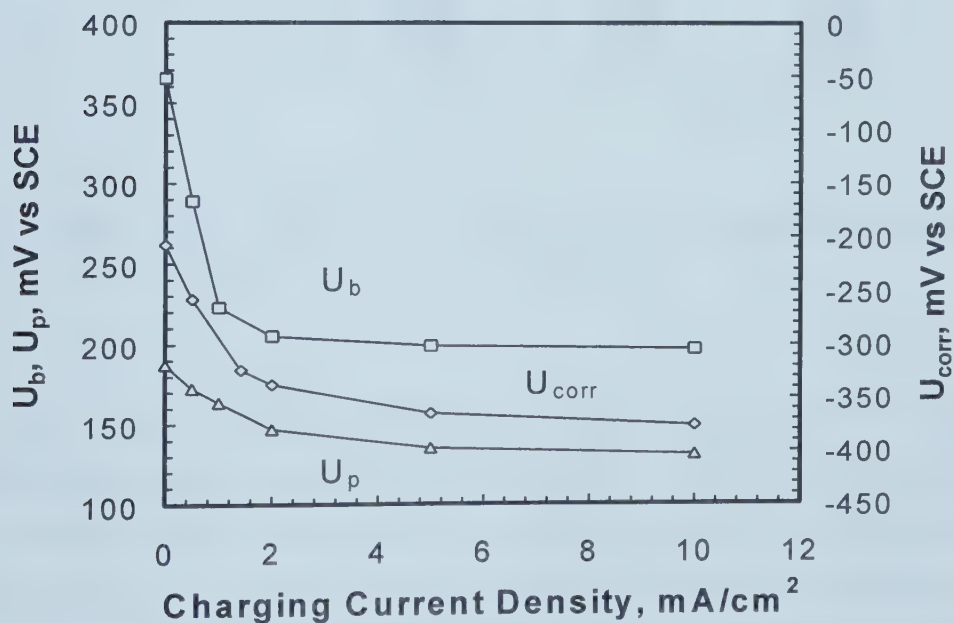


Figure 7-21. The changes in breakdown, protection and corrosion potentials with charging current density. The charging time was 30 minutes.

lines were fitted for each potential. It can be concluded that corrosion, pitting and protection potentials obey a normal distribution. The mean and standard deviation values can be estimated by drawing 50% and 84% lines.⁹ The intersections of the curves and the 50% line correspond to the mean values of the potentials. Furthermore the standard deviation of the specimens is approximately equal to the potential difference between the intersections with the 50% and 84% lines.

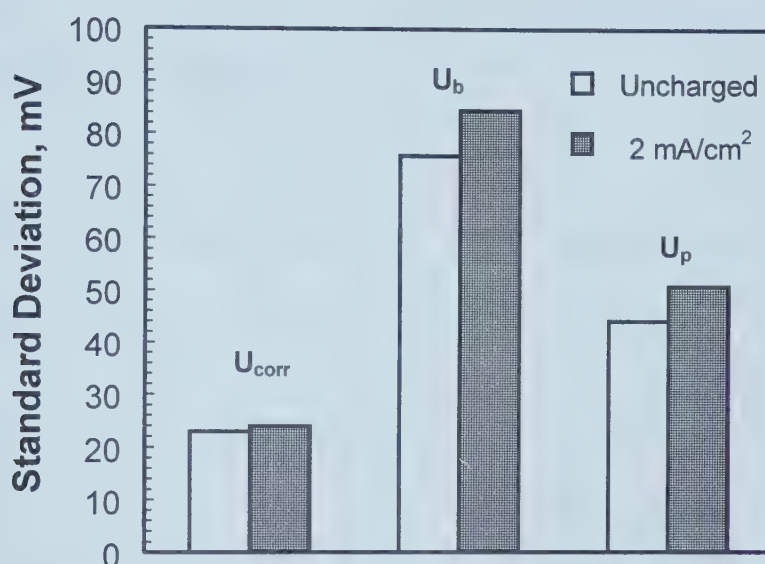


Figure 7-22. The effect of hydrogen on the standard deviation of corrosion, breakdown and protection potentials.

The changes in pitting, protection and corrosion potentials with charging current density are shown in Figure 7-21. From these plots, it is obvious that hydrogen decreases the corrosion, pitting and protection potentials. The shift of pitting and protection potential in the less noble direction indicates the hydrogen promotion of pitting susceptibility. Figure 7-22 presents the standard deviations of each set of potential data. The pitting potential data are more scattered than the protection potential while the corrosion potential is more reproducible. It seems that hydrogen can increase the standard deviation values. However, since the difference between the uncharged and charged

specimens is small, it was necessary to check whether the two normal distributions have the same variance. Table 7-2 presents the results of the hypothesis $\sigma_H^2 = \sigma_{NH}^2$ against the alternative $\sigma_H^2 > \sigma_{NH}^2$. The σ_H^2 and σ_{NH}^2 values represent the potential variances of the specimens charged at 2 mA/cm² and the uncharged specimens, respectively. s_H^2 and s_{NH}^2 represent the corresponding computed variances. The chosen significance level was $\alpha = 5\%$. c was determined according to the equation $P(v=c) = 1-\alpha$ and a Table of the F-distribution with (n_1-1, n_2-1) degrees of freedom. In our cases $n_1=n_2=15$, and correspondingly, $c=2.49$. The calculation results proved that hydrogen had no obvious effect on the three potential variances.

Table 7-2. Test of the Hypothesis $\sigma_H^2 = \sigma_{NH}^2$ against the Alternative $\sigma_H^2 > \sigma_{NH}^2$

Specimens	U_b		U_p		U_{corr}	
Computed Variance	S_H^2	S_{NH}^2	S_H^2	S_{NH}^2	S_H^2	S_{NH}^2
	7140.25	5745.64	2580.64	1944.81	571.21	524.41
$v_O = S_H^2 / S_{NH}^2$	1.243		1.327		1.089	
Results	$v_O < c$, accept the hypothesis		$v_O < c$, accept the hypothesis		$v_O < c$, accept the hypothesis	

7.3. CRITICAL CONCENTRATION OF CHLORIDE IONS FOR FILM BREAKDOWN

The potentiostatic measurements were used to study the effect of hydrogen on the stability of passive films. A constant potential vs. SCE was applied to the charged and uncharged specimens in the chloride ion free borate buffer solution. After passivation for 10 minutes, NaCl at various concentrations was added to the solution. The current

responses to the application of a constant potential and addition of chloride ions were recorded. The total testing time was 3600 seconds and the sampling interval was 1 point per second.

7.3.1. Current Responses of Uncharged Specimens

Figure 7-23 shows the current responses of the uncharged specimens to the application of a potential of 0.3 V vs. SCE and addition of chloride ions. The application of the potential leads to current decay before the chloride ions are added to the solution. This current decay indicates that the surface is passivated. The addition of chloride ions does not interrupt the current decay when the concentration of chloride ions is lower than 3250 ppm. When the concentration of chloride ions reaches 4000 ppm, the addition of chloride ions obviously affects the current response. The current begins to increase instead of decrease and the anodic current noise transients can be observed.

The details of the anodic current noise transients are shown in Figure 7-24. The current transients have the familiar shape of a relatively slow rise and a rapid current decrease. The relatively slow current increase is the result of the adsorption of chloride ions on passive films leading to film rupture and the resulting rapid current decrease indicates the repassivation after pit initiation.¹⁰ This current increase and the appearance of current noise transients are due to the breakdown of passive films. The current then increases rapidly to a high level due to stable pit growth. From the curve, it can be observed that the stable pit growth stage comes earlier when the concentration of chloride ions is higher. Also, the current density at this stage is higher with a higher concentration of chloride ions. The very important point is that, from the curve, there is a critical concentration of chloride ions for the breakdown of a passive film. For the uncharged specimens, this concentration lies in the range of 3250 - 4000 ppm.

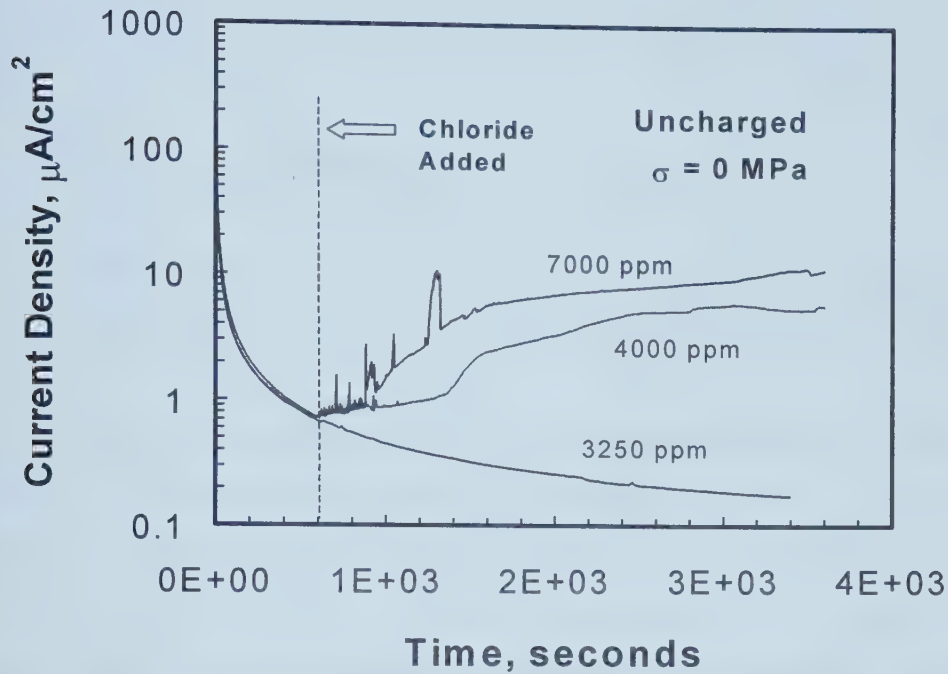


Figure 7-23. The current responses of unstressed and uncharged 304 specimens to the application of a potential of 0.3 V vs. SCE and additions of chloride ions of different concentrations.

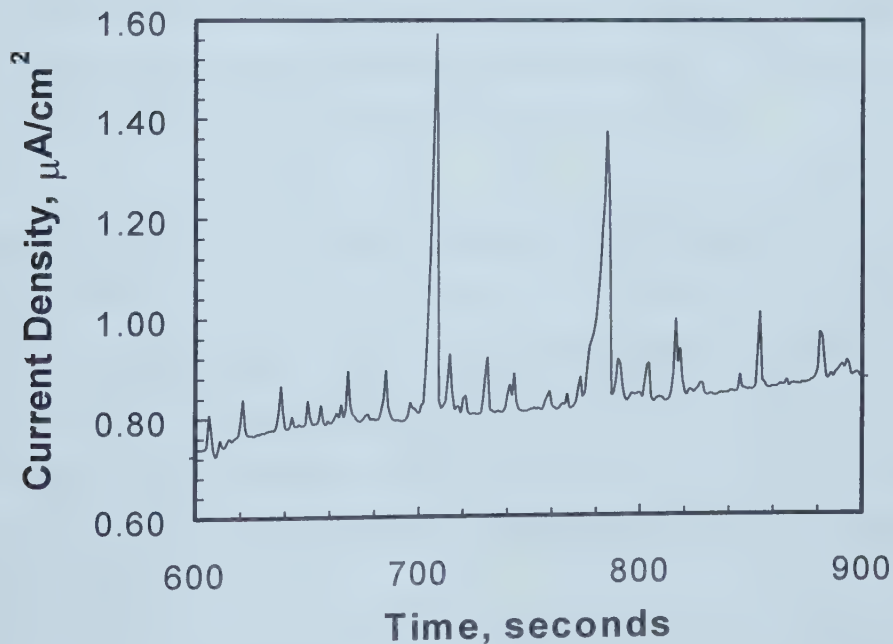


Figure 7-24. The details of the current transients of the uncharged and unstressed 304 specimens that appeared due to the addition of 4000 ppm chloride ions during the application of a potential of 0.3 V vs. SCE.

7.3.2. Effects of Hydrogen on Breakdown of the Passive Films

7.3.2.1. Current Responses of Charged Specimens

Figure 7-25 shows the current response of the specimens to which a potential of 400 mV vs. SCE was applied. The concentration of chloride ions added was 200 ppm.

There were three different types of current responses after the addition of chloride ions. For the uncharged specimen, the addition of chloride did not interrupt the passivation of the specimen. When hydrogen charging current density reached a certain value, there was an immediate increase in current after the chloride addition. This current increase came from the breakdown of the passive film and subsequent pitting corrosion. For the specimens charged at high current densities, the current tended to increase at first and then remained at quite a high level. The surface could not be repassivated after the breakdown of the passive film. When the charging current density was an intermediate value, the specimen could be passivated after the breakdown of the passive film. These results indicate that hydrogen facilitates the breakdown of the passive film and the subsequent pitting process, and hinders the repassivation process.

Figure 7-26 shows the current responses of specimens to the application of a potential of 300 mV vs. SCE. The concentration of chloride added was 200 ppm. When the charging current density was 0.5 mA/cm^2 , there was a time delay for the anodic current increase after the addition of chloride ions. This time delay can be considered as the initiation time for the breakdown of the passive film. The time delay for the specimen charged at 0.5 mA/cm^2 was 54 seconds. No time delay was observed for the specimens charged at 5 mA/cm^2 .

7.3.2.2. Effects of Concentration of Chloride Ions on Breakdown of Passive Films

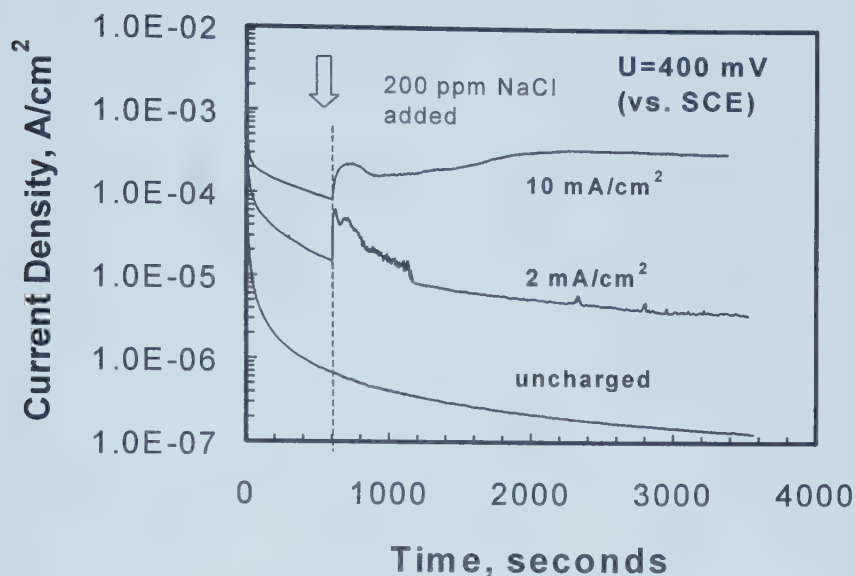


Figure 7-25. The current responses of the uncharged and charged 304 SS specimens to the application of a constant potential. The charging time was 30 minutes. The samples were passivated at 400 mV in the borate buffer solution for 10 minutes, followed by addition of 200 ppm NaCl.

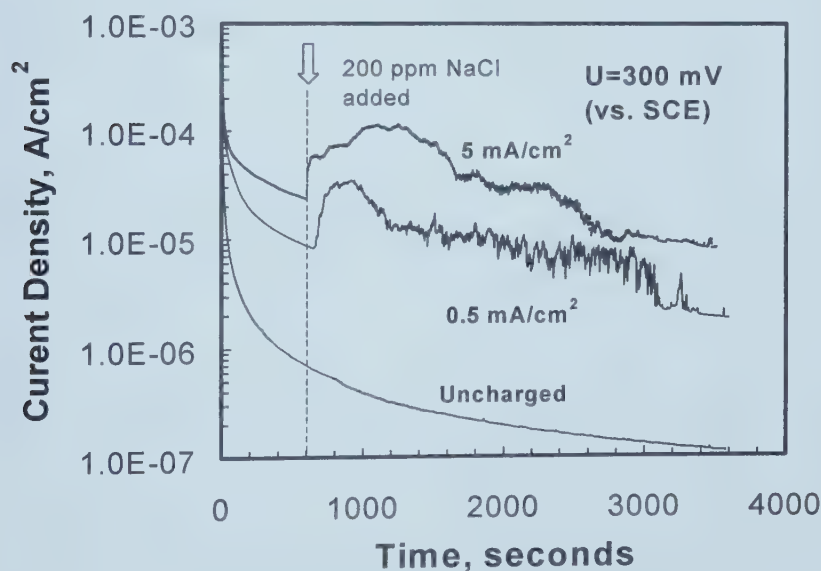


Figure 7-26. The current responses of the uncharged and charged 304 SS specimens to the application of a constant potential. The charging time was 30 minutes. The specimens were passivated at 300 mV in the borate buffer solution for 10 minutes, followed by addition of 200 ppm NaCl.

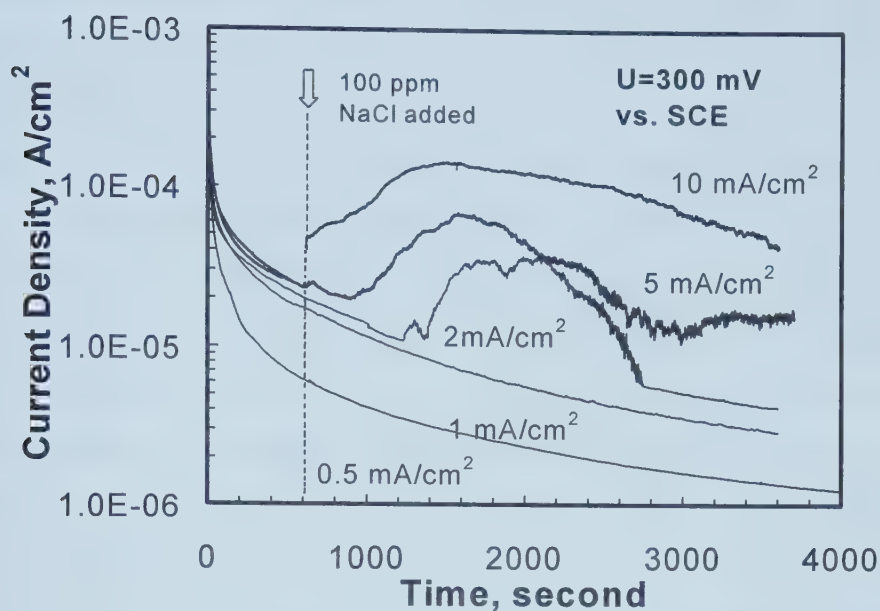


Figure 7-27. The current responses of the charged 304 SS specimens to the application of a potential of 0.3 V vs. SCE. The charging time was 30 minutes. The specimens were passivated at 300 mV vs. SCE in the borate buffer solution for 10 minutes, then 100 ppm NaCl was added to the solution.

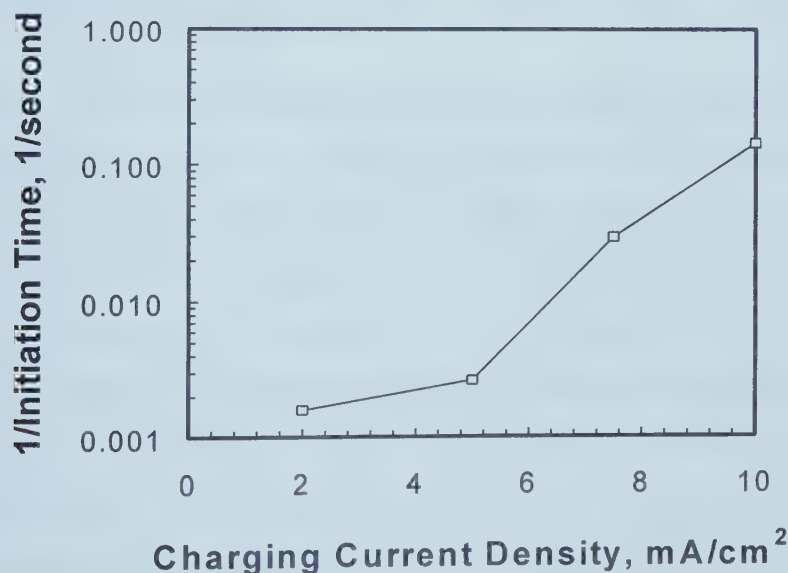


Figure 7-28. The reciprocal of initiation time for film breakdown vs. charging current density. The 304 SS specimens were charged at different charging current densities for 30 minutes, and then a constant potential of 300 mV was applied for 1 hour in the borate buffer solution. 100 ppm of NaCl was added into the solution 10 minutes after the beginning of the application of the potential.

To clearly observe the effect of concentration of chloride ions on the film breakdown, the current responses of the specimens to the application of a potential of 300 mV vs. SCE and the addition of NaCl of 100 ppm were recorded. The results are shown in Figure 7-27. No breakdown of passive film was observed when the charging current density was lower than 2 mA/cm^2 , while breakdown of passive film was observed on the specimen charged at 0.5 mA/cm^2 if the concentration of chloride was 200 ppm (Figure 7-26). When the charging current density was higher than 2 mA/cm^2 , breakdown of the passive film began after a period of initiation time. The pitting initiation time decreased with an increase in the charging current density. The initiation time after the addition of NaCl for 10 mA/cm^2 charged one was less than 10 seconds (~ 7 seconds) while it was more than 10 minutes for the one charged at 2 mA/cm^2 . When the charging current density is 5 mA/cm^2 , the initiation time is 380 seconds. Comparing Figure 7-26 with Figure 7-27, it is obvious that increase in chloride concentration will promote the film breakdown.

7.3.2.3. Effects of Hydrogen on the Initiation Time and the Critical Concentration of Chloride Ions for Film Breakdown

Figure 7-27 shows that the initiation time for film breakdown decreases with charging current density. The initiation time vs. charging current density curve is shown in Figure 7-28. It could be concluded that hydrogen promotes the breakdown process of passive films. Also from Figure 7-27, it can be observed that there is a critical charging current density for the film breakdown at the experimental conditions. There should be a critical concentration of chloride ions for the film breakdown at each charging condition. To investigate the effect of hydrogen on this critical concentration, the current responses to the additions of various concentrations of chloride ions were measured on specimens charged at various current densities.

Figures 7-29 and 7-30 show the current responses of the specimens charged at 0.5 mA/cm^2 and 2 mA/cm^2 , respectively, to the application of a 300 mV vs. SCE potential. NaCl of various concentrations was added into the solution 10 minutes after the

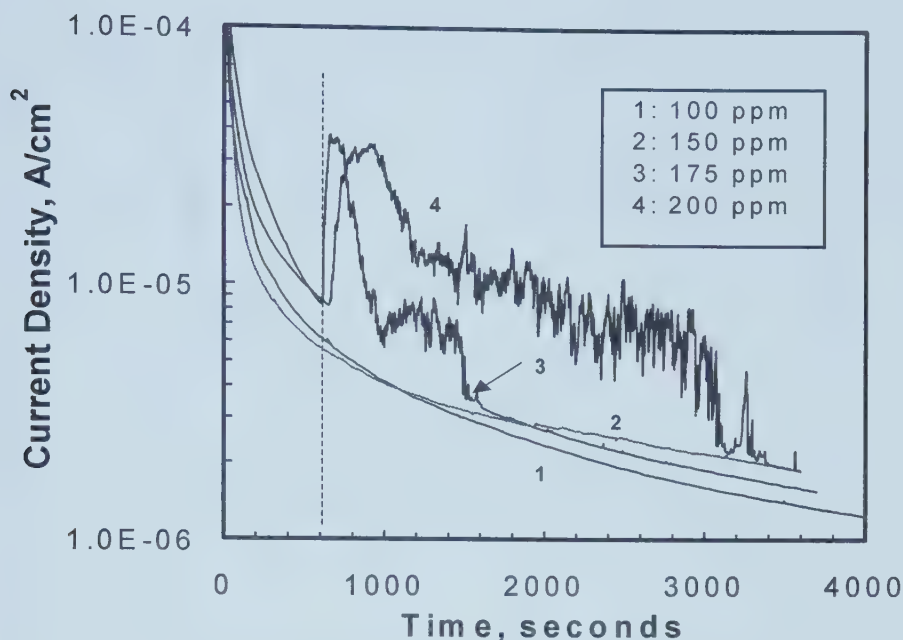


Figure 7-29. The current responses of the 304 SS specimens charged at 0.5 mA/cm^2 for 30 minutes to the application of a constant potential. The specimens were passivated at 300 mV in the borate buffer solution for 10 minutes, then NaCl was added.

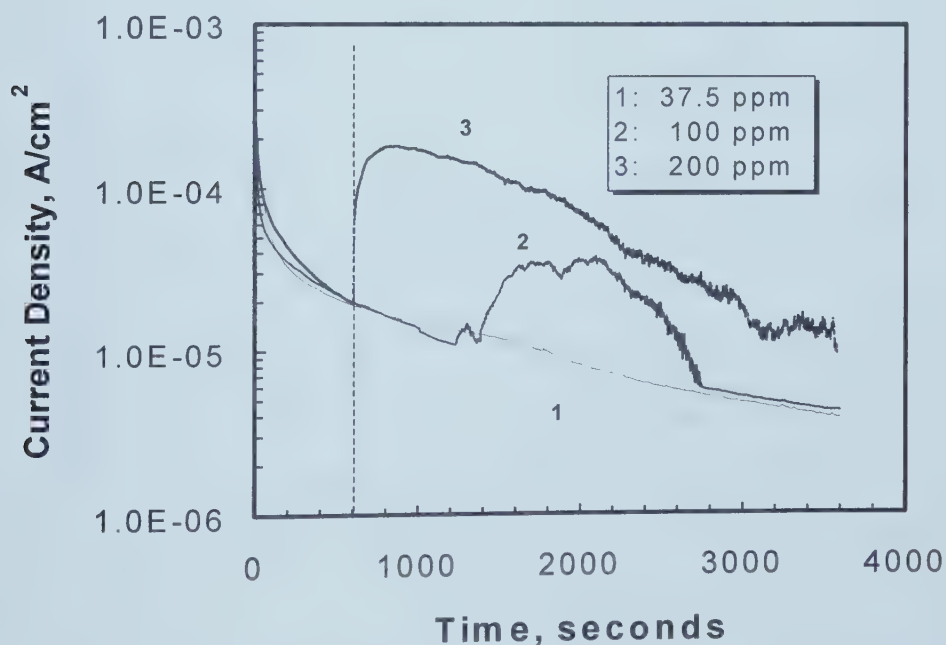


Figure 7-30. The current response to the application of a 300 mV vs. SCE potential on the 2 mA/cm^2 charged 304 SS specimens. The test solution was borate buffer solution. After 10 minutes from the beginning of the measurements, chloride ions were added.

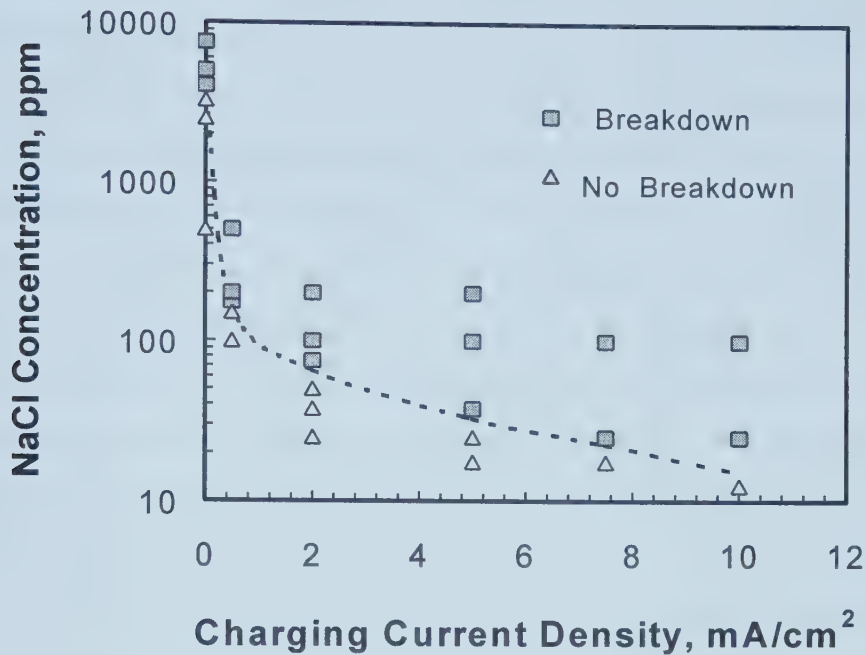


Figure 7-31. The critical concentration of chloride ions for film breakdown vs. charging current density curve for the unstressed 304 SS specimens.

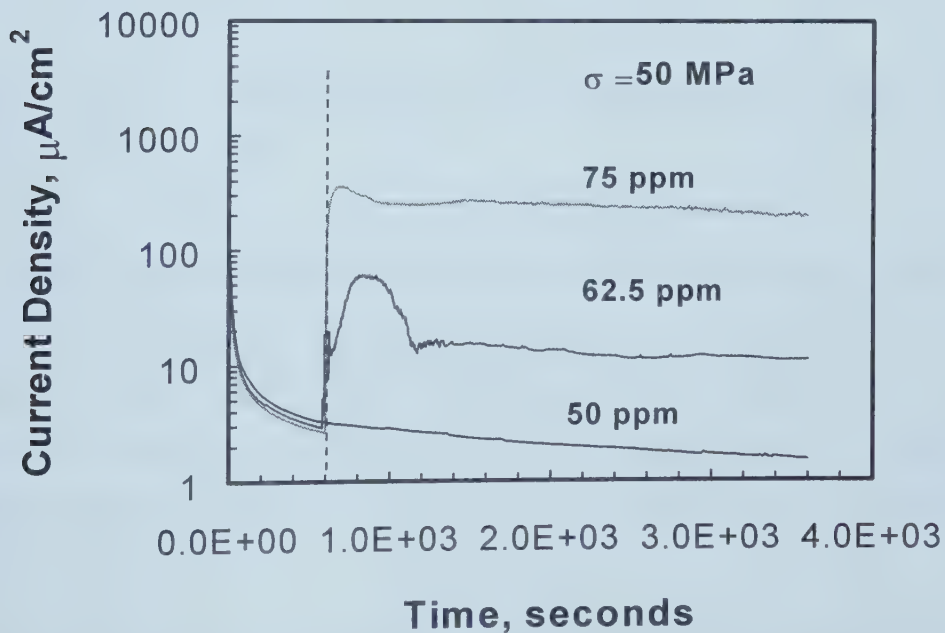


Figure 7-32. The current response curves for the 304 SS specimens charged at 2 mA/cm² for 30 minutes to the application of a constant potential of 0.3 V vs. SCE. The test solution is the borate buffer solution. After 10 minutes from the beginning of the measurement, sodium chloride was added into the solution. The specimens were tensile loaded at 50 MPa during the tests.

beginning of the test. For the specimens charged at 0.5 mA/cm^2 , the passive films do not break down until the concentration of chloride ions is higher than a critical concentration. In this case the critical concentration is around 165 ppm. For the specimens charged at 2 mA/cm^2 , breakdown of the passive film was observed when the NaCl was only 100 ppm. By comparing the charged specimens (Figures 7-29 and 7-30) with the uncharged specimens (Figure 7-23), it is revealed that hydrogen can greatly decrease the critical concentration of chloride ions for the breakdown of passive films. The critical concentration decreases from about 3500 ppm for the uncharged specimens to about 165 ppm for the specimens charged at 0.5 mA/cm^2 . The effect of hydrogen on the critical chloride ion concentration is shown in Figure 7-31. The critical chloride concentration decreases with the charging current density (or hydrogen amount). When the charging current density increases to 10 mA/cm^2 , the critical chloride concentration drops to around 20 ppm. A decrease in the critical chloride concentration also indicates an increase in susceptibility to film breakdown.

7.3.2.4. Effects of Stress on Breakdown of Passive Films

7.3.2.4.1. Effects of Stress on the Critical Concentration of Chloride Ions for Breakdown of Passive Films

In order to investigate the effect of stress on the breakdown of passive films, some of the uncharged specimens and the specimens charged at 2 mA/cm^2 for 30 minutes were subjected to a constant tensile stress during the potentiostatic measurements. The effects of stress on the breakdown of passive films on the specimens charged at 2 mA/cm^2 for 30 minutes are shown in Figures 7-32, 7-33 and 7-34. The stresses applied were 50, 100 and 150 MPa, respectively.

When the concentration of chloride ions is 50 ppm, the film on the specimen stressed under 100 MPa is broken down while the film is not for the unstressed specimen charged under the same charging conditions (Figure 7-23). The critical chloride concentration for film rupture decreases from about 62.5 ppm to about 20 ppm as a result of applying

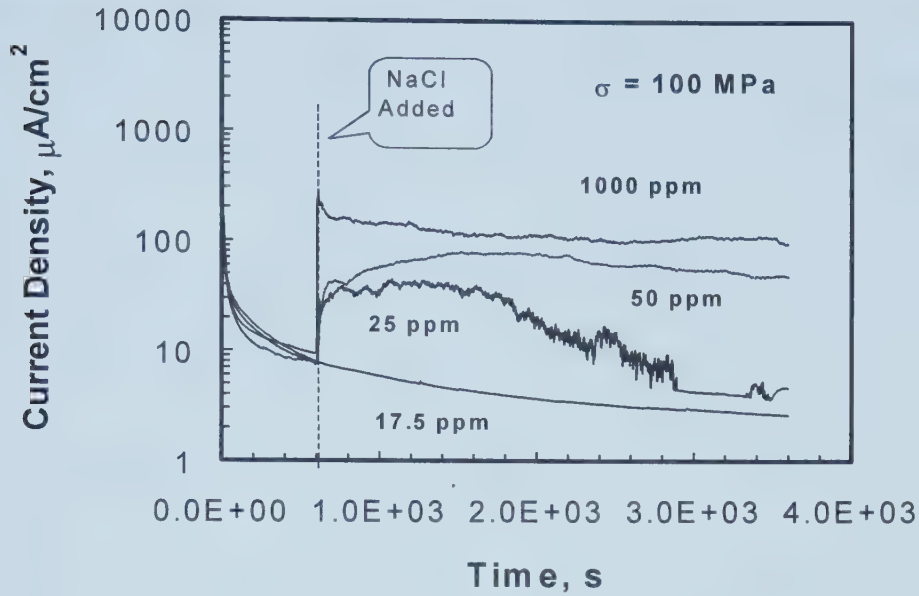


Figure 7-33. The current response curves for 304 SS specimens charged at $2 \text{ mA}/\text{cm}^2$ for 30 minutes to the application of a constant potential of 0.3 V vs. SCE. 10 minutes after the beginning of the measurement, sodium chloride was added into the borate buffer solution. The specimens were loaded at a stress of 100 MPa during the tests.

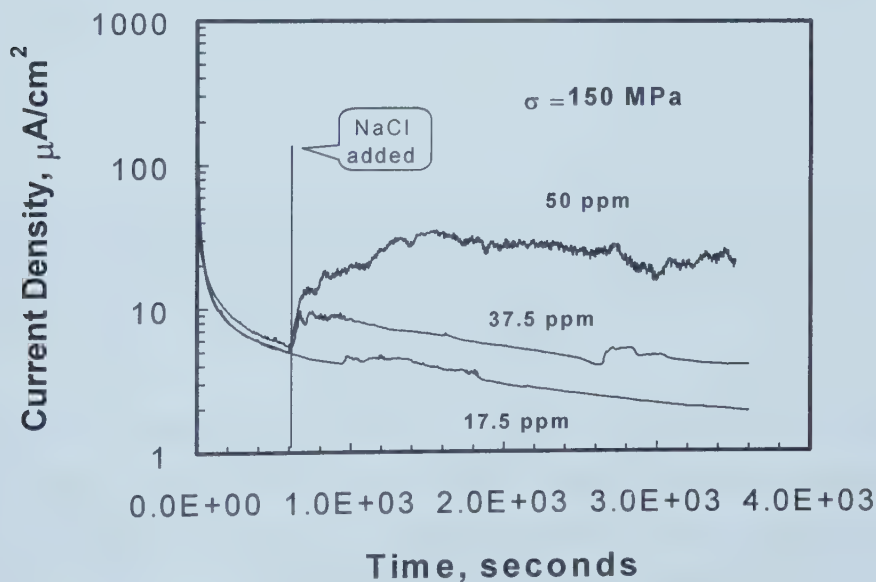


Figure 7-34. The current response curves for 304 SS specimens charged at $2 \text{ mA}/\text{cm}^2$ for 30 minutes to the application of a constant potential of 0.3 V vs. SCE. 10 minutes after the beginning of the measurement, sodium chloride was added into the borate buffer solution. The specimens were loaded at a stress of 150 MPa during the tests.

a stress of 100 MPa on the specimens charged at 2 mA/cm^2 for 30 minutes. This decrease indicates that stress applied can affect the rupture of the passive films. When the stress increases from 50 MPa to 150 MPa, the critical concentration for the breakdown of the passive film decreases.

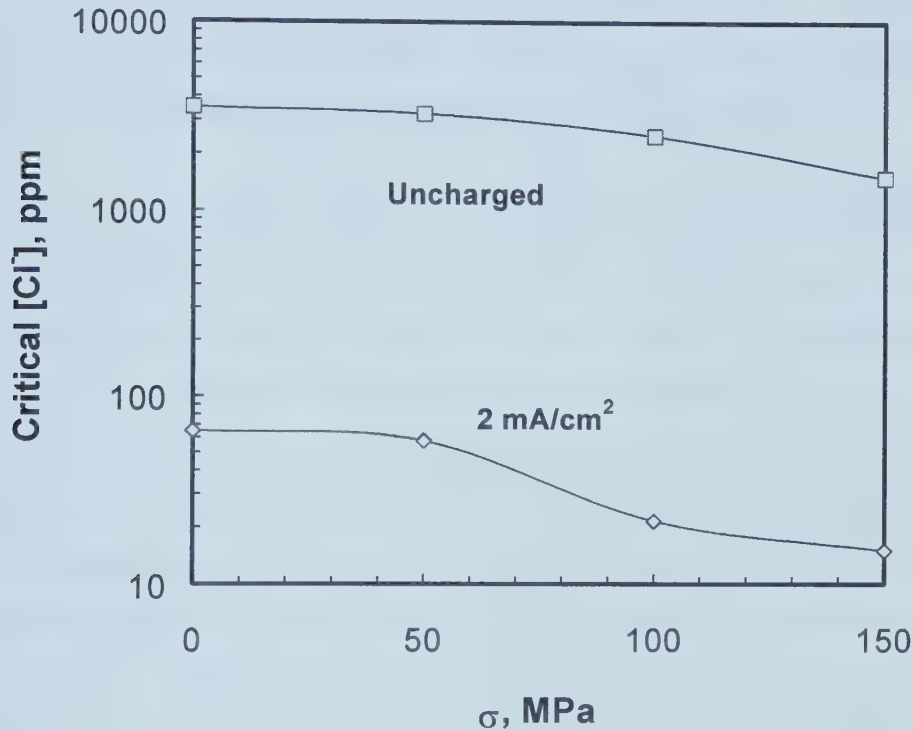


Figure 7-35. The effects of stress on the critical chloride concentrations for the breakdown of passive films formed on uncharged 304 SS specimens and specimens charged at 2 mA/cm^2 for 30 minutes.

Figure 7-35 summarizes the effects of stress and hydrogen charging on the breakdown of passive films. It is obvious that the critical chloride concentration for film breakdown decreases with an increase in the applied stress. For the uncharged specimens, the critical chloride concentration decreases from about 3500 ppm to about 1500 ppm when the applied stress increases from 0 to 150 MPa. If the specimens are charged at 2 mA/cm^2 for 30 minutes, the critical concentration decreases from 62.5 ppm to 15 ppm, correspondingly. Under all the stresses, the charged specimens have lower critical

chloride concentrations than the uncharged ones. It also indicates that hydrogen can promote the rupture of a passive film.

7.3.2.4.2. Surface Morphologies of the Specimens after Potentiostatic Tests

Surfaces of the specimens after the potentiostatic tests were examined in the OLYMPUS PME-3 optical microscope. Both surfaces which encountered or did not encounter a current increase or current noise transients were examined.

The surface morphologies are shown in Figure 7-36. No breakdown of the passive film can be found (Figure 7-36a) on the specimen that was hydrogen charged at 2 mA/cm^2 for 30 minutes and was stressed at 50 MPa during the potentiostatic test. The concentration of chloride added was 50 ppm. The surface after the test looked almost the same as before the test. However, an obvious localized breakdown of the passive film can be observed on the surface of the specimen charged under the same conditions (Figure 7-36b) if the applied stress changed to 100 MPa and concentration of chloride added remained at 50 ppm. These observations are consistent with the current responses, which show no current increases or current noise transient for the former specimen, but show a current increase caused by the addition of chloride ions for the latter specimen. Also the surface morphology indicates that an increase in stress can promote the breakdown of passive films. Figure 7-36b shows that the passive film breaks around an inclusion or secondary particle. The same phenomenon was observed in several locations. The inclusions or particles proved to be sulfides or carbides when examined by the EDS (energy dispersive spectroscopy) technique.

The potentiostatic measurements show that hydrogen charging can promote the breakdown of passive films. A deliberately designed test was carried out to confirm this. In this test, a specimen was charged at 2 mA/cm^2 for 30 minutes, and then a stress of 100 MPa was applied during the potentiostatic measurement. The charged area and part of the uncharged area were exposed to the testing solution. The localized breakdown of the

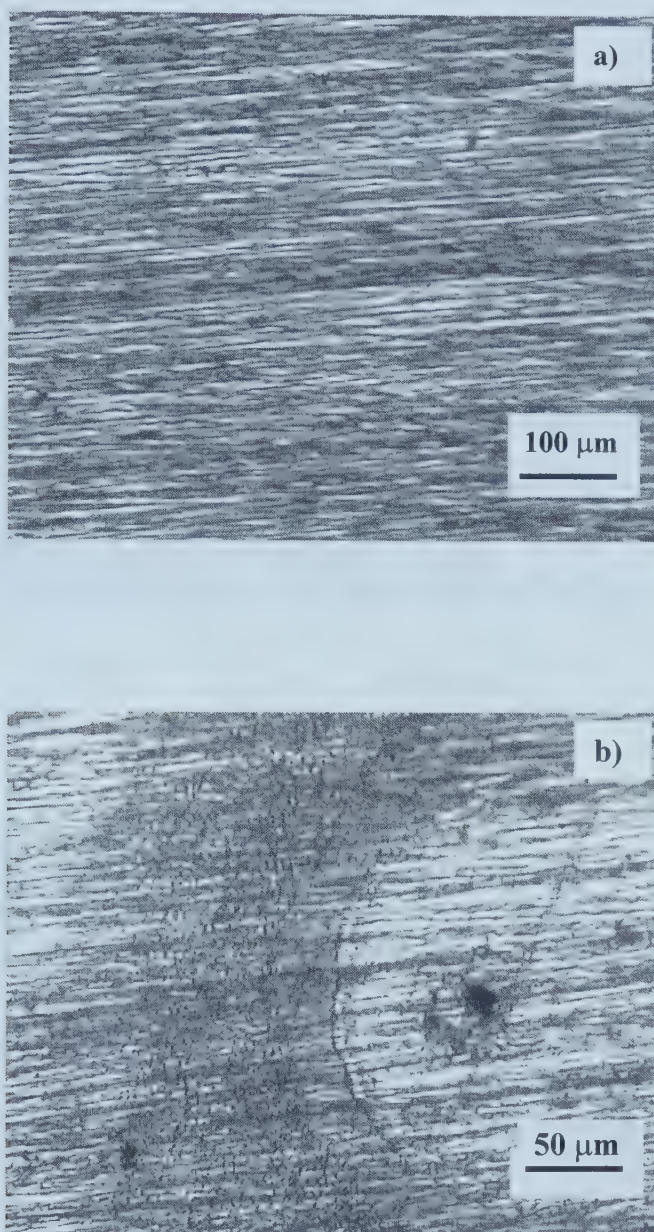


Figure 7-36. The surface morphology after potentiostatic tests of 304 SS specimens charged at 2 mA/cm^2 for 30 minutes. The applied stresses are a) 50 MPa and b) 100 MPa, respectively. The concentration of chloride ions added is 50 ppm.

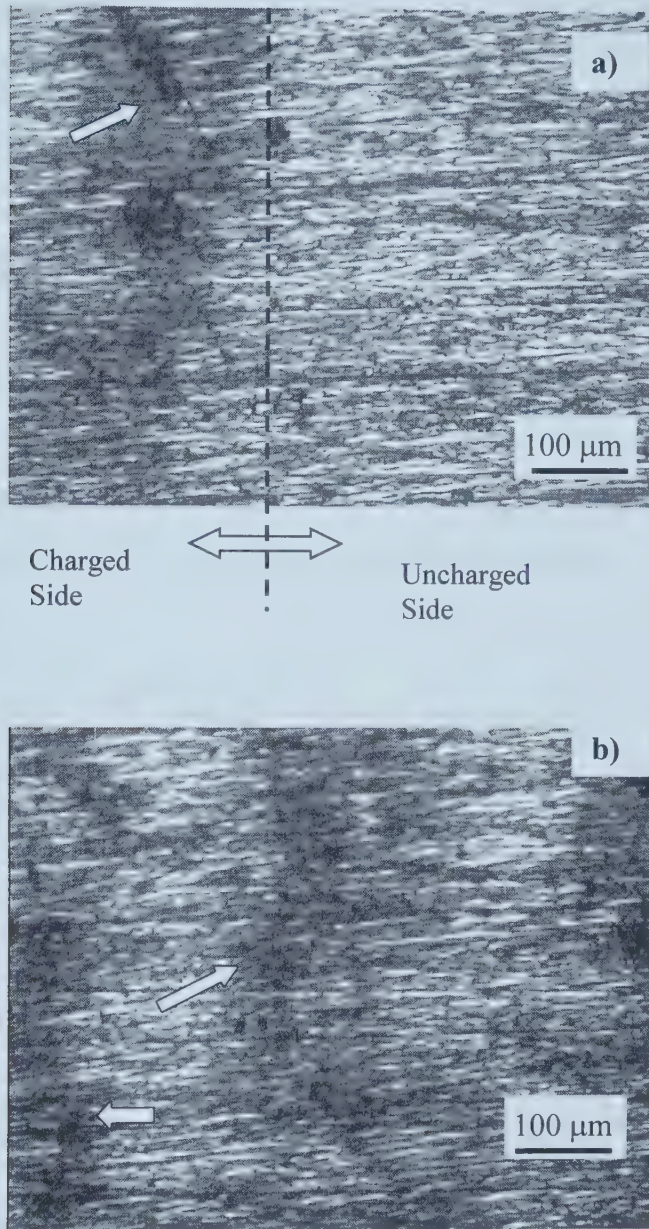


Figure 7-37. The surface morphologies of the 304 SS specimen after potentiostatic testing. The morphology around the charged/uncharged boundary a) and at the charged side b). The specimen was stressed at 100 MPa during the potentiostatic test. The concentration of chloride added is 100 ppm.

passive film (see arrows in Figure 7-37) only occurred on the charged part. No corrosion trace was observed on the uncharged section (Figure 7-37 a). This observation supports the potentiostatic measurement results.

7.4. HYDROGEN-ENHANCED EFFECTS OF CHLORIDE IONS ON PASSIVITY

7.4.1. Hydrogen Enhanced Effects of Cl^- on Breakdown Potential

7.4.1.1. Effects of Hydrogen on Breakdown Potential for Specimens in Chloride Free Solution

Polarization curves were measured on the uncharged and charged specimens. From the measured curves the breakdown potentials were obtained.

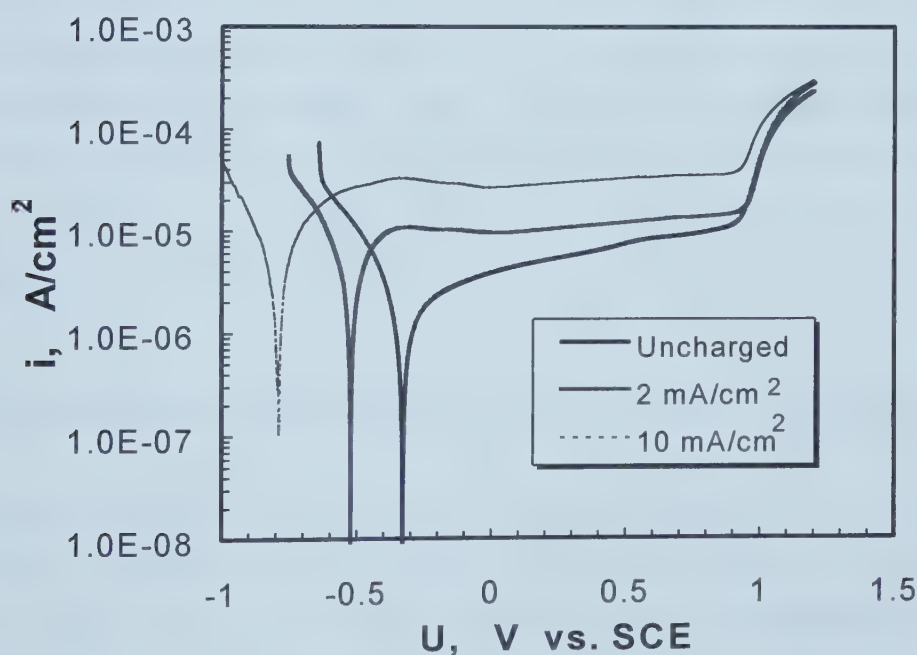


Figure 7-38. The polarization curves of the uncharged and charged 304 SS specimens. For the charged specimens the charging time was 30 minutes. The curves were measured in a borate buffer solution without chloride ions.

Figure 7-38 shows the polarization curves of uncharged and charged specimens in the chloride-free borate buffer solution. For the charged specimens, the hydrogen charging time was 30 minutes. The corrosion potential decreases with an increase in hydrogen charging current while hydrogen increases the passive current density. The hydrogen charging has no effect on the transpassive potential in this case; the transpassive potential stays at about 910 mV vs. SCE. This indicates that hydrogen has no obvious effect on the breakdown of passive films if there are no chloride ions present in the borate buffer solution.

To check whether hydrogen-induced martensite and surface cracking can affect the polarization curves, a charging condition of 20 mA/cm² and 2 hours was chosen to guarantee the formation of martensite and surface cracking. After charging, the charged specimen was baked at 50°C for 72 hours to bake the hydrogen out of the specimen. To keep the experimental conditions the same, the uncharged specimen was also baked at the same temperature for the same time. The polarization curves plots were measured in the borate buffer solution after the specimens were cathodically reduced at -0.3 V vs. open circuit potential for 1000 seconds. Figure 7-39 shows the measured polarization curves. After baking, the charged and uncharged specimens have almost identical curves, which indicates martensite and surface cracks have no obvious effect on the polarization behavior.

7.4.1.2. Effects of Chloride Ions on Breakdown Potential for Uncharged Specimens

Figure 7-40 presents the effect of Cl⁻ on the polarization curves of the uncharged specimens. Chloride ions have little effect on the corrosion potential. The current density in the passive region increases slightly with the chloride concentration. The increase of current appearing around 0.5 V is associated with the electro-oxidation of Cr (III) to Cr (VI) in the film and to the formation of soluble CrO₄²⁻.¹¹ [Cl⁻] increases the current density around the peak much more obviously than that in the range of U<0.5 V. This indicates that chloride can facilitate the electro-oxidation of Cr (III) to Cr (VI). When

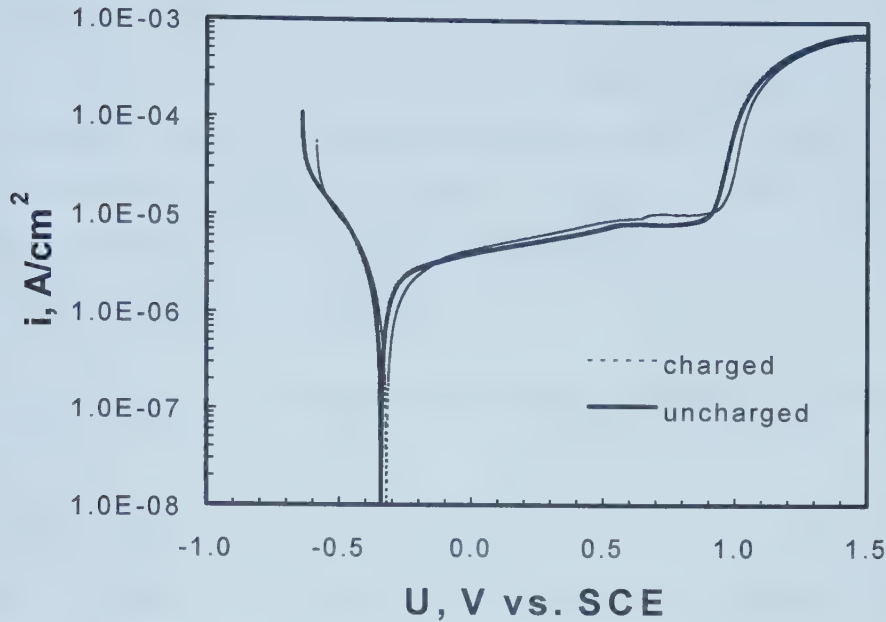


Figure 7-39. The polarization curves of the uncharged and charged 304 SS specimens. The curves were measured after samples were baked at 50°C for 3 days and cathodically reduced at -0.3 V vs. U_{corr} for 1000 seconds in borate buffer solution.

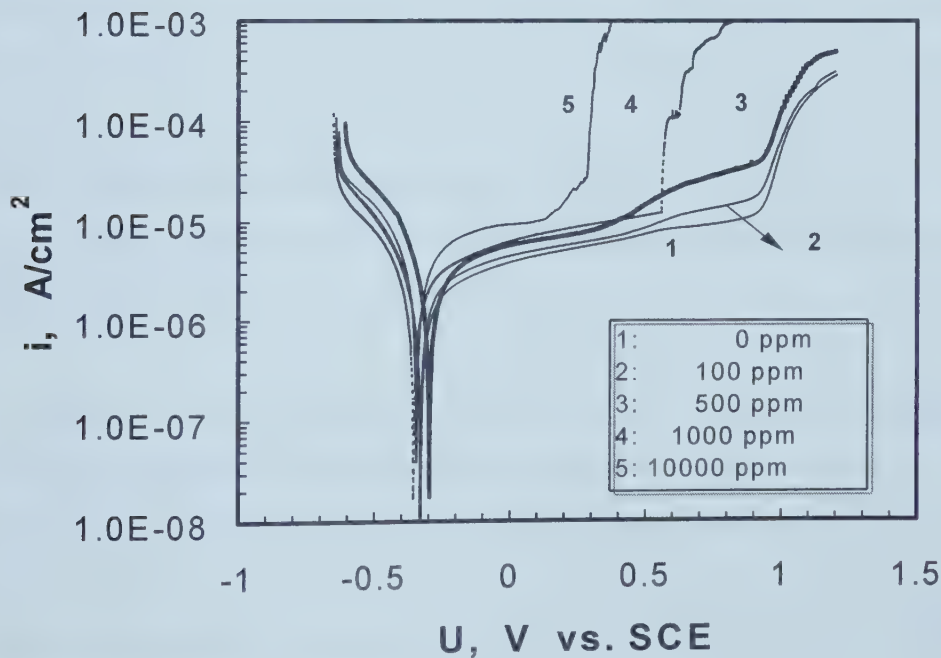


Figure 7-40. The polarization curves of uncharged 304 SS specimens measured in the borate buffer solutions containing different chloride concentrations.

chloride concentration is less than 500 ppm, an increase in chloride concentration does not affect the transpassive potential. Only when the chloride concentration is higher than a critical concentration does the breakdown of passive film occur. When the chloride concentration reaches 1000 ppm, the breakdown potential (U_b) drops to 534 mV vs. SCE. The breakdown potential drops to 284 mV vs. SCE when the $[Cl^-]$ increases to 10000 ppm. These results show that chloride ions can affect the breakdown of passive films only when the concentration is sufficiently high.

7.4.1.3. Effects of Hydrogen on Breakdown Potential for Specimens in Chloride-containing Solutions

The polarization curves of the specimens charged at 5 mA/cm² for 30 minutes are shown in Figure 7-41. From the curves measured in the borate buffer solutions containing various chloride concentrations, it can be found that Cl^- can increase the anodic current density in the passive range. Comparing Figure 7-41 with Figure 7-40, it is obvious that Cl^- has a much stronger effect on the anodic current density and the breakdown potential for the charged specimens than for the uncharged specimens. The U_b decreases with an increase in $[Cl^-]$. The addition of 100 ppm Cl^- does not significantly influence the polarization behavior for the uncharged specimens, but drops the breakdown potential from 910 mV to 346 mV for the charged specimens. As shown in Figure 7-38, hydrogen charging does not affect the breakdown potential if the solution does not contain any chloride ions. This indicates that hydrogen can enhance the effect of chloride ions in the breakdown of a passive film.

Figure 7-42 shows the polarization curves of the specimens charged at different current densities for 30 minutes in the borate buffer solution containing 100 ppm NaCl. The passivation potential range narrows with an increase in the charging current densities. The important thing is that from this plot, it is quite obvious that hydrogen can greatly affect the breakdown potential. The breakdown potential decreases with increasing charging current density.

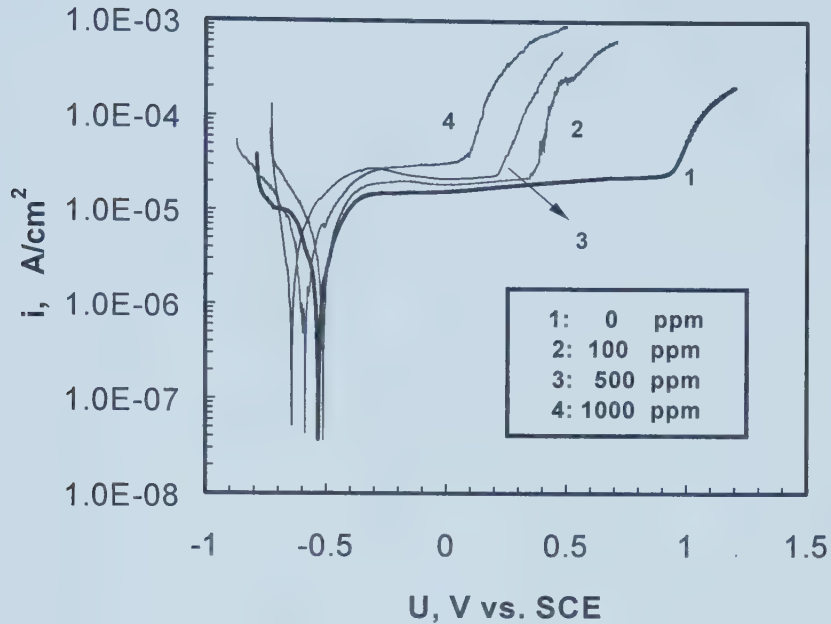


Figure 7-41. The polarization curves of the 304 SS specimens measured in the borate buffer solutions containing different Cl⁻ concentrations. The specimens were at charged 5 mA/cm² for 30 minutes.

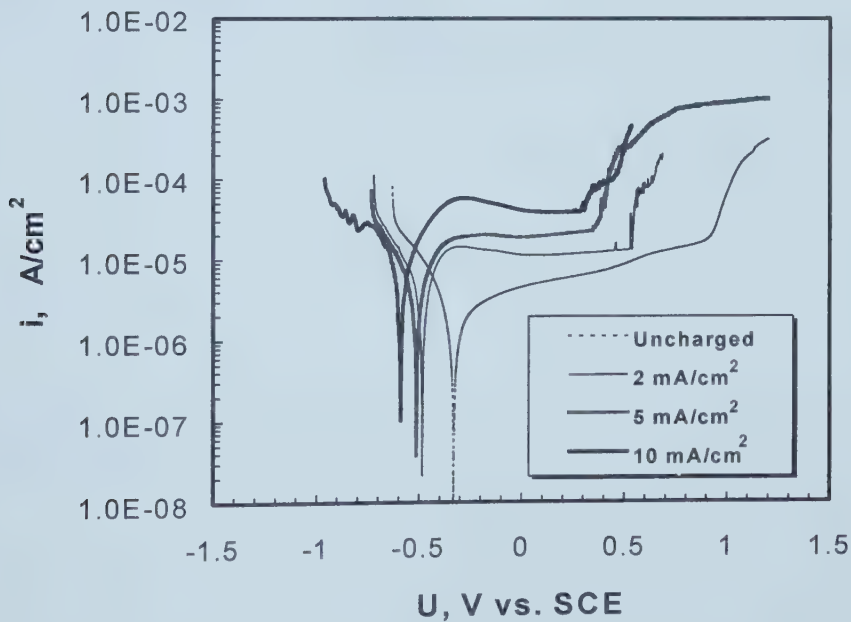


Figure 7-42. The polarization curves of the 304 SS specimens measured in the borate buffer solution containing 100ppm [Cl⁻]. The specimens were charged at different current densities for 30 minutes.

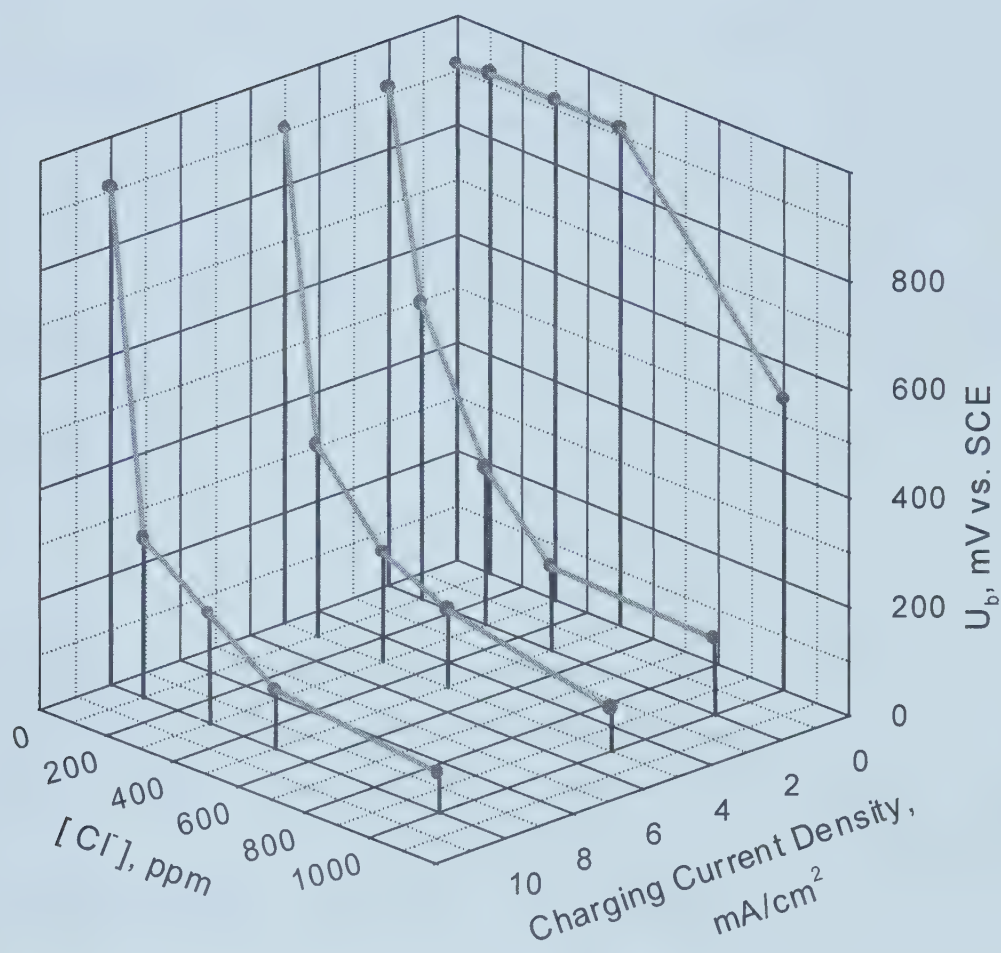


Figure 7-43. The synergistic effects of hydrogen and chloride on the breakdown potential of 304 SS.

Table 7-3. Effects of Hydrogen and $[\text{Cl}^-]$ on Open Circuit Potential (U_{corr}), Passive Current Density (i_p) and Breakdown Potential (U_b) or Transpassive Potential (U_{tp})

Experimental Conditions	U_{corr}	i_p	U_b or U_{tp}
$[\text{Cl}^-]=0$	↓ with i_H ↑	↑ with i_H ↑	No effect when i_H ↑
$[\text{Cl}^-]>0$ uncharged	No obvious effect when $[\text{Cl}^-]$ ↑	↑ with $[\text{Cl}^-]$ ↑	No effect when $[\text{Cl}^-] \leq 500$ ppm; ↓ when $[\text{Cl}^-] > 1000$ ppm.
$[\text{Cl}^-]>0$, charged	↓ with i_H ↑	↑ with i_H ↑ or $[\text{Cl}^-]$ ↑	↓ with i_H ↑ or $[\text{Cl}^-]$ ↑

The change in U_b with $[\text{Cl}^-]$ and hydrogen is summarized in Figure 7-43 to clearly exhibit the effect of hydrogen and Cl^- on the breakdown potential. U_b of the charged specimens decreases drastically with $[\text{Cl}^-]$. In the chloride-containing solutions, U_b drops quickly with an increase in hydrogen charging current density. From Figure 7-42, the hydrogen-enhanced effect of Cl^- on U_b can be easily observed.

7.4.2. Synergistic Effects of Hydrogen and Cl^- on Anodic Current Density in Passive Range

To study the interaction between hydrogen and Cl^- , both hydrogen uncharged and charged specimens were passivated at 0.1 V vs. SCE in the borate buffer solutions containing different chloride concentrations. The current density decay curves for the uncharged and charged specimens are presented in Figures 7-44 and 7-45, respectively. It is shown that chloride ions can increase the anodic current density.

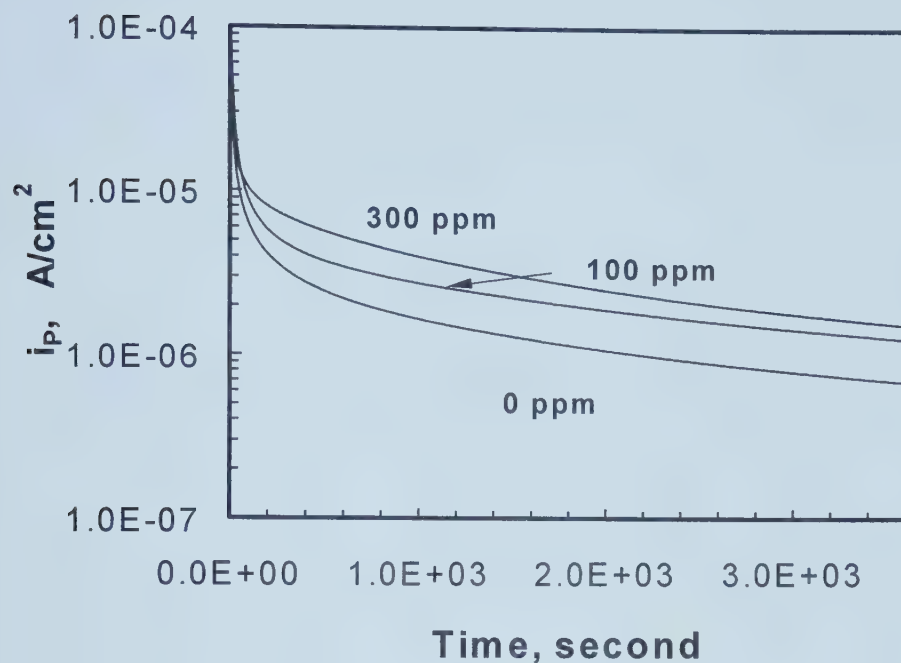


Figure 7-44. The current decay curves of the uncharged 304 SS specimens. The specimens were passivated at 0.1 V vs. SCE in the borate buffer solutions containing different $[\text{Cl}^-]$.

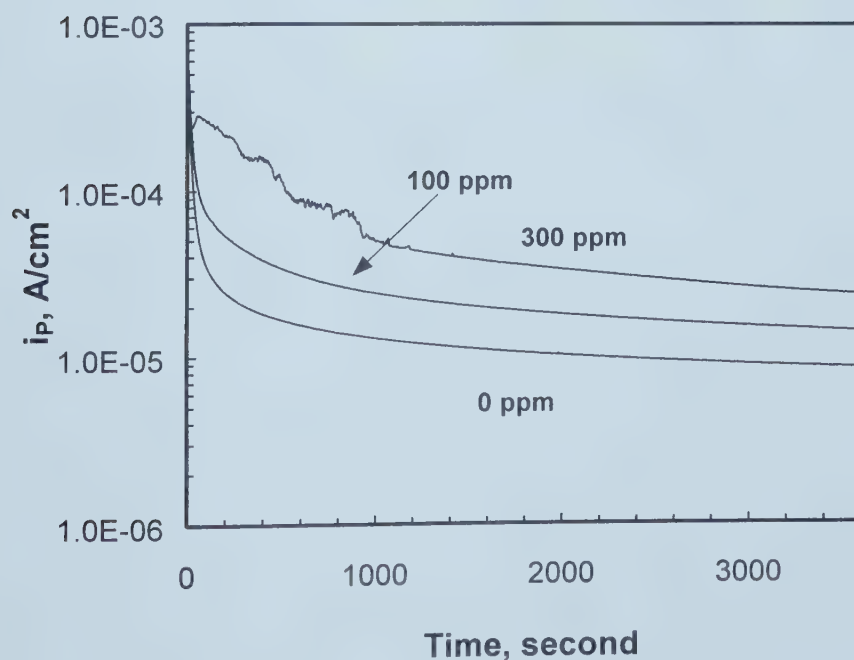


Figure 7-45. The current decay curves for the 304 SS specimens charged at 5 mA/cm^2 for 30 minutes. The specimens were passivated at 0.1 V vs. SCE in the borate buffer solutions containing different $[\text{Cl}^-]$.

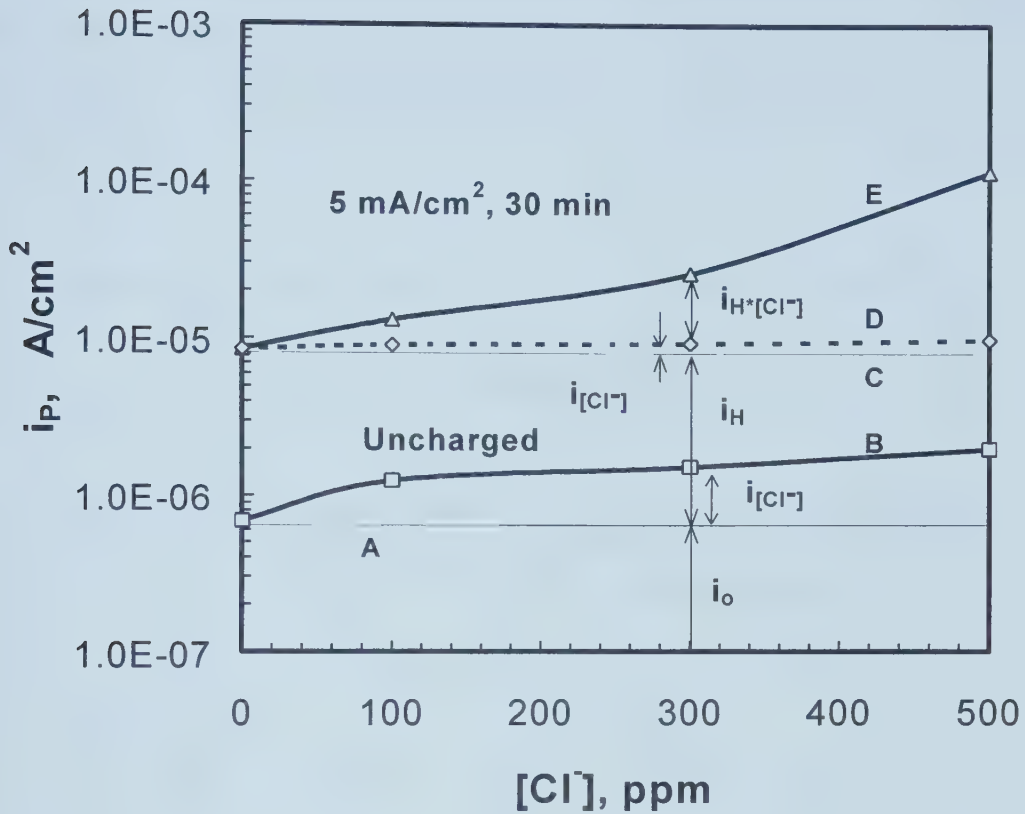


Figure 7-46. The change in anodic current density with chloride ion concentration for the uncharged 304 SS specimens and specimens charged at 5 mA/cm^2 for 30 minutes.

The current density at 3600s is used to indicate the effect of hydrogen and Cl^- on the anodic current density. The changes in anodic current density with chloride concentration and hydrogen charging current density are shown in Figures 7-46 and 7-47, respectively. In order to clearly show the changes in the anodic current density (i_P), a logarithmic scale has been used. In Figures 7-46 and 7-47, line A corresponds to the anodic current density of an uncharged specimen in the chloride-ion-free solution (i_o), while line C shows the anodic current density measured from a charged specimen in a chloride-free solution. Hydrogen charging is found to increase the anodic current density. The current density difference between line C and line A (i_H) is the increase in the anodic current density contributed by the presence of hydrogen in a specimen only. For a charged specimen in a

chloride-free solution, the anodic current density can be expressed as: $i_p = i_o + i_H$. It should be mentioned here that i_H has contributions from both the anodic dissolution of the passive film and the oxidation of hydrogen diffusing to the specimen surface, since the applied potential (0.1V vs. SCE) is higher than the equilibrium potential of hydrogen (-0.7 V vs. SCE).

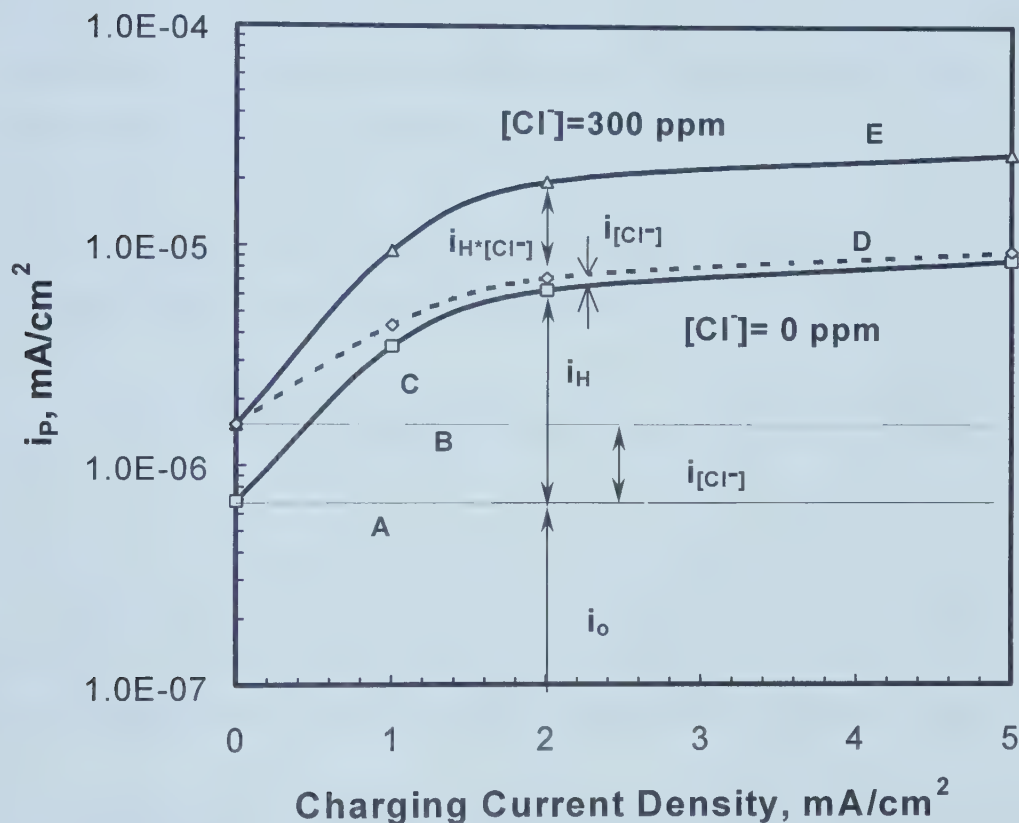


Figure 7-47. The change in the anodic current density with the charging current density in the Cl^- free borate buffer solution and the solution containing 300 ppm Cl^- .

Line B presents the anodic current density measured from an uncharged specimen in a chloride containing solution. Chloride ions can increase the anodic current density. The current density difference between line B and line A ($i_{[\text{Cl}^-]}$) indicates the current increase contributed by chloride ions only. For an uncharged specimen in the chloride containing

solutions, the anodic current density can be expressed as: $i_p = i_o + i_{[Cl^-]}$. The dashed lines (line D) in Figures 7-46 and 7-47 are drawn to represent the sum of i_o , $i_{[Cl^-]}$ and i_H . Line E presents the anodic current density for a charged specimen in a chloride-containing solution. It is observed that the effect of chloride ions and effect of hydrogen on the anodic current density are not simply arithmetically additive. The fact that anodic current densities of the charged specimens in the chloride-containing solutions are higher than the sum of i_o , $i_{[Cl^-]}$ and i_H , indicates there is a synergistic effect between hydrogen and chloride ions on the anodic current density. The current density difference between line E and line D ($i_{H*[Cl^-]}$) indicates this synergistic effect.

As shown in Figures 7-46 and 7-47, the anodic current density of a charged specimen in chloride-containing solution can be expressed as:

$$i_p = i_o + i_H + i_{[Cl^-]} + i_{H*[Cl^-]} \quad [7-6]$$

It can be observed that with an increase in $[Cl^-]$ (Figure 7-46) or with an increase in hydrogen current density (Figure 7-47), the synergistic effect of hydrogen and Cl^- on the anodic current density increases. The results are presented in Figures 7-48 and 7-49.

7.4.3. The Effects of Hydrogen and Cl^- on the Polarization Resistance and Double Layer Capacitance

The polarization resistance R_p and double layer capacitance C_{dl} were obtained by measuring the AC impedance. The effects of hydrogen and chloride ions on the Nyquist plots are shown in Figure 7-50. A parallel resistance and capacitance equivalent circuit is used to extract the values of polarization resistance and double layer capacitance. Figures 7-51 and 7-52 present the changes in R_p and C_{dl} with $[Cl^-]$ for the uncharged specimens, and with hydrogen charging current density for the charged specimens in the Cl^- free borate buffer solution, respectively. Both hydrogen and Cl^- decrease the R_p

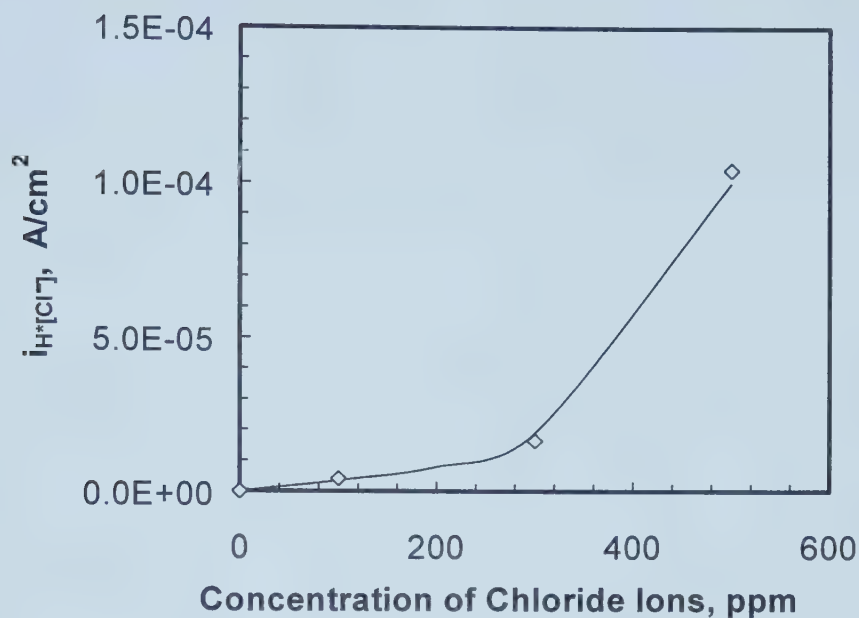


Figure 7-48. The change in the increase of current density, due to the synergistic effect of hydrogen and chloride, with concentration of chloride ions.

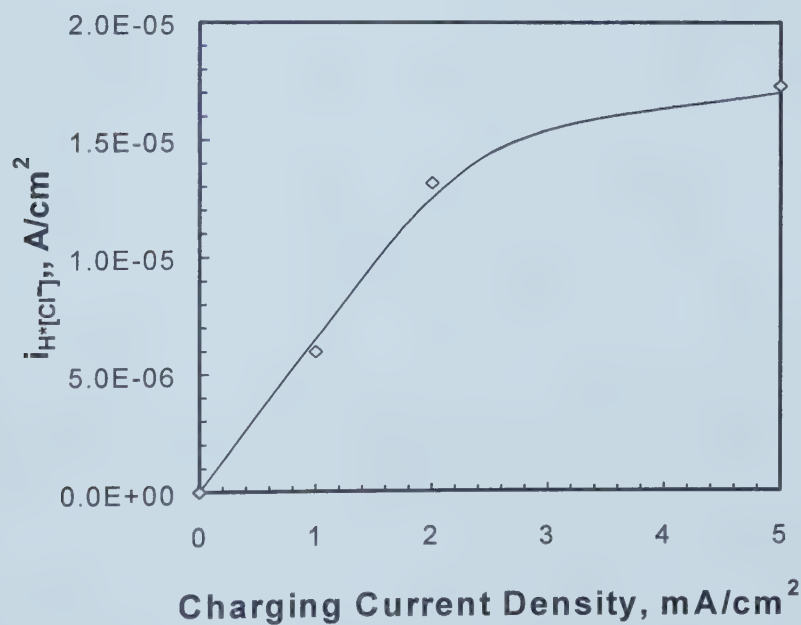


Figure 7-49. The change in the current increase, due to the synergistic effect of hydrogen and chloride, with charging current density.

and increase the C_{dl} . The decrease in R_p with hydrogen or with $[Cl^-]$ is consistent with the increase in the anodic current density. Figure 7-53 shows the changes in R_p and C_{dl} with $[Cl^-]$ for the specimens charged at 5 mA/cm^2 for 30 minutes. R_p value drastically decreases from $3.72\text{E}+04 \text{ Ohm}\cdot\text{cm}^2$ to $2.02\text{E}+03 \text{ Ohm}\cdot\text{cm}^2$ when the $[Cl^-]$ increases from 0 ppm to 500 ppm, mostly in first 100 ppm.

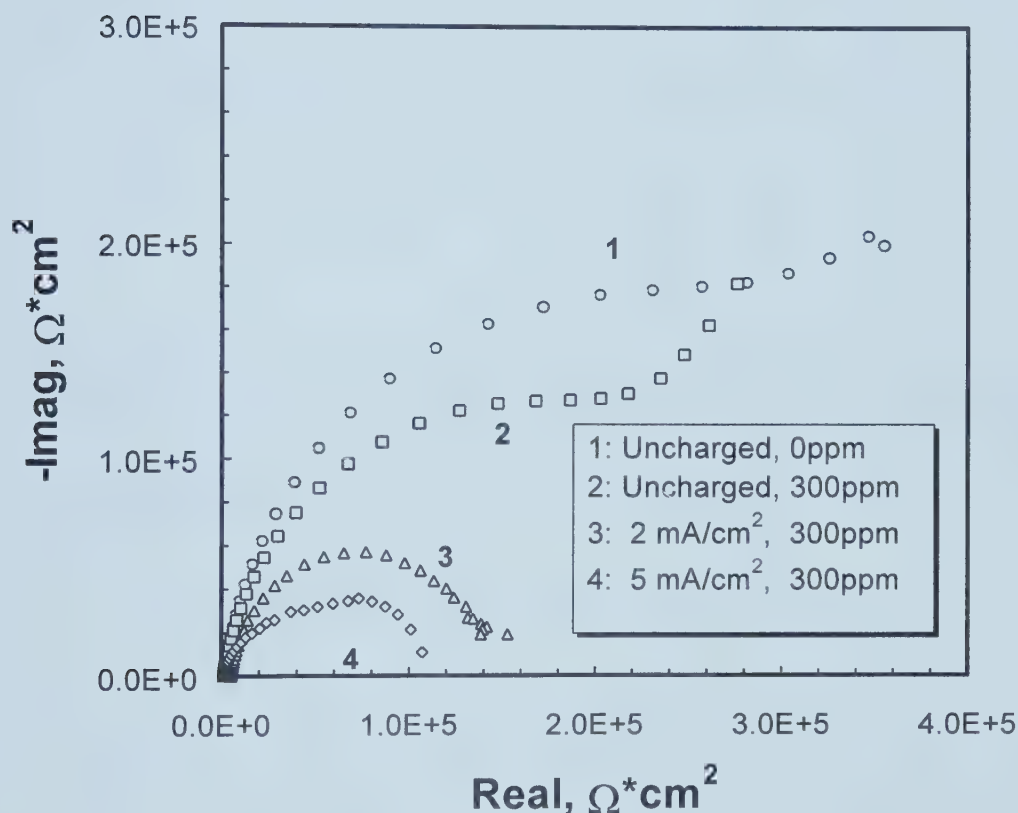


Figure 7-50. The effects of concentration of chloride ions or hydrogen charging current density on the Nyquist plot.

7.5. DISCUSSION

The results shown above clearly exhibit that hydrogen can decrease the stability of the surface film and there is an interaction between hydrogen and chloride ions on the

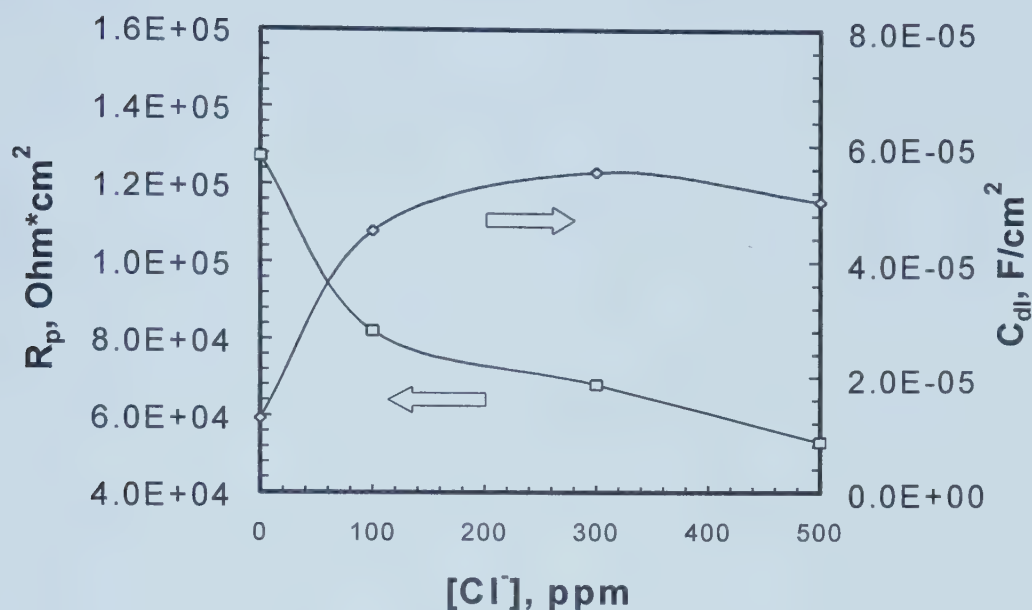


Figure 7-51. The changes in the polarization resistance and double layer capacitance of the uncharged 304 SS specimens with $[Cl^-]$ in the borate buffer solution. The specimens were passivated at 0.1 V in the borate buffer solutions containing different chloride concentrations for 2 hours, then the AC impedance was measured at 0.1 V in the same solutions.

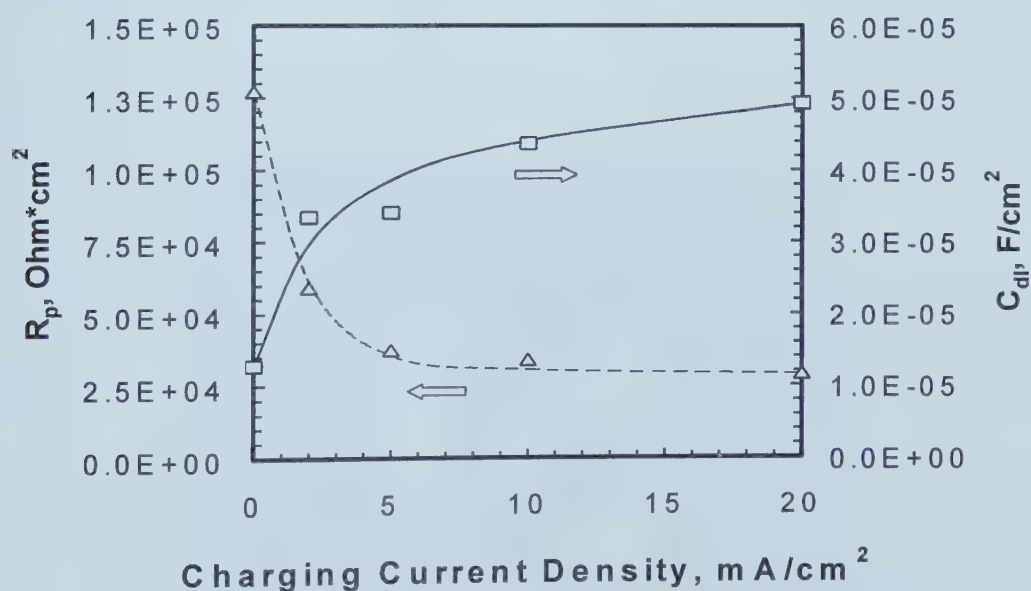


Figure 7-52. The changes in the polarization resistance and double layer capacitance with charging current density. The AC impedance was measured in the Cl^- free borate buffer solution at 0.1 V vs. SCE after 2 hour passivation in the same solution and at the same DC potential.

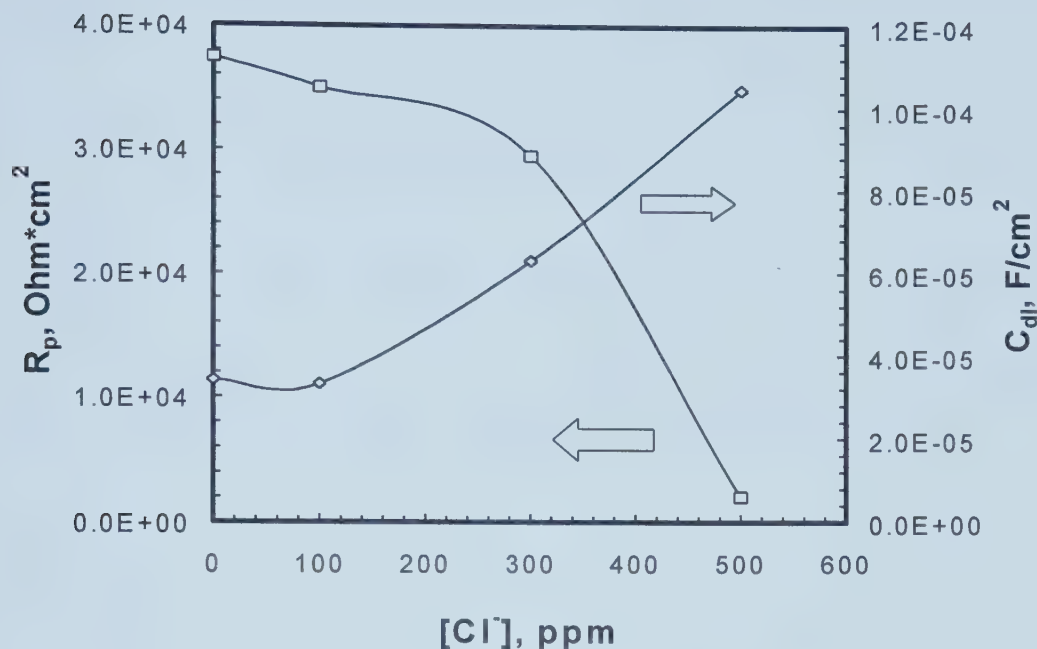


Figure 7-53. The changes in the polarization resistance and double layer resistance of the charged 304 SS specimens. The specimens were charged at 5 mA/cm² for 30 mins, passivated at 0.1 V in the borate buffer solutions containing different chloride concentrations for 2 hours, and then the AC impedance was measured at 0.1 V in the same solutions.

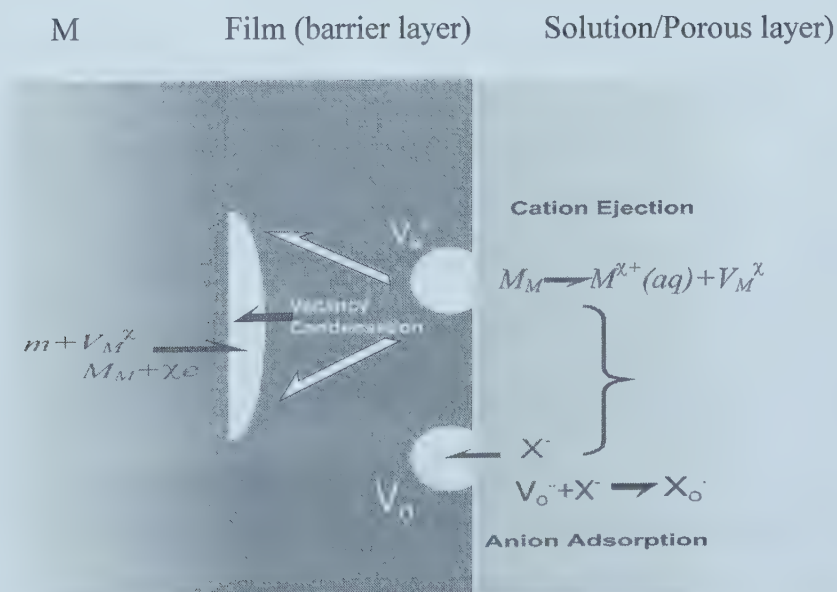
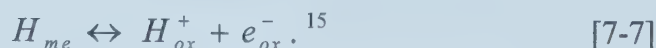


Figure 7-54. Point Defect Model.³⁷

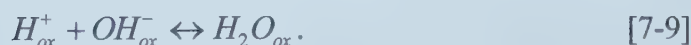
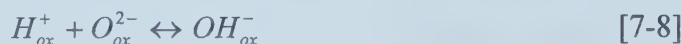
passivity. Hydrogen decreases the stability of the surface film on a metal by influencing the properties of the film in the following possible ways:

7.5.1. Increase in H_2O/O^{2-} and OH^-/O^{2-} Ratios

Hydrogen in a passive film is considered to be present as a charged species (protons)^{12,13,14} because passivating oxides have ionic bonding character, and also because passive films support a strong electric field. Hydrogen can penetrate into the passive film from the metal side and ionize. The reaction can be written as:

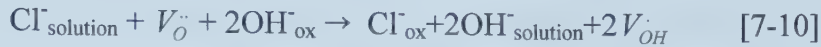


Because the hydrogen in an oxide exists as protons, there is a strong coulombic interaction between the hydrogen and oxygen ions in the oxide. Some of the penetrated hydrogen protons combine with oxide ions or hydroxyl ions to form hydroxyl ions or water in the passive layer according to the following reactions:



This increases the H_2O/O^{2-} and OH^-/O^{2-} ratios, and therefore, the mean cationic valence decreases for electrical neutrality. According to the opinions of Fugassi and Haney¹⁶, Cl^- ions can easily displace OH^- ions or H_2O in the passive film because the Cl^- ion is a stronger Lewis base than either OH^- ions or H_2O . Yolken et al.,¹⁷ found that when a passive film that formed on an iron surface in a 0.1 N Na_2NO_2 solution containing tritiated water was allowed to undergo breakdown in a chloride solution, the chloride ions extracted the same quantity of hydrogen that they had measured in the outer layer of the passive film. Cl^- is incorporated or enters the passive film in a process involving place

exchange of OH^- and Cl^- .¹⁸ McBee and Kruger¹⁹ proposed the following exchange process:



where $V_{\text{O}}^{\cdot\cdot}$ is an oxygen vacancy and V_{OH}^{\cdot} is a hydroxide vacancy.

With increasing hydrogen concentration in the adjoining metal, the concentration of hydrogen-containing species in the passive film increases²⁰. This will promote the above substitution of OH^- ions by Cl^- ions, therefore decreasing the resistance to pitting initiation with increasing hydrogen-charging.

7.5.2. Interactions between Hydrogen Protons and Defects in Passive Films

There are many defects in the surface film.^{21,22} The passive film over nonmetallic inclusions tends to be even more defective.^{11,23} The formation of corrosion pits is facilitated by the existence of these weak sites in the surface film.²⁴ It is possible that only part of the hydrogen protons in a passive film is associated with the change in cation valence. Some hydrogen protons can also accumulate around these defects to form localized positive charge regions. As a result of the electrostatic force between anions and protons, the chloride ions are attracted and adsorb on the film surface adjacent to these localized positive charge regions. This attraction promotes the formation of localized clusters (islands) of high concentration of Cl^- . It is generally acknowledged that the adsorption of aggressive halide anions on the surface film is the first step in the events leading to pitting initiation.²⁵ The migration of chloride ions into the film is accelerated due to the high chloride concentration in the islands and with the assistance of the electrical field force between the opposite charges. This favors the accumulation of chloride ions around these defects which form the active sites for pitting corrosion. The acceleration of the migration of Cl^- ions also facilitates the exchange process between the

Cl^- and OH^- ions. This is one of the reasons why the critical chloride concentration for pitting corrosion decreases with the hydrogen charging. Film breakdown occurs after the local chloride concentration exceeds a critical value. Because of the formation of localized positively charged regions, hydrogen decreases the stability of the film. The high hydrogen concentration in metals can easily form more localized positive regions in the surface film, increase the concentration of protons around the defects and therefore promote the pitting corrosion processes.

7.5.3. Changes in Electronic Structures

It is well known that passive films on most metals exhibit semiconducting or insulating behavior.²⁶ Because dissolution, film formation and breakdown all involve the movement of electrons and ions from the metal through the passive film, electronic properties are a significant aspect of the nature of the passive film and may play an important role in the film breakdown mechanism.²⁷ The close relationship between susceptibility to pitting nucleation and the defective nature of the oxide films is directly connected with its ionic and electronic conductivity characteristics. Thus the effect of chloride ions and hydrogen on the breakdown of a passive film can be explained in terms of semiconductor electronics.

Photoelectrochemical measurements^{28,29} indicate that passive films on stainless steel are highly disordered. The disorder means that an electron at a given atomic site in the material finds itself in a different environment from an electron found at another site containing the same species. The defects in the passive films are registered as localized states and introduce a high density of localized states.³⁰ It has been found for the highly disordered films (with larger disorder energy) that the density of states function extends significantly into the bandgap region of the material.³¹

It is found in p-type Si that a high density of hydrogen beneath the surface generates strong distortions and structural defects in the lattice which could create deep levels

within the bandgap.³² Our results²⁸ show similarly that hydrogen can increase the disorder degree of the passive films on stainless steels.

It is interesting to note that materials with a lower number of localized states have a good resistance to localized corrosion. Deep localized states may occur at sites where the structure of the film is heavily distorted, such as nonmetallic inclusions and hence such a point may act as a potential pit nucleation site.²⁷

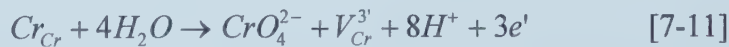
According to the physics of semiconductors,³³ a cation vacancy acts as an acceptor while an oxygen vacancy acts as a donor. When an oxygen vacancy exists in the film, the valence electrons of the excess metal atoms are captured by the oxygen vacancy that behave as effective positive charges, creating an additional coulombic field. This field perturbs the periodicity of the potential energy of the crystal. The excess electron occupies a level below the conducting band. The energy levels lying below the conduction band are called donor levels. When cation vacancies exist, each of these vacancies constitutes a localized negative charge. At the same time the adjacent oxygen atom has incomplete bonds. In this situation the appearance of acceptor levels above the valence band can be observed.

As we all know, halide ions especially chloride ions, play a very important role in the breakdown of passive films. Sato³⁴ explained the effect of chloride ions on the breakdown of passive films in terms of semiconductor electronics. He claimed that the adsorption or incorporation of a chloride ion was accompanied by the appearance of an electron acceptor level in the lower part of the forbidden energy gap of the matrix oxide, because a chloride anion is more electronegative or has a lower valence than the matrix oxide ions. Unfortunately the whole reasoning is wrong. This conclusion was simply extended by citing the following statement: “atoms of the admixture of lower valency than the parent atoms introduce into the forbidden band energy levels (or level) which lie above the valence band. They are called acceptor levels.”³³ Actually in that book “the parent atoms” are metal atoms instead of oxygen atoms. First, let us consider a crystal

oxide MO that contains foreign chlorine atoms which substitute for oxygen atoms in the sublattice. In this case, only one electron contributes to binding while there is one excess electron. The excess electron occupies a level lying below the conduction band, which is called a donor level. Second, let us consider the incorporation of Cl^- into an oxygen vacancy. In this case, because the outer electron orbit of Cl is completely filled, the incorporation itself seems not to affect the energy levels directly. Therefore, the effect of chloride ions on the breakdown of passive films should be treated in a way which is different from Sato's.

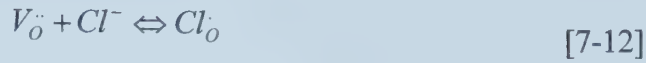
The Cl^- ions in a passivating solution can provide an even higher number of defects in these films. The absorption of chloride ions into a passive film may increase the cation vacancy concentration for the following reasons:

(1) The addition of an aggressive anion, such as Cl^- to a solution in contact with a passive metal causes a burst of cations to be released from the passive film surface.³⁵ As a consequence, the cation vacancy concentration on the surface increases. At a high potential, the generation of cation vacancies may be related to the reaction of electro-oxidation of Cr^{3+} to form soluble CrO_4^{2-} :³⁶



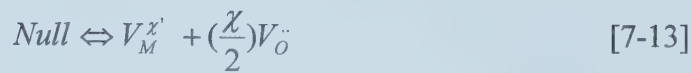
in which Cr_{Cr} represents a Cr^{3+} cation in the passive film. The current peak appearing around 0.5 V in Figure 7-39 is associated with the electro-oxidation of Cr (III) to Cr (VI) in the film and to the formation of soluble CrO_4^{2-} . The current density increases around the peak much more obviously than that in the range of $U < 0.5$ V. This indicates that chloride can facilitate this electro-oxidation reaction and hence the generation of cation vacancies.

(2) Cl^- can fill the anion vacancies by the reaction^{37,38,39}:



where $V_{\text{O}}^{\cdot\cdot}$ and $\text{Cl}_{\text{O}}^{\cdot\cdot}$ represent the oxygen vacancy at the film/solution interface and a chloride ion occupying an oxygen vacancy at the same location, respectively.

The system responds to the loss of oxygen vacancies by generating cation vacancy/oxygen vacancy pairs via a Schottky-pair type of reaction:



where $V_{\text{M}}^{\times'}$ represents a cation vacancy. The newly generated oxygen vacancies can in turn react with additional Cl^- ions at the film/solution interface to generate more oxygen and cation vacancies (Figure 7-54). The Cl^- absorption and cation vacancy generation is autocatalytic.

An absorbed Cl^- may desorb along with a surface cation to form a $(V_{\text{M}}^{\times'}) \cdot (V_{\text{O}}^{\cdot\cdot})$ pair. This process is perhaps favored in those cases where the anion has a tendency to complex with the cation (e.g., in the case of iron in chloride solutions), rather than forming an insoluble compound. The cation vacancy may submerge into the film (barrier layer) by the outward movement of a cation, resulting in the regeneration of an isolated surface oxygen vacancy. Because the anion vacancy may then absorb another anion, this process, too, is autocatalytic.

From Eq. [7-12] and Eq. [7-13] it is easy to understand that the cation vacancy generation rate increases with $[\text{Cl}^-]$ in the solution or anion vacancy concentration at the film surface.

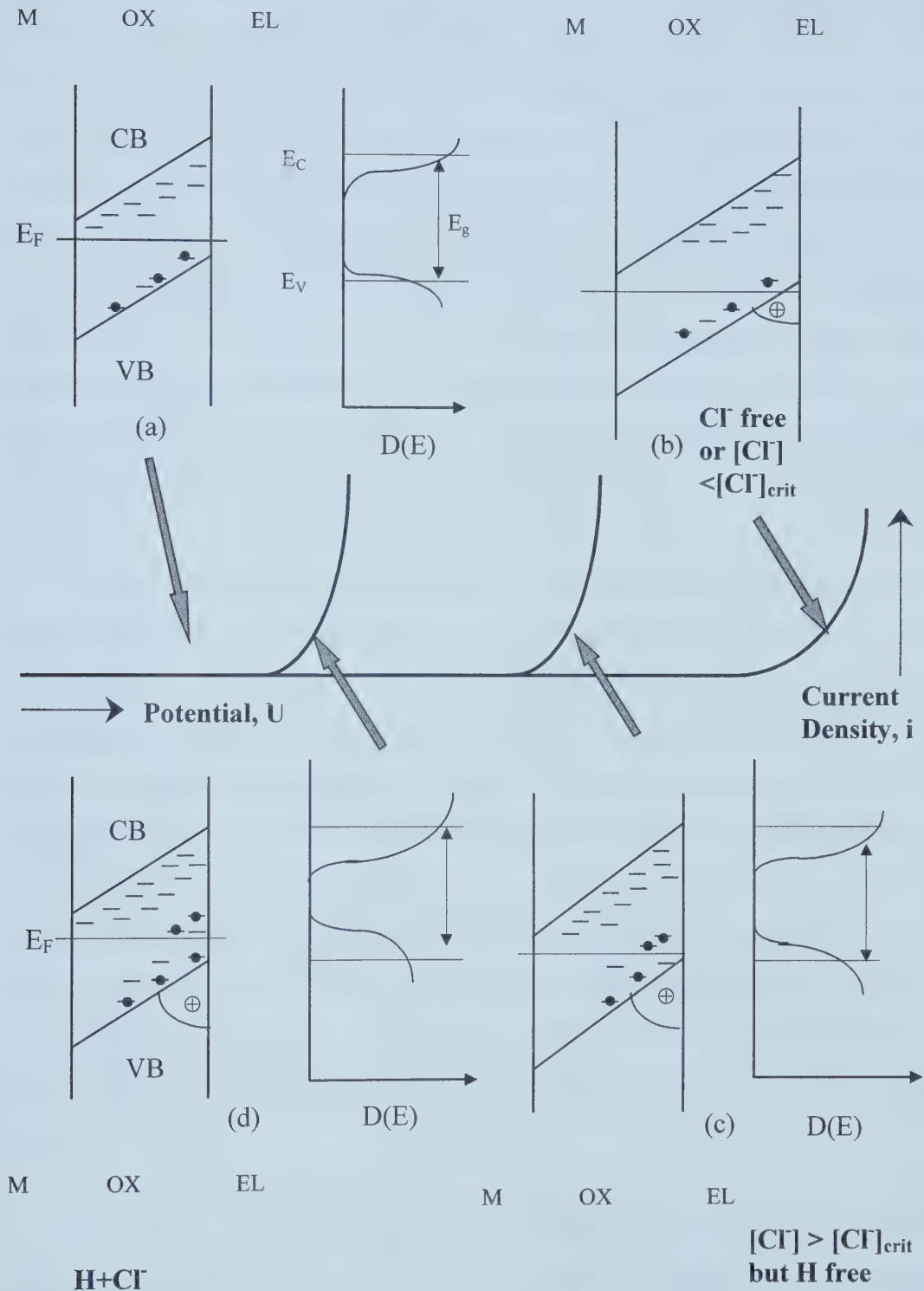


Figure 7-55. Schematic band structures at anodic polarization ($U > U_{FB}$), distributions of the localized states at the weak surface sites of passive films and their relationships with the breakdown of the passive films.

Anodic overpotential η ($\eta = U - U_{FB}$) will lead to upward band bending which lowers the Fermi level of the metal. Sato³⁴ stated that the electrostatic potential gradient (electric field strength) in the film increases with an increase in the applied anodic polarization, under an assumption that the thickness of the passive film was independent of potential. However, this is highly unlikely to be true. The thickness of the passive film actually is potential dependent. The steady-state film thickness is generally found to vary linearly with applied potential.^{40,41} Even Sato himself revealed in another paper⁴² that the electric field strength in the film (barrier layer) was constant in the potential range of passivity. Therefore, the potential dependence of the film thickness should be taken into account for band bending. The slope of band bending should be independent of potential, rather than increasing with the applied potential as Sato³⁴ supposed.

For the uncharged specimens in the Cl^- free solution, even though there are some localized states in the electronic energy gap, the density of these localized acceptor states is low (Figure 7-55(a)). The effective accumulation of positive holes only occurs when the anodic polarization applied can make the Fermi level of metals lower than the valence band in the outermost layer of the film (Figure 7-55 (b)). Then electron tunneling occurs through the film leaving positive holes at the outermost layer of the film. As the result of the positive surface charge there is an anodic increase in the potential difference of a Helmholtz layer $\Delta\Phi_H$.³⁴ Because $\Delta\Phi_H$ is the driving force for the dissolution of a passive film, an anodic increase in $\Delta\Phi_H$ can increase the dissolution rate of the film. This positive charge accumulation on the surface can finally lead to quick dissolution of the passive film. In this case, large anodic polarization is needed to be in the transpassive region.

When Cl^- is added to the solution and only when $[Cl^-]$ is sufficiently high, the cation vacancy concentration of the uncharged specimens, as mentioned above, will have an obvious increase at the film surface especially around localized weak sites (with high defect concentration). Therefore the density of the localized acceptor states greatly increases. In this case, the positive holes can effectively accumulate at the surface around

some weak sites when the anodic polarization makes the Fermi level lower than a sufficient amount of localized acceptor states but still higher than valence band edge (Figure 7-55 (c)). This means that less anodic polarization is needed to break down the passive film.

As indicated by photoelectrochemical measurements,²⁸ hydrogen can increase the disorder degree (or defect concentration) of the passive films. Hence it is assumed that the oxygen vacancy concentration at the passive film surface is higher for a hydrogen charged specimen than for an uncharged specimen. In Cl^- free solution, the autocatalytic process of cation vacancy generation does not occur. For the charged specimens in the Cl^- free solution, the increase in density of the localized acceptor states around weak sites is limited (similar to Figure 7-55 (a) and (b)). A large overpotential is needed to make the Fermi level lower than the valence band so that the dissolution of the film can be accelerated. Therefore in the chloride-free solution, with an increase in charging current density, the transpassive potential does not change. However, for the hydrogen-charged specimens in Cl^- containing solutions, due to the high oxygen vacancy concentration on the surface especially around the weak sites, the chance (or rate) of Cl^- adsorption into oxygen vacancies increases, which greatly promotes the autocatalytic generation of cation vacancies. Therefore for the passive film on a charged specimen in a Cl^- containing solution, the generation rate of cation vacancies, and hence the density of localized acceptor states, is higher than that for an uncharged specimen in the same solution (Figure 7-55 (d)). As a result, the breakdown potential for a charged specimen in Cl^- containing solutions is low.

The effect of hydrogen on the localized thinning of the passive film should be taken into account in the passive film breakdown process. According to Macdonald³⁹, the generated cation vacancies will diffuse towards the passive film/metal interface. The penetration of cation vacancies is favored around the localized highly disordered region (weak sites). If the transportation rate of cation vacancies across the passive film exceeds the annihilation rate of cation vacancies by emission of cations from the metal matrix to

the film, the condensation of cation vacancies at the film/metal interface will lead to local detachment of the film from the underlying metal (Figure 7-54). The localized detachment makes the passive film cease to grow; the passive film around this region begins to thin as a result of the continued dissolution. Because of the high degree of disorder for the passive film on the charged specimens, and also due to the fact that the chloride in solution can make the passive film more defective, the detachment of the passive film from the underlying metal becomes easier for the charged specimens in Cl^- containing solution. Dean and Stimming³⁰ found that the density of localized states in the band gap increased with a decrease in film thickness. The localized thinning of the passive film increases the density of localized states, and in return promotes the breakdown of the passive film.

Nonmetallic inclusions are possible sites for pit nucleation. It has been shown that pitting starts almost exclusively at nonmetallic inclusions and that sulfide are especially detrimental.⁴³ The passive film over inclusions and their immediate surrounding areas tends to be more defective than film over more perfect metal.^{44,23} Inclusions and their immediate surroundings may form preferential sites for the adsorption and incorporation of chloride ions. This defective nature of the film and the easy incorporation of chloride ions into the film around inclusions cause a high density of localized states. Therefore, inclusions are widely considered to be the most effective pit nucleation sites.⁵

Chloride ions have been found to migrate over the steel surface toward the areas of high stress, where favorable defective sites are present.⁴⁵ This means that stress can promote the adsorption of chloride ions. Under stressed conditions, the passive film might be more defective than under stress-free conditions. Stress probably increases the concentration of oxygen vacancies on the surface, which can facilitate the incorporation of chloride ions into the film and consequently increases the generation rate of cation vacancies. According to the analysis above, film breakdown will be promoted.

7.6. SUMMARY

It is clearly shown that hydrogen has obvious effects on the passivity and the breakdown behavior of passive films.

It is found that hydrogen can affect the breakdown of passive films only in the solutions containing chloride ions. There are synergistic effects of hydrogen and chloride ions on the anodic current density and the breakdown potential. Hydrogen can increase pit initiation, increase pit density, promote pit growth and hinder the repassivation process. Inclusions and particles are the favorite initiation sites for pit initiation. Pickling can greatly decrease the density of inclusions, and hence decrease the pit density.

There is a critical chloride concentration to break down a passive film. Hydrogen can decrease this critical concentration. Application of a tensile stress also has the same effect. The critical concentrations of chloride ions for film breakdown are always higher for the uncharged specimens than those for hydrogen-charged specimens in all the stress ranges investigated in this study.

Several explanations are proposed to explain the phenomena. The explanations are probably not exclusive.

REFERENCES

1. U. R. Evans, J. Chem. Soc.(London), (1927): p.1020.
2. H. J. Engell and N.D. Stolice, Z. Phys. Chem., 20 (1959): p.113.
3. T. P. Hoar, Trans. Faraday Soc., 45, (1949): p.683.
4. C. Vanlengenhaghe, L. Klimczek-Mathien, J. Mennier and M. Pourbaix, International Conf. Corro. Reactor Materials, Salzburg (1962).
5. G. Hultquist, S. Zakipour and C. Leygraf, "On the Influence of Both Passive Film Composition and of Non-Metallic Inclusions on the Initiation of Localized Corrosion of Stainless Steel", Passivity of Metals and Semiconductors, ed. by M. Froment,

- Elsevier Science Publishers, (1983): p. 399.
6. N. G. Thompson and B. C. Syrett, *Corrosion*, 48, (1992): p. 649.
 7. T. Shibata, *Corrosion*, 52 (1996): p. 813.
 8. Yifan Zhu, Yu Pan and Baoming Wei, *J. of Chinese Society of Corrosion and Protection*, 7 (1987): p. 199.
 9. Erwin Kreyszig, *Introductory Mathematical Statistics-Principles and Methods*, John Wiley & Sons, Inc., 1970, p. 159.
 10. John L. Dawson, "Electrochemical Noise Measurement: The Definitive In-situ Technique for Corrosion Applications?", *Electrochemical Noise Measurement for Corrosion Application*, ed. by J. R. Scully, P. R. Roberge, D. L. Reichert, and J. L. Dawson, (1996): p.3.
 11. N. Ramasubramian, N. P. Preocanin and R. D. Davison, *J. Electrochem. Soc.*, 132, (1985): p.793.
 12. M. E. Armacanqui and R. A. Oriani, *Corrosion*, 44 (1988): p. 698.
 13. R. Ruetschi and R. Giovanoli, *J. Electrochem. Soc.*, 135 (1988): p.2663.
 14. Rak-Hyun Song, Su-Il Pyun and R. A. Oriani, *Electrochimica Acta*, 36 (1991): p. 825.
 15. S. I. Pyun, C. Lim and R. A. Oriani, *Corros. Sci.*, 33 (1992): p. 437.
 16. P. Fugassi and E. G. Haney, *Titanium Science and Technology*, Ed. By R. I. Jaffee and H. M. Burte), p. 2611. Plenum Press, New York, (1973): p. 2611.
 17. H. T. Yolken, J. Kruger and J. P. Calvert, *Corros. Sci.*, 8 (1968): p. 103.
 18. P. Marcus and J. -M. Herbelin, *Corros. Sci.*, 34 (1993): p. 1123.
 19. C. L. McBee and J. Kruger, *Passivity and its Breakdown on Iron and Iron Base Alloys*, Ed. By R. W. Staehle and H. Okada, NACE, Houston, TX, (1976): p. 131.
 20. R. H. Song, SU-Il Pyun and R. A. Oriani, *J. Electrochem. Soc.*, 137 (1990): p. 1703.
 21. Z. Szklarska-Smialowska, *Advances in Localized Corrosion*, Ed. by H. Isaacs, U. Bertocci, J. Kruger And S. Smialowska, NACE, (1987): p. 41.
 22. M. Janik-Czachor, *J. Electrochem. Soc.*, 128 (1981): p. 514C.
 23. M. Janik-Czachor and A. Szummer, *Passivity of Metals and Semiconductors*, Ed. by

- M. Froment, Elsevier, (1983): p. 547.
24. Z. Szklarska-Smialowska, Pitting Corrosion of Metals, NACE, Houston, Texas, (1986): p.383.
 25. H. J. Engell, *Electrochimica. Acta*, 22 (1977): p. 990.
 26. U. Stimming, *Electrochim. Acta*, 31, (1986): p. 415.
 27. P. Schmuki and H. Böhni, *Werkst. Korros.*, 42 (1991): p.203.
 28. Q. Yang, M.Z. Yang and J. L. Luo, "Effects of Hydrogen on Disorder Degree of Passive Films and Pitting Susceptibility of Type 310 Stainless Steel", the 8th International Symposium on Passivity of Metals and Semiconductors, May 5-14, 1999, Jasper, Alberta, Canada.
 29. A. D. Paola, D. Shukla and U. Stimming, *Electrochim. Acta*, 36 (1991): p.345.
 30. M. H. Dean and U. Stimming, *Corros. Sci.*, 29 (1989): p.199.
 31. V. Halpern, *Philos. Mag. B*, 49 (1984): p. L57.
 32. P. d. Mierry, A. Etcheberry, R. Rizk, P. Etchegoin and M. Aucouturier, *J. Electrochem. Soc.*, 141 (1994): p. 1539.
 33. Z. M. Jarzebski, *Oxide Semiconductors*, translated by Dr. B. Grzybowska-Swierkosz, Pergamon Press, Headington Hill Hall, Oxford, (1973): p.66.
 34. N. Sato, *J. Electrochem.Soc.*, 129 (1982): p.255.
 35. K. E. Heusler and L. Fischer, *Werkstoff. Korros.*, 27 (1976): p. 551.
 36. M. U. MacDonald and D. D. MacDonald, *J. Electrochem. Soc.*, 132 (1985): p. 555.
 37. C. Y . Chao, L. F. Lin, and D. D. MacDonald, *J. Electrochem. Soc.*, 128 (1981): p. 1187.
 38. L. F. Lin, C. Y. Chao, and D. D. MacDonald, *J. Electrochem. Soc.*, 128 (1981): p. 1194.
 39. D. D. Macdonald, *J. Electrochem. Soc.*, 139 (1992): p. 3434.
 40. L. Zhang, D. D. Macdonald, E. Sikora and J. Sikora, *J. Electrochem. Soc.*, 145 (1998): p.898.
 41. K. G. Weil, *Z. Electrochem.*, 59 (1955): p. 711.
 42. N. Sato, *Passivity and its Breakdown on Iron and Iron-based Alloys*, R. Staehle and H. Okada Eds., NACE, Houston, Texas (1976): p.1.

43. B. E. Wilde and J. S. Amijo, *Corrosion*, 23 (1967): p. 208.
44. Z. Szklarska-Smialowska, *Advances in Localized Corrosion*, Ed. by H. Isaacs, U. Bertocci, J. Kruger And S. Smialowska, NACE, (1987): p. 41.
45. J. Mankowski and Z. Szklarska-Smialowska , *Corros. Sci.*, (1975): p. 493.

Chapter 8. Summary and Future Work

8.1. SUMMARY

The effects of hydrogen on passivity and corrosion-related behavior of stainless steels have been investigated in this thesis. Some important and novel results have been revealed:

(1) The critical charging conditions for martensite transformation for 304 stainless steel were determined. The critical charging time for the transformation decreases with the charging current density. Surface cracking is closely related to martensite transformation in 304 stainless steel. When the charging current density is lower than 0.2

mA/cm^2 , no martensite transformation is found no matter how long the specimen is charged. This charging current density is defined as a threshold charging current density, which indicates the stability of austenite. For 304 stainless steel, no cracking can be found on specimens without martensite transformation. The critical charging period is longer for the surface cracking than for the martensite transformation. *In situ* observations after hydrogen charging prove that surface cracking mainly occurs during aging after charging rather than during charging. The surface cracking develops very quickly in the first couple of hours.

(2) Mott-Schottky measurements show that passive films formed on stainless steels have the character of n-type semiconducting films. Hydrogen charging can increase the donor concentration of the film. A hysteresis appeared on the capacitance vs. potential curve, indicating that passive films on stainless steels are highly disordered (defective). The appearance of Urbach tails on the photocurrent spectra confirms the high degree of disorder of passive films on stainless steels. From the slope of the Urbach tail, the disorder energy of the films can be calculated. The important finding is that hydrogen can increase the disorder energy (degree) of the films. Hydrogen also increases the photocurrent response.

(3) The ASTM G48 Method A immersion tests reveal that hydrogen can shorten the pitting initiation time and increase the number of pit initiation sites (pit density). Hydrogen can also affect the pit growth. Both the average pit diameter and apparent pit area percentage increase linearly with the logarithm of the immersion time. The slopes increase with hydrogen charging current density. Pits prefer to initiate around inclusions. Decreasing the surface inclusion density by pickling decreases the pit density.

(4) Hydrogen increases the breakdown and protection potential, indicating an increase in the susceptibility to pitting corrosion. It is found that both hydrogen and chloride ions can increase the anodic current density. The effect is not simply arithmetically additive; instead there is a synergistic effect of hydrogen and chloride ions on the increase in anodic current density. Hydrogen also enhances the deleterious effect of chloride ions on the breakdown potential. In the chloride free solutions, hydrogen has no effect on the

breakdown. However, for the charged specimens in the chloride-containing solutions, even at low charging current density or low concentration of chloride ions, the breakdown potential has an obvious decrease. The breakdown potential decreases with an increase in the charging current density or in the concentration of chloride ions.

(5) Potentiostatic experiments show that hydrogen promotes the film breakdown and hinders the repassivation process. There is a critical concentration of chloride ions for the film breakdown. This critical concentration decreases with an increase in the charging current density. Stress also has the same effect on this critical concentration. An applied tensile stress promotes the breakdown of passive films. The critical concentration of chloride decreases with an increase in the applied tensile stress. The critical concentration is always lower for the hydrogen charged specimens than for the uncharged specimens in the investigated stress range.

(6) AC impedance measurements indicate hydrogen decreases the polarization resistance R_p and increases the double layer capacitance. The decrease in R_p with hydrogen or with chloride ion concentration is consistent with the increase in the anodic current density in the passive range. It reinforces the synergistic effects of hydrogen and chloride ions on the anodic current density.

8.2. SUGGESTIONS AND FUTURE WORK

The hydrogen charging method applied in this research is cathodic hydrogen charging. The electrochemical behavior of the charged surface was then measured. The advantages of this method are that it is easy, quick and economical. However, it should be noted here that this method leads to surface phase transformation and surface cracking. Even though this research shows, that if passive films are present, these do not affect the passive current density and Mott-Schottky behavior greatly, in a strict sense it is better to carry out research on the surface without martensite and surface cracking. If so, the results come from the effect of hydrogen on the passivity without any doubt.

Other possible charging alternatives are charging in hydrogen gas or charging with a Devanathan double cell. The gas charging method needs a special charging chamber where the pressure is controllable. This method can also cause phase transformation and surface cracking. The Devanathan double cell is widely used for hydrogen permeation. The advantage of charging in this cell is that a cathodic current density or potential is applied to the one side of the specimen to charge hydrogen, while the electrochemical behavior of the output side can be measured. Only the charging side encounters surface phase transformation and cracking. By so doing, the effect of surface damage can be avoided and the hydrogen permeation flux can be well controlled. Charging by using a double cell looks to be ideal and should be recommended. However, due to the low diffusivity of hydrogen in austenitic stainless steels, the hydrogen permeation time is quite long. So a very thin foil should be used.

To fully understand the effect of hydrogen on the passivity and corrosion-related behavior, information about the changes in the compositions and structures of passive films due to the hydrogen charging is extremely important. More research is needed. My recommendations for future work include:

- (1) the investigation of the changes in $\text{OH}^-/\text{O}^{2-}$ and $\text{H}_2\text{O}/\text{O}^{2-}$ ratios in the passive film and changes in cation valence;
- (2) the investigation of hydrogen-induced active sites;
- (3) the investigation of the compositional and structural changes due to the presence of hydrogen;
- (4) and the investigation of the kinetics of the synergistic effect of hydrogen and Cl^- on the passive current.

The chemical analysis of the uppermost atomic or molecular layer of a solid is a fundamental problem in surface science. Static SIMS is a very powerful technique in this field. SIMS should be used to analyze the chemical composition changes due to hydrogen charging. XPS analysis should be employed to study the valence changes of cations in the passive film due to the presence of hydrogen in it. The surface morphology changes

upon polarization of hydrogen-charged and uncharged specimens should be observed with AFM. Auger electron spectroscopy and ellipsometry should also be used in the future research to reinforce and complement the results of this study.

The photoelectrochemical measurements have only been carried out in chloride-free solution. The effect of chloride ions on the photocurrent response needs to be revealed. It is important to investigate whether chloride ions increase the disorder degree of the passive films or not. Also the effect of the formation potential of the passive films on the photo-current response needs to be studied.

The study can also be extended to other alloy systems to see whether the effects of hydrogen revealed in this research can also be applied to other alloys.

Appendix: Publications and Presentations during Graduate Study

A.1. PAPERS AND PRESENTATIONS RELATED TO THIS THESIS

A.1.1. Refereed Papers: Published & Accepted

1. Q. Yang and J. L. Luo, The Effects of Hydrogen on the Breakdown of Passive Films Formed on Type 304 Stainless Steel, *Thin Solid Films*, in press.
2. Q. Yang and J. L. Luo, The Hydrogen-Enhanced Effects of Chloride Ions on the Passivity of Type 304 Stainless Steel, *Electrochimica Acta*, in press.
3. Q. Yang and J. L. Luo, Martensite Transformation and Surface Cracking of Hydrogen Charged and Outgassed Type 304 Stainless Steel, *Materials Science and Engineering A*, in press.

4. Q. Yang, L. J. Qiao, S. Chiovelli and J. L. Luo, Critical Hydrogen Charging Conditions for Martensite Transformation and Surface Cracking in Type 304 Stainless Steel, *Scripta Materialia* (USA), 40, No. 11, p1209-1214, (1999)
5. M. Z. Yang, J. L. Luo, Q. Yang, L. J. Qiao, Z. Q. Qin and P. R. Norton, Effects of Hydrogen on Semiconductivity of Passive Films and Corrosion Behavior of 310 Stainless Steel, *Journal of Electrochemical Society*, 146, p2107 (1999).
6. M. Z. Yang, Q. Yang and J. L. Luo, Effects of Hydrogen on Passive Film and Corrosion of AISI 310 Stainless Steel, *Corrosion Science*, 41, p741 (1999).
7. Q. Yang, L. J. Qiao, S. Chiovelli and J. L. Luo, Effects of Hydrogen on Pitting Susceptibility of Type 310 Stainless Steel, *Corrosion*, 54, No. 8, p628 (1998).

A.1.2. Refereed Conference Papers

1. Q. Yang and J.L. Luo, Effects of Hydrogen and Stress on the Corrosion Behavior of 304 Stainless Steel in Chloride-Containing Solution, Proceedings Volume 99-27, *An International Symposium in Honor of Professor Norio Sato: Passivity and Localized Corrosion*, M. Seo, B. MacDougall, H. Takahashi and R. H. Kelly, Eds., the Electrochemical Society, Inc., Pennington, NJ, USA, p397.
2. Q. Yang, M.Z. Yang and J.L. Luo, Effects of Hydrogen on Disorder Degree of Passive Films and Pitting Susceptibility of Type 310 Stainless Steel, *the 8th International Symposium on the Passivity of Metals and Semiconductors*, Jasper, Alberta, Canada, May 9-14, 1999 (in press).
3. Y. M. Zeng, W. Y. Chu, L. J. Qiao, Q. Yang and J. L. Luo, Effects of Hydrogen on Film Structure and Pitting Susceptibility of Nickel and 310 Stainless Steel, *Corrosion 98*, Paper No. 249, NACE, San Diego, CA, March 22-28, 1998.

A.1.3. Papers in Conference Proceedings

1. J. L. Luo and Q. Yang, Synergistic Effects of Hydrogen and Chloride Ions on the Breakdown of Passive Films on Type 304 Stainless Steel, Proceedings of *NACE*

International Northern Area Eastern Conference, Ottawa, October 24-27, 1999, session 7, pp. 1-7.

2. Q. Yang and J. L. Luo, The Effects of Hydrogen on the Pitting Corrosion Behavior of 304 Stainless Steel, Proceedings of the International Symposium on Environmental Degradation of Materials and Corrosion Control in Metals, M. Elboujdami and E. Ghali, Eds., *the 38th Annual Conference of Metallurgists of CIM*, Quebec City, Quebec, August 22-26, p.303-312, 1999.
3. Q. Yang, J. L. Luo and S. Chiovelli, Hydrogen Induced Martensite Transformation and Surface Cracking in Type 304 Stainless Steel, Proceedings of the International Symposium on Materials for Resource Recovery and Transport, *the 37th Annual Conference of Metallurgists of CIM*, Calgary, Alberta, August 16-19, p161-175, 1998.

A.1.4. Conference Presentations

1. Effects of Hydrogen on Passivity and Corrosion Related Behavior of Stainless Steels, the *11th Materials Science Conference*, Kingston, Ontario, Canada, June 16-18, 1999.
2. The Effects of Hydrogen, Chloride Ions and Stress on the Passivity of Stainless Steels, *the 38th Annual Conference of Metallurgists of CIM*, Quebec City, Quebec, August 22-26, 1999.
3. Hydrogen Effect on Passive Film and Pitting Susceptibility of Type 304 Stainless Steel, *the 37th Annual Conference of Metallurgists of CIM*, Calgary, Alberta, August 16-19, 1998.

A.2. PUBLICATIONS AND PRESENTATIONS RELATED TO OTHER RESEARCH TOPICS

A.2.1. Refereed Paper(s)

University of Alberta Library



0 1620 1262 9612

B45408